



**HAL**  
open science

# Retrieval of Aerosol Chemical Composition based on aerosol optical properties

Shuo Wang

► **To cite this version:**

Shuo Wang. Retrieval of Aerosol Chemical Composition based on aerosol optical properties. Atmospheric and Oceanic Physics [physics.ao-ph]. Université du Littoral Côte d'Opale; Anhui Institute of Optics and Fine Mechanics (AIOFM), Hefei, china, 2020. English. NNT : 2020DUNK0567 . tel-03178823

**HAL Id: tel-03178823**

**<https://theses.hal.science/tel-03178823>**

Submitted on 24 Mar 2021

**HAL** is a multi-disciplinary open access archive for the deposit and dissemination of scientific research documents, whether they are published or not. The documents may come from teaching and research institutions in France or abroad, or from public or private research centers.

L'archive ouverte pluridisciplinaire **HAL**, est destinée au dépôt et à la diffusion de documents scientifiques de niveau recherche, publiés ou non, émanant des établissements d'enseignement et de recherche français ou étrangers, des laboratoires publics ou privés.



# Thesis

Ecole doctorale des Sciences de la Matière, du Rayonnement et de  
l'Environnement, Université Lille Nord de France

**Shuo WANG**

Discipline: Physics

Laboratoire d'Optique Atmosphérique, Université de Lille

Laboratoire de Physico Chimie de l'Atmosphère, Université du Littoral Côte d'Opale

---

## **Retrieval of Aerosol Chemical Composition based on Aerosol Optical Properties**

## **Estimation de la composition chimique des aerosols à partir de leurs propriétés optiques**

---

Jean-Claude ROGER	Rapporteur	University of Maryland
Xiaodan GUAN	Rapporteuse	Lanzhou University
Xiaoqing JIA	Examinatrice	Zhejiang University
Marc MALLET	Examineur	Météo-France-CNRS
Weixiong ZHAO	Co-encadrant	Chinese Academy of Science
Weijun ZHANG	Co-directeur	Chinese Academy of Science
Suzanne CRUMEYROLLE	Encadrante	Université de Lille
Weidong CHEN	Directeur	Université du Littoral Côte d'Opale

## Abstract

Aerosol chemical composition is an essential factor to better understand aerosol interactions with climate change, atmospheric environment and human health. Aerosol optical property is closely associated to chemical composition. Nowadays, vertical and global aerosol optical properties are measured. Development of aerosol chemical composition retrieval algorithm based on optical properties is essential to derive aerosol chemical composition with high spatial and temporal resolution. This thesis aims to test and improve the present methods for aerosol chemical composition classification and retrieval.

- (1) **Ångström Exponent (AE) methods:** These methods are based on Scattering (SAE) and Absorption (AAE) AE to derive absorption coefficients by different aerosols or distinguish aerosol types, but many studies used different SAE and AAE values or thresholds. To understand these discrepancies, SAE and AAE dependencies to particle size, relative coating thickness and wavelength pairs were studied for different absorbing aerosols. The results reveal that SAE and AAE depend on wavelength pairs used for calculations and are also greatly influenced by aerosol size, thus knowledge of aerosol size information could reduce the uncertainty of calculating absorption coefficients by different aerosols using AAE. As aerosol particles could exist within the same size bin, SAE and AAE cannot be used to distinguish different compositions effectively by setting thresholds.
- (2) **k-based methods:** These methods aim to retrieve the mass concentrations of different aerosol compounds based on the imaginary part of Complex Refractive Index (CRI,  $m = n + k i$ ). For the application and examination of the  $k$ -based methods, columnar aerosol chemical compositions were retrieved based on CRI and spectral variation of Single Scattering Albedo (dSSA) using long-term AERONET measurements. Dependence of retrieved columnar aerosol chemical compositions on regional transported was investigated in different seasons. This result is comparable to seasonal aerosol emission distribution and transport process. But the

reliable aerosol chemical composition at the same level is still needed to verify this algorithm.

- (3) ***k-ρ* method:** To tackle the difficulty to distinguish Organic Carbon (OC), from Mineral Dust (MD), a new method based on CRI imaginary part (*k*) and aerosol density ( $\rho$ ) was developed. This algorithm was used to obtain the real-time aerosol chemical composition variation during an observation campaign in Shouxian. The retrieved aerosol chemical compositions were consistent with in-situ measurements. The weaker agreement ( $R^2=0.43$ ) of MD compared to the other species is due to the larger uncertainties from retrievals and measurements.

**Key words:** aerosol chemical compositions; Ångström exponent; complex refractive index; aerosol density; in-situ measurement; remote sensing

## Acknowledgements

It is closed to the end of my doctoral work, and I would like to express my sincere appreciate to some people, who have great influence on my work and life during this period.

First of all, I want to give my great gratitude to my director and supervisor in France, Prof. Weidong Chen from Laboratoire de Physico Chimie de l'Atmosphère, Université du Littoral Côte d'Opale, and Suzanne Crumeyrolle from Laboratoire d'Optique Atmosphérique, Université Lille. I am very appreciated to get the opportunity to have a wonderful experience in France with the help of Prof. Chen. He not only guided me in the scientific work but also life in France, and he also introduced the peers in my field to help with my PhD project, especially my nice supervisor Suzanne Crumeyrolle. Suzanne is cheerful and approachable, and is very patient with my work. She always pointed out new ideas when I was confused, and I really cherish the time to discuss with her about the scientific problems.

I am very grateful to my co-director, Prof. Weijun Zhang, and co-supervisor, Weixiong Zhao, from Anhui Institute of Optics and Fine Mechanics, Chinese Academy of Science. They guided me to start my research career, and supported me with excellent research conditions to assist my PhD project. Especially, they offer me the opportunity to abroad for further study.

My sincere gratitude is also reserved for my thesis committee members: Prof. Jean-Claude ROGER, Prof. Xiaodan GUAN, Prof. Xiaojing JIA and Doctor Marc MALLET. This thesis is polished under their carefully review. They also gave me instructive suggestions and comments, which is helpful for my future study in this field.

I would like to acknowledge the head of department Philippe Goloub, Oleg Dubovik, and Philippe Dubuisson to offer me the opportunity to study in LOA. I sincerely appreciate to Yevgeny Derimian, Souichiro Hioki and Benjamin Torres for their help on my research. I am grateful to learn from Romain De Filippi and Fabrice Ducos about the servers and Linux system. Thanks to all staffs in LOA for their friendly

and sincere help.

I am very cheerful to have a great and unforgettable time in France with my dear friends and fellows, and special thanks to Jian Chen, Cheng Chen, Qiaoyun Hu, Huazhe Shang, Nan Yin, etc. I appreciate the memories to share different kinds of food and enjoy travel with Simone Guilbert, Lucie Leonarski, Macos Herreras Giralda, Milygros Herrera and Autoine Rimboud. I am also grateful to the help and accompany from Gaoxuan Wang, Lingshuo Meng and Fengjiao Shen in LPCA, especially Jingjing Wang.

I'm highly thankful to staffs in Laboratory of Atmospheric Physico-Chemistry, Anhui Institute of Optics and Fine Mechanics Xiaofeng Tang, Xuejun Gu, Changjin Hu, Yanbo Gai, Bo Fang, Xiaoxiao Lin and Yang Zhang in China to help with my work. And I am very appreciating to share this unforgettable period with Xuezhe Xu, Qiao Ma, Nana Wei, Zuoying Wen, Nana Yang, Chunhui Wang, Jiacheng Zhou, Hui Yu, Yukuan Chen, etc.

Finally, I would like to give thanks to my beloved parents and families for their continuous encourage and support.

## Contents

<b>Abstract</b> .....	<b>i</b>
<b>Acknowledgements</b> .....	<b>iii</b>
<b>Contents</b> .....	<b>v</b>
<b>List of figures</b> .....	<b>x</b>
<b>List of tables</b> .....	<b>xvii</b>
<b>Chapter 1 Introduction</b> .....	<b>1</b>
<b>Chapter 2 Aerosol microphysical and optical properties</b> .....	<b>11</b>
2.1 Aerosol microphysical properties .....	11
2.1.1 Aerosol size distribution .....	11
2.1.2 Aerosol density.....	14
2.2 Aerosol optical properties .....	16
2.2.1 Extinction, scattering and absorption coefficients .....	16
2.2.2 Single scattering albedo .....	18
2.2.3 Ångström exponent.....	18
2.2.4 Complex refractive index.....	19
2.3 Mixing rules.....	21
2.3.1 External mixing.....	22
2.3.2 Internal mixing.....	22
2.4 Conclusions .....	26
<b>Chapter 3 Observation of aerosol properties</b> .....	<b>27</b>
3.1 Remote sensing.....	27

3.2 In-situ measurement .....	30
3.2.1 Aerosol size distribution measurement .....	30
3.2.2 Aerosol optical property measurement .....	33
3.2.3 Aerosol chemical composition measurement.....	38
3.3 Conclusions .....	40
<b>Chapter 4 Study on Ångström exponent .....</b>	<b>42</b>
4.1 AE methods description.....	42
4.1.1 Calculation of absorption coefficients of different species with AAE	42
4.1.2 Qualitative classification of aerosol chemical compositions with SAE and AAE.....	45
4.2 Robustness of methods based on Ångström exponent .....	47
4.2.1 Simulation of SAE and AAE with Mie theory .....	47
4.2.2 SAE and AAE for BrC.....	48
4.2.3 SAE and AAE for MD .....	50
4.2.4 SAE and AAE of BC .....	52
4.2.5 SAE and AAE for BC coating with clear shell.....	54
4.3 Conclusions .....	60
<b>Chapter 5 Study on aerosol chemical composition retrieval based on the imaginary part of complex refractive index .....</b>	<b>61</b>
5.1 <i>k</i> -based methods description.....	61
5.2 Columnar aerosol chemical compositions dependence on regional transport.	65
5.2.1 Geographical location and emission distribution around Beijing.....	65
5.2.2 Backward trajectories and cluster analysis .....	68

5.2.3 Aerosol physical and optical properties of each cluster .....	72
5.2.4 Aerosol chemical components of each cluster .....	75
5.3 Conclusions .....	79
<b>Chapter 6 Development and application of <math>k</math>-<math>\rho</math> method for campaign at Shouxian</b>	<b>81</b>
6.1 Development of $k$ - $\rho$ method to retrieve aerosol chemical compositions.....	83
6.2 Site and data.....	85
6.2.1 Site description.....	85
6.2.2 Instruments and method.....	86
6.2.3 Comparison of results derived from measurement and retrieval .....	88
6.3 Results .....	91
6.3.1 Aerosol size distribution and optical properties.....	91
6.3.2 Retrieved effective density and complex refractive index.....	94
6.3.3 Aerosol chemical composition retrieval and its temporal variations..	95
6.3.4 Comparison with filter sampled results .....	97
6.4 Numerical simulation and sensitivity test.....	99
6.4.1 Numerical test .....	99
6.4.2 Sensitivity to <i>a priori</i> inputs .....	101
6.5 Conclusions .....	106
<b>Chapter 7 Conclusions and perspectives .....</b>	<b>108</b>
7.1 Conclusions .....	108
7.2 Perspectives .....	112
<b>Résumé .....</b>	<b>114</b>

i. Étude sur l'exposant Ångström.....	115
i.1. Description des méthodes AE.....	116
i.2. simulation de SAE et AAE avec la théorie de Mie.....	116
i.3. SAE et AAE pour BrC, MD et BC.....	117
i.4. Conclusion.....	119
ii. Étude sur la récupération de la composition chimique des aérosols basée sur la partie imaginaire de l'indice de réfraction complexe.....	120
ii.1. Site et méthode.....	121
ii.2. Composants chimiques des aérosols de chaque groupe.....	122
ii.3. Conclusion.....	123
iii. Développement et application de la méthode $k$ - $\rho$ pour la campagne à Shouxian .....	124
iii.1. Site et méthode.....	125
iii.2. Résultats de la mesure et de l'extraction.....	126
iii.3. Comparaison de la composition chimique des aérosols à partir de la récupération et de la mesure.....	128
iii.4. Sensibilité aux intrants a priori.....	129
iii.5. Conclusion.....	129
<b>Appendix.....</b>	<b>131</b>
A1 Mie theory.....	131
A2 Aerosol chemical composition retrieval with $n$ , $k$ and dSSA.....	133
A3 Emission distributions of BC, OC and SO <sub>2</sub> +NO <sub>x</sub> .....	135
<b>Abbreviations and Acronyms.....</b>	<b>139</b>

**Reference ..... 144**

## List of figures

Figure 1.1 Evaluation of radiative forcing in 2011 relative to 1750 and aggregated uncertainties for the main driver influencing climate change from the 5 <sup>th</sup> assessment report of IPCC (Stocker, 2014).....	2
Figure 1.2 Aerosol sources and sinks in the atmosphere ( <a href="http://www.ems.psu.edu">http://www.ems.psu.edu</a> ). ..	4
Figure 2.1 Schematic multi-modal particle size distributions with typical transformations and example particle types within each mode ( <a href="https://www.dwd.de">https://www.dwd.de</a> ). .....	12
Figure 2.2 Aerosol possible shapes in the real atmosphere. (a) Spherical; (b) spherical particle with voids inside; (c) irregular particle; (d) irregular particle with voids inside.....	15
Figure 2.3 Spectral variation of imaginary part of complex refractive index for OC and MD (the result of Kirchstetter et al. (2004) is from laboratory combustion, and the results of Shamjad et al. (2016) is from analysis with field measurement. Tar ball is a kind of OC).....	21
Figure 2.4 Externally mixed (a) and internally mixed (b) aerosols.....	21
Figure 2.5 Mixing rules for internal mixing. (a) MG theory; (b) BR theory; (c) C-S model; (d) VAM model .....	22
Figure 2.6 Schematic for BC coated with a clear shell (left) and brown shell (right). Incident rays (1 and 1') are not deviated by the shell and are absorbed by BC core ( $b_{abs,BC\_core}$ ); Ray 2 and 2' are refracted by the coating (lensing effect) and then meet the BC core where they will be absorbed by BC core known as the lensing effect ( $b_{abs,BC\_lens}$ ); Rays 3, 3', and 4' are refracted by the clear shell but not enough to meet the BC core and then Ray 4' is absorbed by the BrC shell ( $b_{abs,BrC\_shell}$ ) while Ray 3 and 3' are leaving the particle.....	24

---

Figure 3.1 Distribution of global AERONET sites ( <a href="https://aeronet.gsfc.nasa.gov/">https://aeronet.gsfc.nasa.gov/</a> )..	29
Figure 3.2 Schematic of electrostatic classifier with long DMA. ....	31
Figure 3.3 Schematic of CPC.....	32
Figure 3.4 Schematic of APS (TSI, 2004).....	33
Figure 3.5 Illustration of CRDS technique (Wojtas et al., 2013). ....	35
Figure 3.6 Schematic diagram of IBBCEAS for aerosol extinction measurement (Zhao et al., 2017c).....	35
Figure 3.7 Schematic diagram (left) and forward scattering truncation geometry (right) of ISIN (Varma et al., 2003).....	36
Figure 3.8 Schematic diagram of a three-wavelength cavity enhanced albedometer (Xu et al., 2018a).....	38
Figure 4.1 Aerosol classification schemes with SAE and AAE from Cazorla et al. (2013) and Cappa et al. (2016).....	46
Figure 4.2 Simulation of SAE dependence on wavelength couples for BrC with different geometric mean diameters. Figure 4.3 ~ 4.9 use the same marks. The symbol ‘×’ indicates the wavelength pair used in scheme by Cazorla et al. (2013), and ‘o’ represents for the scheme from Cappa et al. (2016)....	49
Figure 4.3 Simulation of AAE dependence on wavelength couples for BrC at different geometric mean diameters.....	50
Figure 4.4 Simulation of SAE dependence on wavelength couples for MD with different geometric mean diameters (GMD). (a) ~ (d) for dust with single mode with GMD of 200, 300, 400 and 500; (e) and (f) for dust with single mode with GMD of 300 nm for fine mode (GMD <sub>f</sub> ) and 3 μm and 4 μm for coarse mode (GMD <sub>c</sub> ).....	51
Figure 4.5 Simulation of AAE dependence on wavelength couples for MD at different geometric mean diameters.....	52

Figure 4.6 Simulation of SAE dependence on wavelength couples for BC at different geometric mean diameters.....	53
Figure 4.7 Simulation of AAE dependence on wavelength couples for BC with different geometric mean diameters. ....	54
Figure 4.8 Simulation of SAE dependence on wavelength couples for BC with core geometric mean diameter of 100 nm, but varied relative coating thickness ( $GMD_{shell}/GMD_{core}$ ).....	55
Figure 4.9 Simulation of AAE dependence on wavelength couples for BC with core geometric mean diameter of 100 nm, but varied relative coating thickness ( $GMD_{shell}/GMD_{core}$ ).....	56
Figure 4.10 Simulation of $AAE_{BC\_CS,880-950}$ (a), $AAE_{BC\_CS,370-880}$ (b), $AAE_{BC\_CS,370-880} - AAE_{BC\_CS,880-950}$ (c) and $AAE_{BC\_CS,370-880}/AAE_{BC\_CS,880-950}$ (d) for BC coating with clear shell impacted by the geometric mean diameter of BC core ( $GMD_{core}$ ) and the relative coating thickness ( $GMD_{shell}/GMD_{core}$ )..	57
Figure 4.11 BC absorption (370 nm) uncertainties using $AAE_{370-880}$ of 1 (a) and $AAE_{370-880}$ equal to $AAE_{880-950}$ (b). ....	59
Figure 5.1 SSA spectra for BrC and dust (Wang et al., 2013) from simulation with Mie theory. BrC and Dust have the same $k$ values at the four wavelengths, but different size distributions. Case 1 has $k$ of 0.0122 at 440 nm, and 0.0013 at 675, 870 and 1020 nm; case 2 has $k$ of 0.0525 at 440 nm, and 0.005 at other three wavelengths.....	64
Figure 5.2 Geographical location of Beijing site (marked by the red dot), and the region of North China Plain is marked with solid black ellipse. The main dust sources impacting Beijing are marked by dashed black ellipses (A: Taklimakan desert; B: Tengger desert, Maousu desert, Ulan Buh desert and Badain Jaran desert; C: Hunshdak desert).....	66
Figure 5.3 Spatial distribution of TSP emission in the four seasons from 2005 to 2014.	

---

Beijing is marked by the black triangle.....	67
Figure 5.4 Spatial distribution of the ratio of seasonal mean TSP emission to the total average TSP emission from 2005 to 2014.....	68
Figure 5.5 Percentage changes in the total spatial variance (TSV) against the number of clusters for different seasons. The black arrow marks the appropriate number of clusters. ....	70
Figure 5.6 72-hour daily air mass backward trajectory clusters ending at Beijing in four seasons, together with satellite products from Aqua level 3 products. The colors of the trajectories represent different clusters, which are also used for distinguishing the corresponding columnar aerosol properties in the following text. ....	71
Figure 5.7 Seasonal variations of aerosol size distributions for different clusters.....	73
Figure 5.8 Spectral variations of AOT, SSA, AAOT, n and k for different seasons and different clusters. ....	74
Figure 5.9 Average of volume fractions for five components in different seasons and different clusters. ....	76
Figure 5.10 Average of columnar mass concentrations for the five components in different seasons and different clusters. ....	78
Figure 6.1 Aerosol mass concentrations for polluted (left) and clear (right) days (Hu et al., 2012).....	81
Figure 6.2 Geographical location and surroundings of the observation site.....	85
Figure 6.3 Illustrations of the SMPS and APS data merging operation. (a) Complete size distribution of SMPS (red) and APS (blue) number concentrations ( $dN/d\log(D_p)$ ) are shown along with particle diameter ( $D_p$ ) respectively (mobility diameter ( $D_m$ ) for SMPS, and aerodynamic diameter ( $D_a$ ) for APS). The dashed blue line is the APS curve with size correction by	

converting aerodynamic diameter to mobility diameter. (b) Zooms in the overlap region.....	87
Figure 6.4 Comparison of measured and retrieved, from Mie theory, extinction and scattering coefficients.....	89
Figure 6.5 Relative frequency of the differences between measured and calculated extinction and scattering coefficients. ....	89
Figure 6.6 The comparison of effective density ( $\rho_e$ ) by merging APS to SMPS diameter with density calculated with VAM rule ( $\rho_{VAM}$ ) (a); the comparison between the imaginary part of refractive index retrieved from Mie theory ( $k_{Mie}$ ) and calculation from VAM rule ( $k_{VAM}$ , b and c). ....	90
Figure 6.7 Relative frequency of the differences between $\rho_e$ and $\rho_{VAM}$ (a), and $k_{Mie}$ and $k_{VAM}$ ((b) for $k$ at 365 nm and (c) for $k$ at 532 nm). ....	90
Figure 6.8 Time series of size distribution, meteorological conditions and optical properties during the observation period at Shouxian site. Two pollution periods (P1, from 15:00 LT on 7 December to 13:00 LT on 8 December, and P2, from 16:00 LT on 8 December to 11:00 LT on 9 December) are marked with red and magenta rectangles respectively and one clean period (P3, from 21:00 LT on 9 December to 15:00 LT on 11 December) marked with blue dashed lines. (a) Particle number size distribution; (b) wind speed and wind direction; (c) extinction and scattering coefficients, (d) absorption coefficient, and (e) single scattering albedo at 365 and 532 nm. ....	91
Figure 6.9 24 h backward trajectories ending at Shouxian site at 500 m above ground level during two pollution periods (P1 and P2). The green and blue lines correspond to the periods of development and decline of pollution events, respectively. The red lines correspond to the period that extinction remains at a high level ( $b_{ext} > 800 \text{ Mm}^{-1}$ at 365 nm).....	93
Figure 6.10 Retrieved (a) aerosol effective density ( $\rho_e$ ), and (b) the real ( $n_{Mie}$ ) and (c)	

imaginary ( $k_{Mie}$ ) part of CRI at 365 and 532 nm from experimental observation data.....	94
Figure 6.11 Retrieved (a) volume fractions, and mass concentration (MC) of (b) BC, (c) OM, (d) MD and (e) SNA. Average mass fraction of each chemical component on (f) all observation days, (g) pollution period P1, (h) pollution period P2, and (i) clear period P3.....	96
Figure 6.12 Comparison and linear regression between the measured and retrieved mass concentrations. (a,f): the sum of the mass concentrations of BC, OM, MD, and SNA from measurement ( $mSum_{meas}$ ) and retrieval ( $mSum_{retr}$ ); (b,g): $mEC_{meas}$ and $mBC_{retr}$ ; (c,h): $mOM_{meas}$ and $mOM_{retr}$ ; (d,i): $mMD_{meas}$ and $mMD_{retr}$ ; (e,j): $mSNA_{meas}$ and $mSNA_{retr}$ . The solid red lines are the results of linear fit, and the dashed magenta lines are the 1:1 lines. ....	98
Figure 6.13 Numerical test flow chart of aerosol chemical composition retrieval algorithm. Solid parts: generation of numerical experimental data with randomly generated fractions of BC, OM, MD and SNA; dashed parts: retrieval of aerosol chemical composition. ....	100
Figure 6.14 Comparison of assumed and retrieved volume fractions of (a) BC, (b) OM, (c) MD, and (d) SNA. The red lines are the linear fit results.....	101
Figure 6.15 The mass concentration differences in the mean level between the <i>a priori</i> inputs used in this study (Baseline) and the possible high and low limit from literatures (table 6.1 and 6.2). (a) ~ (d) are for the mass concentration of BC, OM, MD and SNA respectively.....	103
Figure 6.16 The same as figure 6.15 but for OM dominated case.....	104
Figure 6.17 The same as figure 6.15 but for MD dominated case.....	105
Figure 6.18 The same as figure 6.15 but for SNA dominated case. ....	106
Figure A1.1 Coordinate centred on the spherical particle with radius of $r$ . ....	131

Figure A3.1 Spatial distribution of BC emission in the four seasons from 2005 to 2014.  
..... 135

Figure A3.2 Spatial distribution of the ratio of seasonal mean BC emission to the total  
average BC emission from 2005 to 2014. .... 136

Figure A3.3 Spatial distribution of OC emission in the four seasons from 2005 to 2014.  
..... 136

Figure A3.4 Spatial distribution of the ratio of seasonal mean OC emission to the total  
average OC emission from 2005 to 2014. .... 137

Figure A3.5 Spatial distribution of primary SO<sub>2</sub>+NO<sub>x</sub> emission in the four seasons  
from 2005 to 2014. .... 137

Figure A3.6 Spatial distribution of the ratio of seasonal mean SO<sub>2</sub>+NO<sub>x</sub> emission to  
the total average SO<sub>2</sub>+NO<sub>x</sub> emission from 2005 to 2014. .... 138

## List of tables

Table 2.1 Material density for different aerosol chemical compositions within previous studies.....	14
Table 2.2 AAE values for BC, OC and MD from previous studies (the values without specific wavelength are fitted results with multi wavelengths). ....	19
Table 2.3 The values of wavelength independent $n$ and $k$ from previous studies. ....	20
Table 3.1 Satellite sensors and their global coverage period, spatial resolution, wavelength range.....	28
Table 3.2 Commonly used instruments for aerosol extinction, scattering and absorption coefficient measurements. ....	34
Table 5.1 Summary of aerosol chemical composition retrieval methods based on $k$ .	65
Table 5.2 Mean aerosol optical properties value for the four seasons at 675 nm. ....	74
Table 5.3 Seasonal mean values of retrieved aerosol chemical composition volume fractions and mass concentrations.....	78
Table 6.1 Imaginary parts of the refractive index ( $k$ ) at 365 and 532 nm used for aerosol chemical composition retrieval in this study (baseline, font in bold), and the low (superscript with L) and high (superscript with H) limits for sensitivity test. ....	84
Table 6.2 Material densities and ratio of OM to OC (OM/OC) used for aerosol chemical composition retrieval in this study (baseline, font in bold), as well as the low (superscript with L) and high (superscript with H) limits for sensitivity test.....	84
Table 6.3 List of the mean, minimum and maximum values of each optical parameter during the observation period.....	92
Table 6.4 The effective density, imaginary refractive index and volume fractions of	

different cases for sensitivity test. ....	102
Table A2.1 CRI, MAE and density for each composition used in this study (Li et al., 2015).....	135

## Chapter 1 Introduction

Lately, global warming (Ramanathan and Carmichael, 2008; Zhou and Tung, 2013), air pollution (Tao et al., 2014), extreme weather (Kaufman et al., 2005; Zhang et al., 2007; Zhang and Mao, 2015; Zuo et al., 2019) and respiratory diseases (Dockery and Pope, 1994; Tellez-Rojo et al., 2020) have aroused great attention, and atmospheric aerosol plays an essential role on these issues.

The scientific consensus advocating the impact of humans on the atmosphere was made public in the first reports of the Intergovernmental Panel on Climate Change (IPCC) in 1990 and 1995. These reports make the connection between the rise of the sea level and the global ice melt, the temperature increase (+ 0.74 °C between 1906 and 2005, IPCC, 2007) and the increase in anthropogenic greenhouse gases. The overall impact of present-day atmospheric aerosols is estimated to be cooling, globally counterbalancing a significant fraction of the warming associated with greenhouse gases (IPCC, 2013). The climate could be affected by aerosol via three aspects: (1) direct effect, (2) indirect effect and (3) semi-direct effect.

Aerosol impacts the radiative balance by scattering and absorbing the solar radiation, which is called **direct effect** (Bellouin et al., 2005; Chung et al., 2005; Chung, 2005; Heald et al., 2014). The increasing aerosol in the atmosphere can reduce the energy flux arriving at the Earth's surface, thus producing a cooling effect. Absorbing aerosols absorb light and thereby warm the atmosphere, but also cool the surface (Andreae et al., 2005). Even though great progress has been made in recent years to reduce the uncertainty of total aerosol direct effect at the top of the atmosphere, it is still substantial compared to uncertainties associated with greenhouse gases. The global average direct effect is estimated to be  $-0.27 \text{ W m}^{-2}$  with large uncertainties ( $-0.77 \sim 0.23 \text{ W m}^{-2}$ , figure 1.1). Moreover, the uncertainty of individual radiative forcing for several aerosol components (eg. BC, OC, nitrate, etc) is large (Myhre et al., 2013).

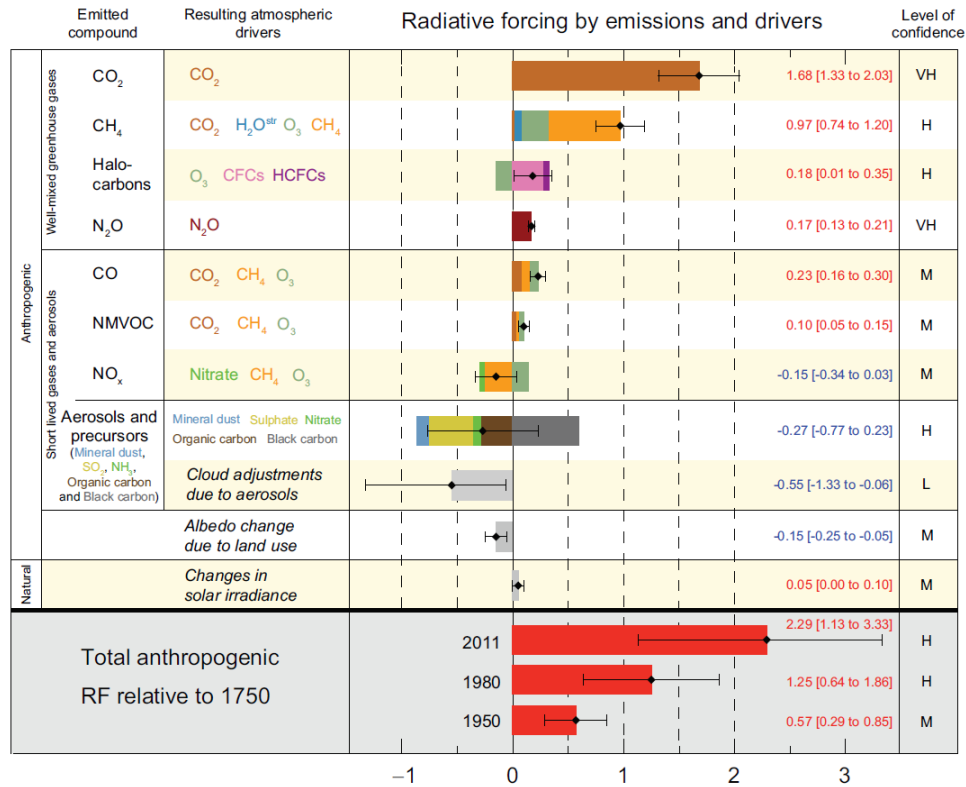


Figure 1.1 Evaluation of radiative forcing in 2011 relative to 1750 and aggregated uncertainties for the main driver influencing climate change from the 5<sup>th</sup> assessment report of IPCC (Stocker, 2014).

In addition to their direct effect, aerosol could also act as Cloud Condensation Nuclei (CCN), and change macro and micro properties of cloud (cloud cover, height, lifetime, droplet size distribution and liquid water content) and its optical properties (scattering and absorbing) (Boucher, 1999; Koch and Del Genio, 2010; Li et al., 2017), which could influence radiative forcing indirectly, and it is named as **indirect effect** (Crumeyroille et al., 2013; Kaufman et al., 2005; Li et al., 2011). More aerosols produce more, but smaller, droplets in a cloud, and make it more reflective. Smaller droplets are less likely to coalesce into raindrops, and thus the lifetime of clouds is extended, again increasing the cloud albedo. The indirect effect leads to a cooling of the climate and is estimated at  $-0.55 \text{ W m}^{-2}$  ( $-1.33$  to  $-0.06 \text{ W m}^{-2}$ ).

Aerosol vertical distribution affects vertical temperature variation, and then

changes atmosphere stability and cloud formation, which is named as **semi-direct effect** (Ding et al., 2016; Huang et al., 2018; Wilcox et al., 2016). Absorbing aerosols could warm the atmosphere where they are suspended by absorbing the atmospheric radiation, which is a main factor for global warming (Heald et al., 2014; Myhre et al., 2013). Moreover, absorbing aerosols could either increase or decrease cloud cover depending on cloud type and the location of absorbing species in reference to clouds (Koch and Del Genio, 2010).

The large uncertainties related to aerosol impact on earth radiative balance are mainly due to a partial knowledge of their properties. Indeed, atmospheric aerosols are emitted by different sources and subject to aging processes upon interactions between particles and gases, making their physical, chemical, and optical properties constantly evolving (Peng et al., 2016; Sun et al., 2015a; Sun et al., 2015b; Wang et al., 2017b; Xu et al., 2016). Indeed, these particles could be produced naturally (e.g. volcanoes and biomass burning episodes) or by anthropogenic sources (e.g. industries and traffic). Moreover, we can distinguish primary from secondary aerosols. Primary aerosols are emitted within the atmosphere directly in the solid phase. The primary marine aerosol is dominated by the sea salts generated by sea spray, and primary continental aerosol is generated from fossil fuel combustion, biomass burning, soil dust, volcano eruption (figure 1.2). Secondary aerosols are formed via chemical transformation from gaseous precursors, like  $\text{SO}_2$ ,  $\text{NO}_x$  and  $\text{NH}_3$ , etc (Bauer et al., 2007a; Berglen, 2004; Huang et al., 2016; Levin and Cotton, 2008).

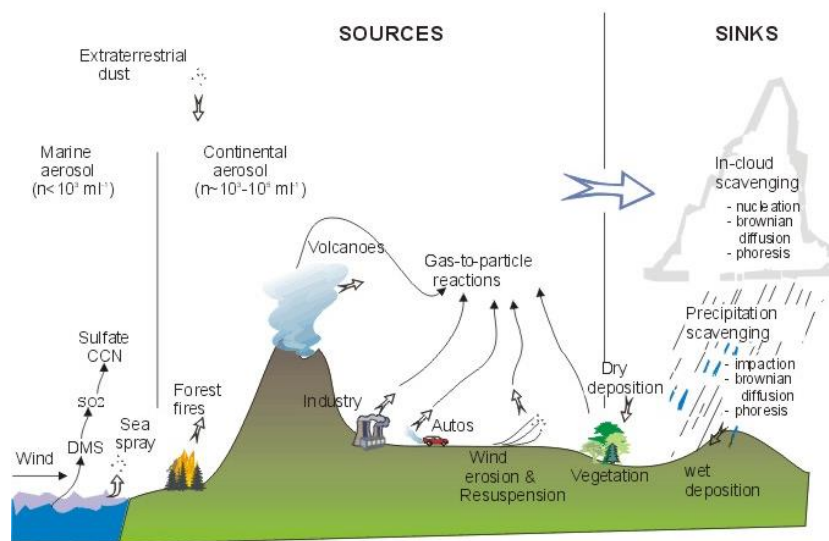


Figure 1.2 Aerosol sources and sinks in the atmosphere (<http://www.ems.psu.edu>).

The aerosol microphysical processes within the atmosphere could modify aerosol properties through **coagulation** of two particles together or through **condensation** of condensable gases, such as  $\text{SO}_2$  or  $\text{NO}_2$  (Alonso et al., 1999; Crumeyrolle et al., 2008). Both mechanisms are size depending and lead to particle diameter increasing. Coagulation is more important for ultrafine particles (diameter  $< 100 \text{ nm}$ ) since they are typically in greater number than fine (diameter  $< 2 \text{ }\mu\text{m}$  or  $2.5 \text{ }\mu\text{m}$ ) and coarse (diameter  $> 2 \text{ }\mu\text{m}$  or  $2.5 \text{ }\mu\text{m}$ ) particles, and have high mobility (Seigneur, 2019). Those particles coagulate preferentially with fine particles of diameter ranging from about 50 to 500 nm. Coagulation rates become negligible for coagulation with particles larger than  $2.5 \text{ }\mu\text{m}$  because their number concentration is quite low. Different with coagulation, condensation may not take place on ultrafine particles, because of their strong curvature that could causes evaporation. The condensation rate is more important with diameter ranging from 30 to 300 nm for polluted urban area (Pierce and Adams, 2007). Condensation is also influenced by environmental conditions. Indeed, lowering the temperature and decreasing vapor pressure are largely known to increase the condensation occurrence which is the mechanism of ultrafine particle growth (Pierce and Adams, 2007).

Aerosol particles are mainly concentrated within the boundary layer, closer to the sources. As aerosols could stay within the atmosphere from a few hours to a few weeks, they could be transported vertically up to the stratosphere and horizontally in both hemispheres (Hu et al., 2019; Ramanathan and Carmichael, 2008). Aerosol particles are removed from the atmosphere by **wet and dry deposition** (figure 1.2). Wet deposition removes gases and particles from the atmosphere and deposits them on the surface throughout precipitations, including the deposition in cloud (serving as CCN or captured by cloud droplet) and below cloud (washout by raindrops) (Chate et al., 2003). In opposition, dry deposition corresponds to particles reaching surfaces via sedimentation, interception, and diffusion processes (Vong et al., 2010). These processes are depending on aerosol properties, such as their hygroscopicity and size.

The different sources and various micro- and macro- physical processes lead to a huge diversity of aerosols in terms of optical, physical and chemical properties. This could explain the complexity to study aerosol properties and their impacts.

Aerosol chemical composition is closely related to the emission sources, and is therefore essential to provide to all governments information to make policy, and then effectively alleviate exacerbation of global warming. In this study, three absorbing species were considered: Black Carbon (BC), Organic Carbon (OC) and Mineral Dust (MD) and scattering species (SNA): Sulfate (S), Nitrate (N) and Ammonium (A).

Among the three absorbing species, BC is distinguished for the strong absorption from ultraviolet (UV) to near-infrared. It is recognized as the second most important factor, after CO<sub>2</sub>, for global warming (Bond et al., 2013; Ramanathan and Carmichael, 2008). The primarily emitted BC is hydrophobic, lacy-structured and made of smaller spherules or monomers (Chung et al., 2012a; Liu et al., 2018). As BC is emitted with condensable gases, it could be aging quickly due to coagulation, oxidation of the intrinsic OC, and coating (Riemer et al., 2010). During this process, the BC particles tend to be more spherical and become internally mixed with other species (Wu et al., 2018b). The absorption coefficient of coated BC could be significantly enlarged (by 1 ~ 2.3 at 532 nm) when coated with absorbing or non-absorbing species (Lack and Cappa,

2010; Liu et al., 2015a; Liu et al., 2017; Peng et al., 2016; Xu et al., 2018b).

OC was treated by most climate models as pure scattering aerosol (Myhre et al., 2007; Stier et al., 2007), but recent studies (Chen and Bond, 2010; Kirchstetter et al., 2004; Shamjad et al., 2015) proved that some OC can also absorb light, especially in UV, and are known for this reason as Brown Carbon (BrC). The mass concentration of OC could be converted to Organic Matter (OM) or Organic Aerosol (OA) with a factor ranging from 1.3 to 2.16, depending on the source and age of particles (El-Zanan et al., 2012; Malm et al., 2011; Putaud et al., 2000; Russell, 2003; Tao et al., 2017; Turpin and Lim, 2001; Xing et al., 2013). The OM to OC ratio used in our study is 1.6 referring to observations by Xing et al. (2013) at different sites in China. OM is the main mass contributor to fine particles (20 ~ 50%, Tao et al., 2017), even though it has smaller density ( $\sim 1.2 \text{ g cm}^{-3}$ , Rissler et al., 2014). It contains numbers of species, and they have different physical and optical properties. According to their hygroscopic properties, OM can be divided into Water Soluble Organic Matter (WSOM) and Water Insoluble Organic Matter (WIOM) (Carbone et al., 2010; Gurganus et al., 2015).

Soil or mineral dust is the main contributor in term of atmospheric aerosol mass concentration. It could be emitted by natural (wind erosion) or anthropogenic processes (such as agriculture, deforestation and traffic on dirt road, Engelbrecht and Derbyshire, 2010). Similar to BrC, the MD absorption decreases with increasing wavelength in the visible spectrum, which brings further difficulties to distinguish both species using only absorbing property. MD is characterized with large size, higher density ( $2.6 \text{ g cm}^{-3}$ , Wagner et al., 2012), irregular shape and low hygroscopicity (Li et al., 2014). Its physical properties are therefore entirely different from OC.

SNA are purely scattering aerosols and mostly have a cooling effect on the climate by directly scattering light and playing the role of CCN (Lelieveld and Heintzenberg, 1992; Mitchell and Johns, 1997). The gas to particle process is the main source of SNA, which dominate 25 ~ 48 % in  $\text{PM}_{2.5}$  (Tao et al., 2017). They have strong hygroscopicity, and could decrease visibility greatly exerting an important effect on environment

quality (Kim et al., 2012; Tang and Munkelwitz, 2010; Wexler and Clegg, 2002). They can also coat on other particles such as BC or dust, and then alter optical properties of the original particle (Bauer et al., 2007b; Lim et al., 2018).

Methods to identify aerosol chemical compositions include direct measurement of aerosol chemical compositions with off-line methods dominated by filter sampling analysis (Tao et al., 2017; Xue et al., 2016; Zhao et al., 2017b) and on line methods based on aerosol mass spectrum techniques (Canagaratna et al., 2007; Jayne et al., 2000; NG et al., 2011; Sun et al., 2015a). The available techniques to measure aerosol chemical composition have shortcomings such as low resolution, high cost, or complexity of implementation and are only limited to in-situ measurements at very limited locations around the world. Because air pollution horizontal extension varies a lot even in one city (Liao et al., 2017) and usually lasts for a few days (Guo et al., 2014; Xu et al., 2016), comprehensive and continuous aerosol chemical composition measurements with high temporal and spatial resolution are needed to identify aerosol sources, monitor pollution processes, and evaluate their impact on radiative forcing.

To obtain regional and even global scale information about aerosol chemical composition and evaluate its influence on climate and environment, models, like global circulation models (Koch et al., 2007) and chemical transport models (Chin et al., 2002; Chin et al., 2000; Dore et al., 2015; Rastigejev et al., 2007), are well developed. These models are based on aerosol emission inventory and include horizontal and vertical transport, as well as new particle formation and removal mechanisms. To evaluate model performances, the simulated aerosol chemical compositions are converted to optical properties (e.g. Aerosol Optical Thickness, AOT) using assumed physical and chemical properties, such as size distribution, density, Complex Refractive Index (CRI) and Mass Extinction Efficient (MEE) (Kinne et al., 2006). But the comparison among different models shows large discrepancies mostly due to uncertainties associated with aerosol emission inventories, removal rates, aerosol residence time, MEE and so on (Textor et al., 2006). For example, Myhre et al. (2013) simulated that direct aerosol effect due to total anthropogenic aerosols ranged from  $-0.58$  to  $0.02 \text{ W m}^{-2}$  with 16

models.

Aerosol optical measurements, including in-situ as well as ground-based and satellite remote sensing, allow near-continuous aerosol monitoring throughout the world. As discussed above, different aerosols have distinguished optical and physical properties making it possible to identify aerosol chemical compositions with optical and physical properties. This research could help expand the current knowledge of spatiotemporal variability in aerosol type globally, particularly where chemical composition measurements do not exist but concurrently with optical property measurements (Schmeisser et al., 2017).

To identify aerosol chemical compositions with optical properties, parameters like CRI and Scattering and Absorbing Ångström exponents (SAE and AAE) are used as indicators for aerosol types. Some studies choose to consider AAE and CRI as constants for the three main absorbing species (BC, BrC and MD) (Bahadur et al., 2012; Schuster, 2005; Schuster et al., 2016a). Based on these parameters, two methods are widely used to identify aerosol chemical compositions, including AE methods and  $k$ -based methods.

**AE methods:** AAE is by definition related to the aerosol absorbing species. BC is distinguished from OC and MD with an AAE value around 1 over the whole visible range, while OC and MD have AAE larger than 1 (Bahadur et al., 2012; Hoffer et al., 2017; Olson et al., 2015; Zanatta et al., 2016). Based on these optical characteristics, two method types were built to identify different aerosol chemical compositions:

Absorption contributed by different aerosol species could be calculated with **AAE** alone assuming that AAE is an intrinsic parameter (Bahadur et al., 2012; Chung et al., 2012b; Lack and Langridge, 2013; Wang et al., 2018; Wang et al., 2016; Zhang et al., 2019). However, some studies revealed that AAE also varied with particle size, mixing state and selected wavelength pairs (Lack and Cappa, 2010; Schuster et al., 2016b; Wang et al., 2018; Wang et al., 2016), and a constant AAE might bring large uncertainties. Lack et al. (2013) calculated that the BC absorption coefficient retrieval uncertainties were between 20% and -40% using a fixed BC AAE ranging between 0.55

and 1.7. The uncertainties would be enlarged when BC AAE values are set out of this range. At present, the comprehensive investigation of AAE dependence on wavelength pairs, size and mixing state for all absorbing particles is scarce.

SAE vs. AAE space method (Cappa et al., 2016; Cazorla et al., 2013; Russell et al., 2010; Schmeisser et al., 2017) is developed to improve the classification including aerosol size information. SAE is used to distinguish aerosol chemical compositions by size, because SAE is larger for relatively small particles, and vice versa. BC and OC are generally considered as small particles, while MD is treated as large particles. By setting appropriate thresholds in the SAE vs. AAE space, BC, OC, MD and their mixture can be identified qualitatively (Russell et al., 2010). However, the thresholds to separate aerosol types differ from one study to another (Cappa et al., 2016; Cazorla et al., 2013; Schmeisser et al., 2017).

***k*-based methods:** This method is widely used to quantitatively retrieve aerosol chemical composition based on ground-based remote sensing measurements (Arola et al., 2011; Choi and Ghim, 2016; Li et al., 2013; Schuster, 2005; Schuster et al., 2016a; Wang et al., 2013; Zhang et al., 2018). The main idea is based on the spectral dependence differences of *k* for different absorbing species. BC is distinguished from other species for its strong absorption within the visible spectrum and extremely larger *k* in comparison to OC and MD. To distinguish OC and MD, the size (Schuster et al., 2016a; Zhang et al., 2018) and spectral variation of Single Scattering albedo (dSSA) (Wang et al., 2013) were used as additional parameters to their spectral absorbing properties. However, although MD is the main contributor to the coarse mode (Dubovik et al., 2002), it also exists within the fine mode, and there is a non-negligible fraction of BC and OC within the coarse mode, especially for polluted days (Hu et al., 2012). Up to now, *k*-based methods were only applied to data obtained from remote sensing. Further improvement and verification with directly measured compositions are needed.

Even though great progresses have been made to identify aerosol compositions, the existing methods still have some controversies and lack of verification with directly measured aerosol chemical compositions. The aim of this thesis is to investigate the

following crucial issues:

- (1) How do AAE and SAE perform to distinguish different aerosol types and derive absorptions by different aerosols?
- (2) How do the  $k$ -based methods perform to retrieve columnar aerosol chemical compositions?
- (3) How to realize the closure study between retrieved and measured aerosol chemical compositions?

In chapter 2, we will describe the concepts of aerosol microphysical and optical properties. Chapter 3 will present the technique of remote sensing and in-situ measurement to obtain aerosol properties, especially the instruments used in our study. Chapter 4 is dedicated to the detail description and further investigation of the AE methods. Chapter 5 will introduce the  $k$ -based methods, and its application to study columnar aerosol chemical composition dependence on regional transport. In chapter 6, we develop a new method based on  $k$  and density ( $k$ - $\rho$  method) to retrieve aerosol chemical compositions (BC, OM, MD and SNA) based on in-situ measurement.

## Chapter 2 Aerosol microphysical and optical properties

### 2.1 Aerosol microphysical properties

#### 2.1.1 Aerosol size distribution

Aerosol particle size is a crucial parameter depending on aerosol sources and physical processes within the atmosphere, which determines aerosol lifetime (Williams et al., 2002), scattering ability (Sinclair and La Mer, 1949) and radiative effect (Matsui, 2018).

Most aerosols in the atmosphere are irregular, which makes it difficult to measure their real diameter. There are three commonly used parameters to describe aerosol size, including aerodynamic diameter ( $D_a$ ), optical equivalent diameter ( $D_o$ ) and (electrical) mobility diameter ( $D_m$ ). Aerodynamic diameter is defined according to particle's velocity within quiescent air with low Reynolds number. Optical equivalent diameter means that an aerosol particle has the same scattering coefficient as spherical particle of Polystyrene Latex (PSL,  $m = 1.598 + 0i$  at 532 nm, Pettersson et al., 2004). The electrical mobility diameter is the diameter of a sphere with the same migration velocity in a constant electric field as the particle of interest.

According to the size, aerosol could be divided into few modes: nucleation mode, Aitken mode, accumulation mode, and coarse mode as depicted in figure 2.1. Particles in the nucleation mode (1 ~ 10 nm) are formed by gas to particle conversion. The nucleated particles are numerous but are probably the least stable within the atmosphere. Indeed, it could act as condensation nuclei for any condensation vapour. In a couple of hours, those particles growth up to enrich the Aitken mode (10 ~ 100 nm) mostly made of soot particles from biomass burning and fossil fuel burning. Accumulation mode (100 ~ 1000 nm) particles could come from the growth of Aitken particles, or from direct emissions (natural or anthropogenic) within the atmosphere. The accumulation mode particles are the most stable with the longest residence time within the atmosphere leading to serious influence on air pollution and human health. Coarse mode (> 1000

nm) particles, including dust volcanic ash and sea salt, are usually associated with large mass concentration, but low number concentration.

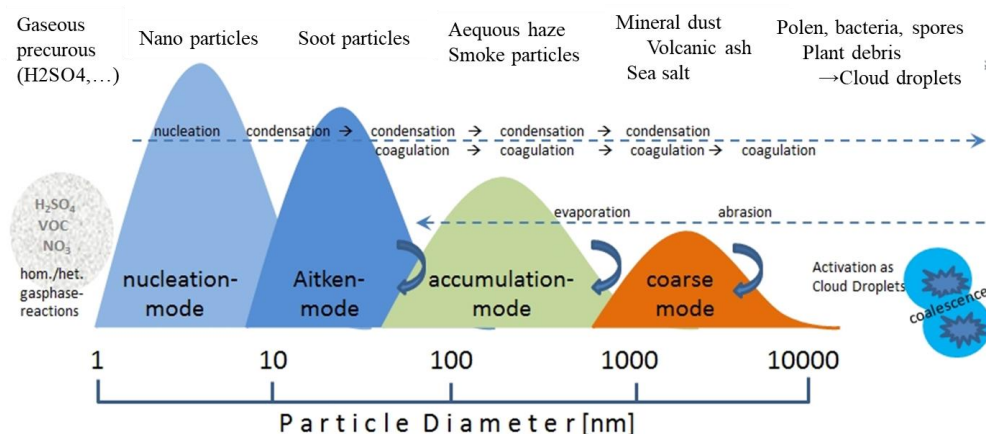


Figure 2.1 Schematic multi-modal particle size distributions with typical transformations and example particle types within each mode (<https://www.dwd.de>).

For monodisperse aerosol, the particle diameter is enough to describe the particle size. While in the atmosphere, aerosol particles are polydisperse due to the various sources. Aerosol Particle Number Size Distribution (PNSD) is defined as the particle number concentration for different size bins. The total particle number concentration is the integration of number concentration over the whole size bins:

$$N = \int N(D_p) dD_p \quad (2.1)$$

where  $D_p$  is the particle diameter,  $N(D_p)$  is the number concentration of particles with diameter ranging within  $dD_p$ , and  $N$  is the total number concentration.

Under the assumption of spherical particles, we can also calculate aerosol surface area and volume concentration with equation (2.2) and equation (2.3).

$$S = \pi/2 \int N(D_p) D_p^2 dD_p \quad (2.2)$$

$$V = \pi/6 \int N(D_p) D_p^3 dD_p \quad (2.3)$$

Generally, aerosol size distribution follows certain statistical laws, and the

commonly used laws to approximately describe the size distribution are log-normal distribution and Junge distribution.

- **Log-normal distribution**

Log-normal distribution is a prevailing law to describe size distribution for aerosol with multi-modes, which is determined by particle Geometric Mean Diameter (GMD,  $D_{pg}$ ) and Geometric Standard Deviation (GSD,  $\sigma_{pg}$ ) (equation 2.4), where  $D_{pg}$  and  $\sigma_{pg}$  could be give as equation 2.5 and 2.6.

$$N(D_p) = \frac{dN}{d \ln D_p} = N_0 \frac{1}{\sqrt{2\pi \ln \sigma_{pg}}} \exp\left(-\frac{1}{2} \left(\frac{\ln(D_p / D_{pg})}{\ln \sigma_{pg}}\right)^2\right) \quad (2.4)$$

$$\ln D_{pg} = \frac{\int \ln D_p N(D_p) d \ln D_p}{\int N(D_p) d \ln D_p} \quad (2.5)$$

$$\ln \sigma_{pg} = \sqrt{\frac{\int N(D_p) (\ln D_p - \ln D_{pg})^2 d \ln D_p}{\int N(D_p) d \ln D_p}} \quad (2.6)$$

Under the assumption of log-normal distribution, particle geometric mean diameter equals to its geometric median diameter. For particles with two or more modes, the new mode size distribution could be added to the previous knowing geometric mean diameter, number concentration and geometric mean deviation. Due to the mentioned advantages, log-normal distribution is widely used to simplify (i) the calculations such as aerosol optical properties from a Mie code and/or (ii) retrievals with remote sensing (Chen et al., 2018; Schuster et al., 2016a).

- **Junge distribution**

Aerosol size distributions could also be described with Junge distribution or named as power-law distribution (Junge, 1955). For particles with diameter between  $D_{p1}$ - $D_{p2}$ , aerosol number concentrations could be calculated with equation 2.7 (Boucher, 2015):

$$N(D_p) = N_0 \frac{\alpha D_{p1}^\alpha D_{p2}^\alpha}{D_{p2}^\alpha - D_{p1}^\alpha} D_p^{-\alpha} \quad (2.7)$$

$N_0$  is the total particle number concentration, and the value of  $\alpha$  falls between 2 and 3. Junge distribution is a simple law to describe aerosol size distribution, and could be used to explain spectral dependence of aerosol light scattering. But this method can't be used for particles smaller than 0.1  $\mu\text{m}$  or particles with two or more modes.

### 2.1.2 Aerosol density

The commonly used definitions about aerosol density include material density ( $\rho_m$ ), particle density ( $\rho_p$ ) and effective density ( $\rho_e$ ).

- **Aerosol material density**

Aerosol material density is an intrinsic physical property, depending only on aerosol chemical composition and not on particle shape. Material densities for different aerosols are given in table 2.1.

Table 2.1 Material density for different aerosol chemical compositions within previous studies.

Aerosol types	Material density ( $\text{g cm}^{-3}$ )	Reference
Black carbon	2	Lowenthal et al., 2000
	1.8	Bond and Bergstrom, 2006
	1.5	Cheng et al., 2008
Organic carbon	1	Schkolnik et al., 2007
	1.2	Ebert et al., 2004
	1.4	Cheng et al., 2008
Mineral dust	2.6	Wagner et al., 2012
	2.8	Hu et al., 2012
	2.4	Pio et al., 2014
Ammonium sulfate	1.73	Cheng et al., 2008
	1.76	Tang, 1996
	1.77	Mallet et al., 2003; Tang, 1996
Ammonium nitrate	1.73	Tang, 1996
Sodium chloride	2.2	Tang, 1996
	2	Cheng et al., 2008

For particle mixed with different aerosols, material density of the particle is the average density of all material included in the particle (DeCarlo et al., 2004; Hu et al., 2012):

$$\rho_m = \frac{\sum_{species} \rho_{m,i} V_i}{\sum_{species} V_i} = \sum_{species} \rho_{m,i} f_i \quad (2.8)$$

$\rho_{m,i}$  and  $f_i$  are the material density and volume fraction for aerosol  $i$ , respectively.

#### ▪ Aerosol particle density

Aerosol particle density ( $\rho_p$ ) is the ratio of particle mass ( $m_p$ ) and volume ( $V_p$ ):

$$\rho_p = m_p / V_p \quad (2.9)$$

For a homogeneous particle (figure 2.2a, c),  $\rho_p$  is equal to  $\rho_m$ . If the particle has any void inside (figure 2.2b, d), particle volume ( $V_p$ ) is the sum of aerosol material volume ( $V_m$ ) and void volume ( $V_{void}$ ):

$$V_p = V_m + V_{void} \quad (2.10)$$

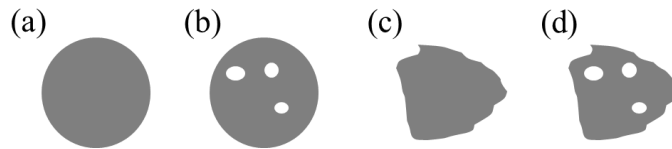


Figure 2.2 Aerosol possible shapes in the real atmosphere. (a) Spherical; (b) spherical particle with voids inside; (c) irregular particle; (d) irregular particle with voids inside.

Here, aerosol material density is the ratio of aerosol particle mass to aerosol material volume:

$$\rho_m = m_p / V_m \quad (2.11)$$

So, it could be found that  $\rho_p$  is smaller than  $\rho_m$ .

Aerosol particle density could also be obtained through the following relationship between particle mobility diameter ( $D_m$ ) and aerodynamic diameter ( $D_a$ ) (Khlystov et al., 2004; Li et al., 2018):

$$D_m = \frac{D_a \sqrt{\rho_0 \chi}}{\sqrt{\rho_p}} \quad (2.12)$$

Where  $\rho_0$  is the reference density with a value of  $1 \text{ g cm}^{-3}$ , and  $\chi$  is the shape factor, and it is equal to 1 for spherical particle.

### ▪ Aerosol effective density

In most cases, atmospheric aerosols are not spherical (figure 2.2c-d), and effective density ( $\rho_e$ ) is defined as the mass to volume ratio by assuming a spherical shape with diameter equal to the measured mobility diameter (DeCarlo et al., 2004; Hu et al., 2012):

$$\rho_e = \frac{m_p}{\frac{\pi}{6} D_m^3} \quad (2.13)$$

$m_p$  and  $D_m$  are the particle mass and diameter, respectively. The ratio of  $\rho_p$  and  $\rho_e$  is defined as the  $\chi$  (Hand and Kreidenweis, 2002; Hudson et al., 2007):

$$\chi = \frac{\rho_p}{\rho_e} \quad (2.14)$$

$\rho_e$  is equal to  $\rho_m$  and  $\rho_p$  under the hypothesis of spherical particle with no void space enclosed. Therefore,  $\rho_e$  could be calculated as equation 2.15:

$$\rho_e = \left(\frac{D_a}{D_m}\right)^2 \quad (2.15)$$

## 2.2 Aerosol optical properties

### 2.2.1 Extinction, scattering and absorption coefficients

According to Beer-Lambert law, when a beam of light at wavelength of  $\lambda$  enters a medium, it could be attenuated as the following equation:

$$\frac{I}{I_0} = \exp[-b_{\text{ext},\lambda} L] \quad (2.16)$$

$$b_{\text{ext},\lambda} = -\frac{1}{L} \ln\left(\frac{I}{I_0}\right) \quad (2.17)$$

Where  $dI$  is the light intensity variation influenced by the medium with a distance of  $dl$ .  $b_{\text{ext},\lambda}$  is the attenuation coefficient, which is also called extinction coefficient. The light extinction coefficient could be divided into the sum of two terms corresponding to scattering and absorption coefficient ( $b_{\text{scat},\lambda}$  and  $b_{\text{abs},\lambda}$ ):

$$b_{\text{ext},\lambda} = b_{\text{scat},\lambda} + b_{\text{abs},\lambda} \quad (2.18)$$

Aerosol extinction, scattering or absorption efficiency ( $Q_{\text{ext/scat/abs}}$ ) is the ratio of extinction, scattering or absorption cross section ( $\sigma_{\text{ext/scat/abs}}$ ) to the geometric cross section. The following equation presents  $Q_{\text{ext/scat/abs}}$  for a spherical particle with radius of  $r$ :

$$Q_{\text{ext/scat/abs}} = \frac{\sigma_{\text{ext/scat/abs}}}{\pi r^2} \quad (2.19)$$

Mass Extinction, Scattering or Absorption Efficiency (MEE/MSE/MAE) is defined as the ratio of extinction or scattering or absorption coefficient to the mass concentration (MC):

$$\text{MEE/MSE/MAE} = b_{\text{ext/scat/abs}}/\text{MC} \quad (2.20)$$

MEE/MSE/MAE depends on aerosol chemical composition and particle size. These parameters are widely used as inputs for climate model to convert aerosol mass concentration into optical properties (Myhre et al., 2013).

Columnar AOT ( $\tau_{\text{ext}}$ ) is the integration of extinction coefficient from the bottom to the top of the atmosphere.

$$\tau_{\text{ext}} = \int_0^{\infty} b_{\text{ext}} dz = \int_0^{\infty} (b_{\text{scat}} + b_{\text{abs}}) dz \quad (2.21)$$

AOT is a parameter to assess the aerosol loading over the whole column of atmosphere. It is currently used as an indicator for air pollution level, and also an important factor to study aerosol radiative effect and evaluate model performance. AOT could be obtained from ground-based remote sensing and satellite observation.

Similarly, the integration of aerosol scattering or absorption coefficient from the ground to the top of the atmosphere is defined as Scattering or Absorption Aerosol Optical Thickness (SAOT or AAOT,  $\tau_{scat/abs}$ ):

$$\tau_{scat/abs} = \int_0^{\infty} b_{scat/abs} dz \quad (2.22)$$

### 2.2.2 Single scattering albedo

Single scattering albedo (SSA) is defined as the ratio of scattering to extinction coefficients, cross sections or efficiencies:

$$\omega = \frac{b_{scat} / \sigma_{scat} / Q_{scat}}{b_{ext} / \sigma_{ext} / Q_{ext}} = \frac{b_{scat} / \sigma_{scat} / Q_{scat}}{(b_{scat} + b_{abs}) / (\sigma_{scat} + \sigma_{abs}) / (Q_{scat} + Q_{abs})} \quad (2.23)$$

SSA is a critical inner aerosol optical property, determining aerosol cooling or warming effect in the atmosphere, which has a large effect on evaluating aerosol direct and semi-direct effect (Loeb and Su, 2010; McComiskey et al., 2008). SSA is not only determined by the fraction of absorbing to non-absorbing aerosol, but also related with aerosol size and mixing state (Ramana et al., 2010). The SSA value falls in the range from 0 to 1. For pure scattering aerosol, the SSA is 1, and 0 is for pure absorbing aerosol.

### 2.2.3 Ångström exponent

Ångström exponent (AE or  $\alpha$ ) is representing the dependence of aerosol optical properties with wavelengths. It could be calculated using the following equation (Ångström, 1930):

$$EAE/SAE/AAE_{\lambda_1-\lambda_2} = -\log\left(b_{ext/scat/abs,\lambda_1} / b_{ext/scat/abs,\lambda_2}\right) / \log(\lambda_1 / \lambda_2) \quad (2.24)$$

Here  $EAE/SAE/AAE_{\lambda_1-\lambda_2}$  is the extinction or scattering or absorbing Ångström exponent with wavelength pair  $\lambda_1$  and  $\lambda_2$ .  $b_{ext/scat/abs,\lambda_1}$  and  $b_{ext/scat/abs,\lambda_2}$  are extinction or scattering or absorbing coefficient at  $\lambda_1$  and  $\lambda_2$ . EAE and SAE are depending on aerosol size, which are used to classify coarse and fine mode aerosol particles (Kaufman et al., 1994; Cazorla et al., 2013; Logan et al., 2013; Yu et al., 2013). SAE < 0.5 usually

appears with coarse particles, such as dust, and  $SAE > 1$  means smaller particles such as BC or OC (Eck et al., 1999; Schuster et al., 2006; Cappa et al., 2016). AAE values of BC, OC and MD observed by different studies are given in table 2.2.

Table 2.2 AAE values for BC, OC and MD from previous studies (the values without specific wavelength are fitted results with multi wavelengths).

Aerosol types	AAE	Site	Reference	
Black carbon	0.7-1	Gosan, Korea	Chung et al., 2012a	
	0.8 (520-880 nm)	SORPES, Nanjing	Wang et al., 2018	
	0.7-1.3	Laboratory study	Kirchstetter et al., 2004	
	0.55 (440-675 nm) 0.85 (675-870 nm)	Multiple sites from AERONET	Bahadur et al., 2012	
	1.2	Boulder, Colorado	Lack and Langridge, 2013	
	1.05 (fresh) 0.9 (compact) 0.95 (coated)	Numerical simulation	Liu et al., 2018	
	6-7			Amazon basin
1.6-1.8	Gosan, Korea			Chung et al., 2012a
organic carbon	3-7(350-500 nm)	Western Arctic	Corr et al., 2012	
	4.55 (440-675 nm)	Multiple sites from AERONET	Bahadur et al., 2012	
	4.0-4.2	Gwangju, Korea	Park et al., 2018	
	4.2-4.8	Gwangju, Korea	Park and Yu, 2018	
	Mineral dust	2.2 (440-675 nm) 1.15(675-870 nm)	Tamanrasset, Solar Village, Hamim, Eilat	Bahadur et al., 2012
		2.34		
2.17		Asian Pacific coast	Russell et al., 2010	
1.82(370-950 nm) 1.89(470-660 nm)		Beijing	Yang et al., 2009	

#### 2.2.4 Complex refractive index

When light from vacuum travels through a material, the path of the light is bent, and the light speed also changes. The refractive index can be treated as the ratio of the light speed within the material over its value within the vacuum:  $n=c/v$ . The refractive index also describes how much the light was refracted by the material. In the

atmosphere, the incident light is reduced by particle scattering and absorption. CRI is defined as  $m = n + k i$ , where  $n$  and  $k$  are the real and imaginary part of CRI.

CRI is treated as an intrinsic parameter for different aerosol chemical compositions, and independent of particle size. CRI is wavelength dependence, but many studies treated  $n$  as constant for different compositions in the visible spectrum (Bond et al., 2013; Kirchstetter et al., 2004; Wagner et al., 2012; Shamjad et al., 2016). The values of  $n$  and  $k$  for different aerosol species used by previous studies are given in table 2.3.

Table 2.3 The values of wavelength independent  $n$  and  $k$  from previous studies.

Aerosol type	$n$	$k$	Reference
Black carbon	2.26	1.26	Moteki et al., 2010
	1.95	0.79	Bond and Bergstrom, 2006; Wang et al., 2016
	1.95	0.66	Bergstrom, 1972
	1.8	0.6	Liu et al., 2018
	1.8	0.54	D'Almeida et al., 1991
	1.75	0.45	Chin et al., 2002
Mineral dust	1.53	--*	Wagner et al., 2012
	1.57	--*	Wang et al., 2013
Organic carbon or brown carbon	1.55	--*	Shamjad et al., 2016
	1.53	--*	Kirchstetter et al., 2004; Wang et al., 2013
	1.53	0.005	Chin et al., 2002
	1.47	0	Schkolnik et al., 2007; Yaws, 1999
	1.4	0	Schkolnik et al., 2007
Ammonium sulfate	1.53	0	Mallet et al., 2003
	1.54	0	Cheng et al., 2008
	1.4	0	Bauer et al., 2007b; Shamjad et al., 2012
	1.43	0	Chin et al., 2002
Ammonium nitrate	1.4	0	Bauer et al., 2007b
	1.54	0	Cheng et al., 2008

\* The corresponding wavelength dependent  $k$  is shown in figure 2.3

$n$  is usually ranging from 1.33 to 1.95. The lowest value 1.33 corresponds to pure water, and 1.95 is the largest value used for BC (Bond and Bergstrom, 2006).  $k$  equals to 0 for purely scattering species, and is usually between 0 and 1 for absorbing species.

Related studies revealed that  $k$  values associated to OC and MD have remarkable wavelength dependence. Their spectral variations, within the visible range, reported by previous studies are shown in figure 2.3.

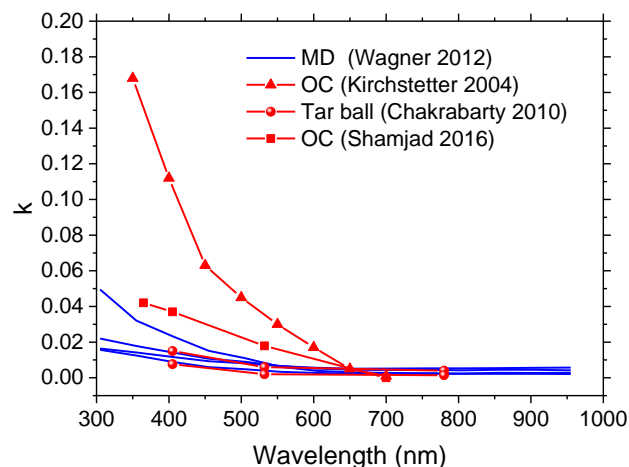


Figure 2.3 Spectral variation of imaginary part of complex refractive index for OC and MD (the result of Kirchstetter et al. (2004) is from laboratory combustion, and the results of Shamjad et al. (2016) is from analysis with field measurement. Tar ball is a kind of OC)

## 2.3 Mixing rules

The diverse aerosol sources and physical and chemical processes within the atmosphere result in complex aerosol mixtures (Lesins et al., 2002). Aerosol could be externally mixed or internally mixed. For external mixing (figure 2.4a), particles are isolated, and every aerosol types have its size distribution; while for internal mixing aerosol, every particle types are composed with different aerosols (figure 2.4b).

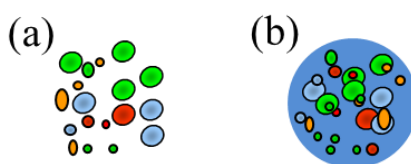


Figure 2.4 Externally mixed (a) and internally mixed (b) aerosols

### 2.3.1 External mixing

Externally mixed aerosol means that there is no coating or conglutination among different aerosol particles, and they can scatter or absorb light independently. The optical properties (eg. extinction, scattering or absorption) for the mixture are the sum of properties of each aerosol type (Mishchenko et al., 2004) (equation 2.25).

$$b_{ext/scat/abs,mix} = \sum_{i=1}^{i=N} f_i b_{ext/scat/abs,i} \quad (2.25)$$

$b_{ext/scat/abs,mix}$  is the equivalent extinction or scattering or absorption coefficient for the mixture of externally mixed aerosols, and  $f_i$  and  $b_{ext/scat/abs,i}$  are the fraction and extinction or scattering or absorption coefficient for each species  $i$ .

### 2.3.2 Internal mixing

External mixing is quite uncommon, and aerosol particles become internally mixed after collision, condensation, and homogeneous or inhomogeneous reactions within the atmosphere. At present, the models to describe internally mixed aerosols include Maxwell Garnett (MG) theory, Bruggeman (BR) theory, Core-Shell (C-S) model and Volume Average Mixing (VAM) model (figure 2.5).

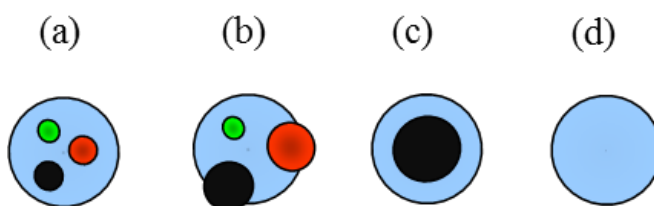


Figure 2.5 Mixing rules for internal mixing. (a) MG theory; (b) BR theory; (c) C-S model; (d) VAM model

- **Maxwell Garnett and Bruggeman theories**

MG theory (figure 2.5a) mostly describes the case of small insoluble particles,

such as black carbon or organic carbon aerosols, suspended in a solution, such as water or sulfate. Mixture described with MG theory could be calculated as insoluble inclusion embedded within a matrix. Dielectric constant for the mixture could be computed with the dielectric constant of each composition and its fraction (equation 2.26) (Bohren and Huffman, 2007):

$$\varepsilon_{MG} = \varepsilon_m(\lambda) \left[ 1 + \frac{3 \sum f_i \left( \frac{\varepsilon_i(\lambda) - \varepsilon_m(\lambda)}{\varepsilon_i(\lambda) + 2\varepsilon_m(\lambda)} \right)}{1 - \sum f_i \left( \frac{\varepsilon_i(\lambda) - \varepsilon_m(\lambda)}{\varepsilon_i(\lambda) + 2\varepsilon_m(\lambda)} \right)} \right] \quad (2.26)$$

$$n(\lambda) = \sqrt{\frac{\sqrt{\varepsilon_{real}^2(\lambda) + \varepsilon_{imag}^2(\lambda)} + \varepsilon_{real}(\lambda)}{2}} \quad (2.27)$$

$$k(\lambda) = \sqrt{\frac{\sqrt{\varepsilon_{real}^2(\lambda) + \varepsilon_{imag}^2(\lambda)} - \varepsilon_{real}(\lambda)}{2}} \quad (2.28)$$

Where  $\varepsilon_{MG}$  is the dielectric constant for the mixture calculated with MG theory,  $f_i$  is the volume fraction of each compound  $i$ , and  $\varepsilon_i(\lambda)$  and  $\varepsilon_m(\lambda)$  are the dielectric constants for pure compound and solute. Dielectric constant is closely related with aerosol scattering and absorbing abilities, which could be converted to CRI with equation 2.27 and 2.28, where  $\varepsilon_{real}(\lambda)$  and  $\varepsilon_{imag}(\lambda)$  are the real and imaginary part of the dielectric constant  $\varepsilon_{MG}$  separately.

For BR theory, all components are the same, and there are no solvents or solutes, which is applicable for the mixing of insoluble species.  $\varepsilon_{BR}$  could be calculated with the following equation (Bohren and Huffman, 2007):

$$\sum f_i \left( \frac{\varepsilon_i(\lambda) - \varepsilon_{BR}(\lambda)}{\varepsilon_i(\lambda) + 2\varepsilon_{BR}(\lambda)} \right) = 0 \quad (2.29)$$

Where  $\varepsilon_{BR}(\lambda)$  is the dielectric constant for the mixture using BR theory, and  $\varepsilon_i(\lambda)$  is the dielectric constant for different compositions. Similarly, the CRI for the mixture can be calculated with  $\varepsilon_{BR}(\lambda)$  using equation 2.27 and 2.28 where  $\varepsilon_{real}(\lambda)$  and  $\varepsilon_{imag}(\lambda)$

are, at this time, the real and imaginary part of the dielectric constant  $\epsilon_{BR}$ .

- **Core-shell model**

Core-shell model is specific to coated aerosols such as insoluble BC or dust coated with soluble compositions. Indeed, optical properties of pure and coated aerosol are entirely different. BC coating, including non-absorbing (or named as clear shell) and absorbing shell (or brown shell) (Lack and Cappa, 2010), could enhance its absorption efficiency, leading to enhancement of its radiative forcing up to 1.4 (Chung et al., 2011).

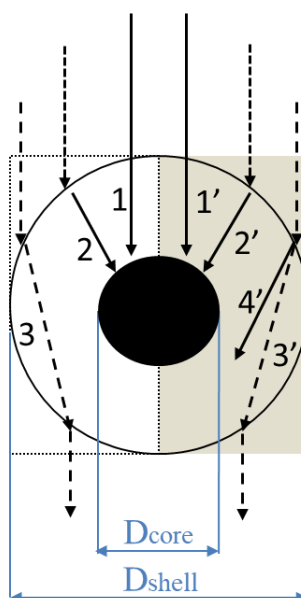


Figure 2.6 Schematic for BC coated with a clear shell (left) and brown shell (right). Incident rays (1 and 1') are not deviated by the shell and are absorbed by BC core ( $b_{abs,BC\_core}$ ); Ray 2 and 2' are refracted by the coating (lensing effect) and then meet the BC core where they will be absorbed by BC core known as the lensing effect ( $b_{abs,BC\_lens}$ ); Rays 3, 3', and 4' are refracted by the clear shell but not enough to meet the BC core and then Ray 4' is absorbed by the BrC shell ( $b_{abs,BrC\_shell}$ ) while Ray 3 and 3' are leaving the particle.

Coating is modifying the aerosol light interactions with the aerosol surface but also with the aerosol core. Indeed, shell is enhancing the core absorption coefficient

due to lensing effect (figure 2.6, Lack and Cappa, 2010). Therefore, the total absorption by BC coated with clear shell (equation 2.30,  $b_{abs,CS}$ ) equals to the absorption by BC ( $b_{abs,BC}$ ), which is the sum of  $b_{abs,BC\_core}$  and  $b_{abs,BC\_lens}$ . Whereas the total absorption of BC coated with absorbing material (equation 2.31,  $b_{abs,BS}$ ) is the sum of absorption by BC and BrC shell ( $b_{abs,BrC\_shell}$ ):

$$b_{abs,CS} = b_{abs,BC} = b_{abs,BC\_core} + b_{abs,BC\_lens} \quad (2.30)$$

$$b_{abs,BS} = b_{abs,BC} + b_{abs,BrC\_shell} = b_{abs,BC\_core} + b_{abs,BC\_lens} + b_{abs,BrC\_shell} \quad (2.31)$$

#### ▪ Volume average mixing model

Volume average mixing model is a simple but prevailing method to calculate physical and optical properties of internally mixed aerosols (figure 2.5d) (Chakrabarty et al., 2010; DeCarlo et al., 2004; Li et al., 2013). For homogeneously mixed aerosol, each particle has the same chemical composition. Density ( $\rho_{VAM}$ ) and CRI ( $n_{VAM}$ ,  $k_{VAM}$ ) of the aerosol population could be calculated with equation 2.32 ~ 2.34, where  $n_i$ ,  $k_i$  and  $\rho_i$  are real and imaginary parts of CRI and density for each compound. Li et al. (2019) obtained similar results with VAM and MG method, and pointed out that VAM could be a better choice for retrieving aerosol chemical compositions because of the simple calculations.

$$n_{VAM}(\lambda) = \sum f_{ii} n_{ii}(\lambda) \quad (2.32)$$

$$k_{VAM}(\lambda) = \sum f_{ii} k_{ii}(\lambda) \quad (2.33)$$

$$\rho_{VAM}(\lambda) = \sum f_{ii} \rho_{ii}(\lambda) \quad (2.34)$$

It should be noted that internal and external mixing rules are two ideal cases, and there is no absolute internal or external mixing in the real atmosphere, and both cases exist simultaneously (Bondy et al., 2018). Internal mixing is more broadly used to calculate aerosol and cloud properties (Jacobson, 2001; Li et al., 2019; Li et al., 2013; Zaveri et al., 2010).

## **2.4 Conclusions**

In this chapter, we introduced aerosol microphysical properties, like size distribution and density, chemical compositions as well as optical properties. Moreover, the mixing rules and their impacts on the different properties were introduced. Aerosol optical properties are closely connected to aerosol chemical composition and physical properties. In order to better understand this link, all these properties need to be observed simultaneously. In the next chapter, commonly used instruments to measure aerosol optical, physical and chemical properties will be described.

## Chapter 3 Observation of aerosol properties

Since aerosol properties are variable in space and time, aerosol property measurements with highly temporal and spatial resolution are needed to figure out aerosol sources and their radiative impacts. To achieve this goal, remote sensing and in-situ measurements have been well developed during the last decades. Therein, remote sensing techniques are optical-based means allowing obtaining aerosol optical properties. In-situ instruments are not only limited to optical property measurements but can also measure microphysical and chemical properties. In this chapter, the related instruments will be given in details, especially the ground-based remote sensing technique and in-situ instruments used in this study.

### 3.1 Remote sensing

Aerosol remote sensing could observe columnar, vertical or global aerosol optical properties based on ground based or space-based instruments.

Satellite could monitor aerosol distribution over the entire world without limitation from geographical conditions. These observations help to better understand aerosol transportation and therefore better estimate aerosol effects on global climate change. Over the past two decades, aerosol measurements based on satellite have made great progresses (Deuzé et al., 2000; Deuzé et al., 1999; Dubovik et al., 2011; Dubovik et al., 2014; Goloub et al., 1999; Hsu et al., 2006; Husar et al., 1997; Levy et al., 2010; Mishchenko et al., 2007; Mishchenko et al., 1999). Sensors like Moderate Resolution Imaging Spectro-radiometer (MODIS), Multi-angular Imaging SpectroRadiometer (MISR), Ozone Monitoring Instrument (OMI) and Polarization and Directionality of the Earth's Reflectances (POLDER) are well developed. Retrieval algorithms, such as single channel method (Stowe et al., 1997), multi channels method (Geogdzhayev et al., 2002; Higurashi and Nakajima, 1999; Martonchik and Diner, 1992), multi angles (Zhang et al., 2011), dark targets (Levy et al., 2010) and deep blue methods (Hsu et al., 2006), have been built to obtain global Aerosol Index (AI), AOT, AE, SSA etc. The global coverage period, spatial resolution, wavelength ranges for these sensors are

given in table 3.1. Satellite products allow identifying aerosol types (Bibi et al., 2017; Li et al., 2019), exploring aerosol transportation (Hu et al., 2019), evaluating aerosol radiative forcing (Sun et al., 2019) and evaluating aerosol emissions (Chen et al., 2019) over a global scale. Daily AOT data at 550 nm from the MODIS sensor carried by Aqua platform will be used in *chapter 5* to show the AOT spatial distribution over north China (resolution of  $1^{\circ}\times 1^{\circ}$ ).

Table 3.1 Satellite sensors and their global coverage period, spatial resolution, wavelength range.

Sensors	Coverage period	Spatial resolution	Wavelength	Reference
MODIS	1~2 day	10×10 km	410-15000 nm	Remer et al., 2005
OMI	1 day	13×24 km	270-500 nm	Levelt et al., 2006
MISR	7-9 days	17.6×17.6 km	446-867 nm	Martonchik et al., 1998
POLDER	2 day	18.5 km	443-1020 nm	Dubovik et al., 2011

Lidar is an active technique that can measure aerosol vertical structure, and it could be ground-based or space-based. Micro-Pulse Lidar Network (MPLNET, <https://mplnet.gsfc.nasa.gov>) is a ground-based network built by American National Aeronautics and Space Administration (NASA) with about 53 sites over the world (Ellsworth et al., 2001; Welton and Campbell, 2002), and it provides products like aerosol heights, extinction, backscatter and aerosol depolarization ratio profiles, etc. Lidar can also be carried on satellite, to measure aerosol vertical profile over a global scale, such as Cloud-Aerosol Lidar with Orthogonal Polarization (CALIOP) on board CALIPSO (Cloud-Aerosol Lidar and Infrared Satellite Observation, <https://www-calipso.larc.nasa.gov/>) (Winker et al., 2007).

Sun photometer is a passive ground-based instrument, and it measures columnar aerosol optical properties. Direct sun measurements are performed at several wavelengths between 340 and 1640 nm (440, 670, 870, 940 and 1020 nm are commonly used). Sky scanning measurements are performed at 440, 675, 870 and 1020 nm. AERONET (AERosol RObotic NETwork) is a federation of ground-based aerosol remote sensing networks developed by NASA using the CIMEL CE-318 sun/lunar/sky

photometer. It has over 1000 observation sites around the world (figure 3.1), providing a globally distributed observation of solar flux, AOT and inversion products with wide angular and spectral retrievals, like SAE, AAE, SSA, CRI, size distribution (Holben et al., 2006, <https://aeronet.gsfc.nasa.gov/>). The AOT uncertainties are approximately 0.01~ 0.02 and are spectrally dependent with higher errors in the UV spectral region (Eck et al., 1999). This AOT uncertainty will change the value of the AE by 0.03 ~ 0.04. Typical errors of retrieved SSA,  $n$  and  $k$  are 0.03, 0.04, relatively corresponding to 30 ~ 50 % respectively (Dubovik et al., 2000). The retrieval aerosol size distribution is given within the range of 0.05~15 nm, with accuracy of 15 ~ 25 % for fine mode dominated aerosols (0.1 ~ 0.7  $\mu\text{m}$ ) and 25 ~ 100 % for aerosols less than 0.1  $\mu\text{m}$  or larger than 0.7  $\mu\text{m}$  (Dubovik et al., 2000).



Figure 3.1 Distribution of global AERONET sites (<https://aeronet.gsfc.nasa.gov/>).

AERONET data have been widely used to evaluate satellite aerosol retrievals (Filonchyk et al., 2019; Kahn and Gaitley, 2015; Kahn et al., 2005; Levy et al., 2007), and is also widely used, in synergy with satellite observations, to compare aerosol optical properties observed over different regions or during different environmental conditions (Xia et al., 2013; Zhang et al., 2016). AERONET products have three quality levels: level 1 is un-screened; level 1.5 is cloud-screened; level 2 is cloud screened and quality-assured. In *chapter 5*, long-term columnar aerosol optical properties and size distribution are used from AERONET (level 2) to retrieve aerosol chemical compositions in Beijing.

## 3.2 In-situ measurement

### 3.2.1 Aerosol size distribution measurement

Since aerosols have large size range from nanometer to micrometer scales, there is no instrument dedicated to measure the whole aerosol size distribution. Therefore, a combination of different instruments based on different techniques is needed. The prevailing instruments include Optical Particle Counter (OPC), Scanning Mobility Particle Sizer (SMPS), and Aerodynamic Particle Sizer (APS). In our study, we employ SMPS (TSI 3936) combining with APS (TSI 3321) to measure the PNSD of PM<sub>2.5</sub> with high resolution.

**SMPS** is composed of an electrostatic classifier and a Condensation Particle Counter (CPC) (Wang and Flagan, 1990). It can measure aerosol particle mobility diameter within the range of 3 ~ 1000 nm. Electrostatic classifier is utilized to select particles according to their size based on particle mobility in an electric field with Differential Mobility Analyser (DMA). Then, CPC aims to measure the number concentration for the size-selected aerosols.

The operation of electrostatic classifier is described as follows (figure 3.2): (1) aerosol sample goes through an inertial impactor, which aims to remove large particles beyond the measurement range; (2) the particles go into a bipolar ion neutralizer to be imparted with high level of positive and negative ions; (3) the charged and neutral particles enter the DMA, and then are separated according to their electrical mobility due to the influence of electric field inside the DMA; (4) the particles with a narrow range of electrical mobility follow the correct trajectory to exit from DMA, after that, they will go through a CPC.

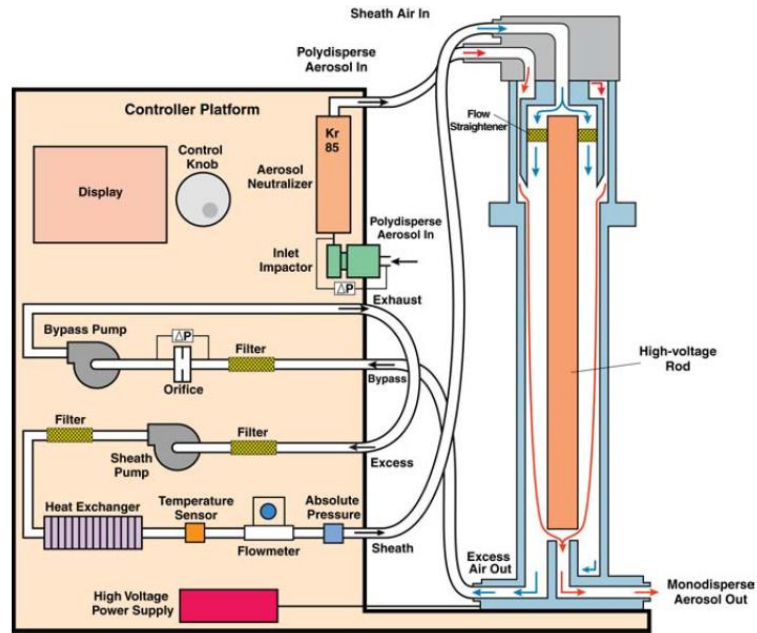


Figure 3.2 Schematic of electrostatic classifier with long DMA.

The operation theory of CPC is given as follows (McMurry, 2000; Minikin et al., 2012) (figure 3.3): (1) CPC allows sampled particles pass by a warm environment saturated with alcohol; (2) the evaporated alcohol together with the sample particles goes to a cold section (the condenser), where the alcohol condensed on aerosol surface to enlarge particle diameter; (3) these particles are then counted when the pass through a laser beam. The CPC of model 3775 can measure particle size down to 4 nm and up to 3  $\mu\text{m}$ . The particle number concentration measurement can be measured accurately within a large range of values (from 0 to  $10^7 \text{ cm}^{-3}$ ), and the single particle counting is up to  $50000 \text{ cm}^{-3}$ . The inlet flow has a high-flow mode operation of  $1.5 \text{ L min}^{-1}$ , and low-flow mode of  $0.3 \text{ L min}^{-1}$ .

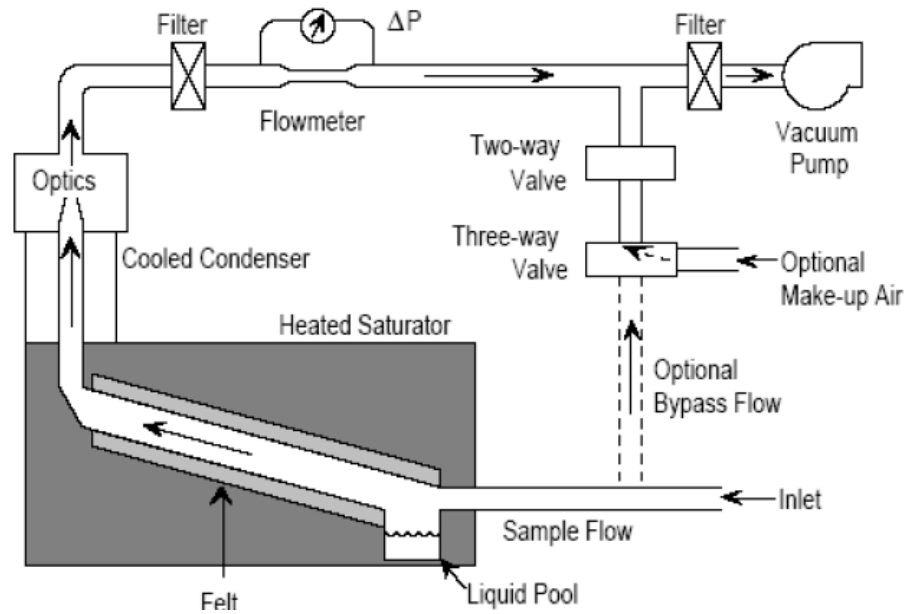


Figure 3.3 Schematic of CPC.

*APS* measures aerosol aerodynamic diameter in the range of  $0.5 \sim 20 \mu\text{m}$  with 52 size bins independently from aerosol inner optical properties (Shen et al., 2002). It records particle's velocity according to their time of flight, and then the diameter could be calculated using the relationship between size and velocity (Chen et al., 2007; Chen and Crow, 1986). Specifically, aerosol particles drawn into the inlet are divided into a sample flow and a sheath flow (figure 3.4). The sample flow goes through the inner nozzle ( $1 \text{ L min}^{-1}$ ). Meanwhile, the sheath flow is filtered ( $4 \text{ L min}^{-1}$ ), and goes through the sheath flow pump, the sharp-edged sapphire orifice and the outer nozzle. Then, it reunites with the sampling flow at the accelerating orifice nozzle. And the flow confines the particles to the centre stream and accelerates the air flow around the particle. Due to inertia, small particles have higher velocity than larger particles. The optical chamber will measure the particle velocity.

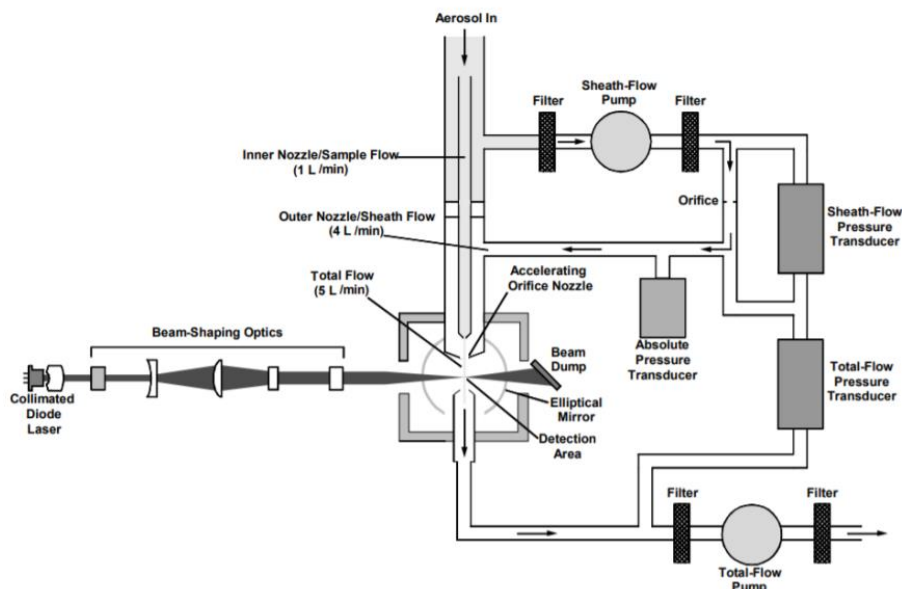


Figure 3.4 Schematic of APS (TSI, 2004).

During our measurement at Shouxian (China, *chapter 6*), the SMPS measurement settings were every 3 min and particle size ranged from 14 to 661 nm. The sampling flow and sheath flow were configured at  $0.3 \text{ L min}^{-1}$  and  $3 \text{ L min}^{-1}$  respectively. We selected both multi-charge and diffusion loss corrections before data processing. The APS has the same time resolution of 3 min and sampling flow rate of  $5 \text{ L min}^{-1}$ . Both instruments were validated with laboratory generated monodisperse PSL and ammonium sulfate.

### 3.2.2 Aerosol optical property measurement

To study aerosol optical physical properties (extinction, scattering and absorption coefficients) measurement techniques have made great progresses. Table 3.2 lists the commonly used aerosol optical instruments.

Table 3.2 Commonly used instruments for aerosol extinction, scattering and absorption coefficient measurements.

Parameters	Instruments	Wavelength (nm) (model)	Reference
$b_{ext}$	CRDS	405, 532, 662	Lack et al., 2012
	CEAS	450-480	Zhao et al., 2013
$b_{scat}$	Nephelometer	450, 525, 635 (Aurora 3000)	Müller et al., 2011
		450, 550, 700 (TSI 3563)	Heintzenberg et al., 2006
$b_{abs}$	Aethalometer	370, 470, 520, 590, 660, 880, 950 (AE33)	Drinovec et al., 2015
	PSAP	467, 530, 660	Arnott et al., 2005
	MAAP	670 (Thermo model 5012)	Hyvärinen et al., 2013
	PAS	404, 532, 658	Lack et al., 2012
$b_{ext} & b_{scat}$	CRDS & IS	532	Dial et al., 2010
	IBBCES & IS	365, 532, 660	Xu et al., 2018a

**Aerosol extinction coefficient measurement** is mainly based on Cavity Ring Down Spectroscopy (CRDS) and Cavity-Enhanced Absorption Spectroscopy (CEAS).

CRDS is built with a laser pulse, a high finesse optical cavity and two concave mirrors with high reflectivity (Wojtas et al., 2013) (figure 3.5). When the laser is injected into the cavity, it will be reflected between both mirrors, and the light intensity within the cavity will be decreased following an exponential function of time. CRDS measures the extinction by calculating the decay rate. CRDS has long effective optical path length, which produces a high sensitivity. This technique has become an effective method to measure trace gases and atmospheric aerosol extinction coefficients (Massoli et al., 2009; Moosmüller et al., 2009). CRDS could be impacted by gas (eg. NO<sub>2</sub>), and it leads to uncertainties for measuring aerosol extinction coefficients. Thus, additional instruments should be included to eliminate influence from gases when using CRDS.

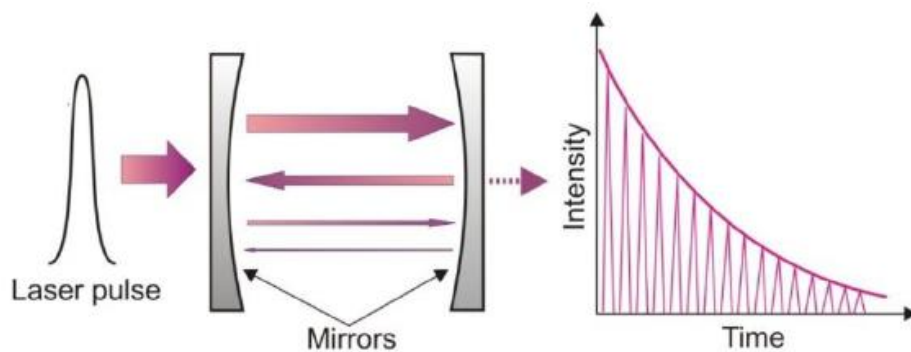


Figure 3.5 Illustration of CRDS technique (Wojtas et al., 2013).

CEAS also uses high-finesse optical cavity. Different from CRDS technique, it measures the extinction coefficient by detecting the transmission of light intensity through the cavity after reflection by both mirrors (figure 3.6). CEAS allows utilizing a broad-band light source, and can realize simultaneous measurement of multiple species with the spectral fitting method. Incoherent Broad-Band Cavity-Enhanced Absorption Spectroscopy (IBBCEAS) is built with this technique (Zhao et al., 2013). The instrument has been widely used to measure aerosol extinction and gas absorption in the laboratory and during field campaigns (Xu et al., 2018a; Xu et al., 2016; Zhao et al., 2017c).

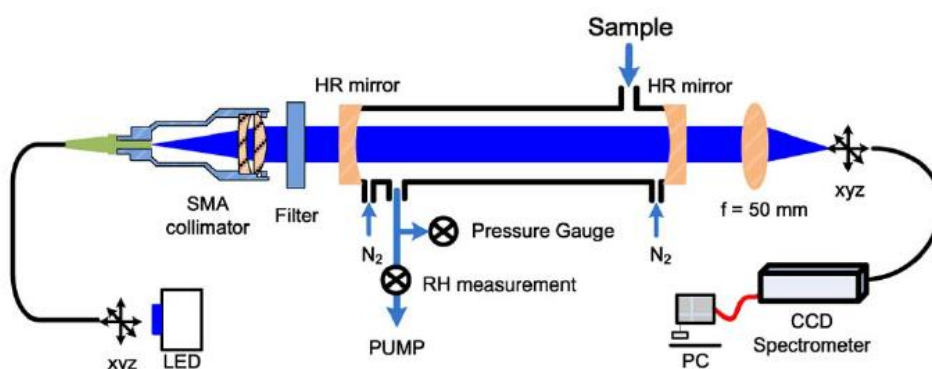


Figure 3.6 Schematic diagram of IBBCEAS for aerosol extinction measurement (Zhao et al., 2017c).

**Aerosol scattering coefficient measurement** is performed determined with an integrated nephelometer. Integrated nephelometer allows collecting scattering light from all space to measure scattering property of polydisperse aerosols. Because of its construction, the scattered light at short ( $<7^\circ$ ) and large angles ( $>170^\circ$ ) cannot be detected, which results in an underestimation of the scattering coefficient (TSI, 3563). This error lies between 5 to 50% depending on aerosol chemical composition, size and shape (Massoli et al., 2009). Varma et al. (2003) designed an ideal Integrating Sphere Integrated Nephelometer (ISIN) attached with truncation-reduction tubes to contain the sample volume and integrate the scattered light. The schematic diagram of the ISIN is shown in figure 3.7. The scattering angle between  $1^\circ$  and  $179^\circ$  can be collected with this instrument, which could reduce scattering uncertainties to only 4 %.

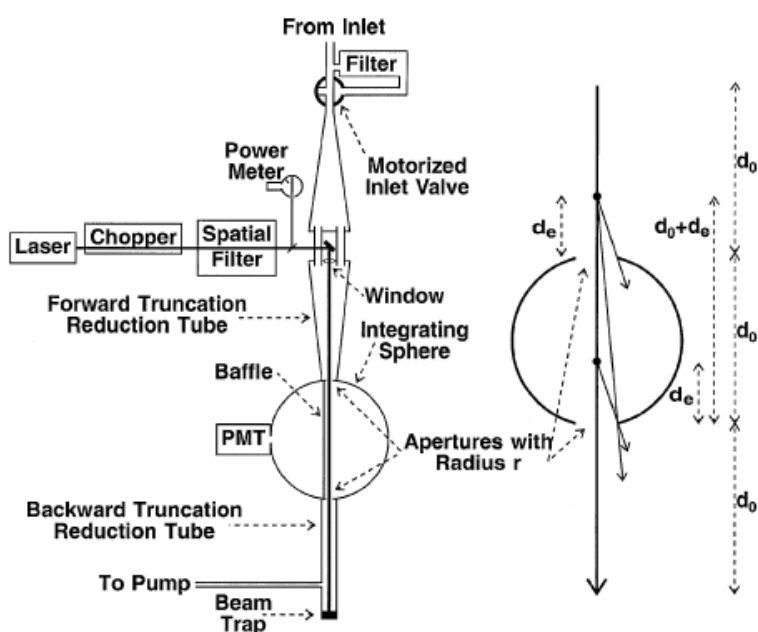


Figure 3.7 Schematic diagram (left) and forward scattering truncation geometry (right) of ISIN (Varma et al., 2003).

**Aerosol absorption coefficient measurements** are mainly based on photoacoustic spectroscopy (PAS) technique and filter-based methods. PAS could measure real-time

aerosol absorption directly. This technique avoids the effect of light scattering by transferring aerosol absorption to sound signal, and improves the accuracy with an error of 5~10% (Lack et al., 2006). PAS has become a mature method to measure aerosol absorption, and could be used as reference for other instruments (Arnott, 2003; Arnott et al., 2005). Most of the commercialized instruments are based on filter measurements such as Particle/Soot Absorption Photometer (PSAP) (Arnott et al., 2005), Multi-Angle Absorption Photometer (MAAP) (Hyvärinen et al., 2013) and Aethalometer (Drinovec et al., 2015). These instruments provide aerosol absorption coefficient by measuring the light attenuation through a filter with particle collected on it.

Above mentioned methods are specific to extinction, scattering or absorption coefficient measurement only, and they are working at different wavelengths and within different volumes. Since the measured optical properties are sensitive to the environmental temperature, pressure and relative humidity, comparison of measurements from different instruments could be tricky, especially the calculation of SSA.

To deal with this problem, CRDS and IBBCEAS have been combined with an integrating sphere, which aims to measure  $b_{ext}$  with CRDS or IBBCEAS and  $b_{scat}$  with the integrating sphere simultaneously (Thompson et al., 2008; Zhao et al., 2014)  $b_{abs}$  and SSA (equation 2.18 and 2.23 in chapter 2). Especially, Zhao et al. (2014) built a one-wavelength Cavity Enhanced Albedometer (CEA) by combining IBBCEAS technique and Integrated Sphere (IS). This CEA has been tested with laboratory and field measurements (Xu et al., 2016; Xu et al., 2018a; Zhao et al., 2014). Recently, a three-wavelength CEA was developed at 365, 532 and 660 nm based on this technique (Xu et al., 2018a). Figure 3.8 is the schematic diagram for this instrument. The detection precisions ( $1\sigma$ , 60 s averaging time) for  $b_{ext}$ ,  $b_{scat}$ ,  $b_{abs}$  are 0.40, 0.26, and 0.43  $\text{Mm}^{-1}$  at 365 nm, 0.04, 0.02, 0.04  $\text{Mm}^{-1}$  at  $\lambda = 532$  nm and 0.28, 0.44 and 0.47 at 660 nm, respectively. The estimated total uncertainties in  $b_{ext}$ ,  $b_{scat}$ ,  $b_{abs}$  and SSA were less than 3.3 %, 3.0 %, 4.5%, and 5.5%, respectively. In this study, the extinction and scattering coefficients were obtained at 365 and 532 nm with the three-wavelength CEA system

during the campaign in Shouxian (*Chapter 6*).

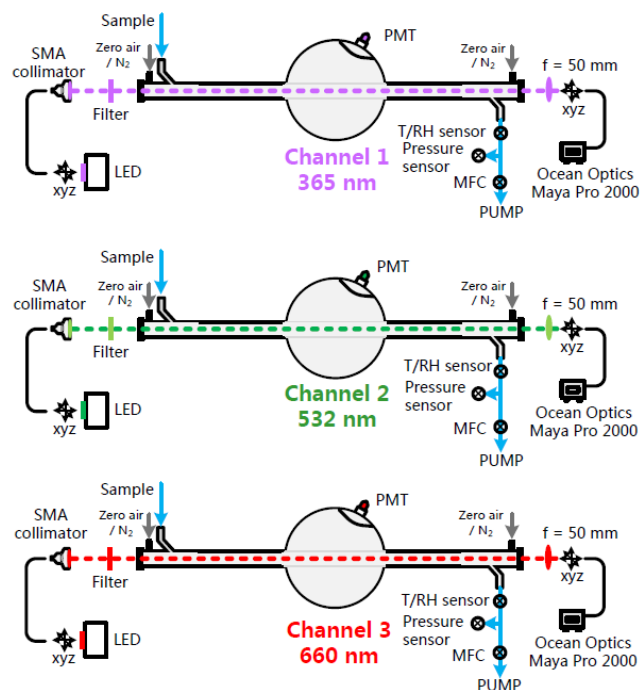


Figure 3.8 Schematic diagram of a three-wavelength cavity enhanced albedometer (Xu et al., 2018a).

### 3.2.3 Aerosol chemical composition measurement

The on-line measurement of aerosol chemical composition is mainly based on Aerosol Mass Spectrometer (AMS) technique, such as Time-of-Flight Aerosol Mass Spectrometer (ToF-AMS) and Aerosol Chemical Speciation Monitor (ACSM), while off-line measurements are performed with filter sampling.

*ToF-AMS* can measure online microphysical properties and chemical compositions of atmospheric non-refractory aerosols based, respectively, on time-of-flight and mass spectrometry techniques (Canagaratna et al., 2007; Jayne et al., 2000). This instrument combines standard vacuum and mass spectrometric technologies. It utilizes an aerodynamic lens inlet focusing particles into a narrow beam. Then, the

particles are efficiently transported into vacuum where particle aerodynamic size could be determined using particle time-of-flight measurement. The particle mass concentration measurement is conducted with electron-impact mass spectrometry after particle thermal vaporization on a resistively heated (at  $\sim 600^{\circ}\text{C}$ ) surface (Jayne et al., 2000). Therefore, size distribution and mass concentration of non-refractory aerosols (ammonium, sulphate, nitrate, chloride and organic components) are provided by AMS with high time-resolution (around 10 minutes). The AMS measurement uncertainties were estimated to be 38% according to Lack's observations (Lack et al., 2012). Even though ToF-AMS provides real-time and reliable measurement of aerosol chemical compositions, its high cost, its complexity of implementation and data processing do not make it a suitable instrument for field measurements (Ng et al., 2011). *ACSM* is a simplified version of AMS without the Time of flight technology. It is cheaper, smaller and simpler to operate in comparison to ToF-AMS (Ng et al., 2011; Sun et al., 2015a). The ACSM measures non-refractory aerosol mass concentration directly from ambient air with relatively high time resolution.

Real-time measurement of non-refractory and refractory aerosols needs to combine different instruments (e.g. Single Particle Soot Photometer: SP2, and Soot Particle Aerosol Mass Spectrometer: SP-AMS), and the high cost as well as the maintenance makes it difficult to deploy widely for long-term measurement at multiple sites.

**Filter sampling** is a traditional and widely used off-line approach to obtain aerosol chemical compositions accurately and comprehensively (Tao et al., 2017; Zhao et al., 2017a; Zhao et al., 2017b). After sampling, the aerosol chemical compositions could be determined by multiple means. Water soluble ions ( $\text{Na}^+$ ,  $\text{NH}_4^+$ ,  $\text{k}^+$ ,  $\text{Mg}^{2+}$ ,  $\text{Ca}^{2+}$ ,  $\text{Cl}^-$ ,  $\text{SO}_4^{2-}$ ,  $\text{NO}_3^-$ , etc) can be extracted with ultrasonic method, and then analyzed by ion chromatography. Elemental Carbon (EC) as well as OC is measured with thermal/optical transmittance aerosol carbon analyzer (Subramanian et al., 2006; Yang et al., 2007; Zhao et al., 2017b). Trace elements, such as Pb, Zn, Cu, Cl, S, Fe, Mn, Cr, K, Ca, Ti and Si, could be obtained with X-ray fluorescence. Although filter sampling

has its disadvantages of low resolution and complex operation process, it is still prevailing for its low cost.

For this study, filter sampling was used to verify the retrieved aerosol chemical compositions from on-line measurements. Specifically, PM<sub>2.5</sub> particles were collected on 47 mm quartz fibre filters every 11.5 h (from 7:30 am to 19:00 pm and 19:30 to 7:00 am in the next day) with a PM<sub>2.5</sub> sampler (SF-PM<sub>2.5</sub>, Sven Leckel Ingenieurburo GmbH). Prior to the field campaign, all filters were baked at 600°C for 6 h in a muffle furnace to remove residual organic matters and other impurities (Yang et al., 2007; Zhao et al., 2017b). After sampling, the filters were stored at -4° C in a freezer until further analysis. To measure the collected PM<sub>2.5</sub> mass concentration, all the filters were pre- and post-weighed with a high-precision digital balance (Sartorius ME5-F Filter Microbalance, Germany) after being stored for 48h in a drying cupboard at a constant temperature (~ 20° C) and humidity (~ 40 %). The main ions, including Na<sup>+</sup>, NH<sub>4</sub><sup>+</sup>, K<sup>+</sup>, Mg<sup>2+</sup>, Ca<sup>2+</sup>, Cl<sup>-</sup>, SO<sub>4</sub><sup>2-</sup> and NO<sub>3</sub><sup>-</sup> were analyzed with ion chromatography (ICS-90; Dionex, USA). The method used to extract inorganic ions was described in details by previous studies (Yang et al., 2007; Zhao et al., 2017b). The concentrations of EC and OC were determined with a thermal/optical transmittance aerosol carbon analyzer (Sunset Laboratory, Inc.) (Subramanian et al., 2006).

### 3.3 Conclusions

To monitor aerosol property, remote sensing and in-situ instruments are available. Aerosol optical properties can be obtained by remote sensing and in-situ measurements, but aerosol chemical compositions could only be provided by in-situ method. As previously said in *chapter 2*, aerosol optical properties are related with aerosol size and chemical compositions, which makes it possible to gain information about aerosol chemical compositions from their optical property measurements. A few available methods for aerosol chemical composition identification based on optical properties will be presented in details in *chapter 4 and 5*.

The long-term columnar aerosol optical dataset from AERONET will be used to

retrieve aerosol chemical compositions based on *k*-based method in *chapter 5*. Then spatial distribution of AOT will be plotted with Aqua level 3 products. These results will be combined with spatial distribution of emission inventories and backward trajectory analysis to study columnar aerosol chemical composition dependence on regional transport, and then evaluate the retrievals.

Chapter 6 aims to improve the *k*-based methods based on previous studies, and realize the closure of aerosol chemical composition. A few of in-situ instruments (SMPS, APS and CEA) will be used to acquire aerosol physical and optical properties as the input the aerosol chemical composition retrieval algorithm, and aerosol chemical composition measured based on filter sampling will used to realize the closure study.

## Chapter 4 Study on Ångström exponent

As given in the introduction (*chapter 1*), AAE was widely used to derive the absorption coefficients by different aerosols (Bahadur et al., 2012; Chung et al., 2012a; Lack and Langridge, 2013; Wang et al., 2016; Zhang et al., 2019), and to identify different aerosol types combining with SAE (Cappa et al., 2016; Cazorla et al., 2013; Russell et al., 2010) (named as AE methods). In this chapter, we will introduce those AE methods in details. The performance of these methods will be explored through a comprehensive investigation on SAE and AAE dependence on aerosol size and wavelength couples using Mie theory (*appendix A1*).

### 4.1 AE methods description

#### 4.1.1 Calculation of absorption coefficients of different species with AAE

Aerosol absorption coefficient is not only limited to the three main absorbing compounds (BC, OC and MD), but also absorbing enhancement by coating, which makes it difficult to distinguish contribution to the absorption coefficient from different species. To simplify the complex mixture, previous studies could be divided into two types: (1) calculation of the absorption by BC, BrC and MD assuming that they are externally mixed and ignoring the impact of coating; (2) determination of absorption by BrC and BC by excluding the influence of MD.

- **Calculation of the absorption coefficients by BC, BrC and MD using AAE**

To estimate the absorption coefficients by BC, OC or BrC and MD, Bahadur et al. (2012) studied AAE from AERONET products observed in different sites all over the world. Each site was chosen as a function of their location in reference to aerosol sources. Each site was either dominated by one type of particles (4 sites: dust region; 8 sites: biomass burning; 17 urban sites: fossil fuel combustion) or by multiple aerosol types (13 nonurban sites: fossil fuel and mixed sources, and 10 sites: mixed emission in California). They assumed that AAE is an intrinsic property for all absorbing aerosols, and not impacted by aerosol mixing state or size. Statistical results were used to

represent AAE values for BC, OC and MD at 440-675 nm ( $AAE_{440-675}$ ) and 675-870 nm ( $AAE_{675-870}$ ), and the results are given in table 2.2. These results for “pure” aerosols were then used to calculate the absorption by BC, OC, and MD at the same wavelength assuming that aerosols are externally mixed:

$$AAOT(\lambda_i) = AAOT_{ref,BC}(\lambda_i / \lambda_{ref})^{-AAE_{BC,i}} + AAOT_{ref,OC}(\lambda_i / \lambda_{ref})^{-AAE_{OC,i}} + AAOT_{ref,MD}(\lambda_i / \lambda_{ref})^{-AAE_{MD,i}} \quad (4.1)$$

Where AAOT is the total AOT due to absorption from AERONET inversion, and  $AAOT_{ref,BC}$ ,  $AAOT_{ref,OC}$ , and  $AAOT_{ref,MD}$  are AOT due to BC, OC and MD absorption separately at reference wavelengths (440, 675, or 870 nm). This method, based on AAE spectral variation, provided an experimental way to retrieve the contribution of different aerosol types.

Chung et al. (2012b) and Xu et al. (2013b) also used similar method to derive the contribution of BC, OC and MD to the absorption coefficients and to evaluate their impacts on radiative forcing. However, the externally mixing assumption for these methods is inconsistent to internally mixing hypothesis of AERONET inversions (Schuster et al., 2016b). Schuster et al. (2016) also pointed that the AAE was determined by the spectral variation of  $k$ , and mineral goethite had increasing  $k$  with wavelength, which would also lead to AAE smaller than 1. Therefore, AAE is not a robust parameter to distinguish MD and carbonaceous aerosols.

#### ▪ **Determination of the absorption attributed by BC and BrC with $AAE_{BC}$**

Even though AAE can't be used to distinguish MD from carbonaceous aerosols effectively (Schuster et al., 2016b), it still works to derive the contribution of BC from those of BrC assuming that there is no MD existing in fine particles (Wang et al., 2016). Since the AAE for BrC changed a lot (1.5~7, table 2.2) due to the varied BrC sources, AAE of BC ( $AAE_{BC}$ ) was usually to derive absorption by BC and BrC because it has a relative narrow variation (0.55~1.3, table 2.2).

The procedures to calculate the BC and BrC absorptions based on  $AAE_{BC}$  are as following: (1) assuming that absorption at longer wavelength is only attributed to BC

(Lack and Langridge, 2013); (2) with known  $AAE_{BC}$ , absorption for BC at shorter wavelengths can be calculated (equation 2.22); (3) The absorption by BrC is the difference between the total and BC absorption coefficients. Since total absorption coefficients at shorter and longer wavelength are measured, the key point to derive BC and BrC contribution is to determine the value of  $AAE_{BC}$ .

A value of 1 is widely used for  $AAE_{BC}$  (Olson et al., 2015). However, a lot of studies demonstrated that  $AAE_{BC}$  was also affected by particle size and mixing state, and was not always equal to 1 (Lack and Cappa, 2010; Liu et al., 2018; Schuster et al., 2016b). Thus, using a constant value of 1 for  $AAE_{BC}$  might bring a large difference in the estimation of BC and therefore of BrC absorption.

Lack et al. (2013) deduced the best estimation of  $AAE_{BC}$  (1.2) during a biomass burning episode, and they also applied AAE attributed method to obtain BrC absorption. They highlighted large differences (at least 34%) between measured and retrieved BrC contribution using  $AAE_{BC}$ . Therefore, the uncertainties should be considered when using this method.

Due to the disagreement with a constant  $AAE_{BC}$  that independent of particle size by recent studies, Zhang et al. (2019) used specific wavelength pair (880-950 nm) to estimate the  $AAE_{BC}$  over the UV-Visible range due to little absorption contributed by BrC at these two wavelengths. They calculated BrC absorption contribution of about 37.4% at 370 nm, which is 20 % higher than the value retrieved by assuming  $AAE_{BC}$  of 1. This study improved the AAE based method, but ignored  $AAE_{BC}$  dependence on wavelength.

Wang et al. (2016) simulated  $AAE_{BC}$  using Mie theory, and pointed that  $AAE_{BC}$  was strongly dependent on particle size, and also varied with the selected wavelength pairs. They calculated possible values of Wavelength Dependence of Absorption Ångström exponent ( $WDA=AAE_{440-870}-AAE_{675-870}$ ) for BC coated with absorbing shell. Based on WDA and AAOT at 675 and 870 nm from AERONET, they obtained  $AAE_{440-870}$  of BC ( $AAE_{BC,440-870}$ ). Assuming that there is no absorption by BrC for wavelength

larger than 600 nm, BC and then BrC absorption at 440 nm can be calculated with known absorption at 870 nm observed by AERONET and the speculated  $AAE_{BC,440-870}$ . This method was applied to derive BrC absorption from in-situ measurement, AERONET observations, and OMI observations, but still no comparable with directly measured BC or BrC absorption. This study estimated uncertainties associated to BrC absorption could reach 110% when BrC contribution is only about 10%.

Wang et al. (2018) measured BC size distribution as well as their coating thickness (SP2) and calculated the average value of  $AAE_{BC,370-520}$  to  $AAE_{BC,520-880}$  ratio ( $\sim 0.65$ ) using Mie theory. They found BrC contribution to absorption coefficient of 10.4 %  $\sim$  23.9 % at 370 nm assuming that BC is the only compound to absorb from 520 to 880 nm. They treated the derived BrC absorption taking into  $AAE_{BC}$  dependence on wavelength into consideration as more reasonable result, because the number of negative BrC absorption reduced a lot than using  $AAE_{BC}$  of 1.

Based on these studies, it could be found that the traditional idea of a constant AAE for BC, BrC and MD is less and less approved, but the knowledge of the AAE values for the three main absorbing species is still vital, especially for  $AAE_{BC}$ . Thus, a deeper and comprehensive investigation of AAE dependency to aerosol size distributions and wavelength couples is needed.

#### **4.1.2 Qualitative classification of aerosol chemical compositions with SAE and AAE**

Since AAE values for BC, BrC and MD vary as a function of size and wavelength (Lack and Cappa, 2010), the aerosol type qualitative classification is uncertain with only AAE. EAE or SAE was then added to distinguish different aerosols by size (Schuster et al., 2016b). Thereby, the EAE/SAE vs. AAE space scheme was then built to distinguish different aerosol types qualitatively.

Russell et al. (2010) found that aerosol particles from urban industrial regions are associated with AAE values closed to 1, while biomass burning aerosols had larger AAE values (1.4~1.6). AAE for aerosol from Saharan desert region had the largest

value ( $>1.5$ ). The EAE for urban industrial and biomass burning aerosols is between 1.5 and 2, and is lower than 1.2 for desert dust. Therefore, Russell et al. (2010) proposed that different absorbing aerosols could be identified by setting proper thresholds in the EAE vs. AAE space.

Based on this idea, Cazorla et al. (2013) built a  $SAE_{440-675}$  vs.  $AAE_{440-675}$  plot space to distinguish different absorbing aerosols and their mixture (figure 4.1a) using the statistical results from the study by Bahadur et al. (2012). To verify this scheme, Cappa et al. (2016) built a  $SAE_{450-550}$  vs.  $AAE_{520-660}$  space (figure 4.1b) to identify aerosol types based on  $PM_{10}$ ,  $PM_{2.5}$  and  $PM_{10}$  measurement in California.

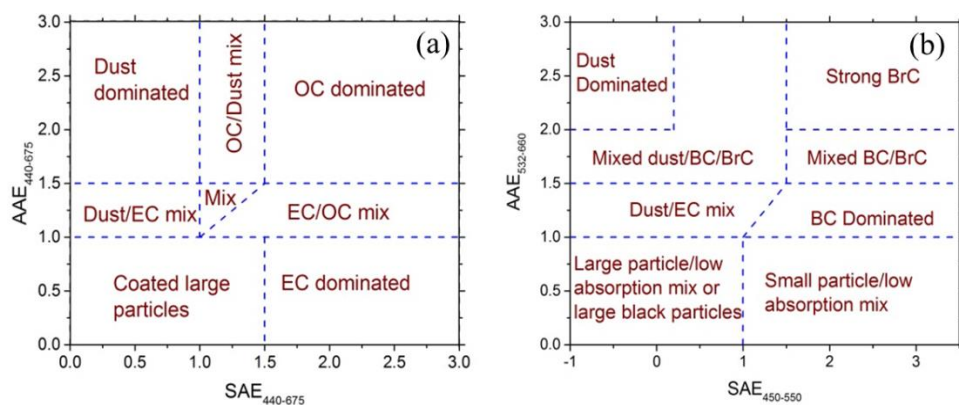


Figure 4.1 Aerosol classification schemes with SAE and AAE from Cazorla et al. (2013) and Cappa et al. (2016).

Cappa et al. (2016) found that there was almost no observation falling in EC dominated region ( $AAE < 1$  and  $SAE > 1.5$ ) like expected for an urban site. Moreover, the lower threshold for  $AAE_{BC}$  should be set at 1. They also pointed that  $AAE_{BC,440-675}$  ( $0.55 \pm 0.24$ ) suggested by Bahadur et al. (2012) was a ‘low-end baseline’, and it is unlikely to be correct. Finally, the thresholds used to frame the EC/OC mixed region in Carzola’s scheme were found to better fit the EC dominated region. SAE and AAE threshold for dust and BrC dominated regions were also corrected as inputs for newly

developed scheme based on  $SAE_{450-550}$  vs.  $AAE_{520-660}$  plot space (Cappa et al. 2016, figure 4.1b).

Schmeisser et al. (2017) used  $SAE_{450-700}$  vs.  $AAE_{450-700}$  space with thresholds from Cappa et al. (2016) to identify aerosol types from in-situ observation at 24 sites. Besides that, they also inferred possible aerosol types with multivariate cluster analysis to group stations with similar optical properties and analysis of backward air mass trajectories. Even though the present  $SAE_{450-550}$  vs.  $AAE_{520-660}$  space worked well for the sites with stable and homogenous aerosol population, it worked poorly for remote marine and Arctic sites. Then, they highlighted that verification of aerosol classification thresholds would be essential to expand and improve aerosol classification schemes.

It should be noted that the above studies by Cazorla et al. (2013), Cappa et al. (2016) and Schmeisser et al. (2017) were based on different instruments and therefore the wavelength couples used are slightly different, which might explain part of the inconsistencies in their results. But how aerosol size and wavelength impact SAE and AAE is still uncertain. Thereby, a further study of SAE and AAE dependence on wavelength pairs is needed.

## 4.2 Robustness of methods based on Ångström exponent

In this section, we comprehensively simulated SAE and AAE for BrC, MD and BC, together with BC coating with clear shell, to study SAE and AAE dependence on wavelength couples and aerosol size.

### 4.2.1 Simulation of SAE and AAE with Mie theory

Mie theory (described in the *appendix A1*) was used to simulate SAE and AAE for three main absorbing species, including BrC and MD, and pure or coated BC. The CRI for BrC was obtained from Kirchstetter et al. (2004), with GMD of 50~300 nm and GSD of 1.8.

CRI imaginary part of MD was given, over the entire range from UV to short IR, in figure 2.3 from Wagner et al. (2012), and the CRI real part was generally set to 1.53

(Wagner et al., 2012). MD was assumed to be monomodal with GMD varying between 200 and 500 nm. The bimodal distribution was built with one fine mode ( $GMD_f = 300$  nm) and a coarse mode ( $3 \mu\text{m} < GMD_c < 4 \mu\text{m}$ ). The GSD is 1.8 for MD, and number concentration for coarse mode is twice the one of the fine mode.

A mean value of  $1.95 + 0.79 i$  was used for CRI of BC suggested by Bond et al. (2006, 2013). GMD was between 10 and 250 nm, and GSD was assumed to be 1.8. CRI of the coating on BC (shell) was  $1.5 + 0 i$ , which is approximately a mean value for SNA (table 2.3), and the ratio of shell diameter to core diameter ( $GMD_{\text{shell}}/GMD_{\text{core}}$ ) was varying between 1 and 3 (Wang et al., 2018).

#### 4.2.2 SAE and AAE for BrC

The simulated SAE and AAE for BrC is shown in figure 4.2 and 4.3.  $SAE_{\text{BrC}}$  has lower value for short wavelength pairs ( $SAE_{\text{BrC},350-400} = 1.5$ ,  $GMD_{\text{BrC}} = 50$  nm) and higher value for long wavelength pairs ( $SAE_{\text{BrC},650-700} = 2.9$ ,  $GMD_{\text{BrC}} = 50$  nm). As the commonly accepted conclusion (Yu et al., 2009),  $SAE_{\text{BrC}}$  decreases with increasing size in our study.  $SAE_{\text{BrC},440-675}$  (used by Cazorla et al., 2013) is higher than  $SAE_{\text{BrC},450-550}$  (used by Cappa et al., 2016) by 0.2, which means that the  $SAE_{\text{BrC}}$  difference at the two wavelength pairs is quite small. Similarly, Cazorla et al. (2013) and Cappa et al. (2016) also used the same threshold ( $SAE > 1.5$ ) to determinate BrC or OC dominated region.

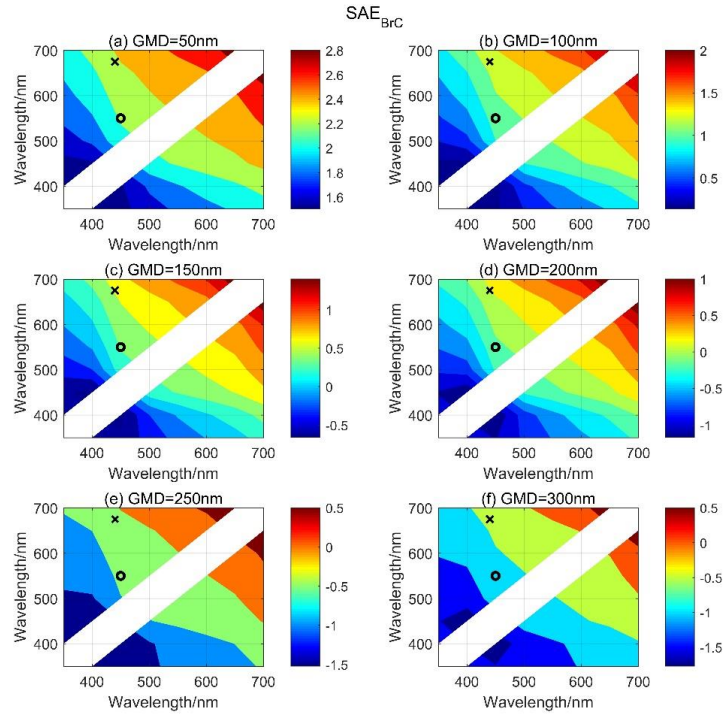


Figure 4.2 Simulation of SAE dependence on wavelength couples for BrC with different geometric mean diameters. Figure 4.3 ~ 4.9 use the same marks. The symbol ‘x’ indicates the wavelength pair used in scheme by Cazorla et al. (2013), and ‘o’ represents for the scheme from Cappa et al. (2016).

The simulated  $AAE_{BrC}$  has dramatically large value, and shows higher dependence on wavelength than size. The discrepancy could be larger than 8 caused by the selected wavelength pair.  $AAE_{BrC,440-675}$  is lower than  $AAE_{BrC,532-660}$ , and the difference is close to 2. According to this simulation, the threshold of AAE for BrC dominated case should be increased by 2 when plotting the measured AAE at 532-660 nm in the scheme by Cazorla et al. (2013), who built the threshold using AAE at 440-675 nm. Similarly, the thresholds of AAE representing for BrC or OC dominated cases are also different for the schemes proposed by Cazorla et al. (2013,  $AAE_{BrC,440-675} > 1.5$ ) and Cappa et al. (2016,  $AAE_{BrC,532-660} > 2$ ). This result highlight the  $AAE_{BrC}$  dependence on wavelength pairs, and it can’t be ignored when setting the threshold for BrC dominated cases. Simulated  $AAE_{BrC,440-675}$  value is about 8.5, which is quite greater than the result of 4.55 from Bahadur et al. (2012) estimated with data from AERONET. This difference could

be explained by the large variety of BrC compounds observed around the world with entirely different properties.

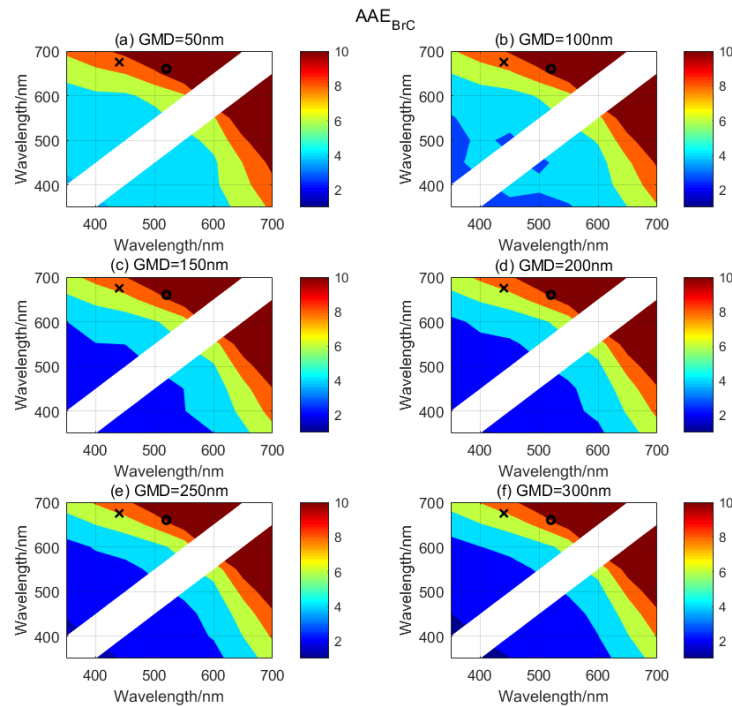


Figure 4.3 Simulation of AAE dependence on wavelength couples for BrC at different geometric mean diameters.

### 4.2.3 SAE and AAE for MD

SAE spectral dependency for MD with different size distributions is shown in figure 4.4. For MD with the same size distribution but different wavelength pairs, the difference of SAE reaches about 1.3, and pairs at short wavelength have lower values than long wavelength for single mode.  $SAE_{MD,440-675}$  used by Cazorla et al. (2013) is larger than  $SAE_{MD,450-550}$  used by Cappa et al. (2016) by about 0.2.

However, for MD with two modes, the SAE spectral dependency shows different trends. Lowest SAE values were observed for wavelengths chosen from 400 to 650 nm. For wavelengths larger than 650 nm, the trend is the same with  $SAE_{MD}$  calculated for a

single mode of MD.  $SAE_{MD,440-675}$  is higher than  $SAE_{MD,450-550}$  by about 0.1. However, the difference of thresholds used by Cappa et al. (2016) ( $SAE_{MD,440-675} < 0.2$ ) and Cazorla et al. (2013) ( $SAE_{MD,450-550} < 1$ ) is far more than 0.1. The large difference between both scheme thresholds might be caused by the MD size distribution.

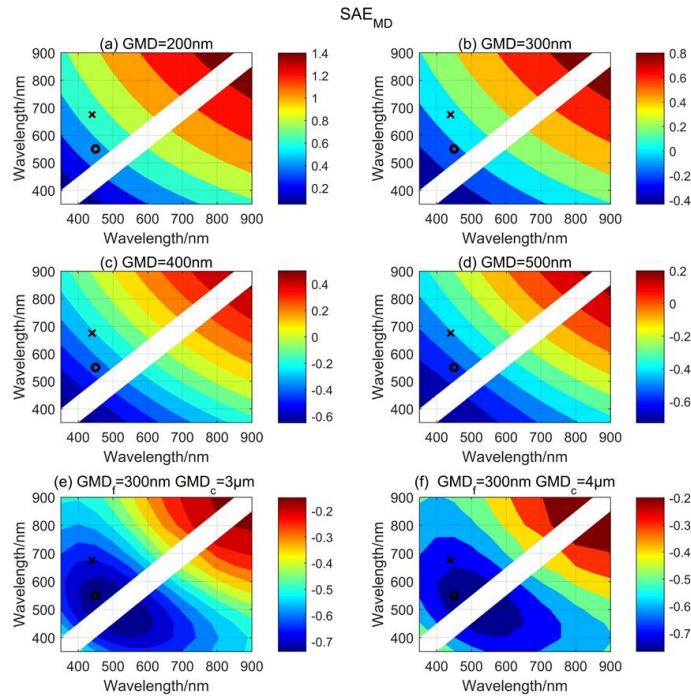


Figure 4.4 Simulation of SAE dependence on wavelength couples for MD with different geometric mean diameters (GMD). (a) ~ (d) for dust with single mode with GMD of 200, 300, 400 and 500; (e) and (f) for dust with single mode with GMD of 300 nm for fine mode ( $GMD_f$ ) and 3  $\mu\text{m}$  and 4  $\mu\text{m}$  for coarse mode ( $GMD_c$ ).

Figure 4.5 is the simulation of AAE dependence on wavelength pairs and size distribution of MD, and it reveals a totally different variation with  $AAE_{BrC}$ . The lower value appears with longer and shorter wavelength pairs, and high  $AAE_{MD}$  accompanies with wavelength pairs around 500-600 nm. The difference of AAE caused by varied wavelength pairs is about 2.  $AAE_{MD}$  could be affected by particle size, and it decreases with increasing size, but the impact is smaller compared with the selected wavelength

pairs.  $AAE_{MD,440-675}$  is lower than  $AAE_{MD,532-660}$ , and the difference is between 0.1 and 0.2. This result can explain that Cappa et al. (2016) used a higher threshold of AAE ( $AAE_{440-675} > 2$ ) to define the MD dominated regions, while Cazorla et al. (2013) used a lower threshold ( $AAE_{532-660} > 1.5$ ). Since we only give the difference caused by wavelength pairs aiming at our simulation, the difference might change when using different CRI and size distribution for MD.

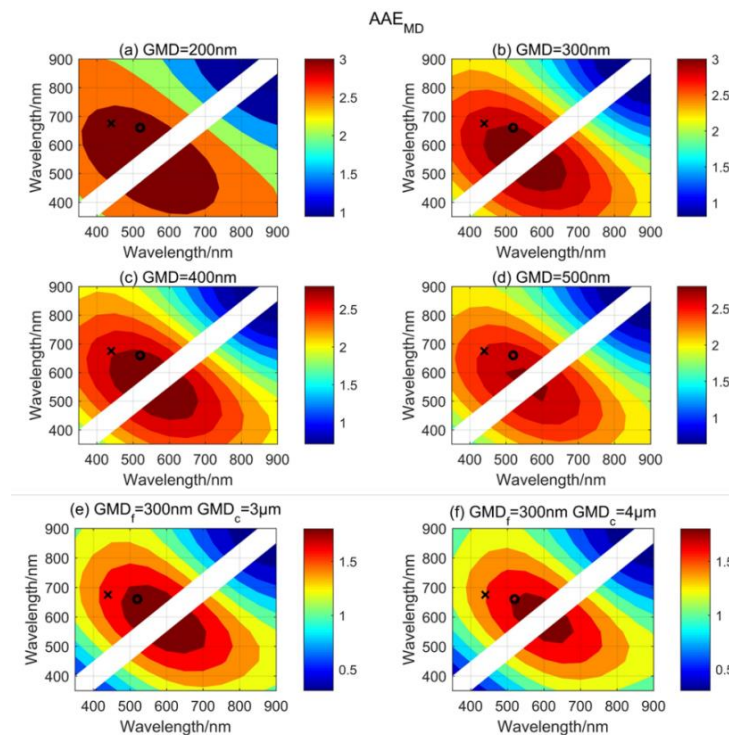


Figure 4.5 Simulation of AAE dependence on wavelength couples for MD at different geometric mean diameters.

#### 4.2.4 SAE and AAE of BC

Figure 4.6 shows the  $SAE_{BC}$  dependence on wavelength plotted with varied geometric median diameters.  $SAE_{BC}$  has a large scale from 0 to 2.6, and varies a lot when selecting different wavelength pairs. For example, the SAE difference reaches 1.2 for BC with GMD of 100 nm. In general,  $SAE_{BC}$  values are smaller when using shorter

wavelength pairs, and vice versa.  $SAE_{440-675}$  ( $SAE_{440-675} > 1.5$  for EC dominated) used by Cazorla et al. (2013) is slightly larger than  $SAE_{450-550}$  ( $SAE_{450-550} > 1.5$  for BC dominated) by Cappa et al. (2016) by about 0.1, indicating the two wavelength couples has little influence on  $SAE_{BC}$ .

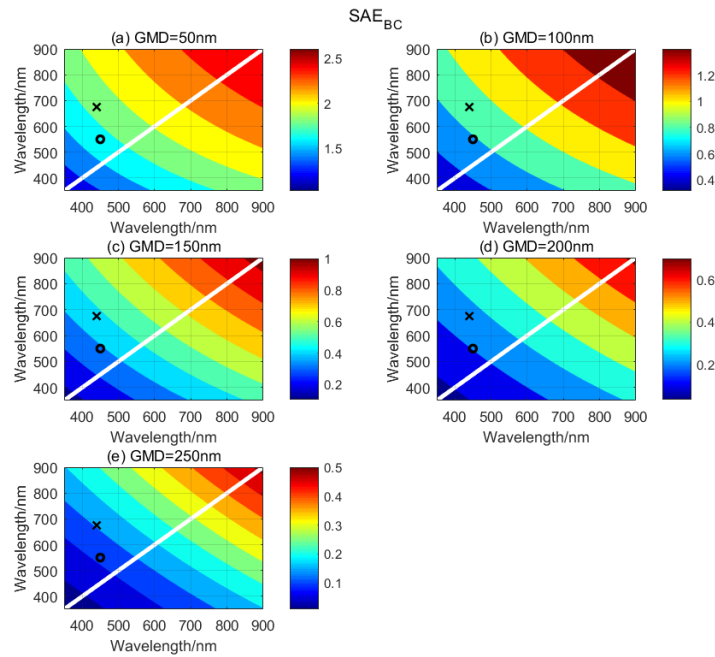


Figure 4.6 Simulation of SAE dependence on wavelength couples for BC at different geometric mean diameters.

The simulated results show that AAE of BC is not a constant, and varies a lot with wavelength pairs and size distributions (figure 4.7), which is consistent with Chung et al. (2012a) that  $AAE_{BC}$  is usually lower than 1 (table 2.3).  $AAE_{BC}$  from simulation varies from 0.45 to 1.12 when BC size is 50 nm, and from -0.23 to 0.12 if BC size is fixed at 250 nm. Zhang et al. (2019) also observed  $AAE_{BC}$  of 0.7 at 880-950 nm from Aethalometer (model AE33) measurements in Guangzhou. Similar to the wavelength dependence of  $SAE_{BC}$ ,  $AAE_{BC}$  is lower for shorter wavelength pairs, and has larger value with longer wavelength pairs.  $AAE_{BC,350-400}$  equals to 0.61 when  $GMD_{BC}$  is 50 nm, and  $AAE_{BC,850-900}$  equals to 1.11 if  $GMD_{BC}$  is set at 50 nm. The wavelength pair

selection could therefore bring discrepancy of about 0.5 ~ 0.8.

This  $AAE_{BC}$  dependence on wavelength was shown by previous studies (Bahadur et al., 2012; Wang et al., 2018). Indeed, Wang et al. (2018) reported  $AAE_{BC,520-880}$  of 0.8 and  $AAE_{BC,370-520}$  of about 0.52. The wavelength dependence of  $AAE_{BC}$  agrees with  $AAE_{BC}$  of 0.55 at 440-675 nm and 0.85 at 675-870 nm shown by Bahadur et al. (2012). In addition to the used wavelength pair,  $AAE_{BC}$  also relates with BC size distribution, and decrease with increasing GMD. Therefore, the assumption that  $AAE_{BC}$  equals 1 or a constant used by previous studies under all conditions is not unreasonable but will bring large uncertainties (Olson et al., 2015; Sandradewi et al., 2008; Zhang et al., 2019).

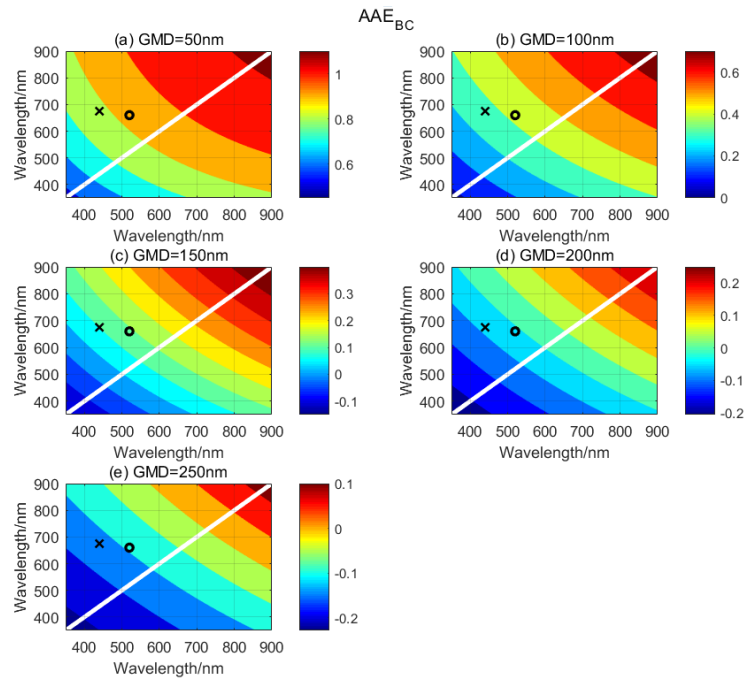


Figure 4.7 Simulation of AAE dependence on wavelength couples for BC with different geometric mean diameters.

#### 4.2.5 SAE and AAE for BC coating with clear shell

To investigate non-absorbing coating impacts on the SAE and AAE of BC ( $SAE_{BC\_CS}$  and  $AAE_{BC\_CS}$ ), we simulated  $SAE_{BC\_CS}$  and  $AAE_{BC\_CS}$  with BC core

geometric standard diameter of 100 nm ( $GMD_{core}=100$  nm), and varying relative coating thickness ( $GMD_{shell}/GMD_{core} = 1\sim 3$ ). The simulation results are given in figure 4.8 and 4.9.

The wavelength dependency of  $SAE_{BC\_CS}$  is similar to pure  $SAE_{BC}$ , and  $SAE_{BC\_CS}$  values difference could be larger than 1 attributed to the wavelength choice. For example,  $SAE_{BC\_CS,850-900}$  is 1.3 when  $GMD_{shell}$  to  $GMD_{core}$  ratio equals 1.5, which is larger than  $SAE_{BC\_CS,350-400}$  (0.4).  $SAE_{BC\_CS}$  decreases with the increasing coating thickness ( $GMD_{shell}/GMD_{core}$  increasing).  $SAE_{BC\_CS,440-675}$  decrease from 0.89 to 0.36, when  $GMD_{shell}$  to  $GMD_{core}$  ratio increase from 1 to 3.

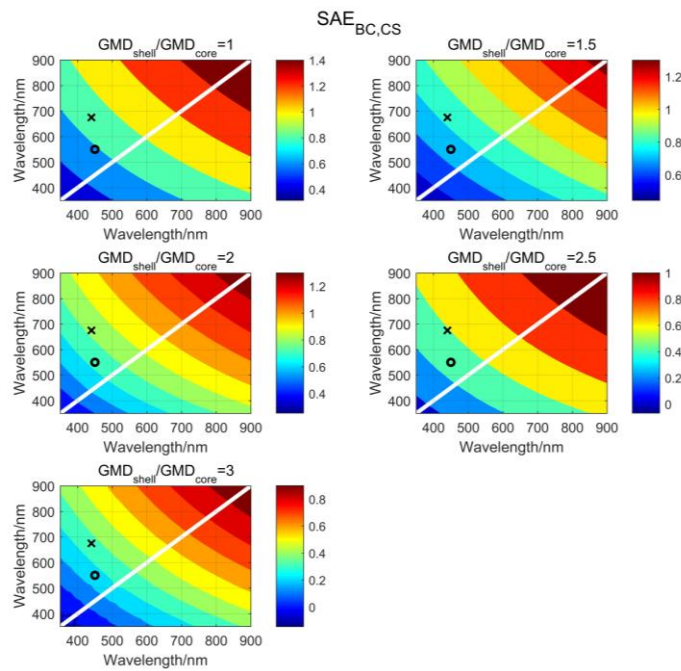


Figure 4.8 Simulation of SAE dependence on wavelength couples for BC with core geometric mean diameter of 100 nm, but varied relative coating thickness ( $GMD_{shell}/GMD_{core}$ ).

Similar to  $SAE_{BC\_CS}$ ,  $AAE_{BC\_CS}$  is also greatly dependent on wavelength couples.  $AAE_{BC\_CS}$  is larger when selecting longer wavelength pairs. For example,  $AAE_{BC\_CS,350-400}$  is about 0.14, while  $AAE_{BC\_CS,850-900}$  is larger (0.83) when the ratio of  $GMD_{shell}$  to

$GMD_{core}$  equals 1.5. Indeed,  $AAE_{BC\_CS,440-675}$  is always larger than  $AAE_{BC\_CS,450-550}$ , and the discrepancy is always lower than 0.1. Compared with selected wavelength couples, the coating thickness seems to have very limited impact on AAE values. For instance,  $AAE_{BC\_CS,440-675}$  varying 0.27 from to 0.48, when  $GMD_{shell}$  to  $GMD_{core}$  ratio is between 1 and 3, the maximum AAE appearing with  $GMD_{shell}$  to  $GMD_{core}$  ratio of 1.5.

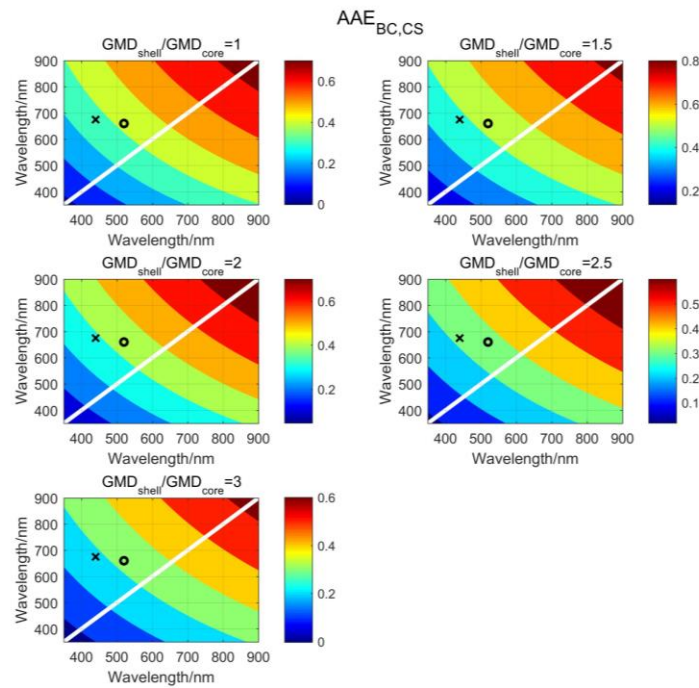


Figure 4.9 Simulation of AAE dependence on wavelength couples for BC with core geometric mean diameter of 100 nm, but varied relative coating thickness ( $GMD_{shell}/GMD_{core}$ ).

To further study  $AAE_{BC\_CS}$  dependence on BC core size and coating thickness, we calculated  $AAE_{BC\_CS}$  at wavelength pairs of 880-950 nm and 370-880 nm ( $AAE_{BC\_CS, 880-950}$  and  $AAE_{BC\_CS, 370-880}$ ). The selected wavelengths (370, 880 and 950 nm) are corresponding to the wavelengths used by Aethalometer (AE33). Absorption at 880 and 950 nm could be attributed to BC alone neglecting the impact from BrC and MD (Zhang et al., 2019). To simplify the mixture, the absorption species only include BC and BrC in the following discussion. The wavelength at 370 nm represents a short wavelength, where the absorption is contributed by BC and BrC, and it could be other wavelengths

with non-negligible absorption by BrC.

$GMD_{shell}$  to  $GMD_{core}$  ratio was set between 1 and 3, and  $GMD_{core}$  ranges from 10 to 250 nm, which covers the possible range of BC core size and relative coating thickness reported by previous studies (Liu et al., 2015a; Peng et al., 2016; Reddington et al., 2013; Wang et al., 2018). The calculated  $AAE_{BC\_CS,880-950}$  and  $AAE_{BC\_CS,370-880}$  as a function of  $GMD_{core}$  and  $GMD_{shell}$  to  $GMD_{core}$  ratio are shown in figure 4.10a-b respectively. The results reveal that  $AAE_{BC\_CS,880-950}$  is larger than 1 for  $GMD_{core}$  lower than 64 nm. When  $AAE_{BC\_CS,880-950}$  is larger than 1, its value mainly depends on  $GMD_{core}$  but less on  $GMD_{shell}$  to  $GMD_{core}$  ratio, especially when  $AAE_{BC\_CS,880-950}$  is between 0.6 and 1. Similar to  $AAE_{BC\_CS,880-950}$ ,  $AAE_{BC\_CS,370-880}$  also mainly depends on  $GMD_{core}$  but less on  $GMD_{shell}$  to  $GMD_{core}$  ratio when  $GMD_{core}$  larger than 42 nm.

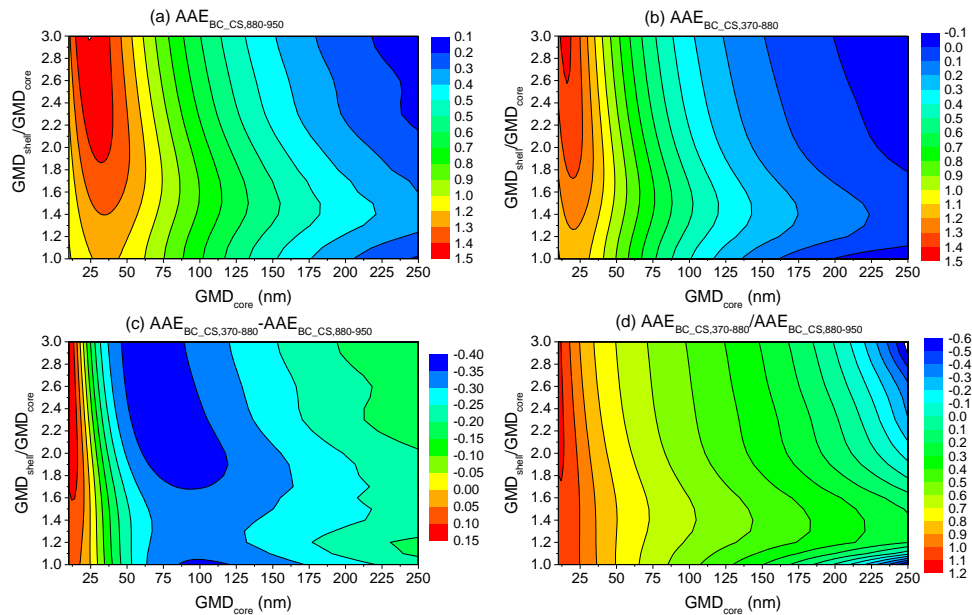


Figure 4.10 Simulation of  $AAE_{BC\_CS,880-950}$  (a),  $AAE_{BC\_CS,370-880}$  (b),  $AAE_{BC\_CS,370-880} - AAE_{BC\_CS,880-950}$  (c) and  $AAE_{BC\_CS,370-880}/AAE_{BC\_CS,880-950}$  (d) for BC coating with clear shell impacted by the geometric mean diameter of BC core ( $GMD_{core}$ ) and the relative coating thickness ( $GMD_{shell}/GMD_{core}$ ).

Thereby,  $AAE_{BC\_CS}$  depends on the wavelength pairs, the BC core size and relative thickness. But the dependence on coating thickness is affected by BC core size. Specially, for BC has relative smaller ( $GMD_{core} < 50$  nm) or larger core size ( $GMD_{core} > 125$  nm),  $AAE_{BC\_CS}$  depends on both BC core size and coating thickness. However, when BC core size is between 50 and 125 nm,  $AAE_{BC\_CS}$  is weakly impacted by coating thickness.

Figure 4.10c-d show the difference between  $AAE_{BC\_CS, 880-950}$  and  $AAE_{BC\_CS, 370-880}$ , and the ratio of  $AAE_{BC\_CS, 370-880}$  to  $AAE_{BC\_CS, 880-950}$  separately. It could be found that  $AAE_{BC\_CS, 370-880}$  is larger than  $AAE_{BC\_CS, 880-950}$  only for  $GMD_{core}$  smaller than 26 nm. In other cases,  $AAE_{BC\_CS, 370-880}$  is always smaller than  $AAE_{BC\_CS, 880-950}$ , and the difference is 0.3~0.4 for particle diameter between 50 and 150 nm. This value is quite large, because the reported BC AAE has a narrow range (0.55~1.3, table 2.2). The comparison highlights the  $AAE_{BC\_CS}$  dependence on wavelength couples.

Figure 4.10d reveals that  $AAE_{BC\_CS, 370-880}$  to  $AAE_{BC\_CS, 880-950}$  ratio mainly depends on  $GMD_{core}$  but less on  $GMD_{shell}$  to  $GMD_{core}$  ratio. Indeed,  $AAE_{BC\_CS, 370-880}$  to  $AAE_{BC\_CS, 880-950}$  ratio is 0.7~0.8, when  $GMD_{core}$  equals to 50 nm and  $GMD_{shell}$  to  $GMD_{core}$  ratio ranges from 1 to 3. For  $GMD_{core}$  with a value of 100 nm, the  $AAE_{BC\_CS, 370-880}$  to  $AAE_{BC\_CS, 880-950}$  ratio is between 0.49 and 0.61. When  $GMD_{core}$  is larger than 100nm,  $AAE_{BC\_CS, 370-880}$  to  $AAE_{BC\_CS, 880-950}$  ratio increases sharply first, and then decreases slowly with the increasing  $GMD_{shell}$  to  $GMD_{core}$  ratio.

As introduced in *section 4.1.1*,  $AAE_{BC}$  is an important for deriving absorption by BC and BrC, but its value still has large discrepancy by different studies. To evaluate the uncertainties on BC absorption due to the choice of  $AAE_{BC}$ , the BC absorption at 370 nm as an example is calculated using different  $AAE_{BC\_CS, 370-880}$  values.

Calculations of BC absorption at 370 nm are made using  $AAE_{BC\_CS, 370-880}$  given in figure 4.10b, then  $AAE_{BC\_CS, 370-880}$  equal to 1 and finally  $AAE_{BC\_CS, 370-880}$  equal to  $AAE_{BC\_CS, 880-950}$  shown in figure 4.10a.  $AAE_{BC\_CS, 370-880}$  shown in figure 4.10b is in consideration of  $AAE_{BC\_CS}$  dependence on BC core size, relative coating thickness and

wavelength pairs, which will be used as the “true” value to calculate the uncertainties. While assuming  $AAE_{BC\_CS,370-880}$  equal to 1 ignores all these three factors, and  $AAE_{BC\_CS,880-950}$  instead of  $AAE_{BC\_CS,370-880}$  neglects the dependence on wavelength pairs. The output uncertainties are shown in figure 4.11a-b respectively.

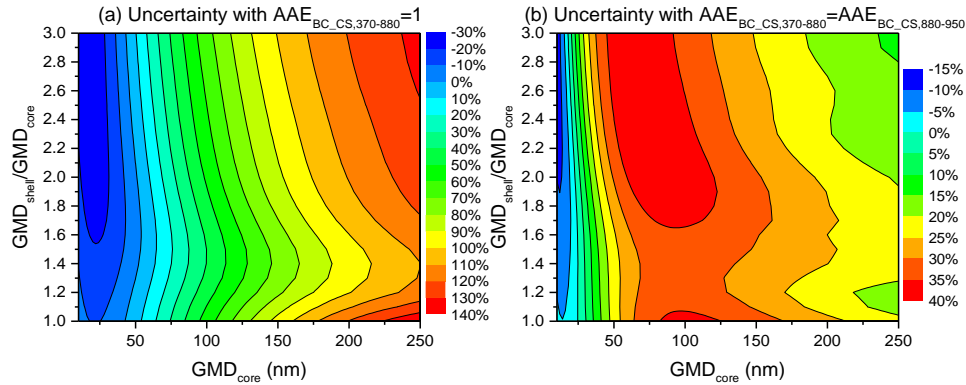


Figure 4.11 BC absorption (370 nm) uncertainties using  $AAE_{370-880}$  of 1 (a) and  $AAE_{370-880}$  equal to  $AAE_{880-950}$  (b).

When using  $AAE_{BC\_CS,370-880}$  equal to 1 (figure 4.11a), it could be found that the BC absorption at 370 is underestimated by up to 30 % for  $GMD_{core}$  smaller than 30 nm; BC absorption uncertainty increases by over 40% when  $GMD_{core}$  larger than 74 nm. For  $GMD_{core}$  between 44 and 54 nm, BC absorption uncertainty could be limited to 10%. When ignoring the absorption spectral dependency of BC (figure 4.11b), the uncertainty is below 40%. The largest uncertainty is observed for  $GMD_{core}$  equal to 76 nm and  $GMD_{shell}$  to  $GMD_{core}$  ratio of 2.2. Hence, using the  $AAE_{BC\_CS,880-950}$  throughout the wavelength range brings smaller errors for BC absorption, and therefore BrC absorption, than using a constant value of 1 when  $GMD_{core}$  larger than 76 nm or smaller than 28 nm. Whereas a constant value of 1 would be a better choice for  $AAE_{BC}$  if  $GMD_{core}$  is between 38 and 72 nm.

Therefore, the AAE dependence on wavelength couples and aerosol size can't be neglected when calculating absorption with AAE attribution method. Moreover, the

difference of SAE and AAE values caused by wavelength selection should be taken into consideration when comparing different schemes built with SAE and AAE. It should be noted that Mie theory is only applicable for spherical particles. BC with diameter smaller than 50 nm corresponds mainly to freshly emitted particles with fractal aggregate and therefore not spherical (Qiao et al., 2018; Zhai et al., 2017). Our conclusions for BC and BC coated with clear shell are specific for well-aged BC particles.

### 4.3 Conclusions

In this part, we introduced the present studies to retrieve aerosol-absorbing types (BrC, MD and BC) based on AAE only or based on SAE vs. AAE space scheme. These methods highlight large discrepancies from one study to another. Thus, we comprehensively investigated SAE and AAE for BrC, MD and BC, together with BC coating with clear shell using Mie simulation results.

The simulated results reveal that SAE and AAE can be significantly influenced by the selected wavelength couples and by particle size. The results could explain the controversy of the SAE and AAE threshold values used to classify different aerosol types. Especially, the difference caused by wavelength pairs should be taken into consideration when using SAE and AAE scheme proposed by previous studies for aerosol type classification.

We also further investigated AAE of BC coated with clear shell, and its dependence on BC core size, relative coating thickness and wavelength pairs. Our study reveals that AAE of pure or coated with clear shell BC is not a constant, and it depends on BC core size and selected wavelength pairs. It should be noted that relative coating thickness has less impact on AAE for well-aged BC ( $125 \text{ nm} > \text{GMD}_{\text{core}} > 50 \text{ nm}$ ). As the observed  $\text{GMD}_{\text{core}}$  is often around  $60 \sim 150 \text{ nm}$  (Cheng et al., 2018; Taylor et al., 2014; Moriet al., 2016), a good knowledge of BC size is helpful to select BC AAE, and then reduces the uncertainty of estimated BC absorption.

## **Chapter 5 Study on aerosol chemical composition retrieval based on the imaginary part of complex refractive index**

Compared with SAE and AAE, CRI is an intrinsic parameter for aerosol chemical compositions, and independent of particle size.  $k$  combining with size or dSSA has been widely used to retrieve aerosol chemical compositions quantitatively (Choi and Ghim, 2016; Schuster et al., 2016a; Wang et al., 2013; Wang et al., 2017a) (given in *section 5.2*). These  $k$ -based methods allow obtaining columnar aerosol chemical compositions, but there is still lacking of verification with reliable columnar aerosol chemical compositions. This chapter aims to study the  $k$ -based methods, and examine its performance by relating the retrieved columnar aerosol chemical compositions using long-term dataset from AERONET with regional transport and emission inventory.

Firstly, we will present progress of  $k$ -based methods in the last decade. Then, the method proposed by Li et al. (2013) is selected for application and preliminarily validation in our study. This method utilizes  $k$ ,  $n$  and dSSA (named as  $k$ - $n$ -dSSA method) to retrieve columnar BC, BrC, MD, ammonium sulfate (AS) as a proxy for dry scattering components, and Aerosol Water Content (AW) representing liquid water in the aerosol (*appendix A2*). The  $k$ - $n$ -dSSA method was chosen because this method could retrieve the main aerosol chemical compositions in the atmosphere, and the retrieved aerosol chemical compositions (BC, BrC, MD, AW and AS) can be speculated with emission sources and air mass backward trajectory analysis, which would be helpful to examine the algorithm. Some of the contents in this chapter have been published in the journal of Atmospheric Environment (<https://www.sciencedirect.com/science/article/abs/pii/S1352231017306064>).

### **5.1 $k$ -based methods description**

The main idea of  $k$ -based methods to derive aerosol chemical compositions is based on the absorption spectral dependence. As given in *chapter 1*, BC can be

extracted from the other absorbing species due to its stronger absorption from UV to IR spectrum. Schuster et al. (2005) classified aerosols into three types: BC, scattering particles (AS) and AW. This study was the first to use  $k$  and  $n$  to retrieve columnar BC concentration assuming that BC is the only absorbing aerosol with no spectral dependency within the atmosphere.

However, recently OC and MD have been found to have significant absorptions, especially at short wavelengths. Moreover, their absorption spectral dependencies (in the UV to visible range) are similar with higher absorption in UV, but decrease distinctly with wavelength in the visible spectrum (figure 2.3) (Hoffer et al., 2006; Kirchstetter et al., 2004; Wagner et al., 2012). Based on this characteristic, Dey et al. (2006) retrieved columnar BC, BrC or MD and AW fractions over Kanpur using MG and BR theories (*chapter 2* for more details) based on the  $k$  and  $n$  taking into absorption by OC or MD.

Similarly, Arola et al. (2011) also retrieved BC, OC, AS (a proxy for scattering species in dry aerosol) and AW based on the spectral variation of OC absorption in biomass burning regions of South America and Africa. The retrieved OC was compared to model result with the global Oslo CTM, and they found that model values were higher in biomass burning regions than  $k$ -based retrieval except for India and China.

Since OC and MD have similar absorption dependence on wavelength (figure 2.3), it is not realistic to distinguish both species based only on the imaginary part of CRI. To deal with this problem, aerosol size or size related parameters, like the spectral variation of SSA (dSSA), were selected as additional parameters to distinguish OC and MD. Indeed, MD is usually observed within the coarse mode while carbonaceous aerosols mainly appear within fine mode.

Schuster et al. (2016a) used aerosol size as additional information to distinguish MD from OC. They retrieved BC and BrC in fine mode together with hematite and goethite for coarse mode. This study estimated the retrieval uncertainty of about 52% for BC, 50% ~ 440% for BrC and 97% for mineral dust.

Similarly, Xie et al. (2017) used  $k$ ,  $n$ , Volume Fraction ratio of fine to Coarse mode

(VFC), Sphericity (SPH) and Hygroscopic Growth Factor (HGF) to derive BC, BrC, Primary Organic Matter (POM), and AS in fine mode aerosol, as well as MD, Sea Salt (SS) and AW in coarse mode. The retrieved results were compared with aerosol chemical compositions in PM<sub>2.5</sub> analyzed with in-situ filter sampling, with square of correlation coefficient (R) of 0.79 for retrieved and measured BC, R equal to 0.8 for retrieved BrC and measured OC, and R of 0.82 and 0.84 for retrieved AS with measured sulfate and nitrate separately.

Zhang et al. (2018) also utilized hygroscopicity to distinguish WSOM and WIOM. Based on  $n$ ,  $k$  and hygroscopicity, they retrieved BC, WSOM, WIOM, AS and AW in fine mode aerosols, and MD and AW in coarse mode aerosols. The retrieved BC, OM and AS were compared with in-situ measured aerosol chemical compositions in PM<sub>1</sub> with R of 0.73, 0.59 and 0.89 respectively.

Previous studies revealed that SSA for dust dominated regions increases with wavelength, while SSA for carbonaceous aerosol regions decreases with wavelength (Dubovik et al., 2002; Li et al., 2015a; Russell et al., 2010). Wang et al. (2013) simulated the spectral variation of SSA for BrC and MD using the same  $k$  values but different size distributions. They found that BrC SSA reached a maximum at 675 nm, while dust SSA always increased with wavelength (figure 5.1). So they used dSSA (SSA<sub>675</sub>-SSA<sub>870</sub>) to differentiate BrC and dust. They also added spectral variation of  $k$  to distinguish BC from other species, and  $n$  to separate AW for its lowest  $n$  (1.33). Finally, they developed an algorithm (named as  $k$ - $n$ -dSSA method) to retrieve five aerosol categories, including three dry absorbing components (BC, BrC, and MD), and two scattering components (AW and AS). Further details about this algorithm are given in *appendix A2*. After obtaining the columnar aerosol mass concentration, the retrieved BC columnar mass concentration was compared with in-situ measured BC concentration by Aethalometer (AE51), with R of 0.77 (Li et al., 2013).

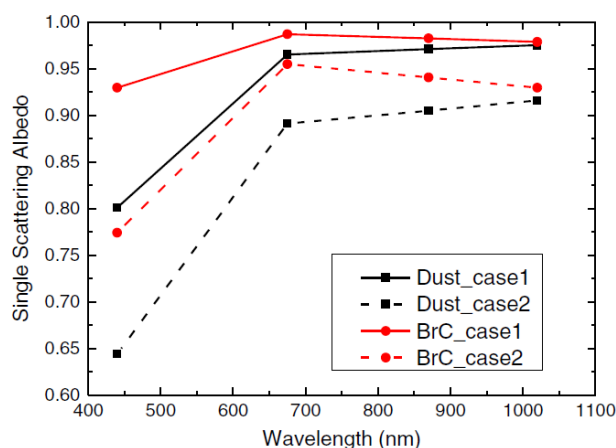


Figure 5.1 SSA spectra for BrC and dust (Wang et al., 2013) from simulation with Mie theory. BrC and Dust have the same  $k$  values at the four wavelengths, but different size distributions. Case 1 has  $k$  of 0.0122 at 440 nm, and 0.0013 at 675, 870 and 1020 nm; case 2 has  $k$  of 0.0525 at 440 nm, and 0.005 at other three wavelengths.

This method was also extended to retrieved BC, MD, AW, AS, water soluble organic carbon (WSOC) and water insoluble organic carbon (WIOC) combining MG theory and VAM model by Choi and Ghim (2016). To verify the retrieved columnar aerosol chemical compositions, Choi and Ghim (2016) also compared BC and AS with surface measurement, they find BC is closely related with the surface concentration ( $R=0.78$ ), while AS has weak correlation between the columnar and surface concentration ( $R=0.38$ ), which was presumed to be AS presenting above planetary boundary layer because of cloud processing.

It could be found that great progresses have been made during the last decade to retrieve aerosol chemical compositions using  $k$ -based methods based on remote sensing (table 5.1). Some studies compared their results with in-situ measured compositions and they had fairly good correlation, and the  $k$ -based methods seem to be a proper way to retrieve aerosol chemical composition quantitatively.

Table 5.1 Summary of aerosol chemical composition retrieval methods based on  $k$ .

Reference	Compositions	Parameters	Mixing rules	Data source
Schuster, 2005	BC, AS, AW	$k, n$	MG	AERONET
Dey et al., 2006	BC, AS, OC/MD, AW	$k, n$	MG+BR	AERONET
Arola et al., 2011	BC, OC, AS, AW	$k, n$	MG	AERONET
Li et al., 2013	BC, BrC, MD, AS, AW	$k, n, dSSA$	VAM	AERONET
Xie et al., 2014	BC, BrC, MD, AS, AW	$k, n, dSSA$	MG+BR+VAM	AERONET
Schuster et al., 2016a	BC, OC, hematite, goethite	$k, \text{size}$	MG	AERONET
Choi and Ghim, 2016	BC, WSOC, WIOC, MD, AS, AW	$k, n, dSSA$	MG+VAM	AERONET
Xie et al., 2017	BC, BrC, POM, MD, AS, SS, AW	$k, n, VFC, SPH, HGF$	VAM	AERONET
Zhang et al., 2018	BC, WSOM, WIOM, MD, AS, AW	$k, n, HGF, \text{size}$	VAM	AERONET

## 5.2 Columnar aerosol chemical compositions dependence on regional transport

Aerosol loading is not only impacted by local pollutants from fossil fuel, biomass burning, and urban construction (Liu et al., 2014; Yang et al., 2015), but also those from regional transport (Zíková et al., 2016). In some cases, the seasons and the type of surfaces, over which air masses are transported, are more important in determining the aerosol chemical components (Lammel et al., 2003). In this section, we will apply the  $k$ - $n$ - $dSSA$  method proposed by Li et al. (2013) to investigate columnar aerosol chemical composition dependence on regional transport using long-term observation of columnar aerosol properties observed in Beijing.

### 5.2.1 Geographical location and emission distribution around Beijing

North China Plain (NCP) has four distinct seasons corresponding to the emission or transport of varied aerosol types (figure 5.2), and thereby it is a good candidate to study columnar aerosol chemical compositions dependence regional transport in

different seasons. The capital of China, Beijing, located in the north of NCP, was chosen for this study.

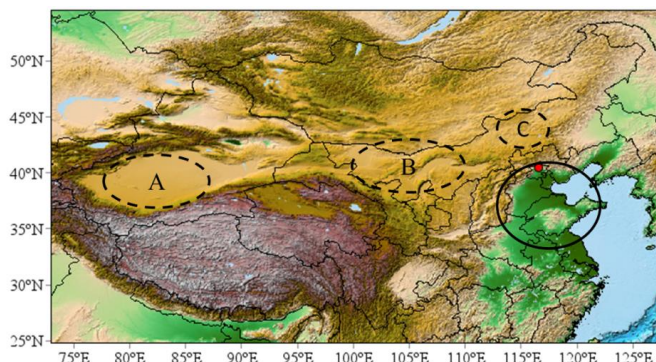


Figure 5.2 Geographical location of Beijing site (marked by the red dot), and the region of North China Plain is marked with solid black ellipse. The main dust sources impacting Beijing are marked by dashed black ellipses (A: Taklimakan desert; B: Tengger desert, Maousu desert, Ulan Buh desert and Badain Jaran desert; C: Hunshdak desert).

The Beijing observation site is on the roof of the Institute of Atmospheric Physics building (39.98°E, 116.38°N, 92 m ASL). As the capital of China, Beijing is located at the junction of mountain Yan, mount Taihang and NCP. The topography of the area reduces the wind speed and restrains the diffusion of pollutants transported from southern cities. The climate in Beijing is a typical continental monsoon climate characterized by four clearly distinct seasons. Bohai is in the southeast of the site, which could bring AW to Beijing impacted by southeast monsoon in summer. The prevailing winds in winter are typically from northwest directions. The geographical and meteorological conditions produce a seasonal variation in the atmospheric aerosol chemical composition. In spring, dust aerosol is dominant and arises from dust storms and floating dust episodes (Sun et al., 2005; Yu et al., 2013). The three main dust emission regions are given in figure 5.2, marked by black dashed ellipses (Gao et al., 2008; Wang, 2004). Biomass burning in early summer and autumn (Li et al., 2010; Zhang et al., 2008), and winter coal heating in the north of China results in frequent and

serious pollution events with high carbonaceous content in particles (Sun et al., 2013b; Zheng et al., 2015). As a result of rapid urbanization and economic development, large amounts of anthropogenic pollutants are emitted from industrial processes and vehicle exhausts throughout the year.

To obtain the aerosol potential sources around Beijing, we downloaded emission inventories from Peking University (<http://inventory.pku.edu.cn/>). The spatial emission distribution of Total Suspended Particles (TSP) (including primary emission from energy production, industry, transportation, agriculture, and so on) from 2005 to 2014 is shown in figure 5.3. Dust and sea salt aerosols are excluded of the analysis because of the necessity to use totally different approaches (Huang et al., 2014).

It could be found that TSP has an obvious spatial difference, with high level in the NCP region, but relatively low emission in the north and west of Beijing. To compare the emission discrepancy among the four seasons, the ratio of the mean TSP emission in different seasons to the total average TSP emission from 2005 to 2014 is shown in figure 5.4. During summer, the TSP emission around Beijing is the lowest, while the highest emission of TSP appears in winter (figure 5.4).

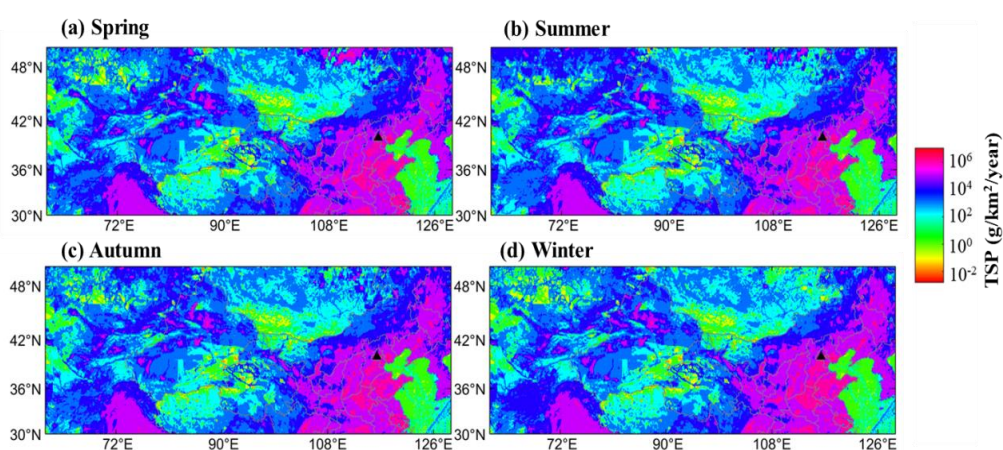


Figure 5.3 Spatial distribution of TSP emission in the four seasons from 2005 to 2014. Beijing is marked by the black triangle.

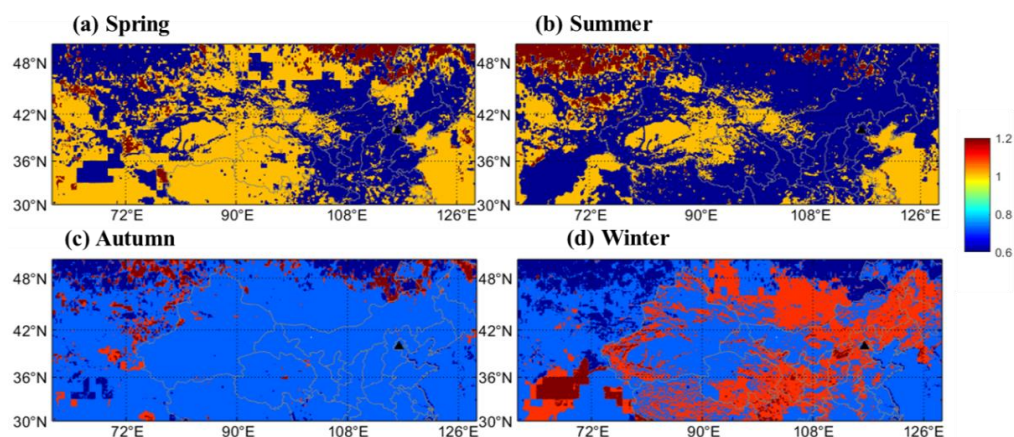


Figure 5.4 Spatial distribution of the ratio of seasonal mean TSP emission to the total average TSP emission from 2005 to 2014.

Similarly, the emission distributions of BC (figure A3.1 and A3.2), OC (figure A3.3 and A3.4) and the sum of SO<sub>2</sub> and NO<sub>x</sub> (indicator for sulfate and nitrate, figure A3.5 and A3.6) are given in appendix A3. Similar to TSP, the emissions of BC, OC and sum of SO<sub>2</sub> and NO<sub>x</sub> have similar spatial distributions, with the highest emission over south of Beijing, and winter has the largest emission around Beijing compared with other seasons.

### 5.2.2 Backward trajectories and cluster analysis

The Hybrid Single Particle Lagrangian Integrated Trajectory model (HYSPLIT) developed by NOAA/ARL (US National Oceanic and Atmospheric Administration/Air Resources Laboratory) was used to calculate the air parcel trajectories. The Global Data Assimilation System (GDAS) was selected for the input meteorological parameters. Although the accuracy of an individual trajectory calculated by HYSPLIT is about 20 ~ 30 % (Draxler et al., 1998), a large dataset of trajectories produces a more meaningful identification of the air mass origin (Freitag et al., 2014; Guirado et al., 2014). Cluster analysis for the large trajectories has been demonstrated to be an effective way to clarify the statistical air mass transportation and identify the main pollution source regions (Pinero-Garcia et al., 2015; Rozwadowska et al., 2010; Wang, 2004; Wehner et al., 2008;

Xia et al., 2007).

Since the aerosol particle concentration is mainly concentrated within the boundary layer (Sun et al., 2013a; Zhang et al., 2009) and assumed to be well mixed at 4 UTC (12 LTC in Beijing) (Wehner et al., 2008), one trajectory per day can well represent the air mass for one full day (Borge et al., 2007; Rozwadowska et al., 2010; Valenzuela et al., 2012; Xu et al., 2013a). Therefore, the 72 h backward trajectories ending at 500 m above ground level in Beijing site were calculated every day at 4 UTC. 949 trajectories over 10 years (from January 2005 to December 2014) were used for the data analysis, which is equal to the available days of aerosol optical data (level 2.0) obtained from AERONET, including 327, 171, 194 and 257 trajectories for spring (March, April and May), summer (June, July and August), autumn (September, October and November) and winter (December, January and February), respectively.

To obtain well-separated and well-representative clusters, the trajectories were grouped according to the geometric distance between individual trajectories (with lower cluster Spatial Variance, SV), taking into account the wind direction and speed of an individual trajectory by using the clustering method given by HYSPLIT model (Kelly et al., 2013; Moroni et al., 2015; Valenzuela et al., 2012; Xu et al., 2013a). The SV is defined as equation 5.1 (Draxler et al., 2009):

$$SV = \sum \text{all trajectories in cluster} \times \left( \sum \text{all trajectory endpoints} \times (D \times D) \right) \quad (5.1)$$

D is the distance between a trajectory endpoint and the corresponding cluster-mean endpoint. The Total Spatial Variance (TSV) can be calculated with (Draxler et al., 2009):

$$TSV = \sum \text{all SV} \quad (5.2)$$

Initially, each trajectory is treated as a cluster, and then paired. The TSV is calculated in each stage. Large changes in TSV mean that significantly different trajectories were grouped into the same cluster. The number just prior to large change in TSV is considered as the approximate number of the clusters (Xia et al., 2007). After balancing the requirement of more clusters and better separated trajectories, the

trajectories were aggregated into 5 groups for different seasons in this work (as shown in figure 5.5).

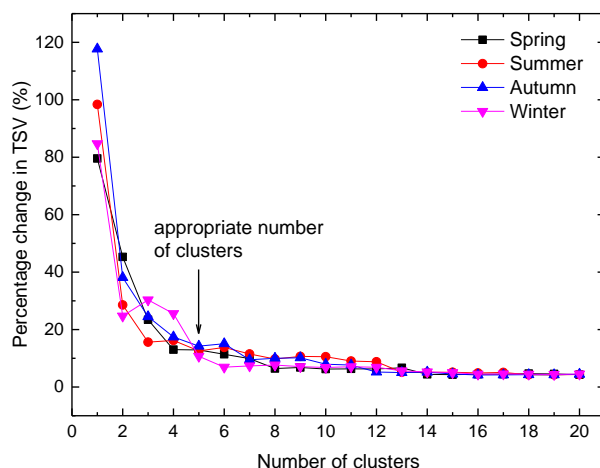


Figure 5.5 Percentage changes in the total spatial variance (TSV) against the number of clusters for different seasons. The black arrow marks the appropriate number of clusters.

The mean backward trajectory clusters in the four seasons from January 2005 to December 2014 are shown in figure 5.6. The backgrounds of the figure are displayed as average AOT obtained from MODIS aerosol products (Aqua level 3 products with a resolution of  $1^{\circ} \times 1^{\circ}$ ) over the same period. The lines in cyan, green, blue, magenta and red represent clusters C1-C5, respectively, and these lines are ranking with a decrease moving speed. There are large seasonal differences in trajectory direction, moving speed and route, which arise from seasonal evolution of the atmospheric circulation (Lau and Song, 1996).

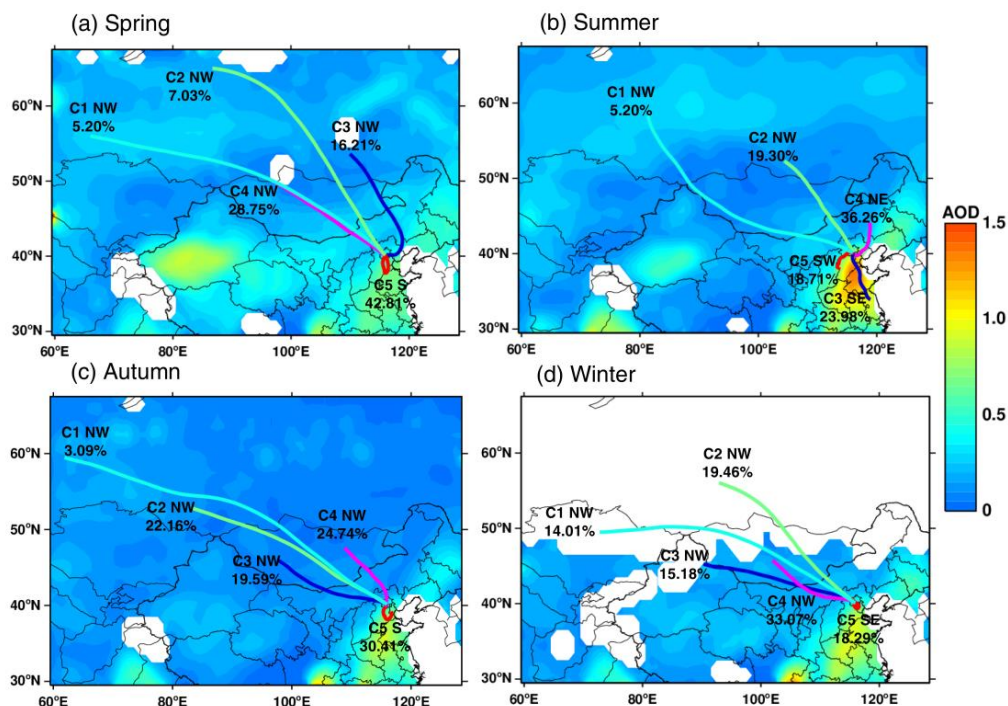


Figure 5.6 72-hour daily air mass backward trajectory clusters ending at Beijing in four seasons, together with satellite products from Aqua level 3 products. The colors of the trajectories represent different clusters, which are also used for distinguishing the corresponding columnar aerosol properties in the following text.

In spring, autumn and winter, a large proportion ( $> 50\%$ ) of total trajectories are associated with higher wind speeds originating from the northwest (NW, clusters C1 to C4). Whereas cluster C5, which has the slowest speed, is mainly from the south (S) in spring and autumn, and from southeast (SE) in winter. Among the three seasons, winter holds the lowest frequency of southerly wind, followed by autumn. In summer, the clusters are well separated in direction and fewer trajectories originating from the northwest (21%). Clusters from south of Beijing, including a faster one from the southeast (SE, cluster C3) and a slower one from the southwest (SW, cluster C5), comprised the largest proportion ( $\sim 43\%$ ) of trajectories. In addition, cluster C4 from the northeast was the most common (36%) of the five clusters in summer. The average AOT distributions across the four seasons indicate that the AOT in south of Beijing is

higher than that in the north, northeast and northwest. This result is consistent with results from emission inventory discussed above. Among the four seasons, summer has the largest AOT. Since there is relatively smaller emission of BC, OC and SO<sub>2</sub>+NO<sub>x</sub> during summer, the large AOT could be attributed to AW increasing concentration (Fan et al., 2006).

### 5.2.3 Aerosol physical and optical properties of each cluster

Average aerosol volume size distributions of the five clusters during different seasons over Beijing exhibit bimodal log-normal structures (figure 5.7). Once more, the lines in cyan, green, blue, magenta and red represent clusters C1-C5, respectively. Clusters from northwest of Beijing (cluster C1 to C4 in spring, autumn, winter, and cluster C1-C3 in summer) have the maximum volume concentrations in coarse mode for all seasons. Conversely, clusters from south of Beijing (cluster C5 in the four seasons and cluster C3 in summer) occur with more fine particles except in spring. The increase of fine mode volume concentrations is associated with a decrease of NW cluster moving speed. Among the four seasons, spring is characterized by a large volume concentration of coarse particles in all clusters. Cluster C1 has a mean peak volume concentration of  $0.39 \mu\text{m}^3 \mu\text{m}^{-2}$  at  $2.24 \mu\text{m}$ , which is twice as large as other seasons, and caused by the frequently occurring dust episodes (Wu et al., 2009). In summer, cluster C3 is the most important contributor to fine mode particles ( $0.15 \mu\text{m}^3 \mu\text{m}^{-2}$ ) at  $0.26 \mu\text{m}$ , while cluster C5 contributes the most to fine mode particles during other seasons.

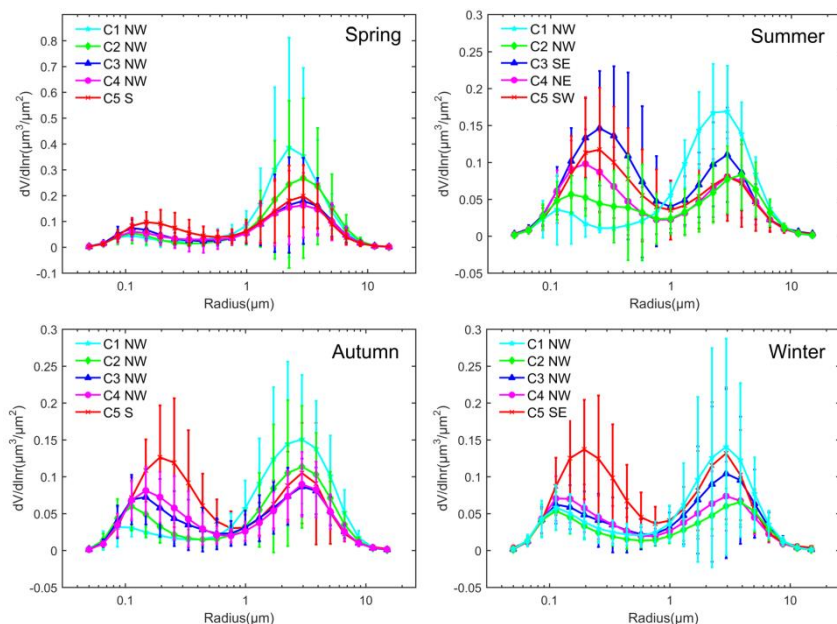


Figure 5.7 Seasonal variations of aerosol size distributions for different clusters.

Figure 5.8 shows the spectral variations of AOT, SSA, AAOT,  $n$  and  $k$ , which vary distinctly for different clusters observed during different seasons. Generally, aerosol optical properties show a pronounced difference for different clusters, which is consistent with the study by Xia et al. (2007). In general, AOT and SSA values are closely associated with the air masses directions and speeds. High AOTs and SSAs are always observed over Beijing when air masses are transported from south and surrounding areas of Beijing (cluster C5 for the four seasons together with cluster C3 in summer). Table 5.2 gives the average aerosol optical properties value at 675 nm during the four seasons. AOT has a maximum seasonal mean value of 0.79 in summer, which is consistent with Aqua MODIS measurements. During winter, AOT in Beijing has the lowest value (0.59). Seasonal variation of AOT is quite different with the TSP emission, which is probably due to the contribution of water in aerosol. Aerosol water is not included in the estimation of TSP emission, but it can lead to aerosol hygroscopic growth and then increase scattering ability (Liu et al., 2013b).

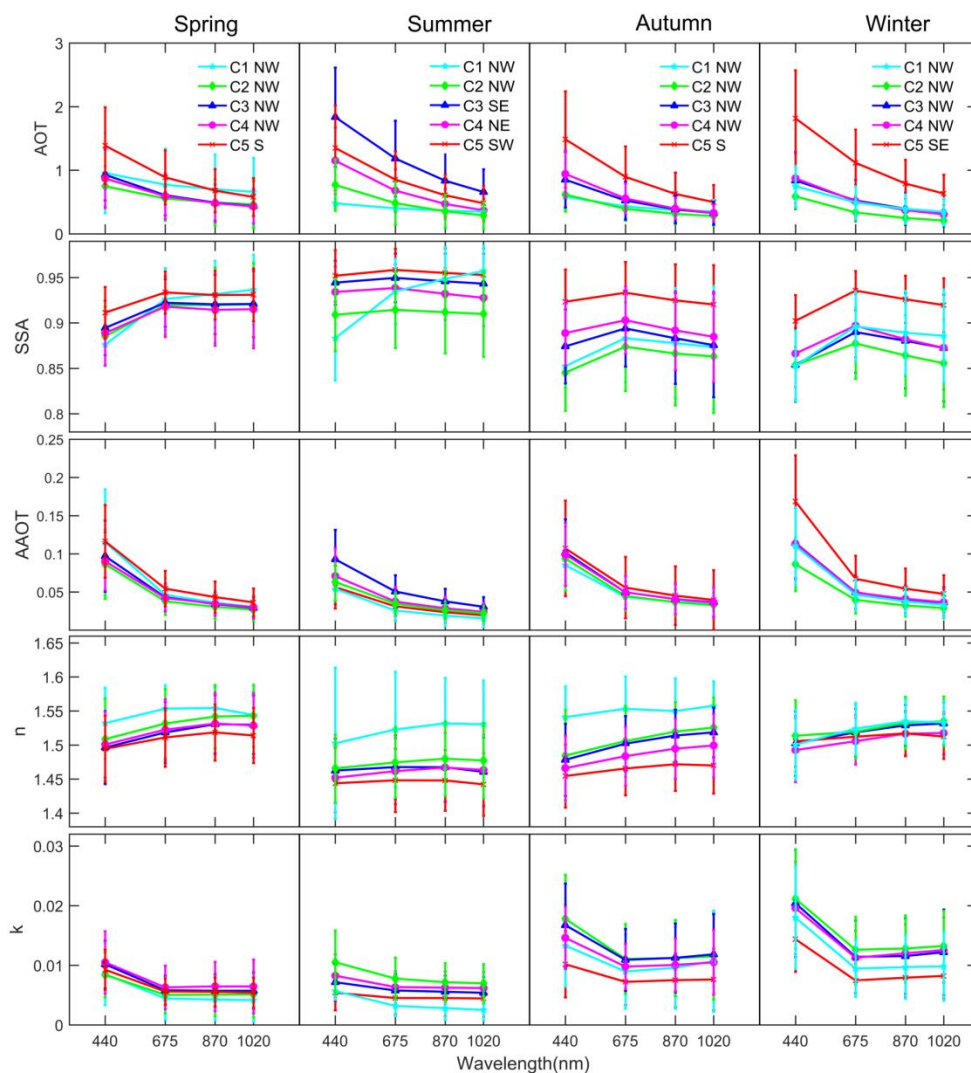


Figure 5.8 Spectral variations of AOT, SSA, AAOT, n and k for different seasons and different clusters.

Table 5.2 Mean aerosol optical properties value for the four seasons at 675 nm.

Season	AOT	SSA	AAOT	n	k
Spring	0.73±0.42	0.93±0.03	0.047±0.021	1.519±0.045	0.006±0.003
Summer	0.79±0.50	0.94±0.03	0.039±0.020	1.464±0.050	0.006±0.003
Autumn	0.61±0.38	0.90±0.05	0.050±0.028	1.489±0.048	0.009±0.005
Winter	0.59±0.41	0.90±0.04	0.050±0.024	1.514±0.036	0.011±0.005

The mean value of SSA is the highest (0.94) during summer and the lowest during winter (0.9). This result is consistent with emission maps showing more scattering

particles during summer and more absorbing particles during winter. Additionally, spectral variations for different clusters have different trends. AOT is decreasing from 440 to 1020 nm except for cluster C1 during spring and summer that shows no obvious spectral dependence. The values of SSA always increase from 440 to 675 nm and decrease from 675 to 870 nm. Again, for cluster C1 during spring and summer, the SSA increase from 440 to 1020 nm. This trend is attributed to greater dust inputs (Huang et al., 2010; Yu et al., 2013). Generally, AAOT is less influenced by cluster origins in contrast to AOT and SSA. In summer, AAOT has a minimum mean value of 0.039. Whereas during winter, there is a dramatic decrease in AAOT from 440 nm (0.17) to 675 nm (0.05) observed for cluster C5, which denotes more absorbing organic aerosol or mineral dust presence.

$n$  shows a small spectral dependency in comparison to  $k$ , but differs by season and cluster. Clusters from south of Beijing (C5 during the four seasons and C3 in summer) always have lower  $n$ . During summer, aerosols over China show the lowest values of  $n$  (table 5.2) associated with the highest water content (Schuster et al., 2009). In general, the value of  $k$  decreases when wavelength increases with two distinct tendencies from 440 to 675 nm and from 675 to 1020 nm. A sharp decline in  $k$  from 440 to 675 nm is observed in winter, which is likely related to an increasing content of BrC or dMD during this period (Chen and Bond, 2010).

#### 5.2.4 Aerosol chemical components of each cluster

Section 5.2.3 showed that aerosol size distribution and optical properties are well separated by different clusters. To have a deeper knowledge on columnar aerosol chemical compositions, a  $k$ - $n$ - $dSSA$  based inversion algorithm (given in appendix A2) was used to calculate columnar aerosol volume fractions for different clusters during the four seasons.

As presented in figure 5.9, spring is characterized by a large amount of MD, contributing at around 45 % (table 5.3), especially when air masses coming from the northwest (over 50 % MD for cluster C1 and C2). MD mass concentration reaches a

maximum average value of  $0.95 \text{ g m}^{-2}$  for cluster C1, which is ascribed to the frequently occurring dust episodes during this season (Sun et al., 2005; Yu et al., 2013). The proportion of MD tends to decrease when air mass wind speed decrease (from cluster C1 to cluster C5), due to lower emission of MD (Engelbrecht and Derbyshire, 2010).

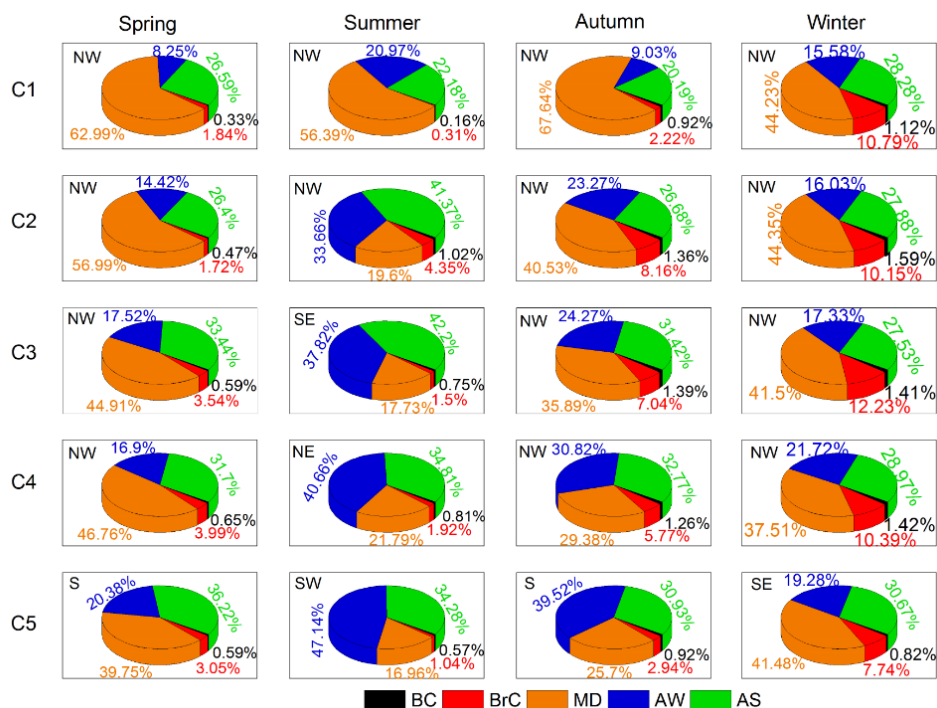


Figure 5.9 Average of volume fractions for five components in different seasons and different clusters.

In summer, AW has the largest proportion (40%) compared to other seasons. AW is well separated by the clusters for the special geographical position of Beijing, with moist air transported by southeast wind and dry air coming from the northwest. The columnar water content increases from cluster C1 (21 %) to cluster C5 (47.1 %). There is also a large fraction of AS (37 %), especially within C3 air masses. As previously said, the large AS fraction is related with summer monsoon flux that brings high amount of  $\text{SO}_2$  and  $\text{NO}_x$  aerosols. This result is consistent with the conclusion from seasonal distribution of AOT and TSP emissions with the emission source spatial distribution of

SO<sub>x</sub> and NO<sub>x</sub> (Sun et al., 2015b). MD shows the lowest fraction (20%) during the wet season when soils are wetter and limit dust generation.

During autumn, there is a distinct increase of BC and BrC, which is consistent with the results reported by Li et al. (2015). They highlighted that the harvesting period in the NCP was linked to large biomass burning episodes during autumn associated. These episodes emit a large amount of BC and BrC, and exert a significant influence on the air quality of the surrounding cities (Yang et al., 2015). Indeed, BC and BrC fraction observed in autumn is twice as much as the one during spring and the BrC volume fraction is three times larger than those observed during summer. In addition, coal heating from late autumn is also a significant source of carbonaceous aerosols. The emission analysis of BC and BrC, shown in figure A3.1 ~ A3.4 (*appendix A3*), confirms that autumn has larger emission compared to spring and summer.

In winter, BC and BrC reach peak proportions of 1.3 % and 10 %, respectively. But the dependence of BC and BrC on the clusters is weak, which is attributed to the inconspicuous spatial difference of emission. Winter is also impacted by dust (41%) at the cost of AW.

Columnar aerosol mass concentrations for different contents not only depend on the volume fractions, but also associate with mass density for different contents and pollution level (Wang et al., 2013). Therefore, we also present the corresponding columnar aerosol mass concentrations in figure 5.10. The seasonal average of the retrieved aerosol chemical composition volume fractions and mass concentrations are also given in table 5.3.

Columnar BC mass concentrations usually increase when the transport speed is weakened (figure 5.10). Maximum value reached for air masses coming from south of Beijing. In summer, air masses coming from the southeast (cluster C3) are enriched with BC (mean value of 0.0052 g m<sup>-2</sup>). BC mass concentration increases appreciably during autumn and winter, and autumn (0.0059 g m<sup>-2</sup>) is slightly higher than winter (0.0056 g m<sup>-2</sup>). This result is not consistent with the emission seasonal variation that

winter has dramatically increasing of BC in winter (about  $1.7 \times 10^5 \text{ g km}^2 \text{ year}^{-1}$ ) compared with autumn (about  $1.2 \times 10^5 \text{ g km}^2 \text{ year}^{-1}$ ) around Beijing (figure A3.1).

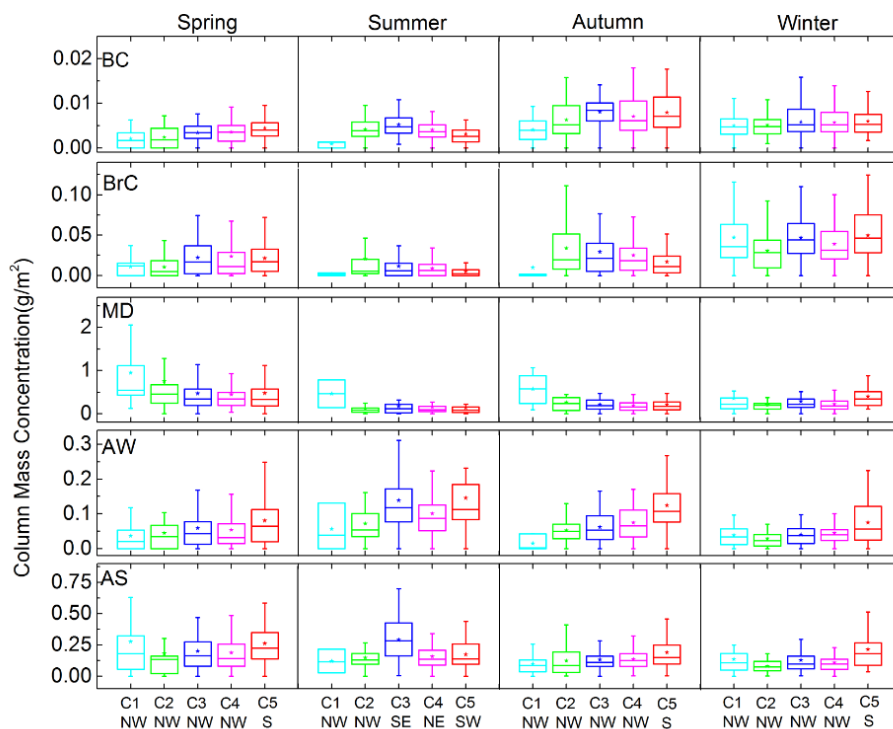


Figure 5.10 Average of columnar mass concentrations for the five components in different seasons and different clusters.

Table 5.3 Seasonal mean values of retrieved aerosol chemical composition volume fractions and mass concentrations.

Seasons	Volume fraction (%)					Mass concentration ( $\text{g m}^{-2}$ )				
	$f_{BC}$	$f_{BrC}$	$f_{MD}$	$f_{AW}$	$f_{AS}$	mBC	mBrC	mMD	mAW	mAS
Spring	0.6	3	45	18	33	0.0037	0.021	0.51	0.065	0.23
Summer	0.8	2	20	40	37	0.0041	0.011	0.16	0.11	0.19
Autumn	1.2	6	33	30	30	0.0059	0.025	0.23	0.08	0.15
Winter	1.3	10	41	19	29	0.0056	0.042	0.28	0.05	0.13

BrC mass concentrations are lowest in summer for almost all clusters and are higher in winter ( $0.042 \text{ g m}^{-2}$ ). In addition, BrC shows no regular dependence on air

mass transport speeds nor directions in winter, because local and smaller regional scale sources are more important in winter (Sun et al., 2015b).

The highest average columnar MD mass concentrations are associated to cluster C1 except during winter. In spring, MD mass concentration remains high for all clusters, reaching a maximum average value of  $0.951 \text{ g m}^{-2}$  for cluster C1, which is ascribed to the frequently occurring dust episodes during this season (Sun et al., 2005; Yu et al., 2013).

AW is well separated by the clusters due to the special geographical position of Beijing, with moist air transported by southeast wind and dry air coming from the northwest. The mean mass concentrations of AS for different clusters have a maximum value for air masses from the south, including cluster C5 in spring, autumn and winter, and cluster C3 (southeast) in summer, which is consistent with the emission spatial distribution of  $\text{SO}_2$  and  $\text{NO}_x$  (figure A3.5 ~ A3.6) (Sun et al., 2015b).

### 5.3 Conclusions

This study presents the first attempt to analyse columnar chemical components in different air mass sources based on multi-year columnar aerosol optical properties in Beijing, a typical site in North China Plain (NCP) region. The *k-n-dSSA* method proposed by Li et al. (2013) was used to retrieve the columnar aerosol chemical compositions.

Air mass origins, classified by different clusters and different seasons, have distinct influences on the aerosol optical properties. The retrieved aerosol chemical compositions are generally consistent with the results from emission and transport analysis. However, the retrieved BC mass concentration in winter is slightly lower than autumn, which is inconsistent with the greatly increasing BC emission around Beijing during winter. Moreover, this study reveals that volume fractions of BC and BrC have weak dependence on air mass source because the increasing BC and BrC emission around Beijing in all directions.

Fast moving clusters from the northwest are the largest contributors of coarse particles associated with MD among the four seasons. The MD concentration variation can be well explained by the MD emission sources (northwest of Beijing) and the emission mechanism highly dependent on wind speed.

Finally, air masses transported from south of Beijing bring larger amounts of AS and AW, reaching the maximum average value of  $0.145 \text{ g m}^{-2}$  and  $0.29 \text{ g m}^{-2}$  respectively in summer, consistent with the spatial distribution of  $\text{SO}_2$  and  $\text{NO}_x$ .

Generally speaking, the *k-n-dSSA* method is preliminarily verified to be reasonable, but the retrieved results need to be further compared with directly measured chemical compositions. These measurements are available at the surface and occasionally over the column through airborne measurements. Since surface in-situ measurements provide reliable observation of aerosol physical, optical and chemical properties, the application of *k-n-dSSA* method or a modified *k*-based method to in-situ measurement will be doable for validation.

## Chapter 6 Development and application of $k$ - $\rho$ method for campaign at Shouxian

As mentioned in *chapter 5*,  $k$ -based methods have been well developed with size or size related dSSA to retrieve the main aerosol compounds quantitatively in the atmosphere (Li et al., 2013; Schuster et al., 2016a; Wang et al., 2013). However, according to size-resolved aerosol chemical composition measurements (figure 6.1), even though MD is the main contributor for coarse mode, there is still a non-negligible fraction of OC within the coarse mode, especially during polluted days over Beijing during winter (Hu et al., 2012). Therefore, using size or size related parameters (e.g. dSSA) may bring additional uncertainties to the retrieval. Other independent parameters need to be found to further constrain the problem. Moreover, the present studies using  $k$ -based methods are all based on remote sensing measurements and lack of comparison to measurements of aerosol chemical compositions integrated over the whole column.

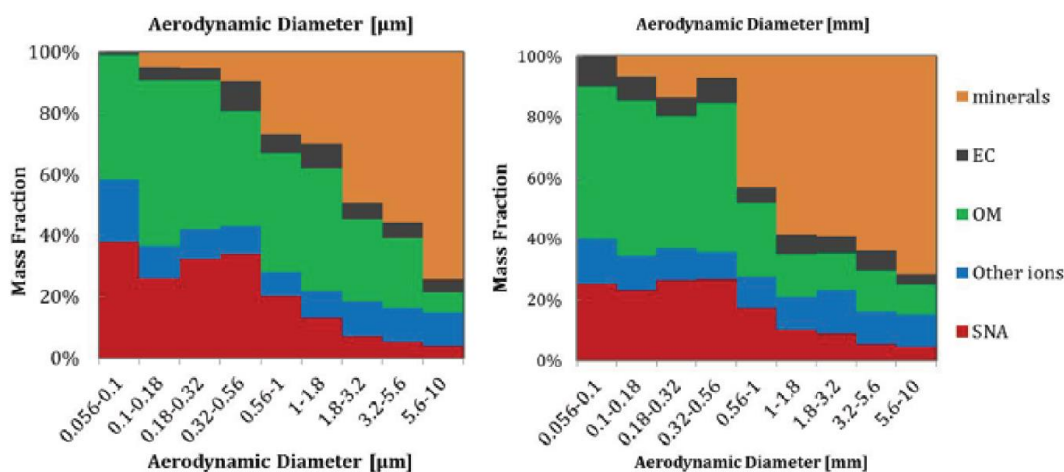


Figure 6.1 Aerosol mass concentrations for polluted (left) and clear (right) days (Hu et al., 2012).

Although in-situ measurement is only limited to a certain site, it could measure aerosol physical, chemical and optical properties. Synergy between all the available

measurements offers opportunities to realize closure studies among aerosol physical, optical and chemical properties. For example, an “optical” closure study was realized between measured and calculated extinction coefficients from IMPROVE or revised IMPROVE equations based on aerosol MEE and mass concentrations (Lowenthal and Kumar, 2016; Xu et al., 2016). A “physical” closure study was also achieved by comparison between measurements and retrievals of aerosol size distributions (Schuster et al., 2019). Algorithms to retrieve aerosol chemical composition based on optical properties with or without physical properties has made great progress (Li et al., 2013; Schuster et al., 2016), but the closure study of aerosol chemical composition is still scarce. Therefore, this chapter aims to improve the  $k$ -based methods by introducing new parameters, and realizes the closure study of retrieved and measured aerosol chemical compositions based on in-situ measurement.

Since the density of OC ( $1.2 \text{ g cm}^{-3}$ , Rissler et al., 2014) is significantly lower than MD ( $2.6 \text{ g cm}^{-3}$ , Wagner et al., 2012), aerosol density could be a good parameter with  $k$  to distinguish the main aerosol species. Indeed, Pitz et al. (2008) and Liu et al. (2015b) investigated the correlation between density and chemical compositions, and found that density could be potentially used to indicate aerosol chemical composition and atmospheric processing. Thereby, we introduced  $\rho$  as additional parameter for aerosol chemical composition retrieval algorithm, named as  $k$ - $\rho$  method.

In this chapter, we will introduce the development of  $k$ - $\rho$  method, and its application to observations performed at Shouxian.  $k$  at 365 and 532 nm were retrieved from Mie theory ( $k_{Mie,365}$  and  $k_{Mie,532}$ ) with extinction and scattering coefficients measured by CEA and PNSD by merging SMPS and APS data.  $\rho$  was derived by converting aerodynamic diameter to mobility diameter, named as effective density ( $\rho_e$ , section 2.1.2). Two pollution periods and one clear period were selected for further analysis on aerosol physical, optical, and chemical properties. To test the algorithm, the retrieved BC, OM, SNA and MD were then compared with aerosol chemical compositions analysed from filter sampling. Because the  $k$  and  $\rho$  for different aerosol chemical compositions vary a lot in previous studies, sensitivity study will be also

conducted to evaluate the impact of both parameters on retrieval uncertainties.

## 6.1 Development of $k$ - $\rho$ method to retrieve aerosol chemical compositions

$k$ - $\rho$  method aims to retrieve the main compounds in dry aerosol, including BC, OM, MD and SNA. Among them, OM mass or volume fraction can be converted to OC using a factor (1.6 for this study, Xing et al., 2013). The following merit function is used:

$$\delta_{fraction}^2 = \frac{(\rho_{retr} - \rho_{VAM})^2}{\varepsilon_{\rho_e}^2} + \frac{(k_{retr, \lambda_1} - k_{VAM, \lambda_1})^2}{\varepsilon_{k_{retr, \lambda_1}}^2} + \frac{(k_{retr, \lambda_2} - k_{VAM, \lambda_2})^2}{\varepsilon_{k_{retr, \lambda_2}}^2} \quad (6.1)$$

$\rho_{retr}$ ,  $k_{retr, \lambda_1}$ , and  $k_{retr, \lambda_2}$  are the density and imaginary part of CRI for the atmospheric aerosol retrieved from in-situ measurements, and  $k$  values are distinguished at  $\lambda_1$  and  $\lambda_2$  for OC and MD.  $\varepsilon_{\rho_{retr}}$ ,  $\varepsilon_{k_{retr, \lambda_1}}$  and  $\varepsilon_{k_{retr, \lambda_2}}$  are the corresponding errors respectively.  $\rho_{VAM}$ ,  $k_{VAM, \lambda_1}$ , and  $k_{VAM, \lambda_2}$  are calculated results with VAM rule (equation 6.2~6.4) under the hypothesis of homogeneous and spherical particles (DeCarlo et al., 2004; Li et al., 2013):

$$\rho_{VAM} = \rho_{BC} f_{BC} + 1.6 \rho_{OC} f_{OC} + \rho_{MD} f_{MD} + \rho_{SNA} f_{SNA} \quad (6.2)$$

$$k_{VAM, 365} = k_{BC, 365} f_{BC} + k_{OC, 365} f_{OC} + k_{MD, 365} f_{MD} \quad (6.3)$$

$$k_{VAM, 532} = k_{BC, 532} f_{BC} + k_{OC, 532} f_{OC} + k_{MD, 532} f_{MD} \quad (6.4)$$

$f$  is the volume fraction of each component. The used literature reported values of  $\rho_m$ ,  $k_{\lambda_1}$ , and  $k_{\lambda_2}$  for each species and OM to OC ratio are *a priori* parameters for the algorithm (table 6.1 and 6.2). A look up table for possible volume fractions is built ( $f_{i,jj}$ ,  $ii = 1, 2, 3$  representing BC, OC, MD and SNA, and  $jj$  is the solution space with steps of 0.05 %, 0.5 % and 0.5 % from 0 to 1 for BC, OC and SNA, respectively). Volume fraction of MD is the remaining part ( $f_{MD} = 1 - f_{BC} - f_{OM} - f_{SNA}$ ). The optimal solution

of  $f_{ii}$  could be found by minimizing  $\delta_{fraction}^2$ .

Table 6.1 Imaginary parts of the refractive index ( $k$ ) at 365 and 532 nm used for aerosol chemical composition retrieval in this study (baseline, font in bold), and the low (superscript with L) and high (superscript with H) limits for sensitivity test.

Aerosol type	$k(365 \text{ nm})$	$k(532 \text{ nm})$	References
<i>BC</i>	<b>0.79</b>	<b>0.79</b>	Bond and Bergstrom, 2006; Moteki et al., 2010
	1.26 <sup>H</sup>	1.26 <sup>H</sup>	
	0.63 <sup>L</sup>	0.63 <sup>L</sup>	
<i>OC</i>	<b>0.042</b>	<b>0.0179</b>	Shamjad et al., 2016; Kirchstetter et al., 2004; Liu et al., 2013
	0.148 <sup>H</sup>	0.03 <sup>H</sup>	
	0.008 <sup>L</sup>	0.002 <sup>L</sup>	
<i>MD</i>	<b>0.014</b>	<b>0.006</b>	Kandler et al., 2007; Wagner et al., 2012
	0.0321 <sup>H</sup>	0.006 <sup>H</sup>	
	0.0125 <sup>L</sup>	0.003 <sup>L</sup>	
<i>SNA</i>	<b>0</b>	<b>0</b>	Flores et al., 2012

Table 6.2 Material densities and ratio of OM to OC (OM/OC) used for aerosol chemical composition retrieval in this study (baseline, font in bold), as well as the low (superscript with L) and high (superscript with H) limits for sensitivity test.

Parameters	Values	Reference
$\rho_{BC}$ (g cm <sup>-3</sup> )	<b>1.8</b> (1.5 <sup>L</sup> , 2 <sup>H</sup> )	Hand and Kreidenweis, 2002; Bond and Bergstrom, 2006; Cheng et al., 2008
$\rho_{OC}$ (g cm <sup>-3</sup> )	<b>1.2</b> (1 <sup>L</sup> , 1.4 <sup>H</sup> )	Ebert et al., 2004; Cheng et al., 2008; Schkolnik et al., 2007
$\rho_{MD}$ (g cm <sup>-3</sup> )	<b>2.6</b> (2.4 <sup>L</sup> , 2.8 <sup>H</sup> )	Wagner et al., 2012; Pio et al., 2014; Hu et al., 2012
$\rho_{SNA}$ (g cm <sup>-3</sup> )	<b>1.75</b> (1.7 <sup>L</sup> , 1.8 <sup>H</sup> )	Tang et al., 1996; Mallet et al., 2003; Hand and Kreidenweis, 2002
OM/OC	<b>1.6</b> (1.3 <sup>L</sup> , 2.16 <sup>H</sup> )	El-Zanan et al., 2012; Malm et al., 2011; Xing et al., 2013

With the retrieved  $f_{ii}$ , the mass concentration for each species ( $MC_{ii}$ ) is calculated with:

$$MC_{ii} = f_{ii} \rho_{m,ii} V \quad (6.5)$$

where  $\rho_{m,ii}$  is the particle material density, and  $V$  is the volume concentration, and it was calculated based on PNSD:

$$V = \frac{\pi}{6} \int N(D_m) D_m^3 dD_m \quad (6.6)$$

The retrieved mass concentration were calculated by repeating the aerosol chemical composition retrieval process with  $\rho_{retr}$ ,  $k_{retr, \lambda_1}$ , and  $k_{retr, \lambda_2}$  varying from higher to lower uncertainty range. The mass concentration differences due to the three parameter variations are calculated separately. Then, these differences can be added in quadrature to get the uncertainties of different inputs on each compound aerosol mass concentration.

## 6.2 Site and data

### 6.2.1 Site description

The observations were made at the Shouxian station (32.56 °N, 116.78 °E), which is one of the earliest five national climatological observatories in China. The site is a rural site surrounded by farmland, and is less affected by urban, industrial and traffic pollution (Xu et al., 2018b). The pollutants are mainly ascribed to regional transport and occasional local residents' biofuel combustion.

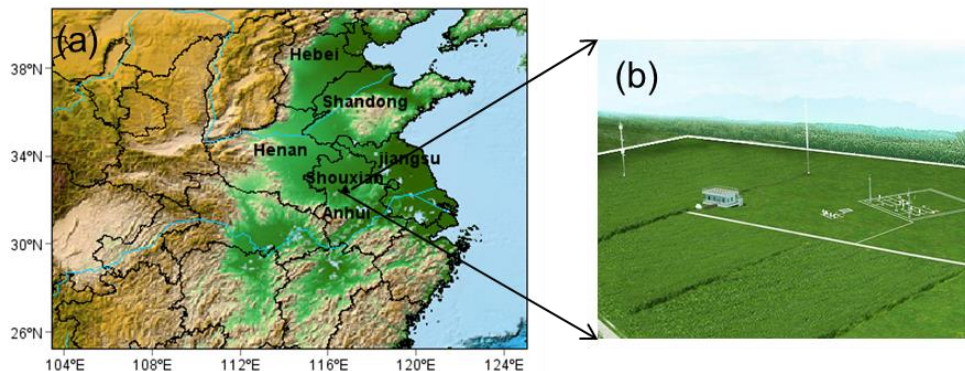


Figure 6.2 Geographical location and surroundings of the observation site.

## 6.2.2 Instruments and method

Upstream the aerosol state-of art instruments, a PM<sub>2.5</sub> cyclone (BGISCC2.654, with a 50 % cut point at 2.5  $\mu\text{m}$ ) was installed in front of the sampling line, and the sample was then dried below 25% relative humidity (RH) using a Nafion dryer. The instruments used for physical and optical property measurements include SMPS, APS and CEA at 365 and 532 nm (*section 3.2.1 and 3.2.2*). Additionally, filter samplings were collected and analysed to obtain aerosol chemical compositions (*section 3.2.3*). Meteorological parameters (wind speed and direction) were obtained from automatic weather station during the field campaign. To ease the readings, the time used in this study is local time (UTC+8:00).

### ▪ Deriving of aerosol density

We obtained aerosol effective density by merging the PNSD of the SMPS and APS data using equation 2.15. Both instruments measure the aerosol size distribution focusing on fine (mobility diameter in 14 - 661 nm) and coarse (aerodynamic diameter in 523 - 2458 nm) particles respectively. The overlap of both instrument measurements starts from the aerodynamic diameter of 523 nm and ends with mobility diameter of 661 nm. The data from the first three APS bins (from 523 to 583 nm) are often considered as unreliable. As suggested by Kassianov et al. (2014), these data are then corrected using a linear logarithmic extrapolation (log-log scale) using the assumption that SMPS and APS data followed a log-linear distribution in the overlap region. The diameter bin number within the overlap depends on the effective density. For  $\rho_e$  of 1 g m<sup>-3</sup>, there are 7 bins for SMPS data and 4 bins for APS data. When  $\rho_e$  equals to 2 g m<sup>-3</sup>, SMPS and APS data have 17 and 9 bins respectively.

The PNSD ( $dN/d\log(Dp)$ ) for SMPS and APS data are plotted with  $D_a$  and  $D_m$  respectively in log-log scale axis (figure 6.3a). Both curves are merged into one by shifting the APS data ( $APS(D_a)$ , solid blue line) horizontally along the abscissa. The abscissa of the shifted APS data ( $APS(D_m, \rho_e)$ , dashed blue line) is converted from  $D_a$  to  $D_m$  (Kassianov et al., 2014). The APS size bins in the overlap region are finally

interpolated to match those of the SMPS to get more corresponding aerodynamic diameter points ( $D_{a,inter}$ ) (figure 6.3b).  $\rho_e$  is then calculated by linear fit of  $D_m^2$  and  $D_{a,inter}^2$  with a forced intercept to 0. The standard error of the slope is considered as the error of effective density ( $\varepsilon_{\rho_e}$ ).

As introduced in *section 2.1.2*, aerosol effective density is not limited to the method mentioned earlier, and it could be also obtained with the ratio of aerosol mass to volume concentration. The method used in our study combining with SMPS and APS has the advantage of real-time measurement of aerosol PNSD and effective density simultaneously (Li et al., 2018).

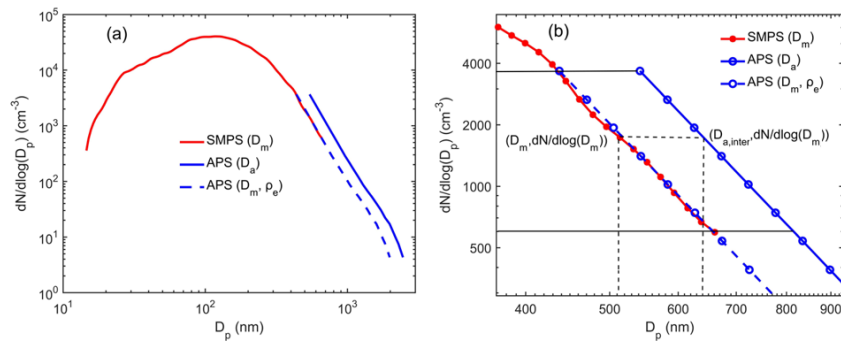


Figure 6.3 Illustrations of the SMPS and APS data merging operation. (a) Complete size distribution of SMPS (red) and APS (blue) number concentrations ( $dN/d\log(D_p)$ ) are shown along with particle diameter ( $D_p$ ) respectively (mobility diameter ( $D_m$ ) for SMPS, and aerodynamic diameter ( $D_a$ ) for APS). The dashed blue line is the APS curve with size correction by converting aerodynamic diameter to mobility diameter. (b) Zooms in the overlap region.

#### ▪ Retrieval of complex refractive index

Under the assumption of internally mixed and spherical aerosol population,  $b_{ext}$  and  $b_{scat}$  can be calculated with Mie theory (Pettersson et al., 2004):

$$b_{ext/scat} = \int N(D_p) \frac{\pi}{4} D_p^2 Q_{ext/scat}(m, x, \lambda) dD_p \quad (6.7)$$

Where  $N(D_p)$  is the particle number concentration at a diameter ( $D_p$ ). The merged PNSD was used in this work.  $Q_{ext,scat}(m,x,\lambda)$  is the particle extinction and scattering efficiency at the wavelength of  $\lambda$ , with specific CRI ( $m$ ) and size parameter ( $x = D_p/\lambda$ ).

A Mie code was used to build a look up table of extinction and scattering coefficients ( $b_{ext\_cal}$  and  $b_{scat\_cal}$ ) for different real ( $n_{Mie}$ ) and imaginary ( $k_{Mie}$ ) parts of CRI.  $n_{Mie}$  was ranging from 1.2 to 1.7 with a step of 0.001, while  $k_{Mie}$  ranged from 0 to 0.07 with a step of 0.0001. The measured extinction ( $b_{ext\_mea}$ ) and scattering ( $b_{scat\_mea}$ ) coefficients were compared to the look-up table values ( $b_{ext\_cal}$  and  $b_{scat\_cal}$ ) in order to find the best solution (the lowest value of  $\delta_{CRI}^2$ , equation 6.8). Indeed, differences between calculated and measured extinction and scattering coefficients were used as input of  $\delta_{CRI}^2$  (Dinar et al., 2008; Xu et al., 2016).

$$\delta_{CRI}^2 = \frac{(b_{ext\_mea} - b_{ext\_cal})^2}{\varepsilon_{ext\_mea}^2} + \frac{(b_{scat\_mea} - b_{scat\_cal})^2}{\varepsilon_{scat\_mea}^2} \quad (6.8)$$

Assuming that  $\varepsilon_{ext\_mea}^2$  and  $\varepsilon_{scat\_mea}^2$  are normal distributions, the values of  $\delta_{CRI}^2$  follow a  $\chi^2$ -distribution with two degrees of freedom  $n$  and  $k$ . The acceptable values of  $n$  and  $k$  have  $\delta_{CRI}^2$  values within  $\delta_{CRI0}^2 \pm 2.298$ , where 2.298 is the  $1\sigma$  error bound with 68.3% confidence level for  $\chi^2$  distribution (Dinar et al., 2008). The errors for  $n_{Mie,365}$ ,  $k_{Mie,365}$ ,  $n_{Mie,532}$  and  $k_{Mie,532}$  are estimated using all values within the lowest and highest range of the acceptable retrievals.

### 6.2.3 Comparison of results derived from measurement and retrieval

The comparisons of  $b_{ext\_mea}$  and  $b_{scat\_mea}$  to  $b_{ext\_cal}$  and  $b_{scat\_cal}$  using the optimal CRI are shown in figure 6.4, which have high correlation ( $R^2$  close to 1). The relative frequency of their relative difference is given in figure 6.5. It could be found that the frequency of the measured and calculated extinction coefficient difference ( $db_{ext} = (b_{ext,mea} - b_{ext,cal})/b_{ext,mea}$ ) is usually lower than 0.5%, and most  $db_{scat}$  is lower than

0.2%.

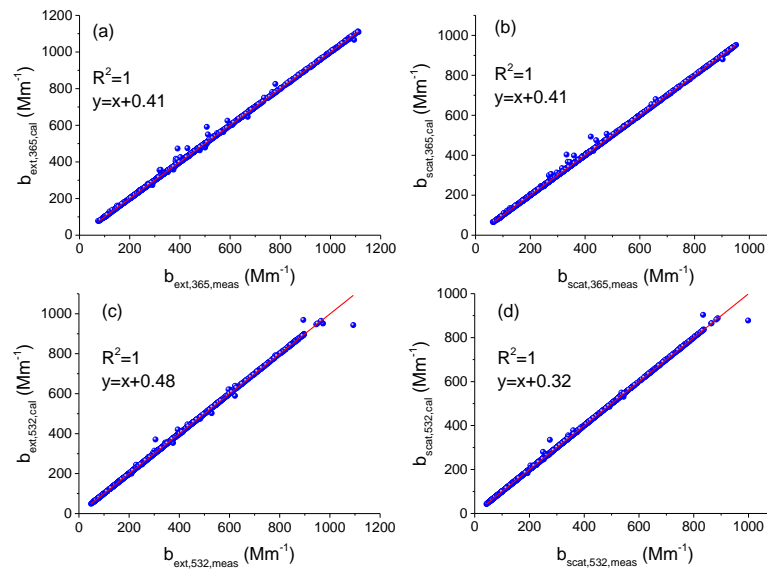


Figure 6.4 Comparison of measured and retrieved, from Mie theory, extinction and scattering coefficients.

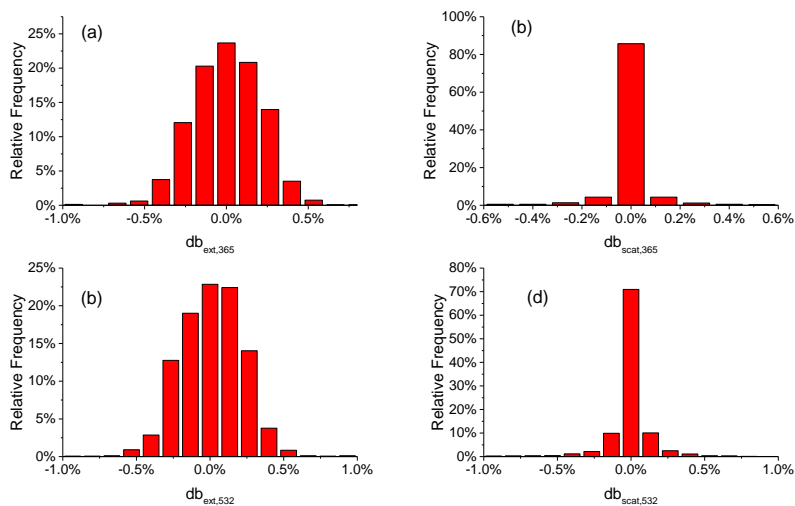


Figure 6.5 Relative frequency of the differences between measured and calculated extinction and scattering coefficients.

The comparison between  $\rho_e$  and calculated density using VAM rule ( $\rho_{VAM}$ ) is shown in figure 6.6a, as well as the comparison between  $k_{Mie}$  and  $k_{VAM}$  at 365 and 532

nm (figure 6.6b-c).  $\rho_e$  and  $\rho_{VAM}$  are in good agreement ( $R^2=0.99$ ), except for the extreme low values from  $\rho_e$  ( $\rho_e < 1.2 \text{ g cm}^{-3}$ ). As previously said (Zhai et al., 2017), these low values are most probably associated with fresh biomass burning aerosols for which effective density might be greatly affected by the shape factor.  $k_{Mie,365}$  and  $k_{VAM,365}$  are also in good consistency ( $R^2 = 0.97$ ) similarly to  $k_{Mie,532}$  and  $k_{VAM,532}$  comparisons. The largest differences of  $k_{Mie,365}$  and  $k_{VAM,365}$  occur for a few points with large  $k_{Mie,365}$  while those of  $k_{Mie,532}$  and  $k_{VAM,532}$  occur over the whole  $k_{Mie,532}$  value range. Relative frequencies of the difference between observed and calculated density and  $k$  ( $dp=(\rho_e-\rho_{VAM})/\rho_e$ ,  $dk=(k_{Mie}-k_{VAM})/k_{Mie}$ ) is shown in figure 6.7.  $dp$  is usually lower than 0.5%, and most  $dk_{365,532}$  is lower than 1%.

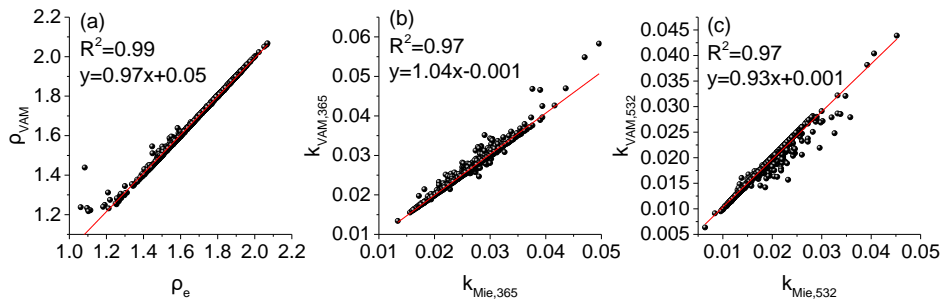


Figure 6.6 The comparison of effective density ( $\rho_e$ ) by merging APS to SMPS diameter with density calculated with VAM rule ( $\rho_{VAM}$ ) (a); the comparison between the imaginary part of refractive index retrieved from Mie theory ( $k_{Mie}$ ) and calculation from VAM rule ( $k_{VAM}$ , b and c).

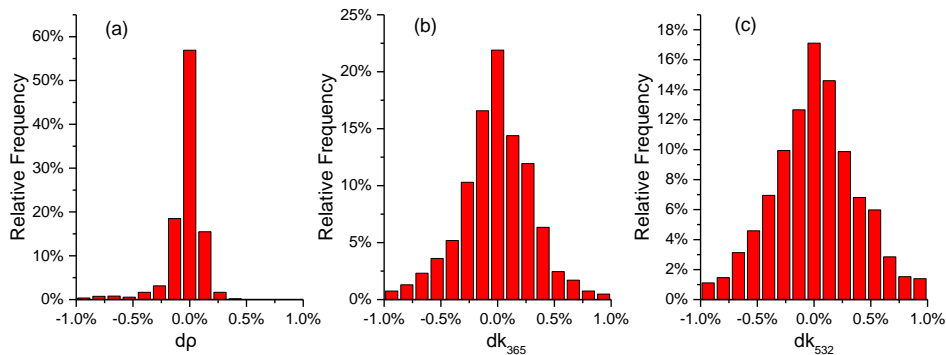


Figure 6.7 Relative frequency of the differences between  $\rho_e$  and  $\rho_{VAM}$  (a), and  $k_{Mie}$  and  $k_{VAM}$  ((b) for  $k$  at 365 nm and (c) for  $k$  at 532 nm).

## 6.3 Results

### 6.3.1 Aerosol size distribution and optical properties

Real time measurements of aerosol size distribution, Wind Speed (WS), Wind Direction (WD), and optical properties ( $b_{ext}$ ,  $b_{scat}$ ,  $b_{abs}$ , and SSA) are shown in figure 6.8. During the measurement period, aerosol particles were mainly concentrated within the fine fraction, with diameter around 100 - 200 nm. Wind speed usually increased in the morning, reached a high value at noon, decreased during the afternoon, and had a relatively low value during the night compared to daytime. The statistical results are shown in table 6.3.

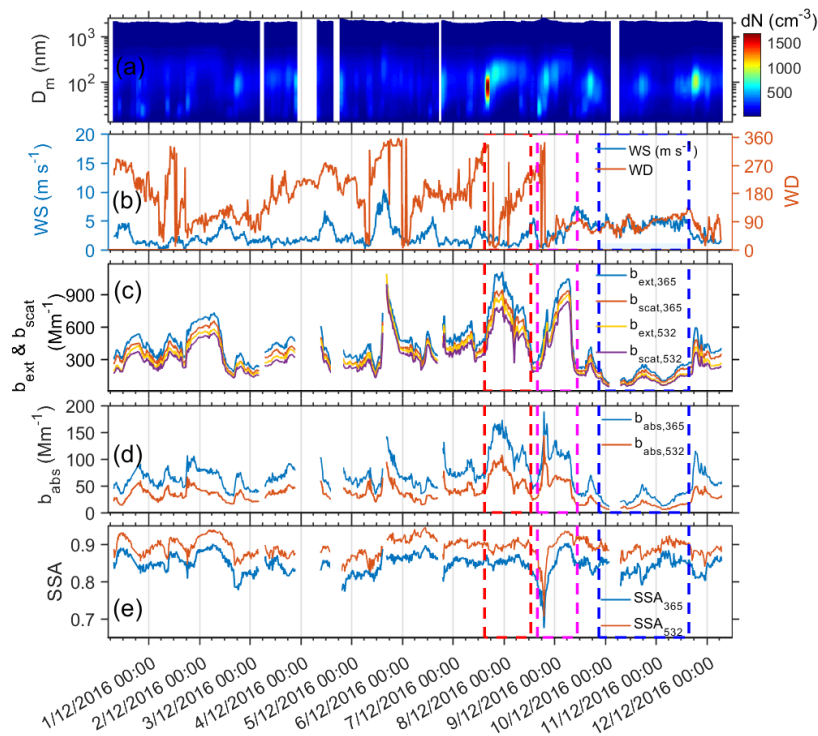


Figure 6.8 Time series of size distribution, meteorological conditions and optical properties during the observation period at Shouxian site. Two pollution periods (P1, from 15:00 LT on 7 December to 13:00 LT on 8 December, and P2, from 16:00 LT on 8 December to 11:00 LT on 9 December) are marked with red and magenta rectangles respectively and one clean period (P3, from 21:00 LT on 9 December to 15:00 LT on 11 December) marked with blue dashed lines. (a) Particle number size distribution; (b) wind speed and wind direction; (c) extinction and scattering coefficients, (d) absorption coefficient, and (e) single scattering albedo at 365 and 532 nm.

Table 6.3 List of the mean, minimum and maximum values of each optical parameter during the observation period.

Parameters	Mean value	Minimum value	Maximum value
$b_{ext,365}$ ( $Mm^{-1}$ )	$451 \pm 229$	74	1112
$b_{ext,532}$ ( $Mm^{-1}$ )	$354 \pm 197$	48	1093
$b_{scat,365}$ ( $Mm^{-1}$ )	$384 \pm 200$	63	952
$b_{scat,532}$ ( $Mm^{-1}$ )	$317 \pm 180$	43	999
$b_{abs,365}$ ( $Mm^{-1}$ )	$67 \pm 32$	11	189
$b_{abs,532}$ ( $Mm^{-1}$ )	$36 \pm 20$	5	143
SSA <sub>365</sub>	$0.85 \pm 0.027$	0.67	0.90
SSA <sub>532</sub>	$0.89 \pm 0.025$	0.71	0.94

The aerosol extinction, scattering and absorbing coefficients ( $b_{ext}$ ,  $b_{scat}$  and  $b_{abs}$ ) measured at 365 nm were on average, about  $451 \pm 229 Mm^{-1}$  (ranged from 74 to 1112  $Mm^{-1}$ ),  $384 \pm 200 Mm^{-1}$  (ranged from 63 to 951  $Mm^{-1}$ ),  $67 \pm 32 Mm^{-1}$  (ranged from 11 to 189  $Mm^{-1}$ ), respectively. The SSA was then retrieved in average at  $0.85 \pm 0.027$  (ranged from 0.67 to 0.9) at 365 nm. At 532 nm, the average  $b_{ext}$ ,  $b_{scat}$  and  $b_{abs}$  are in general lower around  $353 \pm 197 Mm^{-1}$ ,  $317 \pm 180 Mm^{-1}$ ,  $36 \pm 20 Mm^{-1}$  respectively. At this wavelength, SSA average ( $0.89 \pm 0.025$ ) was a bit larger. However, these optical coefficients vary within a large range of values ( $48 < b_{ext} < 1093 Mm^{-1}$ ;  $43 < b_{scat} < 999 Mm^{-1}$ ;  $5 < b_{abs} < 143 Mm^{-1}$ ) highlighting periods with intense pollution events ( $b_{ext} = 1093 Mm^{-1}$ ) and by opposition relatively clean periods ( $b_{ext} = 48 Mm^{-1}$ ).

According to figure 6.8, two different polluted periods, named P1 (from 15:00 LT on 7 December to 13:00 LT on 8 December) and P2 (from 16:00 LT on 8 December to 11:00 LT on 9 December), were selected for further analysis (red and magenta rectangles). Air mass back-trajectories ending at 500 m above the ground level at Shouxian site were calculated (shown in figure 6.9). The green and blue colours represent the back trajectories calculated during the development and disappearance of pollution events, respectively. The red colour corresponds to back trajectories calculated during the periods of low visibility associated to high aerosol concentrations.

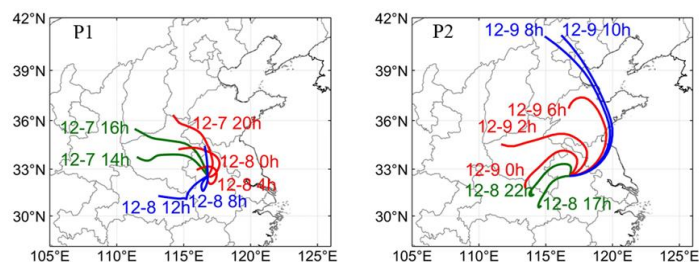


Figure 6.9 24 h backward trajectories ending at Shouxian site at 500 m above ground level during two pollution periods (P1 and P2). The green and blue lines correspond to the periods of development and decline of pollution events, respectively. The red lines correspond to the period that extinction remains at a high level ( $b_{ext} > 800 \text{ Mm}^{-1}$  at 365 nm).

One clear period marked, called P3, was also selected for comparison to pollution episodes (highlighted in blue dashed line in Figure 6.8, from 21:00 LT on 9 December to 15:00 LT on 11 December). The P3 period was associated with a high and stable wind speed of about  $5 \text{ m s}^{-1}$ , and with the lowest values of  $b_{ext}$  and  $b_{scat}$ .

At the beginning of P1 period, there was a peak of particle number concentration with diameter about 80 nm. Then,  $b_{ext}$  and  $b_{scat}$  increased with growing particle size. From 18:00 LT on December 7 to 4:00 LT on December 8,  $b_{ext}$  exceeded  $800 \text{ Mm}^{-1}$  at 365 nm, and wind speed decreased below  $2.5 \text{ m s}^{-1}$ . The peak value was reached at midnight when particles diameter reached 180 nm. After 8:00 LT on December 8,  $b_{ext}$  and  $b_{scat}$  decreased sharply with the increase of wind speed and the rise of the boundary layer. Most of the pollution events observed over Shouxian are dispersed due to these typical meteorological conditions.

During P2 period, there was a dramatical increase of  $b_{abs}$  and decrease SSA from 17:00 LT to 21:00 LT. The highest value of  $b_{abs}$  was  $189 \text{ Mm}^{-1}$  at 365 nm corresponding to  $143 \text{ Mm}^{-1}$  at 532 nm. The lowest value of SSA was only about 0.67 (0.71) at 365 (532 nm). This abrupt change was observed right after the rapid growth of freshly emitted particle (from 26 to 150 nm) at the beginning of P2. After 21:30 LT,  $b_{ext}$  and  $b_{scat}$  continued to increase, and peaked at about 7:00 LT on December 9 (1050 and 938

$\text{Mm}^{-1}$  at 365 nm, and 895 and 836  $\text{Mm}^{-1}$  at 532 nm respectively). SSA also began to increase due to a decrease of  $b_{abs}$  and reached its highest level (0.9 at 365 nm) when  $b_{ext}$  and  $b_{scat}$  peaked. At that time, the local wind direction veered to from north to east. After 7:00 LT on 9 December, the pollutants disappeared with the increase of wind speed from the Northeast. The dramatical variation of physical and optical properties during P2 period is mainly caused by the varied aerosol sources as shown in figure 6.9b.

### 6.3.2 Retrieved effective density and complex refractive index

The evolution of  $\rho_e$  during the observation is shown in figure 6.10. The mean value of  $\rho_e$  is  $1.67 \pm 0.15 \text{ g cm}^{-3}$ , which is close to the value of  $1.66 \pm 0.15 \text{ g cm}^{-3}$  reported by previous study at Shouxian (Li et al., 2018). Using SMPS and APS measurements, Kassianov et al. (2014) retrieved an aerosol density of  $1.68 \pm 0.21 \text{ g cm}^{-3}$ . The average error of  $\rho_e$  was  $0.034 \text{ g cm}^{-3}$ , and the calculated relative error was 2%. During P1 period,  $\rho_e$  held a steady value of about  $1.55 \text{ g cm}^{-3}$  even during the highly polluted period (18:00 LT on December 7 to 4:00 LT on December 8). During P2 period,  $\rho_e$  changed from 1.06 to  $1.9 \text{ g cm}^{-3}$ . The surprisingly low density value ( $1.06 \text{ g cm}^{-3}$ ) is close to the density of biomass burning aerosols in previous studies (Qiao et al., 2018; Zhai et al., 2017).

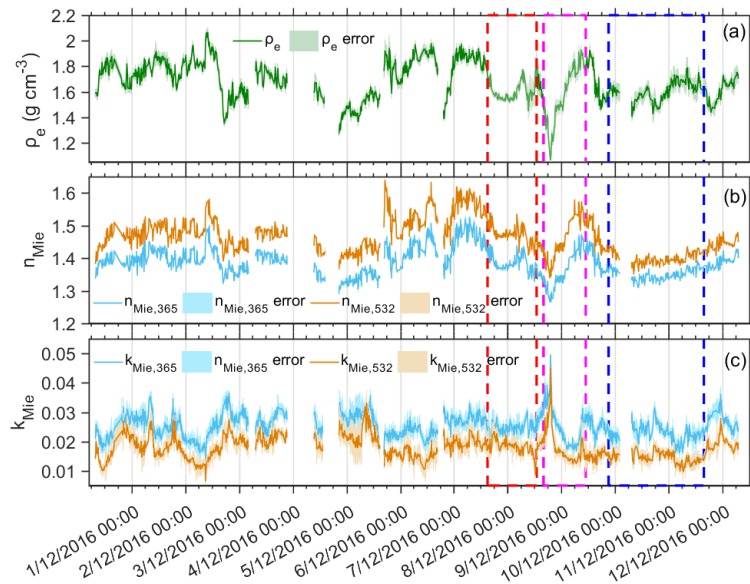


Figure 6.10 Retrieved (a) aerosol effective density ( $\rho_e$ ), and (b) the real ( $n_{Mie}$ ) and (c) imaginary ( $k_{Mie}$ ) part of CRI at 365 and 532 nm from experimental observation data.

The mean values of CRI were  $1.39 (\pm 0.04) + 0.025 (\pm 0.004) i$  at 365 nm and  $1.47 (\pm 0.05) + 0.018 (\pm 0.004) i$  at 532 nm. These values are comparable to dry CRI observed at Huairou site (Xu et al., 2016), at Cape Cod National Seashore (Kassianov et al., 2014), and in Paris (Raut et al., 2009). The mean errors for  $n_{Mie,365}$ ,  $k_{Mie,365}$ ,  $n_{Mie,532}$  and  $k_{Mie,532}$  were 0.003, 0.002, 0.002 and 0.002, and the mean relative errors were estimated to be 2%, 8%, 1.4% and 11% respectively during the observation period. The variation of  $n_{Mie}$  is in phase with  $\rho_e$  in general, and this result is also observed by previous studies (Li et al., 2018; Liu and Daum, 2008; Zhao et al., 2019). During the dramatical change in wind direction and emission of ultrafine particles, the  $k$  peaks at 0.05 at 365 nm during the P2 period. During the P1 period,  $k_{Mie,365}$  was relatively stable, with an average value of 0.025.

The lowest value of  $n_{Mie}$  was found during P2 (1.26 at 365 nm). It's not unusual to retrieve a value for the real part of aerosol CRI lower than the water  $n$  value (1.33). Indeed, Virkkula et al. (2006) derived  $n$  of 1.15 of dry aerosol at 450 nm. The inaccuracies of the method, water in the particles, non-analyzed biogenic particles, or non-spherical particles being responsible for the low values are possible explanations for such low density values (Virkkula et al., 2006).

### 6.3.3 Aerosol chemical composition retrieval and its temporal variations

The retrieved, from  $k$ - $\rho$  method, Volume Fractions (VF) at high time-resolution of BC, OM, MD and SNA are shown in figure 6.11a. The corresponding mass concentrations calculated with equation 6.5 and their errors are given in figure 6.11b-e. The retrieved contribution of each component during the full campaign, P1, P2 and P3 is shown in figure 6.11 f-i. The retrieved mass contributions of BC (mBC), OM (mOM), MD (mMD) and SNA (mSNA) for the entire observation period were 1.7%, 28.8%, 25.3% and 44.2% (figure 6f), with uncertainties of 35.5%, 38%, 61.5% and 54% respectively.

During P1, the mean mass concentrations were 3.5, 52.4, 15.7 and 106.3  $\mu\text{g m}^{-3}$  for BC, OM, MD, and SNA. The SNA fraction was the largest, accounting for 59.7%.

While the mass ratios of BC, OM, and MD were 2%, 29.5% and 8.8%, respectively. Their average uncertainties were 27%, 32%, 152% and 34% respectively due to the uncertainty of  $\rho_e$ ,  $k_{Mie,365}$  and  $k_{Mie,532}$ . High uncertainties of MD are related to its low mass concentrations. At the beginning of period P1, BC, OM and SNA mass concentrations suddenly increased, especially for the fraction of SNA, while MD mass concentration decreased rapidly with the decrease of wind speed. All those pollutants remained at a high and stable level during the night due to light wind conditions limiting the aerosol dispersion.

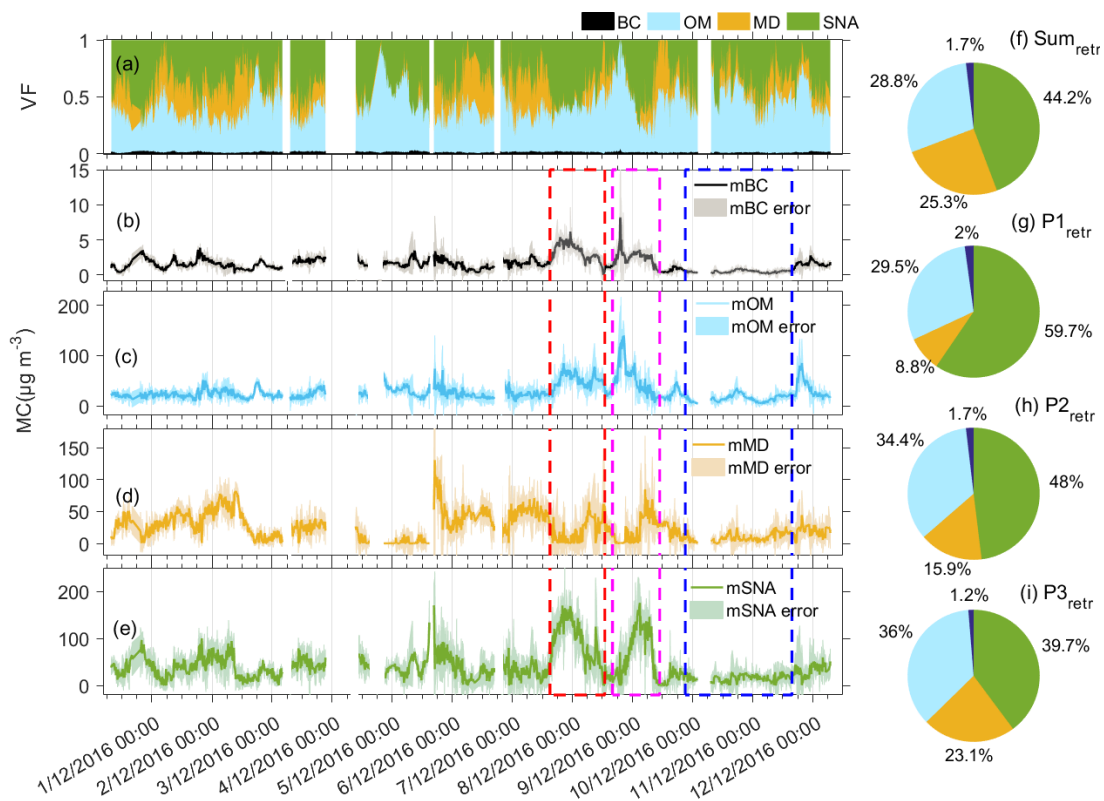


Figure 6.11 Retrieved (a) volume fractions, and mass concentration (MC) of (b) BC, (c) OM, (d) MD and (e) SNA. Average mass fraction of each chemical component on (f) all observation days, (g) pollution period P1, (h) pollution period P2, and (i) clear period P3.

During P2 period, the mean mass concentrations for BC, OM, MD, and SNA were 2.47, 50.3, 23.2 and 70.3  $\mu\text{g m}^{-3}$ , with uncertainties of 46%, 36%, 90% and 49%,

separately. SNA was still the main contributor for the total mass concentration (48%), even if its contribution was much lower than the one observed during the period P1. At the beginning of P2 period, Shouxian site was under the influence of air masses from the southwest. BC and OM increased rapidly leading to a decrease of  $\rho_e$  ( $< 1.2 \text{ g cm}^{-3}$ ) and increase of  $k_{Mie,365}$  and  $k_{Mie,532}$  ( $> 0.04$ ), but SNA and MD concentrations remained low. When the wind direction veered to the northwest, the SNA concentration increased sharply while OM decreased. At the end of the P2 period, the wind speed increased leading to a decrease of BC and SNA mass concentrations and an increase of MD mass concentration.

During P3 period, the aerosol mass concentrations for each compound was low and in average around 0.46, 14.3, 9.2 and 15.8  $\mu\text{g m}^{-3}$  for BC, OM, MD, and SNA, respectively. The corresponding mean uncertainties were 59%, 42%, 103% and 87%. Relative errors are larger than those calculated during P1 and P2 for BC, OM, MD, and SNA mostly due to lower mass concentrations. Since the wind direction and speed were stable, the MD mass concentration was also quite stable. Compared to polluted periods, the SNA fraction decreased to 39.7%, while MD fraction increased to 23.1%. Therefore, MD takes a larger proportion during clean days consistently to previous study (Hu et al., 2012).

### 6.3.4 Comparison with filter sampled results

To verify the feasibility of  $k$ - $\rho$  method, the retrieved mass concentrations are then compared to measured aerosol chemical compositions provided by filter sampling analysis. The total mass concentrations averaged from retrieval ( $m\text{Sum}_{\text{retr}}$ ) and measurement ( $m\text{Sum}_{\text{meas}}$ ) were  $98 \pm 47$  and  $98 \pm 44 \text{ }\mu\text{g m}^{-3}$  respectively, giving confidence on the algorithm results. Moreover, retrieved and measured of each compound mass concentration were also very close. Retrieved (measured) mass concentrations of BC, OM, MD and SNA are  $1.6 \pm 1.02$  ( $1.9 \pm 0.9$ ),  $28 \pm 17$  ( $27 \pm 12$ ),  $25 \pm 20$  ( $22 \pm 15$ ) and  $43 \pm 34$  ( $44 \pm 23$ )  $\mu\text{g m}^{-3}$ .

The MAE at 532 nm is about  $22 \text{ m}^2 \text{g}^{-1}$  calculated from measured absorption (CEA)

and retrieved BC mass concentration. This value is within the range of MAE values reported by previous studies ( $10 - 35 \text{ m}^2\text{g}^{-1}$ : Laing et al., 2020; Mason et al., 2018; Wu et al., 2018; Xu et al., 2016), which demonstrates the robustness of this method.

To further verify the aerosol chemical composition retrieval algorithm, the mean values and standard deviations of retrieved mass concentrations were calculated over the filter sampling period (11.5h). The measured and retrieved aerosol mass concentrations of the sum of all species as well as all species separately (BC, OM, MD and SNA) were compared in figure 6.12a-j.

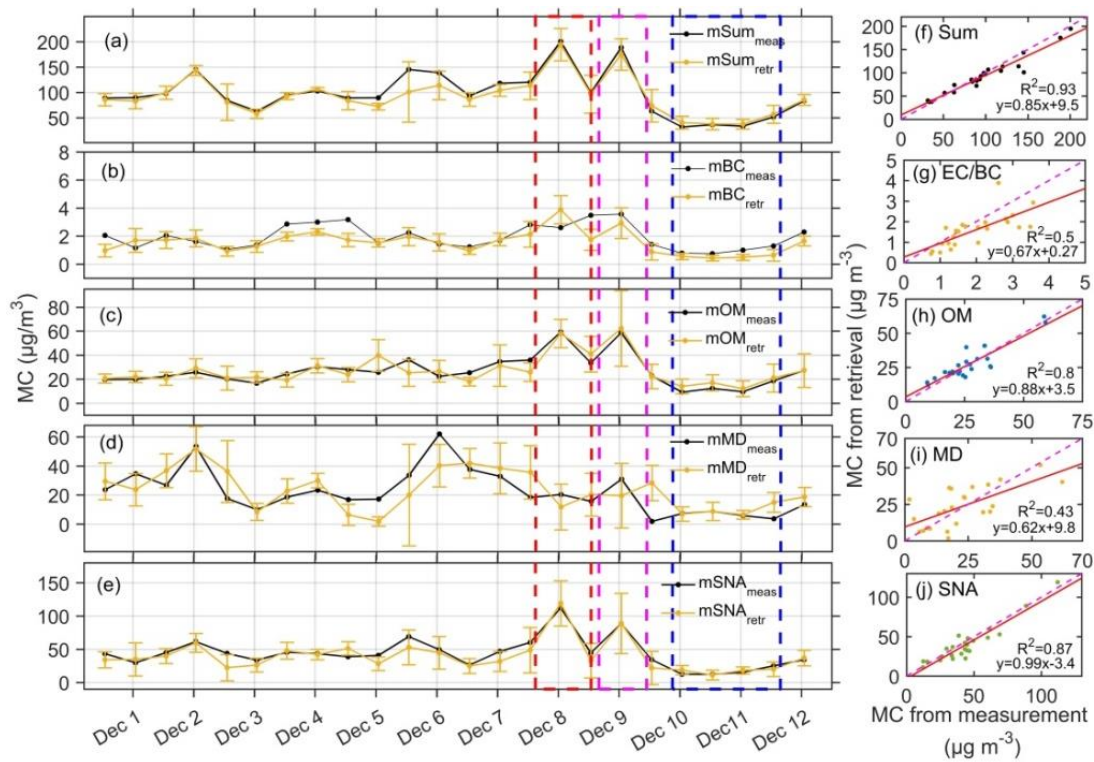


Figure 6.12 Comparison and linear regression between the measured and retrieved mass concentrations. (a,f): the sum of the mass concentrations of BC, OM, MD, and SNA from measurement ( $mSum_{meas}$ ) and retrieval ( $mSum_{retr}$ ); (b,g):  $mEC_{meas}$  and  $mBC_{retr}$ ; (c,h):  $mOM_{meas}$  and  $mOM_{retr}$ ; (d,i):  $mMD_{meas}$  and  $mMD_{retr}$ ; (e,j):  $mSNA_{meas}$  and  $mSNA_{retr}$ . The solid red lines are the results of linear fit, and the dashed magenta lines are the 1:1 lines.

$mSum_{retr}$  and  $mSum_{meas}$  were in fairly good agreement with  $R^2$  of 0.93 and slope of 0.85. Generally,  $mSum_{meas}$  was slightly larger than  $mSum_{retr}$ , especially on 5-6 December, and the difference may be due to water uptake by aerosols during analysis. Even with low relative humidity in the weighing room, a large amount of water still exists on the filter especially on hydrophilic inorganic species (Speer et al., 2003; Sciare et al., 2005). Besides that, the spherical assumption in our algorithm could lead to the error of density and CRI estimation, following the uncertainty of retrieved aerosol mass concentration.

$mBC_{retr}$  and  $mEC_{meas}$  were also broadly consistent ( $R^2=0.5$ , slope= 0.67), except on 8 December (figure 6.12 b,g). This low correlation could be explained by the fact that BC was calculated with optical method, while EC was measured with thermal/optical method. The difference between BC and EC measured by different instruments has been reported by previous studies (Hitzenberger et al., 2006; Sharma et al., 2017).  $mOM_{retr}$  and  $mOM_{meas}$  agreed well ( $R^2=0.8$ , slope=0.88, figure 6.12 c,h).  $mMD_{retr}$  and  $mMD_{meas}$  had weaker agreement than the other three species, especially during 5-6 December, and the linear correlation for MD mass concentrations was moderate ( $R^2=0.43$ , slope=0.62, figure 6.12d,i). As MD mass concentrations were calculated from a difference between the total mass concentration and the mass concentration of few species (BC, OM and SNA), it could also include sea salts, metals and other unspecified compounds.  $mSNA_{retr}$  and  $mSNA_{meas}$  were fairly consistent ( $R^2=0.87$ , slope=0.99, figure 6.12e,j) for clean and polluted periods, indicating that the method is not limited by the pollution levels.

## 6.4 Numerical simulation and sensitivity test

### 6.4.1 Numerical test

The method used for numerical test of aerosol chemical composition retrieval algorithm is shown in figure 6.13, including the following parts:

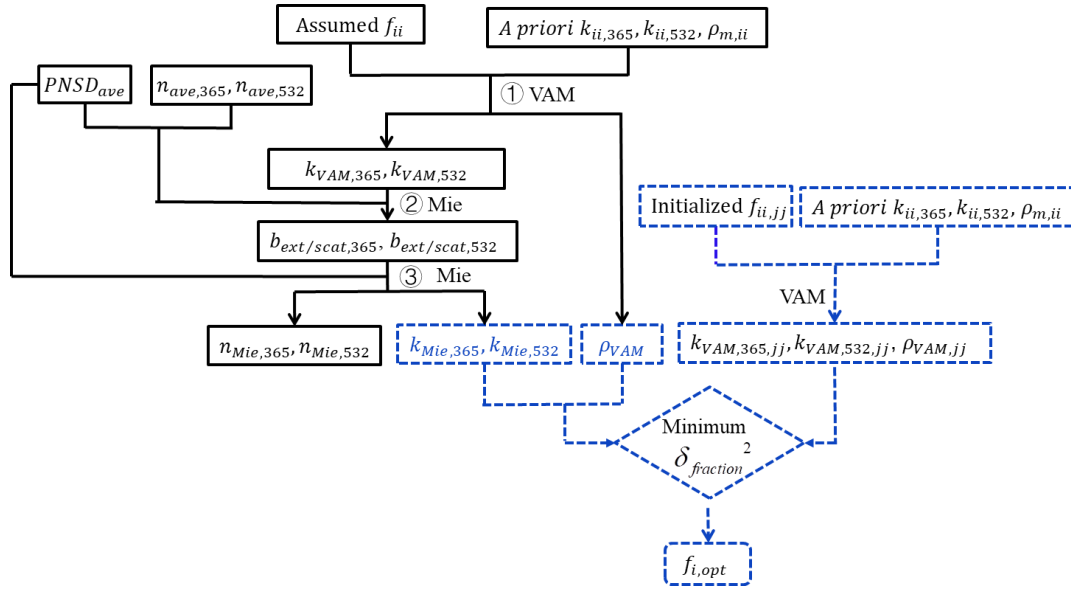


Figure 6.13 Numerical test flow chart of aerosol chemical composition retrieval algorithm. Solid parts: generation of numerical experimental data with randomly generated fractions of BC, OM, MD and SNA; dashed parts: retrieval of aerosol chemical composition.

(1) Generation of experimental data (solid black lines in figure 6.13): The volume fraction of each component ( $f_{ii}$ ,  $ii = 1, 2, 3, 4$ , representing BC, OC, MD, and SNA, which meets the following relationship:  $f_1 + 1.6 \times f_2 + f_3 + f_4 = 1$ ) is randomly generated, and  $1.6 \times f_2$  is the volume fraction of OM. The values of  $f_1, f_2$  and  $f_4$  range from 0 to 0.1, 0 to 1, 0 to 1, respectively.  $f_3$  is the remaining part. VAM rule is used to obtain the density ( $\rho_{VAM}$ ), and the imaginary part of CRI at 365 nm ( $k_{VAM,365}$ ) and 532 nm ( $k_{VAM,532}$ ) for the mixture with *a priori* values of  $\rho_{p,ii}$ ,  $k_{365,ii}$  and  $k_{532,ii}$  (table 6.1 and 6.2). Combining these values with the average, over the full campaign, values of the PNSD and real part of the CRI ( $n_{ave,365} = 1.39$ ,  $n_{ave,532} = 1.47$ ), extinction and scattering coefficients ( $b_{ext,scat,365}$ ,  $b_{ext,scat,532}$ ) are calculated using Mie theory (section 6.2.2). These generated data ( $k_{VAM,365}$ ,  $k_{VAM,532}$  and  $\rho_{VAM}$ ) with known  $f_{ii}$  are used as experimental data for aerosol chemical composition retrieval.

(2) Aerosol chemical composition retrieval (dashed blue lines in figure 6.13): This part is the retrieval of aerosol chemical composition with  $k$ - $\rho$  method as described in section 6.1.

(3) Comparison of the retrieved volume fractions with numerical input values: The scatter plot of these assumed and retrieved aerosol chemical compositions is shown in figure 6.14. The correlation coefficients for these four species are better than 0.99, which indicates the reliability of the algorithm.

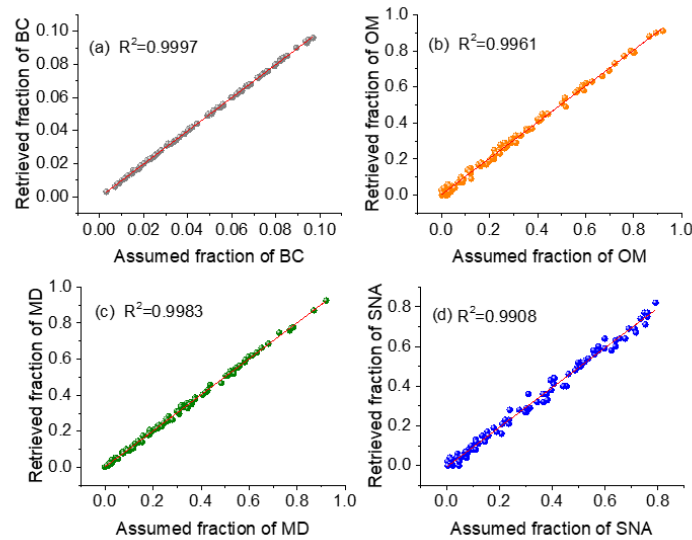


Figure 6.14 Comparison of assumed and retrieved volume fractions of (a) BC, (b) OM, (c) MD, and (d) SNA. The red lines are the linear fit results.

#### 6.4.2 Sensitivity to *a priori* inputs

To estimate the impacts from *a priori*  $\rho_m$ ,  $k$  and OM to OC ratio for each species used in this algorithm, we considered four cases representing the mean level as well as OM, MD, and SNA dominated periods for sensitivity study.

The criteria used to identify the MD, OM and SNA enriched events were based on 1<sup>st</sup> and 99<sup>th</sup> percentiles of  $\rho_e$  and  $k_{Mie}$ . Those criteria are given as follows:

- (1) For the mean level, we used the mean  $\rho_e$ ,  $k_{Mie,365}$  and  $k_{Mie,532}$ .
- (2) OM dominated case was associated to period when  $k_{Mie,365}$  reached the 99<sup>th</sup> percentile of all  $k_{Mie,365}$  retrievals.

(3) Similarly, SNA dominated case was associated to period when  $k_{Mie,365}$  reached the 1<sup>st</sup> percentile of all  $k_{Mie,365}$  retrievals.

(4) Since MD has the highest density among the four species, MD dominating period corresponds to the period of 99<sup>th</sup> percentile  $\rho_e$  observed during the field campaign.

Then, mass concentrations for each case were calculated using the *a priori* inputs for this study as the baseline (table 6.1 and 6.2, font in bold). Table 6.4 lists the values of  $\rho_e$ ,  $k_{Mie,365}$  and  $k_{Mie,532}$ , and the corresponding volume fractions ( $f_{BC}$ ,  $f_{OM}$ ,  $f_{MD}$ , and  $f_{SNA}$ ) for the four species during the four case studies. The absolute and relative mass concentration differences caused by using different *a priori* inputs for each species and for the four case studies are shown in figure 6.15 - 6.18.

Table 6.4 The effective density, imaginary refractive index and volume fractions of different cases for sensitivity test.

Cases	$\rho_e$	$k_{Mie,365}$	$k_{Mie,532}$	$f_{BC}$	$f_{OM}$	$f_{MD}$	$f_{SNA}$
Mean level	1.67	0.025	0.018	0.015	0.41	0.18	0.40
OM dominated	1.40	0.036	0.026	0.023	0.68	0.02	0.28
MD dominated	1.96	0.024	0.015	0.01	0.34	0.46	0.18
SNA dominated	1.65	0.016	0.013	0.013	0.21	0.01	0.77

One can note that the largest differences of mBC, mOM, mMD and mSNA are ascribed to  $k_{OC}$  for almost all cases. Indeed, the  $k_{OC}$  values used as high and low bounds are extremes.  $k_{OC,H}$ , reported by Kirchstetter et al. (2004), was obtained using OC extracted from biomass burning samples and therefore ignored the presence of non-absorbing or low-absorbing OC (e.g. Secondary Organic Aerosols, SOA, Nakayama et al., 2015) , usually found within the atmosphere.  $k_{OC,L}$ , measured in a cleaner environment by Liu et al. (2013) , is also an extremely low value in comparison to previous studies (Shamjad et al., 2017; Shamjad et al., 2016; Sun et al., 2007) .

For the mean level (figure 6.15), using a high limit of  $k_{BC}$  ( $k_{BC,H}=1.26$  from Moteki et al., 2010) leads to the largest difference (37%) of mBC, and the second highest one

(32%) is caused by the low threshold of  $k_{OC}$  ( $k_{OC,L}$ ). The mBC differences caused by material density,  $k_{MD}$  and OM to OC ratio are lower than 20%. Especially, OM to OC ratio,  $\rho_{MD}$  and  $\rho_{SNA}$ , ranging within the values of table 6.2, have very little influence on mBC (<4 %). For mOM, mMD and mSNA, the largest discrepancies are from  $k_{OC}$ . Indeed, mOM and mMD can decrease by 65% and 66%, while mSNA will increase by 86%, when  $k_{OC}$  is set at its maximum value ( $k_{OC,H}$ ). Adversely, mOM and mMD can increase by 57% and 91% respectively, while SNA will decrease by 90% using the low limit of  $k_{OC,L}$ . The relative differences caused by material density,  $k_{BC}$ ,  $k_{MD}$  and OM/OC are less than 26% for mOM, 37% for mMD and 35% for mSNA.

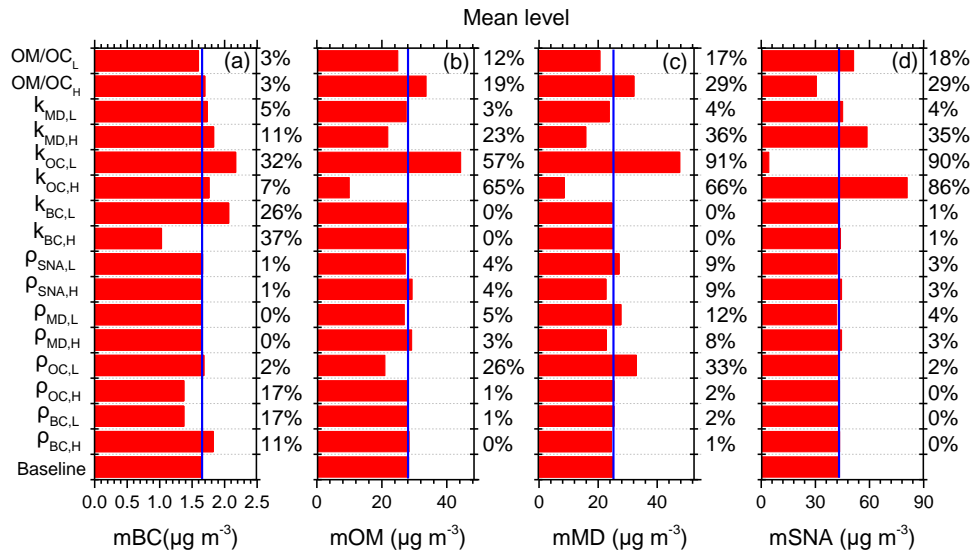


Figure 6.15 The mass concentration differences in the mean level between the *a priori* inputs used in this study (Baseline) and the possible high and low limit from literatures (table 6.1 and 6.2). (a) ~ (d) are for the mass concentration of BC, OM, MD and SNA respectively.

For OM dominated case, the sensitivity to  $k_{OC}$  increases a lot and contributes to maximum differences of 59%, 72%, 413%, and 100% for mBC, mOM, mMD and mSNA respectively. In addition to  $k_{OC}$ , the higher threshold of  $k_{BC}$  (1.26) also exerts a significant influence on mOM (97%). The other parameters show smaller influence on mBC (<25%) and mOM (<25%) for this case. In comparison to the mean level, SNA

has large relative differences when selecting different *a priori* inputs, which could be attributed to the low mass concentration observed during this period ( $4 \mu\text{g m}^{-3}$ ). When mMD is low, the low limit of  $\rho_{OC}$  ( $\rho_{OC,L}$ ) also has a significant impact on mMD uncertainties (389%). Material densities have smaller influence on the retrieved mBC (<18%), mOM (<25%) and mSNA (<18%). The impact from  $k_{MD}$  is even lower here (<20% for all species), but the impact from OM/OC is non-negligible for mSNA (95% difference by  $OM/OC_H$ ).

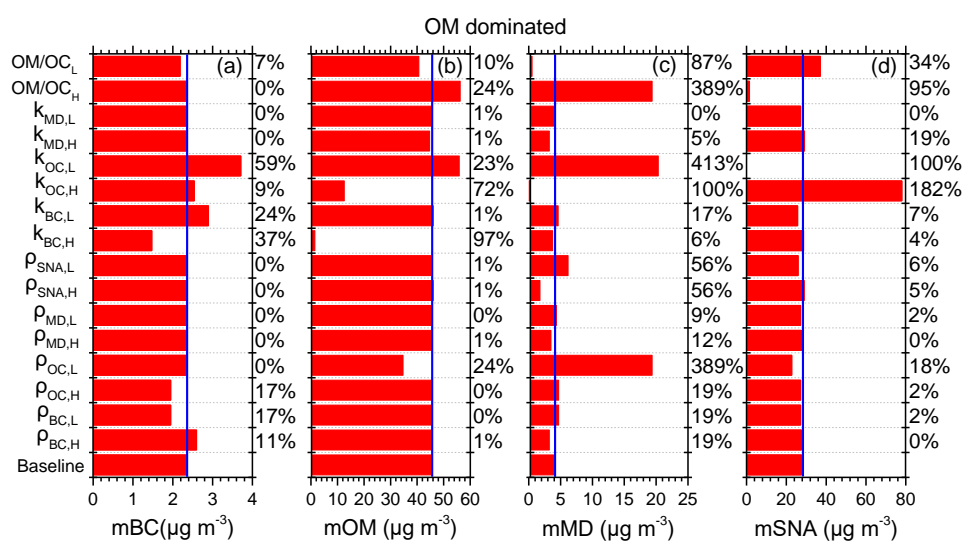


Figure 6.16 The same as figure 6.15 but for OM dominated case.

For MD dominated case (figure 6.17),  $k_{OC}$  is also the main source for the large absolute differences. Interestingly,  $k_{MD,H}$  is another non-negligible factor of mOM (75%) and mSNA (236%) uncertainties. Once more, the material density for the four species has limited effect on the retrieved mass concentrations (<28%) in this case.

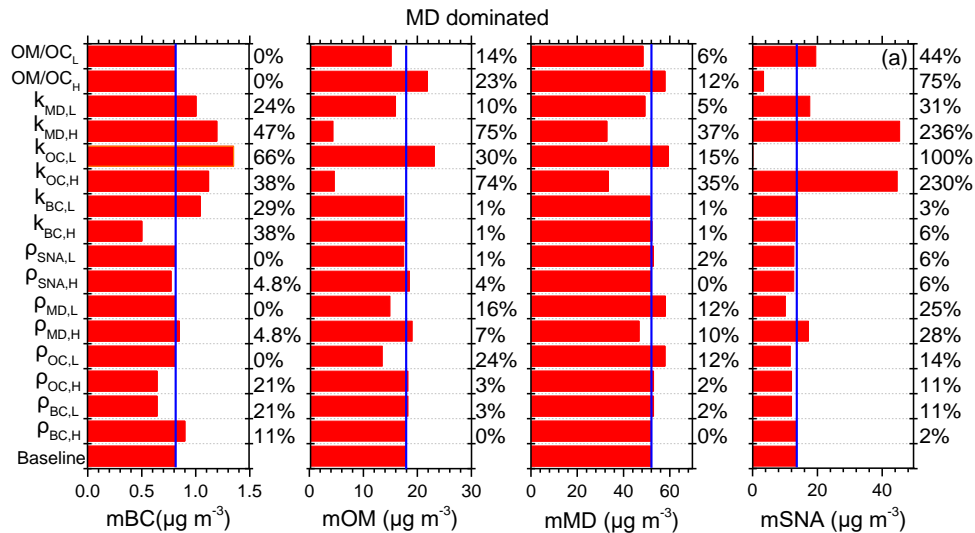


Figure 6.17 The same as figure 6.15 but for MD dominated case.

SNA dominated case (figure 6.18) appeared during a quite clean period ( $\text{PM}_{2.5} < 30 \mu\text{g m}^{-3}$ ) during this field campaign.  $k_{OC}$  has a small impact on mBC, and the largest mBC difference (36%) is due to the selection of  $k_{BC,H}$ . This parameter also has a strong impact on mOM (95%). For mOM, mMD and mSNA,  $k_{OC}$  is still the main contributor to the uncertainties. The mMD differences are quite sensitive to the *a priori* inputs because of their low mass concentration (volume fraction of 1%). Material density has a relative small impact on mBC (<18%), mOM (<29%) and mSNA (5%). Mass concentration differences associated to  $k_{MD}$  and OM/OC are even lower (<5% for mBC, <19% for mOM and <10% for mSNA).

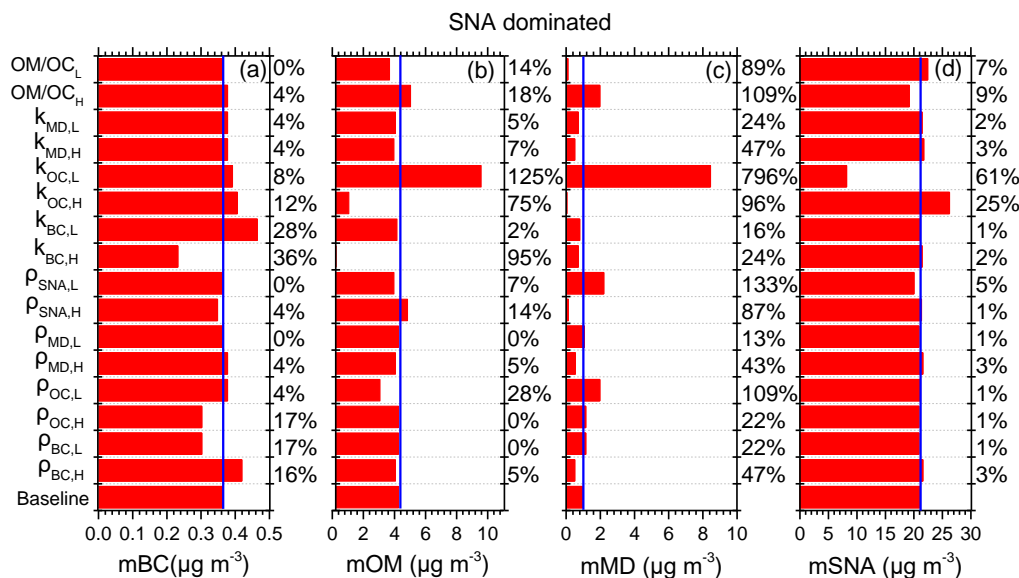


Figure 6.18 The same as figure 6.15 but for SNA dominated case.

In summary, the retrieved aerosol chemical compositions are highly dependent on the selection of  $k_{OC}$  for almost all the cases probably due to extreme thresholds. The large uncertainties caused by  $k_{OC}$  in this study is comparable to the result by Schuster et al. (2016) that the BrC bias could vary from 50% to 440% due to the selection of  $k_{OC}$ . Among the four species, BC has the least sensitivity to these factors. Indeed, the uncertainties associated to mBC from *a priori* inputs, except  $k_{OC}$ , are lower than 48% for all cases. Therefore, a better constrain of aerosol CRI, especially for OC, will reduce the uncertainties from *a priori* inputs.

## 6.5 Conclusions

Even though great progresses have been achieved to retrieve aerosol chemical compositions based on remote sensing measurements, it is still difficult to validate the retrieved composition in comparison to measured results over the column. This work is the first attempt to retrieve the fraction of main aerosol compounds, including BC, OM, SNA and MD, based on  $\rho_e$  and  $k_{Mie}$  retrieved from in-situ measurements. This method is not limited by the wavelengths, and it could be used for composition retrieval at two wavelengths with distinguished values of  $k$  for OC and MD.

The  $k$ - $\rho$  method was applied to further analyse two pollution and one clean episodes observed during a field campaign in Shouxian. The variation of retrieved compositions could be well described by the transition of air mass sources. In addition, a good agreement between retrieved and measured mass concentrations of the four species was also observed ( $R^2=0.8$ , slope=0.88 for OM;  $R^2=0.87$ , slope=0.99 for SNA). The correlation for retrieved BC and measured EC is moderate ( $R^2=0.5$ ). Because BC is defined based on the particle optical property, while EC is defined as non-refractory material. The comparison of retrieved and measured MD mass concentration shows the lowest correlation ( $R^2=0.43$ ) in comparison to the other three species. This is most probably due to the fact that MD mass concentration was not directly measured and that larger uncertainties were associated to MD mass concentration from retrievals.

We performed comprehensive sensitivity tests to estimate the uncertainties on the retrieved mass concentrations. Numerical test revealed that the assumed known composition fractions were highly related with the retrieved compositions with ( $R^2>0.99$ ) for the four species, indicating the feasibility of the algorithm. Sensitivity test was performed to investigate the aerosol chemical composition retrievals impact from *a priori*  $\rho_m$ ,  $k_{365}$ ,  $k_{532}$  and OM to OC ratio for the mean level and OM, MD, and SNA dominated events. The result demonstrated that BC is less sensitive to these *a priori* parameters, and its error is within 48% from the uncertainty of *a priori*  $\rho_m$ ,  $k_{365}$ ,  $k_{532}$ . To reduce the error from *a priori* inputs, a better constrain of  $\rho_m$ ,  $k$  and OM to OC is of great importance, especially the  $k_{OC}$ .

The method provides a reliable tool to monitor the pollution events, identify aerosol sources and verify the retrievals from remote sensing data. By reducing the measurement uncertainties of PNSD,  $b_{ext}$  and  $b_{scat}$ , by improving the accuracy of  $\rho_m$  and  $k$  values of each chemical component, and by considering the aerosol morphology and mixing state, the retrieval accuracy can be further improved. Long-term, comprehensive field observations at different locations are recommended to further validate the applicability of this new algorithm.

## Chapter 7 Conclusions and perspectives

### 7.1 Conclusions

Aerosols have distinguished optical, physical and chemical properties as a function to their sources. Due to the large variety of emission sources (Yao et al., 2016) and due to chemical processes modifying aerosols during their residence time within the atmosphere (Huang et al., 2014; Li et al., 2017), these properties have complex temporal and spatial variations. According to their properties, aerosols will interact differently with solar radiation and therefore have different impacts on earth radiative forcing. Similarly, the health effect is directly related to aerosol chemical and physical properties. Therefore, a better knowledge of aerosol chemical composition is then essential for governments to make policy, and effectively alleviate exacerbation of global warming and atmospheric pollution events.

Direct measurements of aerosol chemical compositions can only be achieved by in-situ measurements at the surface or on-board. However, these measurements are limited to specific locations and the network of available monitoring instruments is pretty scarce around the world. Therefore, continuous measurements at a large scale of aerosol chemical composition are deemed needed to identify aerosol sources, forecast air quality and better evaluate aerosol impact on radiative forcing.

With the development of remote sensing, columnar, vertical and global aerosol optical property could be observed by sun photometer, lidar and instruments on-board satellite. As aerosol optical properties are closely related to their chemical compositions, global observations of aerosol chemical composition are then reachable. Indeed, SAE, AAE, SSA and CRI are independent of aerosol concentration, and rely on aerosol chemical composition, size distribution and mixing state. Among them, CRI is treated as an intrinsic optical parameter. This characteristic makes it a good candidate to identify aerosol chemical compositions from aerosol optical properties. To obtain the columnar and global aerosol chemical composition distribution, methods based on AE (AE methods) and the imaginary part of CRI ( $k$ -based methods) were well developed.

AE methods aim to determine aerosol absorption contribution (AAE alone) and classify aerosol types (SAE vs. AAE space scheme). However, these methods are controversial. Indeed, the fraction of each compound is identified based on AAE or/and SAE thresholds. Those thresholds vary from one study to another for the same type of particles. A comprehensive modelling (Mie code) study on SAE and AAE for BrC, MD, pure and coated BC revealed their high dependency to aerosol size and wavelength couples chosen. This SAE and AAE dependency could explain the discrepancies between two main aerosol classification schemes (Cazorla et al., 2013; Cappa et al., 2016). Moreover, these results also highlight that the assumption of constant AAE within the visible range of wavelength is incorrect for the three tested absorbing species. Especially, the coating thickness as well as the BC core size impacts on retrieval quality was tested. The result demonstrates that BC core size ( $GMD_{core}$  larger than 50 nm) has a stronger impact on AAE than the coating thickness.

Moreover, most of these methods are estimating clear shell (CS) coated BC absorption coefficient assuming  $AAE_{BC\_CS}$  of 1. The uncertainties of this assumption as well as using  $AAE_{BC\_CS,880-950}$  instead of using the real  $AAE_{BC\_CS}$  for specific wavelengths were evaluated. When using a fixed value of 1 for  $AAE_{BC\_CS}$ , the calculated BC absorption has smaller uncertainty (< 35 %) than using  $AAE_{BC\_CS,880-950}$  throughout the wavelength range only for  $GMD_{core}$  between 38 and 72 nm. Especially, BC absorption uncertainty could be limited to 10% for  $GMD_{core}$  between 44 and 54 nm. When  $GMD_{core}$  is larger than 76 nm or smaller than 28 nm, using  $AAE_{BC\_CS,880-950}$  brings smaller uncertainty (< 40 %) than a fixed value of 1. As the observed  $GMD_{core}$  is often around 60 ~ 150 nm (Cheng et al., 2018; Taylor et al., 2014; Moriet al., 2016), a better knowledge of BC core size would be helpful to constrain the  $AAE_{BC}$  range, and then reduce the uncertainty of BC absorption coefficient using AE methods. However, the AAE methods are usually performed without any information on BC core size which may cause large discrepancies on BC absorption coefficient retrievals.

On the other hand,  $k$ -based methods are dedicated to retrieve aerosol chemical compositions quantitatively. As  $k$  is an intrinsic parameter,  $k$ -based methods have been

widely used for retrieving columnar aerosol chemical compositions, such as the *k-n-dSSA* method proposed by Li et al (2013). This method was used to retrieve columnar aerosol chemical compositions (BC, BrC, MD, AW and AS) using long-term (2005-2014) dataset from AERONET in Beijing. The retrieved columnar aerosol chemical compositions were, then, coupled with air mass backward trajectories (HYSPLIT) arriving at 500m over Beijing. The aerosol chemical composition dependence to regional transportation was analysed during different seasons. The retrievals were also compared to the seasonal distribution of emission inventories (BC, OC, and sum of SO<sub>2</sub> and NO<sub>x</sub>) to realize a preliminary validation.

The special geographical location and the emission distribution around Beijing result in a large variety of aerosol properties and trajectory clusters for all seasons. BC and BrC are abundant over north China during winter because of coal heating as well as over the south of Beijing during the remaining seasons. The retrieved BC and BrC fractions are also larger during autumn and winter (cold season). Consistently to emission inventories, those compounds are not associated to a specific cluster and therefore may be coming from all the directions around Beijing. The largest MD concentrations are retrieved during spring, especially influenced by air mass coming from the northwest, where the Taklimakan desert is located. Clusters with large AS and AW fractions are associated with east and south east regions consistently with the seasonal spatial distribution of SO<sub>2</sub> and NO<sub>x</sub> and are highly influenced by the summer monsoon

Over the 10 years' period, the retrieved columnar aerosol chemical compositions and backward trajectory clusters are generally in good agreement with the seasonal distribution of aerosol emission sources. This result suggests the reliability of this method. But the algorithm still needs to be further validated with directly measured aerosol chemical compositions through airborne measurements, or to be applied to in-situ measurements to realize one of the first closure studies between retrieved and measured aerosol chemical compositions.

To realize this closure study, a novel algorithm was built based on *k*-based methods

and applied to in-situ measurements to retrieve dry BC, OM, MD and SNA mass concentrations within the PM<sub>2.5</sub> fraction. Because OC and MD have similar absorption variation in the visible spectrum, aerosol density was introduced together with  $k$  to build this algorithm named  $k$ - $\rho$  method. The second input (e.g. the CRI), not directly measured, was retrieved at 365 and 532 nm based on Mie code, particle size distributions and simultaneously measured aerosol extinction and scattering coefficients.

Along with the physical and optical properties, the aerosol chemical composition was measured from filter-based analysis. Therefore, the measured and retrieved mass concentrations for BC, OM, MD and SNA were compared and showed relatively good agreement for all species except MD. The square of correlation coefficient between retrieved and measured OM (SNA) mass concentrations is around 0.8 (0.87) and the slope around 0.88 (0.99). The square of correlation coefficient for retrieved BC and measured EC mass concentrations is only about 0.5. Part of the discrepancies between EC and BC mass concentrations could be due to the totally different definitions and measurement techniques of both species.

Retrieved and measured MD mass concentrations show the lowest square correlation coefficient ( $R^2=0.43$ ). MD mass concentrations were not directly measured and were estimated by difference between the total mass concentration and the sum of all the above species mass concentrations. Therefore, large uncertainties are associated to MD mass concentration. This could also explain the differences between retrieved and measured MD mass concentrations. Generally, the  $k$ - $\rho$  method shows a promising agreement between retrieved and measured fraction for BC, OM, MD and SNA and can therefore be used as a useful tool to obtain real-time compositions.

To examine the retrieval uncertainties from *a priori* inputs ( $\rho_m$  and  $k$  for different species and OM to OC ratio), sensitivity test was performed for four situations observed during the campaign. OM, MD and SNA dominated cases were selected as well as an average situation called mean level. BC was found to have the least sensitivity to these parameters, and its retrieval uncertainty is below 48 % for all cases. While the retrieved

aerosol chemical compositions are highly dependent on the selection of  $k_{OC}$  for almost all the cases probably due to extreme thresholds chosen to run the sensitivity test. Therefore, determining CRI at varied wavelengths for OC is deemed needed to improve  $k$ -based methods.

## 7.2 Perspectives

This work presents a comprehensive study of aerosol chemical composition classification and retrieval methods based on aerosol optical properties, and physical properties such as size and density. We used simulation results, remote sensing and in-situ measurements to realize the evaluation of the different methods outputs, and finally developed an improved method by introducing aerosol density. Even though, more knowledge needs to be gained on the link between aerosol optical and chemical properties by combining laboratory and field measurements:

(1) Validation of AE methods to derive absorption contributions by different species.

As previously explained, the thresholds used for AAE and SAE to identify all aerosol species are not the same for all studies. This could cause incorrect identification of aerosol species and large discrepancies on the retrieved fraction of all compounds. From the literature, different CRI values for BrC, MD and pure and coated BC could be gathered to evaluate their impacts on SAE and AAE. Moreover, the Mie results of the AAE dependence on BC core size, coating thickness and wavelength pairs needs to be validated using laboratory campaign with known generated samples. A campaign is already planned in 2021 at the PSI institute to gain more knowledge on (1) aerosol optical properties and (2) discrepancies of absorption, extinction and scattering properties measured by all techniques available within the community. At that time, a specific task would be also to retrieve BC absorption at different wavelengths using different AAE assumptions (e.g. equals to 1, AAE calculated over the spectral range of interest or over the near IR spectral range). All these points would be really helpful to better estimate aerosol chemical compositions from optical measurements.

(2) Validation of  $k$ -based method to retrieve columnar aerosol chemical compositions

$k$ -based method can be used to retrieve columnar aerosol chemical compositions, and the  $k$ - $n$ - $dSSA$  method has been preliminarily tested combining aerosol backward trajectories and emission distributions in this thesis. The retrieved columnar aerosol chemical compositions can be further compared with the outputs from models and columnar aerosol chemical compositions integrated from in-situ measurements. Especially, the NASA DISCOVER-AQ campaign performed extensive profiling of aerosol chemical composition with a pair of particle-into-liquid samplers (Crumeyrolle et al., 2014). These profiles were coincident with AERONET site, which makes it possible to verify retrieved columnar aerosol chemical composition with in-situ measurement.

(3) Improvement, application and verification of  $k$ - $\rho$  method.

Closure studies of aerosol physical, optical and chemical properties are the basic content for model development and evaluation of algorithm based on remote sensing. In-situ measurements are an effective tool to achieve this goal, because aerosol chemical compositions, physical and optical properties could be measured accurately in the same controlled environment. In this study, we developed  $k$ - $\rho$  method to retrieve dry BC, OM, MD and SNA mass concentrations based on in-situ observations. This algorithm can be improved by taking aerosol particle shape into consideration. As Mie theory was used, the assumption of spherical particles has to be carried throughout this work. However, aerosol shapes are far from the spherical hypothesis especially for fresh BC and MD. Therefore, a spheroid code as the one developed by Dubovik et al. (2006) needs to be implemented within the algorithm. Then, Shouxian data set could be used to validate the method but also to estimate the errors associated with the spherical assumption. The “improved” method could then be used for typical sites (e.g. enriched in regions of dust, urban fossil fuel, and biomass burning) for algorithm verification and analysis of pollution events.

## Résumé

Les propriétés optiques, physiques et chimiques des aérosols sont fortement dépendante de leurs sources mais aussi des processus chimiques qui modifient les aérosols pendant leur temps de séjour dans l'atmosphère. Les propriétés des aerosols présentent donc des variations temporelles et spatiales complexes. Les impacts sanitaires ou climatiques de ces aerosols sont fortement relié a leurs propriétes. En effet, l'effet sanitaire et climatique des aerosols sont directement liés à leurs propriétés chimiques, physiques et optique (Zhou and Tung, 2013; Tellez-Rojo et al., 2020).

Une meilleure connaissance des propriétes physique, chimique et optique des aérosols est donc essentielle pour élaborer des politiques et atténuer efficacement les effets sanitaires et climatiques de la pollution atmosphérique. Dans cette étude, trois espèces absorbantes ont été prises en compte: le carbone noir (BC), le carbone organique (OC) et les poussières minérales (MD). Par ailleurs, les espèces diffusantes majoritaires (SNA) ont ete considérées: Sulfate (S), Nitrate (N) et Ammonium (A).

Les méthodes d'identification de la composition chimique des aérosols sont à l'heure actuelle limitées à l'analyse de filtres et des spectrometres de masse. Ces techniques experimentales présentent des inconvénients tels qu'une faible résolution temporelle (filtre), un coût élevé ou la complexité de leur mise en œuvre et sont donc limitées à un nombre limité de sites. Comme l'extension horizontale et verticale de la pollution atmosphérique varie beaucoup, même à l'échelle d'une ville, des mesures en continu de la composition chimique des aérosols avec une résolution temporelle et spatiale élevée sont nécessaires pour identifier les sources d'aérosols, surveiller les épisodes de pollution et évaluer leur impact sur le forçage radiatif.

Les differentes mesures optiques des aérosols, comprenant les mesures in-situ ainsi que les mesures par télédétection au sol ou embarqué, permettent une surveillance quasi-continue des aérosols dans le monde entier. L'objectif de ce travail de recherche consiste a relier les propriétés optiques des aérosols à leur propriétés chimiques. Cela permettrait d'élargir nos connaissances actuelles sur la variabilité spatio-temporelle des

différents types d'aérosols à l'échelle mondiale, en particulier dans les zones désertes ou il n'existe pas de station de mesures. Des méthodes pour lier les propriétés chimiques et optiques des aérosols existent déjà et sont basées sur des paramètres tels que l'indice de réfraction complexe (IRC:  $m=n + k i$ ) et les coefficients d'Ångström de diffusion et d'absorption (SAE et AAE) (Schuster et al., 2016a, 2016b; Bahadur et al., 2012; Li et al., 2013). Ces méthodes, même si de grands progrès ont été réalisés, sont encore controversées et ne permettent pas de vérifier expérimentalement les compositions chimiques des aérosols mesurées. L'objectif de cette thèse est d'étudier les questions cruciales suivantes:

- (1) Comment les méthodes basées sur l'AE permettent-elles de distinguer les différents types d'aérosols et de calculer leurs contributions massiques?
- (2) Les méthodes basées sur "k" sont-elles efficaces pour retrouver les compositions chimiques, intégrées sur la colonne, des aérosols?
- (3) Comment réaliser une validation de ces méthodes en comparant leurs résultats avec des mesures de la composition chimique des aérosols?

Pour répondre à ces trois questions, le contenu principal de cette thèse peut être divisé en trois parties. La première partie est consacrée à la description détaillée et à l'étude plus approfondie des méthodes basées sur l'AE. La deuxième partie présentera les méthodes basées sur le paramètre  $k$  ainsi que son application et sa validation sur un super site de mesures. Dans la troisième partie, nous développons une nouvelle méthode basée sur  $k$  et la densité (méthode  $k-\rho$ ) pour estimer les concentrations des principaux aérosols observés (BC, OM, MD et SNA) sur la base de mesures in-situ, et à nouveau comparer les restitutions avec les compositions chimiques mesurées des aérosols.

## **i. Étude sur l'exposant Ångström**

L'AAE est par définition lié aux espèces qui absorbent les aérosols. BC se distingue de OC et MD avec une valeur AAE autour de 1 sur tout le domaine du visible, tandis que OC et MD ont une valeur AAE supérieure à 1. Sur la base de ces

caractéristiques optiques, deux types de méthodes ont été élaborés pour identifier les différentes compositions chimiques des aérosols. Les performances de ces méthodes seront étudiées par le biais d'une étude complète sur la dépendance de la SAE et de l'AAE à la taille des aérosols et aux couples de longueurs d'onde en utilisant la théorie de Mie.

### **i.1. Description des méthodes AE**

L'absorption contribué par les différentes espèces d'aérosols pourrait être calculée avec l'AAE seul en supposant que l'AAE est un paramètre intrinsèque. Cependant, certaines études ont révélé que l'AAE variait également en fonction de la taille des particules, de l'état de mélange et des paires de longueurs d'ondes choisies pour la mesure (Lack and Cappa, 2010; Schuster et al., 2016b; Wang et al., 2018; Wang et al., 2016). Lack et al. (2013) ont calculé que les incertitudes liées à la restitution du coefficient d'absorption associé au BC se situaient entre 20 % et -40 % en utilisant un  $AAE_{BC}$  fixe compris entre 0,55 et 1,7. Les incertitudes seraient accrues lorsque les valeurs de  $AAE_{BC}$  se situent en dehors de cette fourchette. À l'heure actuelle, l'étude exhaustive de la dépendance de l'AAE aux paires de longueurs d'onde, à la taille et à l'état de mélange de toutes les particules absorbantes est rare.

La méthode SAE vs. AAE est développée pour améliorer la classification en prenant en compte une partie de l'informations sur la taille des aérosols observés. En effet, le SAE est utilisé pour distinguer les compositions chimiques des aérosols en fonction de leur taille. BC et OC sont généralement considérés comme des petites particules, tandis que MD est traité comme de grosses particules. En fixant des seuils appropriés dans l'espace SAE vs. AAE, il est possible d'identifier qualitativement les différents types d'aérosols (BC, OC, MD) et leur mélange (Russell et al., 2010). Toutefois, les seuils permettant de séparer les types d'aérosols différent d'une étude à l'autre (Cappa et al., 2016; Cazorla et al., 2013; Schmeisser et al., 2017).

### **i.2. simulation de SAE et AAE avec la théorie de Mie**

Afin de comprendre les limites des méthodes basées sur l'AE, la théorie de Mie

nous a permis de simuler la dépendance spectrale des coefficients d'Angstrom du coefficient de diffusion ou d'absorption (SAE et AAE) en fonction de la taille des aérosols d'intérêts. Les trois principales espèces absorbantes, dont le BrC et le MD, et le BC pur ou enrobé de composés diffusants, ont été étudiés. L'Indice de Refraction Complexe (IRC) pour ces différents types d'aérosols ont été répertoriés dans la littérature (BrC: Kirchstetter et al. (2004), MD: Wagner et al. (2012), BC pur: Bond et al. (2006, 2013), SNA (pellicule de surface):  $1,5+0i$  (Mallet et al., 2003; Chin et al., 2002).

La distribution en taille des aérosols pouvait être monomodale (BrC, BC et MD  $200 < D_p < 500 \text{ nm}$ ) ou bimodale (MD: Mode fin centré sur  $300 \text{ nm}$  et Mode grossier entre  $3$  et  $4 \mu\text{m}$ ). Dans le cas de la bimodale, la concentration en nombre des particules du mode grossier était fixée à deux fois celle du mode fin. Le diamètre des particules de BC modifié par une pellicule de surface est fixé en fonction du rapport du diamètre de la coque au diamètre du noyau ( $GMD_{\text{shell}}/GMD_{\text{core}}$ ) et varie entre  $1$  et  $3$  (Wang et al., 2018).

### **i.3. SAE et AAE pour BrC, MD et BC**

Les résultats de notre étude montrent que la valeur du  $SAE_{\text{BrC}}$  augmente en fonction des longueurs d'onde choisies ( $SAE_{\text{BrC},350-400}=1,5$ ,  $SAE_{\text{BrC},650-700}=2,9$ ,  $GMD_{\text{BrC}}=50 \text{ nm}$ ). De même,  $SAE_{\text{BrC}}$  diminue avec l'augmentation de la taille des particules de BrC. La valeur simulée de  $AAE_{\text{BrC}}$  est extrêmement élevée et montre une plus grande dépendance à la longueur d'onde qu'à la taille. En fonction des longueurs d'onde sélectionnées, l'écart entre deux valeurs de  $AAE_{\text{BrC}}$  pourrait être supérieur à  $8$ . Cette forte dépendance de  $AAE_{\text{BrC}}$  aux longueurs d'onde doit donc être prise en compte afin de fixer les seuils utilisés pour déterminer la présence de BrC.

La dépendance spectrale du SAE des poussières désertiques monodispersées est similaire à celle du  $SAE_{\text{BrC}}$  (augmente avec la longueur d'onde) avec un écart maximal de  $1.3$ . Lorsque ces mêmes particules sont distribuées sur deux modes, la dépendance spectrale du SAE est différente avec un minimum observé entre  $400$  et  $650 \text{ nm}$ . Pour

les longueurs d'onde supérieures à 650 nm, la tendance est la même que celle du  $SAE_{MD}$  calculé pour un seul mode de MD.

La dépendance spectrale du  $AAE_{MD}$  révèle une variation totalement différente de celle de  $AAE_{BC}$ . Les valeurs les plus faibles de  $AAE_{MD}$  apparaissent pour les paires de longueurs d'onde les plus longues et les plus courtes, tandis que le maximum est associé aux paires de longueurs d'onde autour de 500-600 nm. L'écart maximum entre les valeurs extrêmes de  $AAE_{MD}$  est d'environ 2.  $AAE_{MD}$  diminue avec l'augmentation de la taille, mais l'impact est presque insignifiant par rapport à l'impact des paires de longueurs d'onde sélectionnées.

De même,  $SAE_{BC}$  varie de 0 à 2,6 et cette variation est principalement due à la sélection de différentes paires de longueurs d'onde. En général, les valeurs du  $SAE_{BC}$  sont plus petites lorsque l'on utilise des paires de longueurs d'onde plus courtes, et vice versa. De plus, les résultats de la simulation montrent que  $AAE_{BC}$  varie beaucoup en fonction des paires de longueurs d'onde mais aussi en fonction de la distribution en taille des aérosols. De plus nos résultats montrent que cette valeur varie de 0,45 à 1,12 ou strictement inférieure à 0,12 lorsque la taille du BC est de 50 nm ou 250 nm. Comme la dépendance spectrale du  $SAE_{BC}$ ,  $AAE_{BC}$  est plus faible pour les paires de longueurs d'onde courtes, et sa valeur est plus élevée pour les paires de longueurs d'onde longues correspondant à une différence d'environ 0,5 ~ 0,8.

Pour étudier l'impact de la pellicule de surface sur les propriétés optiques d'une particule de BC,  $SAE_{BC\_CS}$  et  $AAE_{BC\_CS}$  ont été simulés avec un diamètre géométrique standard du noyau du BC de 100 nm ( $GMD_{core}=100$  nm), et une épaisseur variable de la pellicule ( $GMD_{shell}/GMD_{core} = 1\sim 3$ ). La dépendance spectrale du  $SAE_{BC\_CS}$  est similaire à celle du  $SAE_{BC}$  pur. La valeur du  $SAE_{BC\_CS}$  diminue avec l'augmentation de l'épaisseur de la pellicule de surface ( $GMD_{shell}/GMD_{core}$  croissant). Tout comme le  $SAE_{BC\_CS}$ ,  $AAE_{BC\_CS}$  dépend également beaucoup des couples de longueurs d'onde choisis.  $AAE_{BC\_CS}$  est plus grand lorsque l'on choisit des paires de longueurs d'onde plus longues. L'impact de la pellicule de surface est très limité et dépend lui-même de la taille du noyau de BC. En particulier, pour les noyaux relativement petits

( $GMD_{core} < 50$  nm) ou grands ( $GMD_{core} > 125$  nm),  $AAE_{BC\_CS}$  dépend à la fois de la taille du noyau et de l'épaisseur du revêtement. Cependant, lorsque la taille du noyau de BC se situe entre 50 et 125 nm,  $AAE_{BC\_CS}$  est faiblement influencé par l'épaisseur du revêtement.

Malgré cette variation importante, certaines études récentes (Olson et al., 2015) ont fait l'hypothèse d'une valeur de l' $AAE_{BC}$  fixe ( $AAE_{BC} = 1$ ). Pour évaluer les incertitudes sur le coefficient d'absorption de BC dues au choix de l' $AAE_{BC}$ , l'absorption de BC à 370 nm, par exemple, est calculée en utilisant différentes valeurs de  $AAE_{BC\_CS,370-880}$ . L'absorption de BC à 370 nm est déterminé en utilisant  $AAE_{BC\_CS,370-880}$ , puis  $AAE_{BC\_CS,370-880}$  égal à 1 et enfin  $AAE_{BC\_CS,370-880}$  égal à  $AAE_{BC\_CS,880-950}$ . Les résultats révèlent que l'utilisation de  $AAE_{BC\_CS,880-950}$  sur toute la gamme de longueurs d'onde entraîne des erreurs plus faibles pour l'absorption de BC, et donc de BrC, que l'utilisation d'une valeur constante de 1 lorsque  $GMD_{core}$  est supérieur à 76 nm ou inférieur à 28 nm. Alors qu'une valeur constante de 1 serait un meilleur choix pour  $AAE_{BC}$  si  $GMD_{core}$  se situe entre 38 et 72 nm.

#### **i.4. Conclusion**

Les résultats simulés révèlent que la SAE et l'AAE peuvent être influencés de manière significative par des couples de longueurs d'onde sélectionnées et par la taille des particules. Les résultats pourraient expliquer la controverse sur les valeurs seuils SAE et AAE utilisées pour classer les différents types d'aérosols. En particulier, la différence causée par les paires de longueurs d'onde devrait être prise en considération lors de l'utilisation du schéma SAE et AAE proposé par des études précédentes pour la classification des types d'aérosols. L'AAE du BC pur ou revêtu d'une enveloppe transparente n'est pas une constante, et elle dépend de la taille du noyau du BC et des paires de longueurs d'onde sélectionnées. Il convient de noter que l'épaisseur relative du revêtement a moins d'impact sur l'AAE pour une BC bien vieillie ( $125 \text{ nm} > GMD_{core} > 50 \text{ nm}$ ).

Dans l'étape suivante, les résultats de Mie sur la dépendance de l'AAE à la taille

du noyau de BC, à l'épaisseur du revêtement et aux paires de longueurs d'onde doivent être validés par une campagne en laboratoire dans des conditions contrôlées. Une campagne est déjà prévue en 2021 à l'institut PSI afin d'acquérir plus de connaissances sur (1) les propriétés optiques des aérosols et (2) les écarts des propriétés d'absorption, d'extinction et de diffusion mesurées par toutes les techniques disponibles au sein de la communauté scientifique. À ce moment-là, une tâche spécifique consisterait également à récupérer l'absorption de BC à différentes longueurs d'onde en utilisant différentes hypothèses d'AAE (par exemple égale à 1, AAE calculée sur la gamme spectrale d'intérêt ou sur la gamme spectrale proche de l'IR). Cette campagne de mesures est essentiel pour mieux estimer les compositions chimiques des aérosols à partir de mesures optiques.

## **ii. Étude sur la récupération de la composition chimique des aérosols basée sur la partie imaginaire de l'indice de réfraction complexe**

L'indice de réfraction complexe (IRC) est un paramètre intrinsèque de la composition chimique des aérosols, et indépendant de la taille des particules. La partie imaginaire de l'IRC ( $k$ ) est largement utilisée pour retrouver quantitativement les aérosols absorbants à partir de mesures de télédétection au sol (méthode basée sur le  $k$ ). L'idée principale est basée sur les différences de dépendance spectrale de  $k$  pour différentes espèces absorbantes. Le BC se distingue des autres espèces par sa forte absorption sur tout le spectre visible et par un  $k$  extrêmement plus grand que OC et MD. Pour distinguer OC et MD, la taille (Schuster et al., 2016a; Zhang et al., 2018) et la variation spectrale de l'albédo de diffusion unique (dSSA) (Wang et al., 2013) ont été utilisées comme paramètres supplémentaires à leurs propriétés spectrales d'absorption. Cependant, les méthodes basées sur  $k$  n'ont été appliquées qu'aux données obtenues par télédétection jusqu'à présent. Une étape de validation en comparaison avec des compositions directement mesurées est donc essentielle. Cette partie vise à étudier les méthodes basées sur  $k$ , et à examiner leurs performances en mettant en relation les restitutions AERONET intégrées sur la colonne des compositions chimiques des

aérosols avec l'inventaire du transport et des émissions régionales.

La méthode proposée par Li et al. (2013) est sélectionnée pour application et validation préliminaire dans notre étude. Cette méthode utilise  $k$ ,  $n$  et dSSA (appelée méthode  $k$ - $n$ -dSSA) pour extraire des données dntegrées sur la colonne de BC, BrC, MD, du sulfate d'ammonium (AS) et de la teneur en eau de l'aérosol (AW, annexe A2). La méthode  $k$ - $n$ -dSSA a été choisie parce que cette méthode permet de récupérer les principales compositions chimiques des aérosols dans l'atmosphère, et que les compositions chimiques des aérosols récupérées (BC, BrC, MD, AW et AS) peuvent être comparées avec les sources d'émission et l'analyse des retro-trajectoires des masses d'air. Une partie du contenu de ce chapitre a été publiée dans le journal of Atmospheric Environment.

### **ii.1. Site et méthode**

La capitale de la Chine, Pékin, située dans le nord de la plaine du nord de la Chine (PCN), a été choisie pour cette étude. La mer de Bohai se trouve au sud-est du site, ce qui amène de l'humidité à Pékin dans le flux de mousson (sud-est) en été. En hiver, les vents dominants sont généralement du nord-ouest. Les conditions géographiques et météorologiques produisent une variation saisonnière de la composition chimique des aérosols atmosphériques. Au printemps, les poussières minérales (MD) sont prédominantes. Trois principales régions d'émission de poussières sont situées au nord-ouest de Pékin. La combustion de biomasse au début de l'été et en automne et le chauffage au charbon en hiver dans le nord de la Chine entraînent des épisodes de pollution fréquents et graves avec une forte teneur en carbone dans les particules.

Pour obtenir les sources potentielles d'aérosols autour de Pékin, les inventaires d'émissions de l'Université de Pékin (<http://inventory.pku.edu.cn/>) ont été utilisés malgré le fait que les poussières minérales ainsi que les aérosols marins ne soient pas inclus. Les particules présentent une différence spatiale évidente, avec un niveau élevé dans la région du PCN, mais des émissions relativement faibles au nord et à l'ouest de Pékin. En été, l'émission de particules autour de Pékin est la plus faible, tandis que

l'émission de particules la plus élevée apparaît en hiver. De plus, les émissions de BC, OC et la somme de SO<sub>2</sub> et NO<sub>x</sub> ont des distributions spatiales similaires, avec l'émission la plus élevée au sud de Pékin ou en hiver tout autour de Pékin.

Le modèle Hybrid Single Particle Lagrangian Integrated Trajectory (HYSPLIT) développé par NOAA/ARL a été utilisé pour calculer les trajectoires des parcelles d'air. Les trajectoires rétrospectives de 72 heures se terminant à 500 m au-dessus du sol sur le site de Pékin ont été calculées chaque jour à 4 UTC. Pour obtenir des groupes bien séparés et bien représentatifs, les trajectoires ont été regroupées en fonction de la distance géométrique entre les trajectoires individuelles. Après avoir tenu compte de la nécessité d'avoir plus de groupes et des trajectoires bien séparées, les trajectoires ont été regroupées en 5 groupes pour différentes saisons dans ce travail. Au printemps, en automne et en hiver, une grande proportion (> 50 %) des trajectoires totales sont associées à des vitesses de vent plus élevées provenant du nord-ouest. Les groupes avec la vitesse la plus faible, sont principalement du sud au printemps et en automne, et du sud-est en hiver. Parmi les trois saisons, c'est en hiver que la fréquence des vents du sud est la plus faible, suivie par l'automne. En été, les groupes sont bien séparés en fonction de leur direction et les trajectoires provenant du nord-ouest sont moins nombreuses (21 %).

## **ii.2. Composants chimiques des aérosols de chaque groupe**

Afin de mieux connaître la composition chimique, intégrée sur la colonne, des aérosols, un algorithme d'inversion basé sur *le k-n-dSSA* (voir l'annexe A2) a été utilisé pour calculer les fractions volumiques et les concentrations massiques des différents types d'aérosols en fonction de leur origines au cours des quatre saisons.

Les concentrations massiques, intégrées sur la colonne, de BC augmentent généralement lorsque la vitesse de transport est faible. En general, les valeurs maximales sont atteintes pour les masses d'air provenant du sud de Pékin. En été, les masses d'air provenant du sud-est sont enrichies en BC (valeur moyenne de 0,0052 g m<sup>-2</sup>). La concentration en masse de BC augmente sensiblement en automne et en hiver,

et les valeurs en automne ( $0,0059 \text{ g m}^{-2}$ ) sont légèrement supérieures à celles observées en hiver ( $0,0056 \text{ g m}^{-2}$ ). Ce résultat n'est pas cohérent avec la variation saisonnière des émissions montrant qu'en hiver les concentrations de BC (environ  $1,7 \times 10^5 \text{ g km}^2 \text{ an}^{-1}$ ) sont considérablement plus importantes que celles émises pendant l'automne (environ  $1,2 \times 10^5 \text{ g km}^2 \text{ an}^{-1}$ ) autour de Pékin.

Les concentrations massiques de BrC sont les plus faibles en été et sont plus élevées en hiver ( $0,042 \text{ g m}^{-2}$ ) quelque soit l'origine des masses d'air. En outre, en hiver, les sources localisées dans les environs de Pékin sont dominantes et, de ce fait, les concentrations de BrC ne montrent aucune dépendance avec la vitesse de déplacement ou la trajectoire des masses d'air.

Les concentrations massiques de MD, intégrées sur la colonne, sont les plus élevées lorsque la vitesse des masses d'air sont les plus importantes, sauf en hiver. Au printemps, la concentration en masse des MD reste élevée pour tous les groupes de retro-trajectoires, atteignant une valeur moyenne maximale de  $0,951 \text{ g m}^{-2}$ . En effet, Sun (2005) et Yu et al (2013) montrent que les épisodes de poussière sont très fréquents pendant cette saison.

Les concentrations en AW sont clairement liées à la position géographique particulière de Pékin. En effet, les masses d'air humide sont transportées par le vent du sud-est et les masses d'air sèches par celui du nord-ouest. Les concentrations massiques moyennes d'AS ont une valeur maximale pour les masses d'air provenant du sud au printemps, en automne et en hiver, et du sud-est en été, en accord avec la distribution spatiale des émissions de  $\text{SO}_2$  et de  $\text{NO}_x$ .

### **ii.3. Conclusion**

D'une manière générale, la méthode *k-n-dSSA* est provisoirement vérifiée comme étant raisonnable, mais les résultats obtenus doivent être comparés avec les compositions chimiques mesurées directement. Ces mesures sont disponibles à la surface et parfois au-dessus de la colonne par des mesures aériennes. Étant donné que les mesures in situ en surface permettent une observation fiable des propriétés

physiques, optiques et chimiques des aérosols, l'application de la méthode  $k$ - $n$ - $dSSA$  ou d'une méthode modifiée basée sur la méthode  $k$  à la mesure in situ sera réalisable pour validation.

### **iii. Développement et application de la méthode $k$ - $\rho$ pour la campagne à Shouxian**

Les méthodes basées sur le paramètre  $k$  ont été développées pour prendre en compte la taille des aérosols ( $D_p$ ,  $dSSA$ ) afin de restituer quantitativement les concentrations des principaux types d'aérosols présents dans l'atmosphère. Cependant, les observations de la composition chimique des aérosols en fonction de la taille montre que même si les MD sont le principal contributeur pour le mode grossier, il y a toujours une fraction non négligeable de OC dans le mode grossier. C'est pourquoi l'utilisation uniquement de paramètres liés à la taille (par exemple,  $dSSA$ ) peut générer des incertitudes importantes aux restitutions. D'autres paramètres indépendants doivent être trouvés pour limiter davantage ce problème. En outre, les études actuelles utilisant ces méthodes sont toutes appliquées à des mesures de télédétection et ne peuvent être validées du à l'absence de comparaison avec des mesures de la composition chimique des aérosols intégrées sur l'ensemble de la colonne.

Bien que les mesures in situ soient géographiquement limitées, leurs grandes variétés permettent de mesurer les propriétés physiques, chimiques et optiques des aérosols. La synergie entre toutes ces mesures disponibles offre des possibilités de réaliser des études de fermeture. Par conséquent, cette étude vise à améliorer les méthodes basées sur le paramètre  $k$  en l'appliquant aux mesures in-situ et en utilisant de nouveaux paramètres pour efficacement distinguer MD et OC. On réalisera une étude de fermeture de la composition chimique des aérosols en comparant les restitutions aux mesures in-situ.

Comme la densité de OC ( $1,2 \text{ g cm}^{-3}$ , Rissler et al., 2014) est nettement inférieure à celle des MD ( $2,6 \text{ g cm}^{-3}$ , Wagner et al., 2012), il pourrait être un excellent candidat pour distinguer les principales espèces d'aérosols. C'est pourquoi nous avons introduit

$\rho$  comme paramètre supplémentaire dans l'algorithme de restitution de la composition chimique des aérosols, appelé méthode  $k$ - $\rho$ .

### iii.1. Site et méthode

Les observations ont été faites à la station de Shouxian (32,56 °N, 116,78 °E), site rural entouré de terres agricoles, et est peu affecté par la pollution urbaine, industrielle et routière. Les instruments utilisés pour les mesures des propriétés physiques et optiques des aérosols secs (PM<sub>2.5</sub>) comprennent le Scanning Mobility Particle Sizer (SMPS), l'Aerodynamic Particle Sizer (APS) et le Cavity Enhanced Albedometer (CEA) à 365 et 532 nm. En outre, des échantillons de filtres ont été collectés et analysés pour obtenir la composition chimique des aérosols. Les paramètres météorologiques (vitesse et direction du vent) ont été obtenus à partir d'une station météorologique automatique pendant la campagne de terrain.

Nous avons obtenu la densité effective des aérosols ( $\rho_e$ ) en fusionnant la distribution du nombre et de la taille des particules (PNSD) des données SMPS et APS. En effet, ces deux instruments mesurent la distribution de la taille des aérosols en se concentrant sur les particules fines (diamètre de mobilité,  $D_m$ , dans 14 - 661 nm) et grossières (diamètre aérodynamique,  $D_a$ , dans 523 - 2458 nm) respectivement. Par principe, les distributions en taille ( $dN/d\log(D_p)$ ) issues des mesures du SMPS et de l'APS peuvent être fusionnées en prenant en compte la densité des particules. Cette dernière ( $\rho_e$ ) est calculée par ajustement linéaire de  $D_m^2$  et  $D_{a,inter}^2$  avec une interception forcée à 0 (figure 2.3). L'erreur associée à la pente est considérée comme l'erreur de densité effective ( $\varepsilon_{\rho_e}$ ).

Un code Mie a été utilisé pour construire un tableau des coefficients d'extinction et de diffusion pour différentes parties réelles et imaginaires de l'IRC. Puis, ces coefficients d'extinction et de diffusion sont comparés avec les mesures afin de trouver l'IRC correspondant le mieux aux aérosols observés. Les erreurs pour  $n_{Mie,365}$ ,  $k_{Mie,365}$ ,  $n_{Mie,532}$  et  $k_{Mie,532}$  sont estimées en utilisant toutes les valeurs des solutions "acceptables".

Sur la base d'études antérieures, un nouvel algorithme (méthode  $k-\rho$ ) a été mis au point pour récupérer les principaux composés des aérosols secs, notamment le BC, la matière organique (OM), le MD et le SNA. Parmi eux, la fraction de masse ou de volume de la OM peut être convertie en OC à l'aide d'un facteur relié à l'écart de densité entre ces deux composés (1,6 pour cette étude, Xing et al., 2013). Plus précisément, la partie imaginaire de l'IRC à 365 et 532 nm a été utilisée pour distinguer le BC du SNA puis les OC des MD. Parallèlement, un tableau a été élaboré avec des fractions volumique supposées allant de 0 à 1 avec des pas de 0,01 %, 0,1 % et 0,1 % pour BC, OC et SNA, respectivement. La fraction volumique de MD était calculé par différence entre la concentration totale et la somme des concentrations BC, OC et SNA.  $\rho_{VAM}$  a été calculée avec le modèle de mélange moyen en volume (VAM), qui est un modèle simple mais largement utilisé pour calculer la densité des aérosols et l'indice de réfraction à partir des propriétés des composés purs. Comme l'hypothèse de particules homogènes et sphériques a été utilisée pour cette étude,  $\rho_{VAM}$  est équivalent à  $\rho_m$  et  $\rho_e$ . De la même manière,  $k_{VAM,365}$  et  $k_{VAM,532}$  ont été calculées à l'aide de la VAM. Les sorties de l'algorithme représentent les solutions optimales correspondant donc à des fractions volumiques des composants calculés avec la VAM. Avec les fractions volumiques extraites, la concentration massique pour chaque espèce ( $MC_{ii}$ ) peut être calculée avec la densité des aérosols et la concentration volumique des particules.

### iii.2. Résultats de la mesure et de l'extraction

Pendant la campagne, les coefficients d'extinction, de diffusion et d'absorption des aérosols ( $b_{ext}$ ,  $b_{scat}$  et  $b_{abs}$ ) mesurés à 365 nm étaient en moyenne d'environ  $451 \pm 229$   $Mm^{-1}$  (compris entre 74 et 1112  $Mm^{-1}$ ),  $384 \pm 200$   $Mm^{-1}$  (compris entre 63 et 951  $Mm^{-1}$ ),  $67 \pm 32$   $Mm^{-1}$  (compris entre 11 et 189  $Mm^{-1}$ ), respectivement. Le SSA a ensuite été récupéré en moyenne à  $0,85 \pm 0,027$  (compris entre 0,67 et 0,9) à 365 nm. À 532 nm, les valeurs moyennes de  $b_{ext}$ ,  $b_{scat}$  et  $b_{abs}$  sont en général plus basses, autour de  $353 \pm 197$   $Mm^{-1}$ ,  $317 \pm 180$   $Mm^{-1}$ ,  $36 \pm 20$   $Mm^{-1}$  respectivement. À cette longueur d'onde, la moyenne du SSA ( $0,89 \pm 0,025$ ) est un peu plus élevée. Deux périodes de pollution

différentes, appelées P1 (de 15:00 LT le 7 décembre à 13:00 LT le 8 décembre) et P2 (de 16:00 LT le 8 décembre à 11:00 LT le 9 décembre), ont été sélectionnées pour une analyse plus approfondie. Une période claire marquée, appelée P3, a également été sélectionnée pour être comparée aux épisodes de pollution (de 21h00 LT le 9 décembre à 15h00 LT le 11 décembre). La période P3 a été associée à une vitesse de vent élevée et stable d'environ  $5 \text{ m s}^{-1}$ , et aux valeurs les plus basses de  $b_{ext}$  et  $b_{scat}$ .

La valeur moyenne dérivée de  $\rho_e$  est de  $1,67 \pm 0,15 \text{ g cm}^{-3}$ , et l'erreur moyenne de  $\rho_e$  était de  $0,034 \text{ g cm}^{-3}$ . Les valeurs moyennes de l'IRC étaient de  $1,39 (\pm 0,04) + 0,025 (\pm 0,004) i$  à  $365 \text{ nm}$  et de  $1,47 (\pm 0,05) + 0,018 (\pm 0,004) i$  à  $532 \text{ nm}$ . Les erreurs moyennes pour  $n_{Mie,365}$ ,  $k_{Mie,365}$ ,  $n_{Mie,532}$  et  $k_{Mie,532}$  étaient de  $0,003$ ,  $0,002$ ,  $0,002$  et  $0,002$ . La variation de  $n_{Mie}$  est en phase avec  $\rho_e$  en général.

Les contributions de masse récupérées de BC (mBC), OM (mOM), MD (mMD) et SNA (mSNA) pour l'ensemble de la période d'observation étaient de  $1,7 \%$ ,  $28,8 \%$ ,  $25,3 \%$  et  $44,2 \%$ , avec des incertitudes de  $35,5 \%$ ,  $38 \%$ ,  $61,5 \%$  et  $54 \%$  respectivement. Pendant P1, les concentrations massiques moyennes étaient de  $3,5$ ,  $52,4$ ,  $15,7$  et  $106,3 \mu\text{g m}^{-3}$  pour BC, OM, MD et SNA. La fraction du SNA était la plus importante, avec  $59,7 \%$ . Alors que les rapports de masse de BC, OM et MD étaient de  $2 \%$ ,  $29,5 \%$  et  $8,8 \%$ , respectivement. Leurs incertitudes moyennes étaient respectivement de  $27 \%$ ,  $32 \%$ ,  $152 \%$  et  $34 \%$  en raison de l'incertitude de  $\rho_e$ ,  $k_{Mie,365}$  et  $k_{Mie,532}$ . Les incertitudes élevées de MD sont liées à ses faibles concentrations massiques. Pendant la période P2, les concentrations massiques moyennes pour BC, OM, MD et SNA étaient de  $2,47$ ,  $50,3$ ,  $23,2$  et  $70,3 \mu\text{g m}^{-3}$ , avec des incertitudes de  $46 \%$ ,  $36 \%$ ,  $90 \%$  et  $49 \%$ , séparément. Le SNA était toujours le principal contributeur pour la concentration massique totale ( $48\%$ ), même si sa contribution était beaucoup plus faible que celle observée pendant la période P1. Pendant la période P3, les concentrations massiques d'aérosols pour chaque composé  $w$  étaient faibles et en moyenne de l'ordre de  $0,46$ ,  $14,3$ ,  $9,2$  et  $15,8 \mu\text{g m}^{-3}$  pour BC, OM, MD, et SNA, respectivement. Les incertitudes moyennes correspondantes étaient de  $59\%$ ,  $42\%$ ,  $103\%$  et  $87\%$ . Les erreurs relatives sont plus importantes que celles calculées pendant P1 et P2 pour BC, OM, MD, et SNA,

principalement en raison de concentrations massiques plus faibles. Comme la direction et la vitesse du vent étaient stables, la concentration massique de MD était également assez stable. Par rapport aux périodes polluées, la fraction SNA a diminué à 39,7 %, tandis que la fraction MD a augmenté à 23,1 %.

### **iii.3. Comparaison de la composition chimique des aérosols à partir de la récupération et de la mesure**

Pour vérifier la faisabilité de la méthode  $k$ - $\rho$ , les concentrations massiques récupérées sont comparées aux compositions chimiques mesurées des aérosols fournies par l'analyse des échantillons de filtres. La moyenne des concentrations massiques totales obtenues par extraction ( $mSum_{retr}$ ) et par mesure ( $mSum_{meas}$ ) était respectivement de  $98 \pm 47$  et  $98 \pm 44 \mu\text{g m}^{-3}$ , ce qui donne confiance dans les résultats de l'algorithme. De plus, les concentrations massiques de chaque composé récupérées et mesurées étaient également très proches. Les concentrations massiques récupérées (mesurées) de BC, OM, MD et SNA sont de  $1,6 \pm 1,02$  ( $1,9 \pm 0,9$ ),  $28 \pm 17$  ( $27 \pm 12$ ),  $25 \pm 20$  ( $22 \pm 15$ ) et  $43 \pm 34$  ( $44 \pm 23$ )  $\mu\text{g m}^{-3}$ .

Les valeurs moyennes et les écarts types des concentrations massiques extraites ont été calculés sur la période d'échantillonnage du filtre (11,5h).  $mSum_{retr}$  et  $mSum_{meas}$  étaient en assez bon accord avec  $R^2$  de 0,93 et la pente de 0,85.  $mBC_{retr}$  et  $mEC_{meas}$  étaient également globalement cohérents ( $R^2=0,5$ , pente= 0,67). Cette faible corrélation pourrait s'expliquer par le fait que la BC a été calculée par une méthode optique, alors que la EC a été mesurée par une méthode thermique/optique.  $mOM_{retr}$  et  $mOM_{meas}$  étaient en bon accord ( $R^2 =0,8$ , pente=0,88).  $mMD_{retr}$  et  $mMD_{meas}$  étaient en plus faible accord que les trois autres espèces, surtout pendant les 5-6 décembre, et la corrélation linéaire pour les concentrations massiques MD était modérée ( $R^2=0,43$ , pente=0,62). Comme les concentrations massiques MD ont été calculées à partir d'une différence entre la concentration massique totale et la concentration massique de quelques espèces (BC, OM et SNA), elles pourraient également inclure des sels marins, des métaux et d'autres composés non spécifiés.  $mSNA_{retr}$  et  $mSNA_{meas}$  étaient assez concordants

( $R^2=0,87$ , pente=0,99) pour les périodes propres et polluées.

### iii.4. Sensibilité aux intrants a priori

Nous avons effectué des tests de sensibilité complets pour estimer les incertitudes sur les concentrations massiques récupérées. Le test numérique a révélé que les fractions de composition connues supposées étaient fortement liées aux compositions extraites avec ( $R^2 > 0,99$ ) pour les quatre espèces, ce qui indique la faisabilité de l'algorithme. Un test de sensibilité a été effectué pour étudier l'impact de la composition chimique des aérosols récupérés à partir a priori  $\rho_m$ ,  $k_{365}$ ,  $k_{532}$  et du rapport OM/OC pour le niveau moyen et les événements dominés par OM, MD et SNA. Les compositions chimiques des aérosols retrouvés dépendent fortement de la sélection du  $k_{OC}$  pour presque tous les cas, probablement en raison de seuils extrêmes. Les grandes incertitudes causées par les  $k_{OC}$  dans cette étude sont comparables au résultat de Schuster et al. (2016) selon lequel le biais du BrC pourrait varier de 50 % à 440 % en raison de la sélection des  $k_{OC}$ . Parmi les quatre espèces, c'est la BC qui est la moins sensible à ces facteurs. En effet, les incertitudes associées à la mBC à partir des apports a priori, à l'exception des  $k_{OC}$ , sont inférieures à 48% dans tous les cas. Par conséquent, une meilleure limitation de l'IRC des aérosols, en particulier pour le OC, réduira les incertitudes liées aux apports a priori.

### iii.5. Conclusion

Dans cette étude, nous avons développé la méthode  $k-\rho$  pour récupérer les concentrations massiques de BC, OM, MD et SNA sèches en se basant sur des observations in-situ. Cet algorithme a été utilisé pour obtenir la variation en temps réel de la composition chimique des aérosols lors d'une campagne d'observation à Shouxian. Les compositions chimiques des aérosols retrouvées étaient cohérentes avec les mesures in-situ. La concordance plus faible ( $R^2=0,43$ ) du MD par rapport aux autres espèces est due aux incertitudes plus importantes des récupérations et des mesures. En réduisant les incertitudes de mesure de PNSD,  $b_{ext}$  et  $b_{scat}$ , en améliorant la précision des valeurs  $\rho_m$  et  $k$  de chaque composant chimique, et en considérant la morphologie et

l'état de mélange des aérosols, la précision de la récupération peut être encore améliorée. Il est recommandé de procéder à des observations complètes et à long terme sur le terrain en différents endroits afin de valider l'applicabilité de ce nouvel algorithme.

**Mots clés:** compositions chimiques des aérosols; Ångström exposant; indice de réfraction complexe; densité d'aérosol; mesure in situ; télédétection

## Appendix

### A1 Mie theory

If particle size is close to or larger than the incident wavelength, most of the light goes as original direction, which is called Mie scattering. In atmosphere, aerosol particles' interaction with light from UV to mid-infrared spectrum could be explained by Mie scattering. Mie theory was firstly developed by Gustav Mie, and concept of this theory could be explained by a plane wave of light incident on a sphere (figure A1), detailed discussion of Mie theory could be found from Van de Hulst (1957).

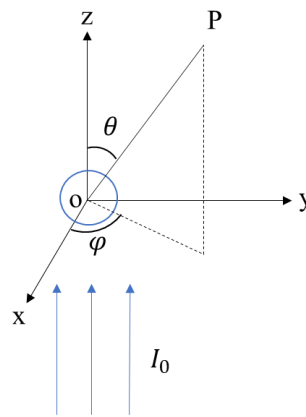


Figure A1.1 Coordinate centred on the spherical particle with radius of  $r$ .

As shown in figure A1.1, when the light with intensity of  $I_0$  and wavelength of  $\lambda$  incident to a particle with radius of  $r$ , the vertical and horizontal scattered light intensity ( $I_{vv}$  and  $I_{hh}$ ) at the direction of  $(\theta, \varphi)$  could be calculated by equation A1 and A2:

$$I_{hh} = \frac{\lambda^2 i_1(\theta) I_0 \sin^2 \varphi}{4\pi^2 r^2} \quad \text{A1}$$

$$I_{vv} = \frac{\lambda^2 i_2(\theta) I_0 \cos^2 \varphi}{4\pi^2 r^2} \quad \text{A2}$$

And the total scattered light intensity ( $I_s$ ) is the sum of  $I_{vv}$  and  $I_{hh}$ :

$$I_s = I_{hh} + I_{vv} = \frac{\lambda^2 I_0}{4\pi^2 r^2} (i_1(\theta) \sin^2 \varphi + i_2(\theta) \cos^2 \varphi) \quad A3$$

Where  $i_1$  and  $i_2$  are the function of scattered light intensity, which are the square of the function of scattered light amplitudes ( $S_1$  and  $S_2$ ):

$$i_1(\theta) = |S_1(\theta)|^2, i_2(\theta) = |S_2(\theta)|^2 \quad A4$$

$S_1$  and  $S_2$  could be calculated with equation A-5 and A-6:

$$S_1 = \sum_{n=1}^{n=\infty} \frac{2n+1}{n(n+1)} (a_n \pi_n + b_n \tau_n) \quad A5$$

$$S_2 = \sum_{n=1}^{n=\infty} \frac{2n+1}{n(n+1)} (a_n \tau_n + b_n \pi_n) \quad A6$$

Where  $a_n$  and  $b_n$  are the Mie coefficients (equation A7 and A8), and they are the function of complex refractive index ( $m$ ) and size parameter ( $x$ ).  $\pi_n$  and  $\tau_n$  are determined by scattering angle  $\theta$  (equation A9 and A10).

$$a_n = \frac{\phi_n(x) \phi_n'(mx) - m \phi_n'(x) \phi_n(mx)}{\zeta_n(x) \phi_n'(mx) - m \zeta_n'(x) \phi_n(mx)} \quad A7$$

$$b_n = \frac{m \phi_n(x) \phi_n'(mx) - \phi_n'(x) \phi_n(mx)}{m \zeta_n(x) \phi_n'(mx) - \zeta_n'(x) \phi_n(mx)} \quad A8$$

$$\pi_n = \frac{P_n^{(1)}(\cos \theta)}{\sin \theta} \quad A9$$

$$\tau_n = \frac{dP_n^{(1)}(\cos \theta)}{d\theta} \quad A10$$

$\phi_n$  and  $\zeta_n$  are two Ricatti-Bessel functions defined by the first kind half-integer-order Bessel function ( $J_n$ ) (equation A11) and the second kind of half-integer-order Bessel function ( $H_n$ ) (equation A12) respectively, and  $\phi_n'$  and  $\zeta_n'$  are the first order

differential function (equation A13 and A14).  $P_n(\cos(\theta))$  is the Legendre function, and  $P_n^{(l)}(\cos(\theta))$  is the association Legendre function.

$$\phi_n(z) = \left(\frac{z\pi}{2}\right)^{1/2} J_n + \frac{1}{2}(z) \quad \text{A11}$$

$$\zeta_n(z) = \left(\frac{z\pi}{2}\right)^{\frac{1}{2}} H_n^2 + \frac{1}{2}(z) \quad \text{A12}$$

$$\phi_n' = \frac{d\phi_n(z)}{dz} \quad \text{A13}$$

$$\zeta_n' = \frac{d\zeta_n(z)}{dz} \quad \text{A14}$$

The extinction and scattering efficiency ( $Q_{ext}$  and  $Q_{scat}$ ) are determined with  $a_n$  and  $b_n$ :

$$Q_{ext} = \frac{2}{x^2} \sum_{n=1}^{\infty} [(2n+1) \text{Re}(a_n + b_n)] \quad \text{A15}$$

$$Q_{scat} = \frac{2}{x^2} \sum_{n=1}^{\infty} [(2n+1) (|a_n|^2 + |b_n|^2)] \quad \text{A16}$$

Then the absorption efficiency ( $Q_{abs}$ ) is the difference of  $Q_{ext}$  and  $Q_{scat}$ :

$$Q_{abs} = Q_{ext} - Q_{scat} \quad \text{A17}$$

Mie theory was also extended for coated particles by imposing boundary conditions between the 1<sup>st</sup> and 2<sup>nd</sup> media as well as the 2<sup>nd</sup> medium and the containing medium. Detailed description could be found from Bohren and Huffman (2007).

## A2 Aerosol chemical composition retrieval with $n$ , $k$ and dSSA

An optimization function by weighting of the four kinds of input information  $\Psi(\varepsilon_n, \varepsilon_{k,blue}, \varepsilon_{k,red}, \varepsilon_{dSSA})$  was used to find the best solution of the chemical fraction, where  $\varepsilon_n$ ,  $\varepsilon_{k,blue}$ ,  $\varepsilon_{k,red}$  and  $\varepsilon_{dSSA}$  were defined as equation A18 ~ A21, and the ‘‘rank position’’ priority strategy was used to find the optimal solution (Li et al., 2013).

$$\varepsilon_n = \frac{|n_{cal} - n_{Aero}|}{n_{Aero}} \quad \text{A18}$$

$$\mathcal{E}_{k,blue} = \frac{|k_{cal,blue} - k_{Aero,blue}|}{k_{Aero,blue}} \quad A19$$

$$\mathcal{E}_{k,red} = \frac{|k_{cal,red} - k_{Aero,red}|}{k_{Aero,red}} \quad A20$$

$$\mathcal{E}_{dSSA} = \frac{|dSSA_{cal} - dSSA_{Aero}|}{|dSSA_{Aero}|} \quad A21$$

$n_{Aero}$ ,  $k_{Aero,blue}$ ,  $k_{Aero,red}$  and  $dSSA_{Aero}$  were obtained directly from AERONET.  $n_{Aero}$  is the average value of the real part of CRI across four bands (440, 675, 870, and 1020 nm) from AERONET inversion products,  $k_{Aero,blue}$  is the imaginary part of CRI at 440 nm,  $k_{Aero,red}$  is the imaginary part of CRI from 675 to 1020 nm, and  $dSSA_{Aero}$  ( $SSA_{Aero,870} - SSA_{Aero,675}$ ) is the spectral variation of SSA at 675 and 870 nm, which can be used to distinguish BrC and MD.

The calculated values,  $n_{VAM}$ ,  $k_{VAM,blue}$ ,  $k_{VAM,red}$ , and  $dSSA_{VAM}$  were calculated by applying the VAM model:

$$n_{VAM} = \sum_{ii=1}^5 f_{ii} n_{ii} \quad A22$$

$$k_{VAM,blue} = \sum_{ii=1}^5 f_{ii} k_{ii,blue} \quad A23$$

$$k_{VAM,red} = \sum_{ii=1}^5 f_{ii} k_{ii,red} \quad A24$$

$$dSSA_{VAM} = \frac{\sum_{ii=1}^3 MAE_{ii,675} \cdot \rho_{m,ii} \cdot f_{ii} \cdot V_{total}}{\tau_{ext,675}} - \frac{\sum_{ii=1}^3 MAE_{ii,870} \cdot \rho_{m,ii} \cdot f_{ii} \cdot V_{total}}{\tau_{ext,870}} \quad A25$$

Where  $n_{ii}$ ,  $k_{ii,blue}$  and  $k_{ii,red}$  represent the real and imaginary parts of the CRI of each component at wavelength  $\lambda$ ,  $ii$  indicates one of the five components, and  $f_{ii}$  is the volume fraction for component  $ii$ . For equation A25,  $ii$  represents the three main absorbing

components, and  $V_{total}$  is the total columnar volume concentration of the aerosol mixture.  $\tau_{ext,675}$  and  $\tau_{ext,870}$  is the AOT at 675 and 870 nm,  $MAE_{ii,675}$  and  $MAE_{ii,870}$  are the mass absorption efficiency for each composition at 675 and 870 nm, and  $\rho_{m,ii}$  is the mass density for each component. The related parameters for each composition are listed in table A2.1 (Li et al., 2015).

Table A2.1 CRI, MAE and density for each composition used in this study (Li et al., 2015).

Types	$n$	$k_{blue}$	$k_{red}$	MAE(675nm)	MAE(870nm)	$\rho_m$ (g cm <sup>-3</sup> )
BC	1.95	0.66	0.66	8.14	6.32	2
OC	1.53	0.063	0.005	0.067	0.05	1.8
MD	1.57	0.01	0.004	0.045	0.035	2.6
AS	1.53	0	0	0	0	2.3
AW	1.33	0	0	0	0	1

### A3 Emission distributions of BC, OC and SO<sub>2</sub>+NO<sub>x</sub>

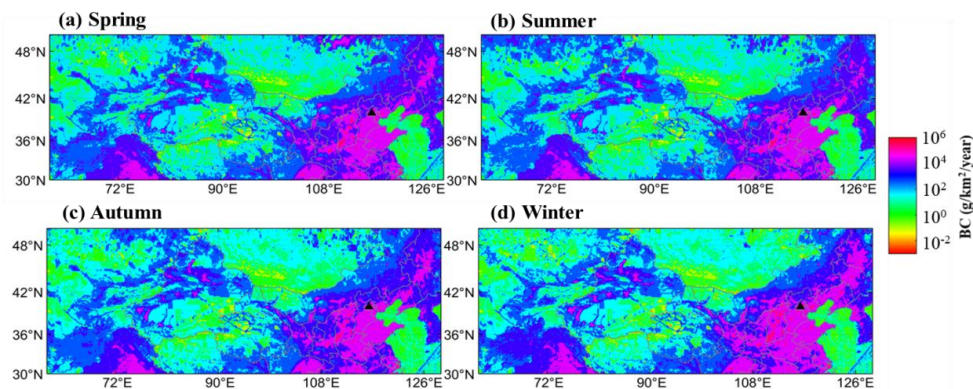


Figure A3.1 Spatial distribution of BC emission in the four seasons from 2005 to 2014.

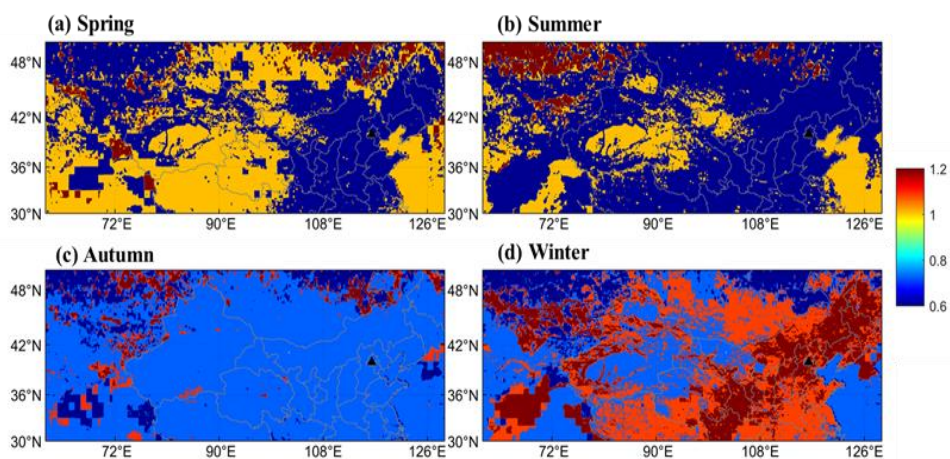


Figure A3.2 Spatial distribution of the ratio of seasonal mean BC emission to the total average BC emission from 2005 to 2014.

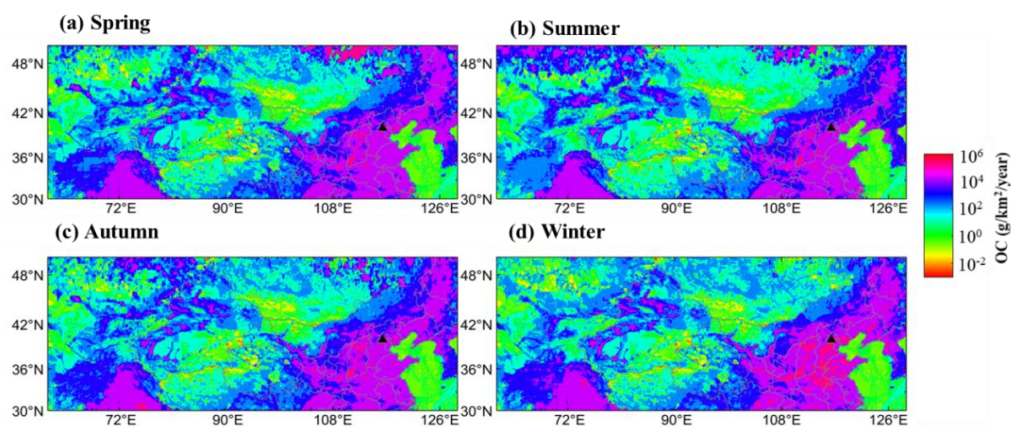


Figure A3.3 Spatial distribution of OC emission in the four seasons from 2005 to 2014.

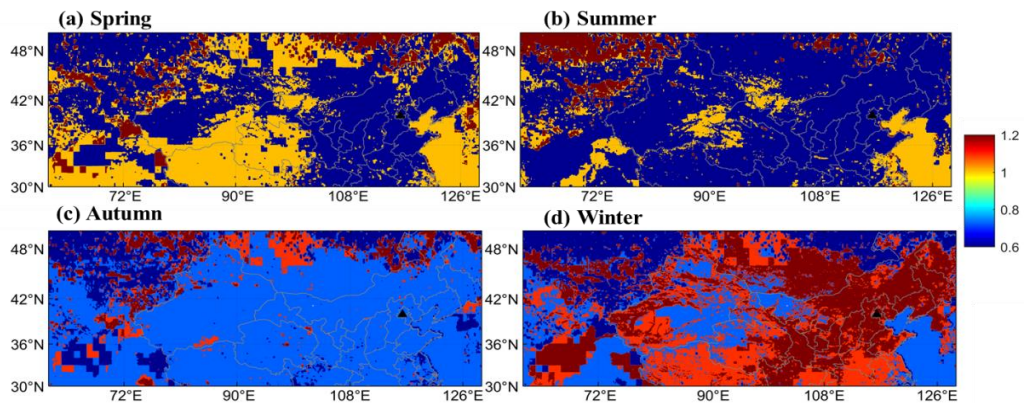


Figure A3.4 Spatial distribution of the ratio of seasonal mean OC emission to the total average OC emission from 2005 to 2014.

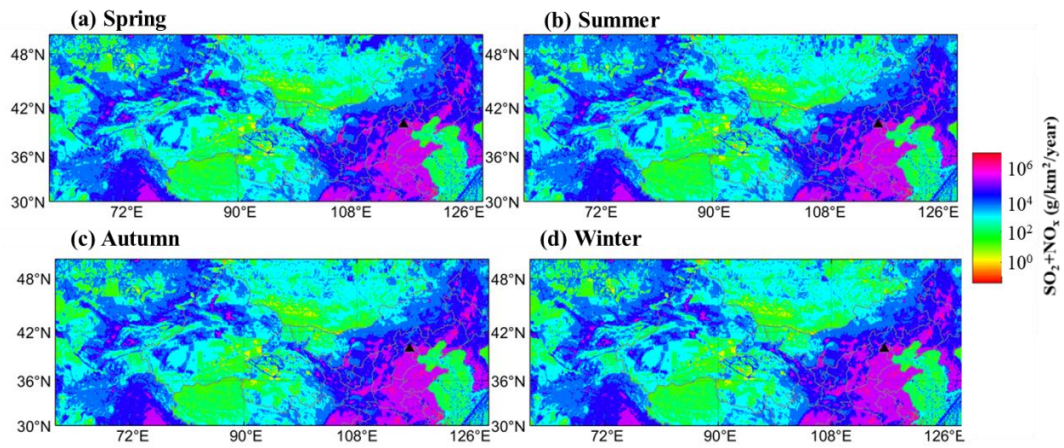


Figure A3.5 Spatial distribution of primary  $\text{SO}_2+\text{NO}_x$  emission in the four seasons from 2005 to 2014.

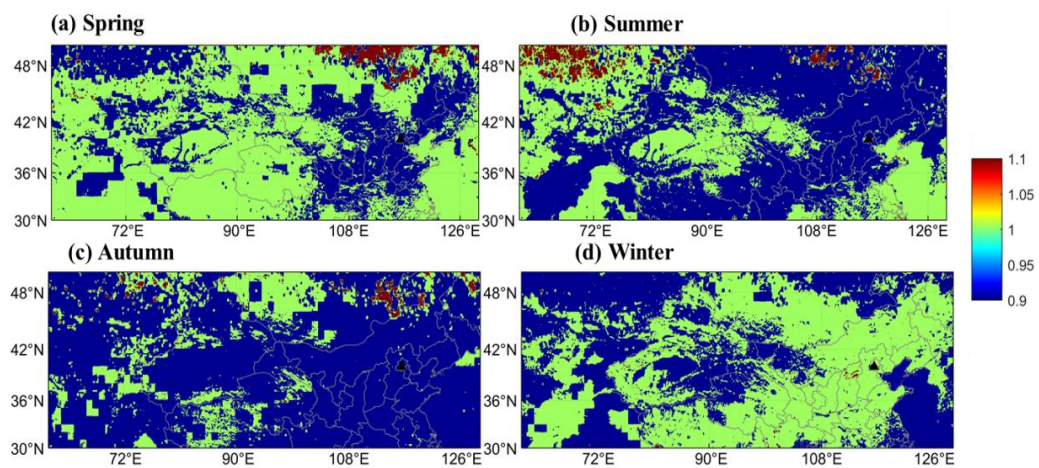


Figure A3.6 Spatial distribution of the ratio of seasonal mean  $\text{SO}_2+\text{NO}_x$  emission to the total average  $\text{SO}_2+\text{NO}_x$  emission from 2005 to 2014.

## Abbreviations and Acronyms

### A

AAE	Absorption Ångström exponent
AAE <sub>BC</sub>	AAE for Black Carbon
AAE <sub>BC_CS</sub>	AAE for Black Carbon coated with Clear Shell
AAE <sub>BrC</sub>	AAE for Brown Carbon
AAE <sub>MD</sub>	AAE for Mineral Dust
AAOT	Absorption Aerosol Optical Thickness
ACSM	Aerosol Chemical Speciation Monitor
AE	Ångström Exponent
AERONET	AERosol RObotic NETwork
AI	Aerosol Index
AMS	Aerosol Mass Spectrometer
AOT	Aerosol Optical Thickness
APS	Aerodynamic Particle Sizer
AS	Ammonium Sulfate
AW	Aerosol Water Content

### B

BC	Black Carbon
BR	Bruggeman
BrC	Brown carbon

### C

CCN	Cloud Condensation Nuclei
CEAS	Cavity Enhanced Absorption Spectroscopy
CEA	Cavity Enhanced Albedometer
CPC	Condensation Particle Counter
CRDS	Cavity Ring Down Spectroscopy
CRI	Complex Refractive Index

C-S	Core-Shell
CS	Clear shell
<b>D</b>	
DMA	Differential Mobility Analyser
dSSA	spectral variation of SSA
<b>E</b>	
EAE	Extinction Ångström exponent
EC	Elemental Carbon
<b>G</b>	
GDAS	Global Data Assimilation System
GMD	Geometric Mean Diameter
GMD <sub>BC</sub>	GMD of BC without coating
GMD <sub>BrC</sub>	GMD of BrC
GMD <sub>c</sub>	GMD of MD for coarse mode
GMD <sub>core</sub>	GMD of BC core with non-absorbing coating
GMD <sub>f</sub>	GMD of MD for fine mode
GMD <sub>shell</sub>	GMD of BC coating shell
GSD	Geometric Standard Deviation
<b>H</b>	
HGF	Hygroscopic Growth Factor
HYSPLIT	Hybrid Single Particle Lagrangian Integrated Trajectory model
<b>I</b>	
IBBCEAS	Incoherent Broad-Band Cavity-Enhanced Absorption Spectroscopy
IPCC	Intergovernmental Panel on Climate Change
ISIN	Integrating Sphere Integrated Nephelometer
<b>M</b>	

MAAP	Multi-Angle Absorption Photometer
MAE	Mass Absorption Efficiency
mBC <sub>retr</sub>	Mass concentration of BC from retrieval
MC	Mass Concentration
MD	Mineral Dust
mEC <sub>meas</sub>	Mass concentration of EC from measurement
MEE	Mass Extinction Efficiency
MG	Maxwell Garnett
mMD <sub>meas</sub>	Mass concentration of MD from measurement
mMD <sub>retr</sub>	Mass concentration of MD from retrieval
MODIS	Moderate Resolution Imaging Spectro-radiometer
mOM <sub>meas</sub>	Mass concentration of OM from measurement
mOM <sub>retr</sub>	Mass concentration of OM from retrieval
MSE	Mass scattering efficiency
mSNA <sub>meas</sub>	Mass concentration of SNA from measurement
mSNA <sub>retr</sub>	Mass concentration of SNA from retrieval
mSum <sub>meas</sub>	Sum of the mass concentrations of BC, OM, MD, and SNA from measurement
mSum <sub>retr</sub>	Sum of the mass concentrations of BC, OM, MD, and SNA from retrieval

## **N**

NCP	North China Plain
NW	Northwest

## **O**

OC	Organic Carbon
OM/OC	Ratio of OM to OC
OPC	Optical Particle Counter

## **P**

PAS	photoacoustic spectroscopy
PNSD	Particle Number Size Distribution
POM	Primary Organic Matter
PSAP	Particle/Soot Absorption Photometer
PSL	PolyStyrene Latex
<b>R</b>	
RH	Relative Humidity
<b>S</b>	
S	South
SAE	Scattering Ångström exponent
SAE <sub>BC</sub>	SAE for Black Carbon
SAE <sub>BC_CS</sub>	SAE for Black Carbon coated with Clear Shell
SAE <sub>BrC</sub>	SAE for Brown Carbon
SAE <sub>MD</sub>	SAE for Mineral Dust
SAOT	Scattering Aerosol Optical Thickness
SE	Southeast
SMPS	Scanning Mobility Particle Sizer
SNA	Sum of Sulfate, Nitrate and Ammonium
SOA	Secondary Organic Aerosols
SP2	Single Particle Soot Photometer
SP-AMS	Soot Particle Aerosol Mass Spectrometer
SPH	Sphericity
SS	Sea Salt
SSA	Single scattering albedo
SV	Spatial Variance
SW	Southwest
<b>T</b>	
ToF-AMS	Time-of-Flight Aerosol Mass Spectrometer

TSP	Total Suspended Particles
TSV	Total Spatial Variance
<b>U</b>	
UV	Ultraviolet
<b>V</b>	
VAM	Volume Average Mixing
VF	Volume Fractions
VFC	Volume Fraction ratio of fine to Coarse mode
<b>W</b>	
WD	Wind Direction
WIOM	Water Insoluble Organic Matter
WS	Wind Speed
WSOM	Water Soluble Organic Matter

## Reference

- Alonso, M., Alguacil, F.J., Martin, M.I., Kousaka, Y., Nomura, T., 1999. Aerosol particle size growth by simultaneous coagulation and condensation with diffusion losses in laminar flow tubes. *J. Aerosol Sci* 30, 1191-1199. doi:10.1016/S0021-8502(99)00020-8
- Andreae, M.O., Jones, C.D., Cox, P.M., 2005. Strong present-day aerosol cooling implies a hot future. *Nature*. 435, 1187-1190. doi:10.1038/nature03671
- Arnott, W.P., 2003. Photoacoustic and filter-based ambient aerosol light absorption measurements: Instrument comparisons and the role of relative humidity. *J. Geophys. Res.* 108. doi:10.1029/2002jd002165
- Arnott, W.P., Hamasha, K., Moosmüller, H., Sheridan, P.J., Ogren, J.A., 2005. Towards Aerosol Light-Absorption Measurements with a 7-Wavelength Aethalometer: Evaluation with a Photoacoustic Instrument and 3-Wavelength Nephelometer. *Aerosol Sci. Technol.* 39, 17-29. doi:10.1080/027868290901972
- Arola, A., Schuster, G., Myhre, G., Kazadzis, S., Dey, S., Tripathi, S.N., 2011. Inferring absorbing organic carbon content from AERONET data. *Atmos. Chem. Phys.* 11, 215-225. doi:10.5194/acp-11-215-2011
- Bahadur, R., Praveen, P.S., Xu, Y., Ramanathan, V., 2012b. Solar absorption by elemental and brown carbon determined from spectral observations. *Proc. Natl. Acad. Sci. U. S. A.* 109, 17366. doi:10.1073/pnas.1205910109
- Bauer, S.E., Koch, D., Unger, N., Metzger, S.M., Shindell, D.T., Streets, D.G., 2007a. Nitrate aerosols today and in 2030: a global simulation including aerosols and tropospheric ozone. *Atmos. Chem. Phys.* 7, 5043-5059. doi:10.5194/acp-7-5043-2007
- Bauer, S.E., Mishchenko, M.I., Lacis, A.A., Zhang, S., Perlwitz, J., Metzger, S.M., 2007b. Do sulfate and nitrate coatings on mineral dust have important effects on radiative properties and climate modeling? *J. Geophys. Res. Atmos.* 112. doi:10.1029/2005JD006977
- Bellouin, N., Boucher, O., Haywood, J., Reddy, M.S., 2005. Global estimate of aerosol direct radiative forcing from satellite measurements. *Nature* 438, 1138-1141. doi:10.1038/nature04348
- Berglen, T.F., 2004. A global model of the coupled sulfur/oxidant chemistry in the troposphere: The sulfur cycle. *J. Geophys. Res.* 109. doi:10.1029/2003jd003948
- Bibi, S., Alam, K., Chishtie, F., Bibi, H., 2017. Characterization of absorbing aerosol types using ground and satellites based observations over an urban environment. *Atmos. Environ.* 150, 126-135. doi:10.1016/j.atmosenv.2016.11.052
- Bohren, C., Huffman, D., 1983. *Light scattering and absorption by small particles.*

- Wiley, New York
- Bohren, C.F., Huffman, D.R., 2007. Absorption and Scattering by a Sphere. John Wiley & Sons, Ltd.
- Bond, T.C., Bergstrom, R.W., 2006. Light Absorption by Carbonaceous Particles: An Investigative Review. *Aerosol Sci. Technol.* 40, 27-67. doi:10.1080/02786820500421521
- Bond, T.C., Doherty, S.J., Fahey, D.W., Forster, P.M., Berntsen, T., DeAngelo, B.J., Flanner, M.G., Ghan, S., Kärcher, B., Koch, D., Kinne, S., Kondo, Y., Quinn, P.K., Sarofim, M.C., Schultz, M.G., Schulz, M., Venkataraman, C., Zhang, H., Zhang, S., Bellouin, N., Guttikunda, S.K., Hopke, P.K., Jacobson, M.Z., Kaiser, J.W., Klimont, Z., Lohmann, U., Schwarz, J.P., Shindell, D., Storelvmo, T., Warren, S.G., Zender, C.S., 2013. Bounding the role of black carbon in the climate system: A scientific assessment. *J. Geophys. Res. Atmos.* 118, 5380-5552. doi:10.1002/jgrd.50171
- Bondy, A.L., Bonanno, D., Moffet, R.C., Wang, B., Laskin, A., Ault, A.P., 2018. The diverse chemical mixing state of aerosol particles in the southeastern United States. *Atmos. Chem. Phys.* 18, 12595-12612. doi:10.5194/acp-18-12595-2018
- Borge, R., Lumbreras, J., Vardoulakis, S., Kassomenos, P., Rodriguez, E., 2007. Analysis of long-range transport influences on urban PM10 using two-stage atmospheric trajectory clusters. *Atmos. Environ.* 41, 4434-4450. doi:10.1016/j.atmosenv.2007.01.053
- Boucher, O., 1999. Air traffic may increase cirrus cloudiness. *Nature* 397, 30-31. doi:10.1038/16169
- Boucher, O., 2015. Atmospheric aerosols, *Atmospheric Aerosols*. Springer, pp. 9-24.
- Canagaratna, M.R., Jayne, J.T., Jimenez, J.L., Allan, J.D., Alfarra, M.R., Zhang, Q., Onasch, T.B., Drewnick, F., Coe, H., Middlebrook, A., Delia, A., Williams, L.R., Trimborn, A.M., Northway, M.J., DeCarlo, P.F., Kolb, C.E., Davidovits, P., Worsnop, D.R., 2007. Chemical and microphysical characterization of ambient aerosols with the aerodyne aerosol mass spectrometer. *Mass Spectrom. Rev.* 26, 185-222. doi:10.1002/mas.20115
- Cappa, C.D., Kolesar, K.R., Zhang, X., Atkinson, D.B., Pekour, M.S., Zaveri, R.A., Zelenyuk, A., Zhang, Q., 2016. Understanding the optical properties of ambient sub- and supermicron particulate matter: results from the CARES 2010 field study in northern California. *Atmos. Chem. Phys.* 16, 6511-6535. doi:10.5194/acp-16-6511-2016
- Carbone, C., Decesari, S., Mircea, M., Giulianelli, L., Finessi, E., Rinaldi, M., Fuzzi, S., Marinoni, A., Duchi, R., Perrino, C., Sargolini, T., Vardè, M., Sprovieri, F., Gobbi, G.P., Angelini, F., Facchini, M.C., 2010. Size-resolved aerosol chemical composition over the Italian Peninsula during typical summer and winter

- conditions. *Atmos. Environ.* 44, 5269-5278. doi:10.1016/j.atmosenv.2010.08.008
- Cazorla, A., Bahadur, R., Suski, K.J., Cahill, J.F., Chand, D., Schmid, B., Ramanathan, V., Prather, K.A., 2013. Relating aerosol absorption due to soot, organic carbon, and dust to emission sources determined from in-situ chemical measurements. *Atmos. Chem. Phys.* 13, 9337-9350. doi:10.5194/acp-13-9337-2013
- Chakrabarty, R.K., Moosmüller, H., Chen, L.W.A., Lewis, K., Arnott, W.P., Mazzoleni, C., Dubey, M.K., Wold, C.E., Hao, W.M., Kreidenweis, S.M., 2010. Brown carbon in tar balls from smoldering biomass combustion. *Atmospheric Chemistry and Physics* 10, 6363-6370. doi:10.5194/acp-10-6363-2010
- Chate, D.M., Rao, P.S.P., Naik, M.S., Momin, G.A., Safai, P.D., Ali, K., 2003. Scavenging of aerosols and their chemical species by rain. *Atmos. Environ.* 37, 2477-2484. doi:10.1016/S1352-2310(03)00162-6
- Chen, B.T., Cheng, Y.S., Yeh, H.C., 2007. Performance of a TSI Aerodynamic Particle Sizer. *Aerosol Sci. Technol.* 4, 89-97. doi:10.1080/02786828508959041
- Chen, B.T., Crow, D.J., 1986. Use of an aerodynamic particle sizer as a real-time monitor in generation of ideal solid aerosols. *J. Aerosol Sci* 17, 963-972. doi:10.1016/0021-8502(86)90022-4
- Chen, C., Dubovik, O., Henze, D.K., Lapyonak, T., Chin, M., Ducos, F., Litvinov, P., Huang, X., Li, L., 2018. Retrieval of desert dust and carbonaceous aerosol emissions over Africa from POLDER/PARASOL products generated by the GRASP algorithm. *Atmos. Chem. Phys.* 18, 12551-12580. doi:10.5194/acp-18-12551-2018
- Chen, Y., Bond, T.C., 2010. Light absorption by organic carbon from wood combustion. *Atmos. Chem. Phys.* 10, 1773-1787. doi:10.5194/acp-10-1773-2010
- Cheng, Y., Li, S.-M., Gordon, M., Liu, P., 2018. Size distribution and coating thickness of black carbon from the Canadian oil sands operations. *Atmos. Chem. Phys.* 18, 2653-2667. doi:10.5194/acp-18-2653-2018
- Cheng, Y.F., Wiedensohler, A., Eichler, H., Su, H., Gnauk, T., Brüggemann, E., Herrmann, H., Heintzenberg, J., Slanina, J., Tuch, T., 2008. Aerosol optical properties and related chemical apportionment at Xinken in Pearl River Delta of China. *Atmos. Environ.* 42, 6351-6372. doi:10.1016/j.atmosenv.2008.02.034
- Chin, M., Ginoux, P., Kinne, S., Torres, O., Holben, B.N., Duncan, B.N., Martin, R.V., Logan, J.A., Higurashi, A., Nakajima, T., 2002. Tropospheric Aerosol Optical Thickness from the GOCART Model and Comparisons with Satellite and Sun Photometer Measurements. *J. Atmos. Sci.* 59, 461-483. doi:10.1175/1520-0469(2002)059<0461:TAOTFT>2.0.CO;2
- Chin, M., Rood, R.B., Lin, S.-J., Müller, J.-F., Thompson, A.M., 2000. Atmospheric sulfur cycle simulated in the global model GOCART: Model description and global properties. *J. Geophys. Res. Atmos.* 105, 24671-24687.

- doi:10.1029/2000jd900384
- Choi, Y., Ghim, Y.S., 2016. Estimation of columnar concentrations of absorbing and scattering fine mode aerosol components using AERONET data. *J. Geophys. Res. Atmos.* 121, 13,628-613,640. doi:10.1002/2016JD025080
- Chung, C., Lee, K., Müller, D., 2011. Effect of internal mixture on black carbon radiative forcing. *Tellus B Chem. Phys. Meteorol.* 64, 10925. doi:10.3402/tellusb.v64i0.10925
- Chung, C.E., Kim, S.W., Lee, M., Yoon, S.C., Lee, S., 2012a. Carbonaceous aerosol AAE inferred from in-situ aerosol measurements at the Gosan ABC super site, and the implications for brown carbon aerosol. *Atmos. Chem. Phys.* 12, 6173-6184. doi:10.5194/acp-12-6173-2012
- Chung, C.E., Ramanathan, V., Decremer, D., 2012b. Observationally constrained estimates of carbonaceous aerosol radiative forcing. *Proc. Natl. Acad. Sci. U. S. A.* 109, 11624-11629. doi:10.1073/pnas.1203707109
- Chung, C.E., Ramanathan, V., Kim, D., Podgorny, I.A., 2005. Global anthropogenic aerosol direct forcing derived from satellite and ground-based observations. *J. Geophys. Res.* 110. doi:10.1029/2005jd006356
- Chung, S.H., 2005. Climate response of direct radiative forcing of anthropogenic black carbon. *J. Geophys. Res.* 110. doi:10.1029/2004jd005441
- Corr, C.A., Hall, S.R., Ullmann, K., Anderson, B.E., Beyersdorf, A.J., Thornhill, K.L., Cubison, M.J., Jimenez, J.L., Wisthaler, A., Dibb, J.E., 2012. Spectral absorption of biomass burning aerosol determined from retrieved single scattering albedo during ARCTAS. *Atmos. Chem. Phys.* 12, 10505-10518. doi:10.5194/acp-12-10505-2012
- Crumeyrolle, S., Chen, G., Ziemba, L., Beyersdorf, A., Thornhill, L., Winstead, E., Moore, R.H., Shook, M.A., Hudgins, C., Anderson, B.E., 2014. Factors that influence surface PM<sub>2.5</sub> values inferred from satellite observations: perspective gained for the US Baltimore–Washington metropolitan area during DISCOVER-AQ. *Atmos. Chem. Phys.* 14, 2139-2153. doi:10.5194/acp-14-2139-2014
- Crumeyrolle, S., Gomes, L., Tulet, P., Matsuki, A., Schwarzenboeck, A., Crahan, K., 2008. Increase of the aerosol hygroscopicity by cloud processing in a mesoscale convective system: a case study from the AMMA campaign. *Atmos. Chem. Phys.* 8, 6907-6924. doi:10.5194/acp-8-6907-2008
- Crumeyrolle, S., Weigel, R., Sellegri, K., Roberts, G., Gomes, L., Stohl, A., Laj, P., Momboisse, G., Bourianne, T., Puygrenier, V., Burnet, F., Chosson, F., Brenguier, J.L., Etcheberry, J.M., Villani, P., Pichon, J.M., Schwarzenboeck, A., 2013. Airborne investigation of the aerosols–cloud interactions in the vicinity and within a marine stratocumulus over the North Sea during EUCAARI (2008). *Atmos.*

- Environ. 81, 288-303. doi:10.1016/j.atmosenv.2013.08.035
- D'Almeida, G.A., Koepke, P., Shettle, E.P., 1991. Atmospheric aerosols: global climatology and radiative characteristics. A Deepak Pub.
- DeCarlo, P.F., Slowik, J.G., Worsnop, D.R., Davidovits, P., Jimenez, J.L., 2004. Particle Morphology and Density Characterization by Combined Mobility and Aerodynamic Diameter Measurements. Part 1: Theory. *Aerosol Sci. Technol.* 38, 1185-1205. doi:10.1080/027868290903907
- Deuzé, J.L., Goloub, P., Herman, M., Marchand, A., Perry, G., Susana, S., Tanré, D., 2000. Estimate of the aerosol properties over the ocean with POLDER. *J. Geophys. Res. Atmos.* 105, 15329-15346. doi:10.1029/2000jd900148
- Deuzé, J.L., Herman, M., Goloub, P., Tanré, D., Marchand, A., 1999. Characterization of aerosols over ocean from POLDER/ADEOS-1. *Geophys. Res. Lett.* 26, 1421-1424. doi:10.1029/1999gl900168
- Dey, S., Tripathi, S.N., Singh, R.P., Holben, B.N., 2006. Retrieval of black carbon and specific absorption over Kanpur city, northern India during 2001–2003 using AERONET data. *Atmos. Environ.* 40, 445-456. doi:10.1016/j.atmosenv.2005.09.053
- Dial, K.D., Hiemstra, S., Thompson, J.E., 2010. Simultaneous Measurement of Optical Scattering and Extinction on Dispersed Aerosol Samples. *Anal. Chem.* 82, 7885-7896. doi:10.1021/ac100617j
- Dinar, E., Abo Riziq, A., Spindler, C., Erlick, C., Kiss, G., Rudich, Y., 2008. The complex refractive index of atmospheric and model humic-like substances (HULIS) retrieved by a cavity ring down aerosol spectrometer (CRD-AS). *Faraday Discuss.* 137, 279-295. doi:10.1039/b703111d
- Ding, A.J., Huang, X., Nie, W., Sun, J.N., Kerminen, V.M., Petäjä, T., Su, H., Cheng, Y.F., Yang, X.Q., Wang, M.H., Chi, X.G., Wang, J.P., Virkkula, A., Guo, W.D., Yuan, J., Wang, S.Y., Zhang, R.J., Wu, Y.F., Song, Y., Zhu, T., Zilitinkevich, S., Kulmala, M., Fu, C.B., 2016. Enhanced haze pollution by black carbon in megacities in China. *Geophys. Res. Lett.* 43, 2873-2879. doi:10.1002/2016gl067745
- Dockery, D.W., Pope, C.A., 1994. Acute respiratory effects of particulate air pollution. *Annu. Rev. Public Health* 15, 107-132
- Dore, A.J., Carslaw, D.C., Braban, C., Cain, M., Chemel, C., Conolly, C., Derwent, R.G., Griffiths, S.J., Hall, J., Hayman, G., Lawrence, S., Metcalfe, S.E., Redington, A., Simpson, D., Sutton, M.A., Sutton, P., Tang, Y.S., Vieno, M., Werner, M., Whyatt, J.D., 2015. Evaluation of the performance of different atmospheric chemical transport models and inter-comparison of nitrogen and sulphur deposition estimates for the UK. *Atmos. Environ.* 119, 131-143. doi:10.1016/j.atmosenv.2015.08.008

- Draxler, RR, Hess, 1998. An overview of the HYSPLIT\_4 modelling system for trajectories, dispersion, and deposition. *Aust. Meteor. Mag.* 47, 295-308
- Draxler, R., Stunder, B., Rolph, G., Taylor, A., 2009. HYSPLIT\_4 user's guide. NOAA Air Resources Laboratory. Silver Spring MD.
- Drinovec, L., Močnik, G., Zotter, P., Prévôt, A.S.H., Ruckstuhl, C., Coz, E., Rupakheti, M., Sciare, J., Müller, T., Wiedensohler, A., Hansen, A.D.A., 2015. The "dual-spot" Aethalometer: an improved measurement of aerosol black carbon with real-time loading compensation. *Atmos. Meas. Tech.* 8, 1965-1979. doi:10.5194/amt-8-1965-2015
- Dubovik, O., Herman, M., Holdak, A., Lapyonok, T., Tanré, D., Deuzé, J.L., Ducos, F., Sinyuk, A., Lopatin, A., 2011. Statistically optimized inversion algorithm for enhanced retrieval of aerosol properties from spectral multi-angle polarimetric satellite observations. *Atmos. Meas. Tech.* 4, 975-1018. doi:10.5194/amt-4-975-2011
- Dubovik, O., Holben, B., Eck, T.F., Smirnov, A., Kaufman, Y.J., King, M.D., Tanré, D., Slutsker, I., 2002. Variability of Absorption and Optical Properties of Key Aerosol Types Observed in Worldwide Locations. *J. Atmos. Sci.* 59, 590-608. doi:10.1175/1520-0469(2002)059<0590:voaaop>2.0.co;2
- Dubovik, O., Lapyonok, T., Litvinov, P., Herman, M., Fuertes, D., Ducos, F., Lopatin, A., Chaikovsky, A., Torres, B., Derimian, Y., 2014. GRASP: a versatile algorithm for characterizing the atmosphere. *SPIE Newsroom* 25
- Dubovik, O., Smirnov, A., Holben, B.N., King, M.D., Kaufman, Y.J., Eck, T.F., Slutsker, I., 2000. Accuracy assessments of aerosol optical properties retrieved from Aerosol Robotic Network (AERONET) Sun and sky radiance measurements. *J. Geophys. Res. Atmos.* 105, 9791-9806. doi:10.1029/2000jd900040
- Dubovik, O., Sinyuk, A., Lapyonok, T., Holben, B.N., Mishchenko, M., Yang, P., Eck, T.F., Volten, H., Muñoz, O., Veihelmann, B., 2006. Application of spheroid models to account for aerosol particle nonsphericity in remote sensing of desert dust. *Geophys. Res. Atmos.* 111. doi:10.1029/2005jd006619111
- Ebert, M., Weinbruch, S., Hoffmann, P., Ortner, H.M., 2004. The chemical composition and complex refractive index of rural and urban influenced aerosols determined by individual particle analysis. *Atmos. Environ.* 38, 6531-6545. doi:10.1016/j.atmosenv.2004.08.048
- Eck, T.F., Holben, B.N., Reid, J.S., Dubovik, O., Smirnov, A., O'Neill, N.T., Slutsker, I., Kinne, S., 1999. Wavelength dependence of the optical depth of biomass burning, urban, and desert dust aerosols. *J. Geophys. Res. Atmos.* 104, 31333-31349. doi:10.1029/1999jd900923
- Ellsworth, J.W., James, R.C., James, D.S., V. Stanley Scott, I., 2001. Global monitoring of clouds and aerosols using a network of micropulse lidar systems, *Proc.SPIE.*

- 4153, 1-8. doi: 10.1117/12.417040
- El-Zanan, H.S., Zielinska, B., Mazzoleni, L.R., Hansen, D.A., 2012. Analytical Determination of the Aerosol Organic Mass-to-Organic Carbon Ratio. *J. Air Waste Manage. Assoc.* 59, 58-69. doi:10.3155/1047-3289.59.1.58
- Engelbrecht, J.P., Derbyshire, E., 2010. Airborne mineral dust. *Elements* 6, 241-246
- Fan, X., Chen, H., Goloub, P., Xia, X.a., Zhang, W., Chatenet, B., 2006. Analysis of column-integrated aerosol optical thickness in beijing from aeronet observations. *China Particuology* 4, 330-335. doi:10.1016/S1672-2515(07)60285-1
- Filonchyk, M., Yan, H., Zhang, Z., Yang, S., Li, W., Li, Y., 2019. Combined use of satellite and surface observations to study aerosol optical depth in different regions of China. *Sci. Rep.* 9, 6174. doi:10.1038/s41598-019-42466-6
- Freitag, S., Clarke, A.D., Howell, S.G., Kapustin, V.N., Campos, T., Brekhovskikh, V.L., Zhou, J., 2014. Combining airborne gas and aerosol measurements with HYSPLIT: a visualization tool for simultaneous evaluation of air mass history and back trajectory consistency. *Atmos. Meas. Tech.* 7, 107-128. doi:10.5194/amt-7-107-2014
- Gao, T., Zhang, X., Li, Y., Wang, H., Xiao, S., Wulan, Teng, Q., 2008. Potential predictors for spring season dust storm forecast in Inner Mongolia, China. *Theor. Appl. Clim.* 97, 255-263. doi:10.1007/s00704-008-0072-y
- Geogdzhayev, I.V., Mishchenko, M.I., Rossow, W.B., Cairns, B., Lacis, A.A., 2002. Global Two-Channel AVHRR Retrievals of Aerosol Properties over the Ocean for the Period of NOAA-9 Observations and Preliminary Retrievals Using NOAA-7 and NOAA-11 Data. *J. Atmos. Sci.* 59, 262-278. doi:10.1175/1520-0469(2002)059<0262:gtcaro>2.0.co;2
- Goloub, P., Tanre, D., Deuze, J.-L., Herman, M., Marchand, A., Bréon, F.-M., 1999. Validation of the first algorithm applied for deriving the aerosol properties over the ocean using the POLDER/ADEOS measurements. *IEEE Trans. Geosci. Remote Sens.* 37, 1586-1596
- Guirado, C., Cuevas, E., Cachorro, V.E., Toledano, C., Alonso-Pérez, S., Bustos, J.J., Basart, S., Romero, P.M., Camino, C., Mimouni, M., Zeudmi, L., Goloub, P., Baldasano, J.M., de Frutos, A.M., 2014. Aerosol characterization at the Saharan AERONET site Tamanrasset. *Atmos. Chem. Phys.* 14, 11753-11773. doi:10.5194/acp-14-11753-2014
- Guo, S., Hu, M., Zamora, M.L., Peng, J., Shang, D., Zheng, J., Du, Z., Wu, Z., Shao, M., Zeng, L., Molina, M.J., Zhang, R., 2014. Elucidating severe urban haze formation in China. *Proc. Natl. Acad. Sci. U. S. A.* 111, 17373-17378. doi:10.1073/pnas.1419604111
- Gurganus, S.C., Wozniak, A.S., Hatcher, P.G., 2015. Molecular characteristics of the water soluble organic matter in size-fractionated aerosols collected over the North

- Atlantic Ocean. *Mar. Chem.* 170, 37-48. doi:10.1016/j.marchem.2015.01.007
- Hand, J.L., Kreidenweis, S.M., 2002. A New Method for Retrieving Particle Refractive Index and Effective Density from Aerosol Size Distribution Data. *Aerosol Sci. Technol.* 36, 1012-1026. doi:10.1080/02786820290092276
- Heald, C.L., Ridley, D.A., Kroll, J.H., Barrett, S.R.H., Cady-Pereira, K.E., Alvarado, M.J., Holmes, C.D., 2014. Contrasting the direct radiative effect and direct radiative forcing of aerosols. *Atmos. Chem. Phys.* 14, 5513-5527. doi:10.5194/acp-14-5513-2014
- Heintzenberg, J., Wiedensohler, A., Tuch, T.M., Covert, D.S., Sheridan, P., Ogren, J.A., Gras, J., Nessler, R., Kleefeld, C., Kalivitis, N., Aaltonen, V., Wilhelm, R.T., Havlicek, M., 2006. Intercomparisons and Aerosol Calibrations of 12 Commercial Integrating Nephelometers of Three Manufacturers. *J. Atmos. Ocean Technol.* 23, 902-914. doi:10.1175/JTECH1892.1
- Higurashi, A., Nakajima, T., 1999. Development of a Two-Channel Aerosol Retrieval Algorithm on a Global Scale Using NOAA AVHRR. *J. Atmos. Sci.* 56, 924-941. doi:10.1175/1520-0469(1999)056<0924:doatca>2.0.co;2
- Hitzenberger, R., Petzold, A., Bauer, H., Ctyroky, P., Pouresmaeil, P., Laskus, L., Puxbaum, H., 2006. Intercomparison of Thermal and Optical Measurement Methods for Elemental Carbon and Black Carbon at an Urban Location. *Environ. Sci. Technol.* 40, 6377-6383. doi:10.1021/es051228v
- Hoffer, A., Gelencsér, A., Guyon, P., Kiss, G., 2006. Optical properties of humic-like substances (HULIS) in biomass-burning aerosols. *Atmos. Chem. Phys.* 5, 3563-3570. doi:10.5194/acp-6-3563-2006
- Hoffer, A., Tóth, Á., Pósfai, M., Chung, C.E., Gelencsér, A., 2017. Brown carbon absorption in the red and near-infrared spectral region. *Atmos. Meas. Tech.* 10, 2353-2359. doi:10.5194/amt-10-2353-2017
- Holben, B.N., Eck, T.F., Slutsker, I., Smirnov, A., Sinyuk, A., Schafer, J.S., Giles, D.M., Dubovik, O., 2006. AERONET's version 2.0 quality assurance criteria. *Proc. SPIE-Int. Soc. Opt. Eng.* 6408
- Hsu, N.C., Tsay, S.-C., King, M.D., Herman, J.R., 2006. Deep blue retrievals of Asian aerosol properties during ACE-Asia. *IEEE Trans. Geosci. Remote Sens.* 44, 3180-3195
- Hu, M., Peng, J., Sun, K., Yue, D., Guo, S., Wiedensohler, A., Wu, Z., 2012. Estimation of size-resolved ambient particle density based on the measurement of aerosol number, mass, and chemical size distributions in the winter in Beijing. *Environ. Sci. Technol.* 46, 9941-9947. doi:10.1021/es204073t
- Hu, Q., Goloub, P., Veselovskii, I., Bravo-Aranda, J.-A., Popovici, I.E., Podvin, T., Haeffelin, M., Lopatin, A., Dubovik, O., Pietras, C., Huang, X., Torres, B., Chen, C., 2019. Long-range-transported Canadian smoke plumes in the lower

- stratosphere over northern France. *Atmos. Chem. Phys.* 19, 1173-1193. doi:10.5194/acp-19-1173-2019
- Huang, K., Zhuang, G., Lin, Y., Li, J., Sun, Y., Zhang, W., Fu, J.S., 2010. Relation between optical and chemical properties of dust aerosol over Beijing, China. *J. Geophys. Res.* 115. doi:10.1029/2009jd013212
- Huang, R.J., Zhang, Y., Bozzetti, C., Ho, K.F., Cao, J.J., Han, Y., Daellenbach, K.R., Slowik, J.G., Platt, S.M., Canonaco, F., Zotter, P., Wolf, R., Pieber, S.M., Bruns, E.A., Crippa, M., Ciarelli, G., Piazzalunga, A., Schwikowski, M., Abbaszade, G., Schnelle-Kreis, J., Zimmermann, R., An, Z., Szidat, S., Baltensperger, U., El Haddad, I., Prevot, A.S., 2014. High secondary aerosol contribution to particulate pollution during haze events in China. *Nature* 514, 218-222. doi:10.1038/nature13774
- Huang, X., Liu, Z., Zhang, J., Wen, T., Ji, D., Wang, Y., 2016. Seasonal variation and secondary formation of size-segregated aerosol water-soluble inorganic ions during pollution episodes in Beijing. *Atmos. Res.* 168, 70-79. doi:10.1016/j.atmosres.2015.08.021
- Huang, X., Wang, Z., Ding, A., 2018. Impact of Aerosol - PBL Interaction on Haze Pollution: Multiyear Observational Evidences in North China. *Geophys. Res. Lett.* 45, 8596-8603. doi:10.1029/2018gl079239
- Huang, Y., Shen, H., Chen, H., Wang, R., Zhang, Y., Su, S., Chen, Y., Lin, N., Zhuo, S., Zhong, Q., 2014. Quantification of global primary emissions of PM<sub>2.5</sub>, PM<sub>10</sub>, and TSP from combustion and industrial process sources. *Environ. Sci. Technol.* 48, 13834-13843
- Hudson, P.K., Gibson, E.R., Young, M.A., Kleiber, P.D., Grassian, V.H., 2007. A Newly Designed and Constructed Instrument for Coupled Infrared Extinction and Size Distribution Measurements of Aerosols. *Aerosol Sci. Technol.* 41, 701-710. doi:10.1080/02786820701408509
- Husar, R.B., Prospero, J.M., Stowe, L.L., 1997. Characterization of tropospheric aerosols over the oceans with the NOAA advanced very high resolution radiometer optical thickness operational product. *J. Geophys. Res. Atmos.* 102, 16889-16909
- Hyvärinen, A.P., Vakkari, V., Laakso, L., Hooda, R.K., Sharma, V.P., Panwar, T.S., Beukes, J.P., van Zyl, P.G., Josipovic, M., Garland, R.M., Andreae, M.O., Pöschl, U., Petzold, A., 2013. Correction for a measurement artifact of the Multi-Angle Absorption Photometer (MAAP) at high black carbon mass concentration levels. *Atmos. Meas. Tech.* 6, 81-90. doi:10.5194/amt-6-81-2013
- Jacobson, M.Z., 2001. Global direct radiative forcing due to multicomponent anthropogenic and natural aerosols. *J. Geophys. Res. Atmos.* 106, 1551-1568. doi:10.1029/2000jd900514
- Jayne, J.T., Leard, D.C., Zhang, X., Davidovits, P., Smith, K.A., Kolb, C.E., Worsnop,

- D.R., 2000. Development of an Aerosol Mass Spectrometer for Size and Composition Analysis of Submicron Particles. *Aerosol Sci. Technol.* 33, 49-70. doi:10.1080/027868200410840
- Junge, C., 1955. The size distribution and aging of natural aerosols as determined from electrical and optical data on the atmosphere. *Journal of Meteorology* 12, 13-25
- Kahn, R.A., Gaitley, B.J., Martonchik, J.V., Diner, D.J., Crean, K.A., Holben, B., 2005. Multiangle Imaging Spectroradiometer (MISR) global aerosol optical depth validation based on 2 years of coincident Aerosol Robotic Network (AERONET) observations. *J. Geophys. Res. Atmos.* 110. doi:10.1029/2004JD004706
- Kahn, R.A., Gaitley, B.J., 2015. An analysis of global aerosol type as retrieved by MISR. *J. Geophys. Res. Atmos.* 120, 4248-4281. doi:10.1002/2015jd023322
- Kandler, K., Benker, N., Bundke, U., Cuevas, E., Ebert, M., Knippertz, P., Rodríguez, S., Schütz, L., Weinbruch, S., 2007. Chemical composition and complex refractive index of Saharan Mineral Dust at Izaña, Tenerife (Spain) derived by electron microscopy. *Atmos. Environ.* 41, 8058-8074. doi:10.1016/j.atmosenv.2007.06.047
- Kassianov, E., Barnard, J., Pekour, M., Berg, L.K., Shilling, J., Flynn, C., Mei, F., Jefferson, A., 2014. Simultaneous retrieval of effective refractive index and density from size distribution and light-scattering data: weakly absorbing aerosol. *Atmos. Meas. Tech.* 7, 3247-3261. doi:10.5194/amt-7-3247-2014
- Kaufman, Y.J., Koren, I., Remer, L.A., Rosenfeld, D., Rudich, Y., 2005. The effect of smoke, dust, and pollution aerosol on shallow cloud development over the Atlantic Ocean. *Proc. Natl. Acad. Sci. U. S. A.* 102, 11207-11212. doi:10.1073/pnas.0505191102
- Kelly, G.M., Taubman, B.F., Perry, L.B., Sherman, J.P., Soulé, P.T., Sheridan, P.J., 2013. Relationships between aerosols and precipitation in the southern Appalachian Mountains. *Int. J. Climatol.* 33, 3016-3028. doi:10.1002/joc.3632
- Khlystov, A., Stanier, C., Pandis, S.N., 2004. An Algorithm for Combining Electrical Mobility and Aerodynamic Size Distributions Data when Measuring Ambient Aerosol Special Issue of Aerosol Science and Technology on Findings from the Fine Particulate Matter Supersites Program. *Aerosol Sci. Technol.* 38, 229-238. doi:10.1080/02786820390229543
- Kim, H.K., Lee, M.J., Jung, H.J., Eom, H.J., Maskey, S., Ahn, K.H., Ro, C.U., 2012. Hygroscopic behavior of wet dispersed and dry deposited NaNO<sub>3</sub> particles. *Atmos. Environ.* 60, 68-75. doi:10.1016/j.atmosenv.2012.06.011
- Kinne, S., Schulz, M., Textor, C., Guibert, S., Balkanski, Y., Bauer, S.E., Berntsen, T., Berglen, T.F., Boucher, O., Chin, M., Collins, W., Dentener, F., Diehl, T., Easter, R., Feichter, J., Fillmore, D., Ghan, S., Ginoux, P., Gong, S., Grini, A., Hendricks, J., Herzog, M., Horowitz, L., Isaksen, I., Iversen, T., Kirkevåg, A., Kloster, S., Koch, D., Kristjansson, J.E., Krol, M., Lauer, A., Lamarque, J.F., Lesins, G., Liu,

- X., Lohmann, U., Montanaro, V., Myhre, G., Penner, J., Pitari, G., Reddy, S., Seland, O., Stier, P., Takemura, T., Tie, X., 2006. An AeroCom initial assessment – optical properties in aerosol component modules of global models. *Atmos. Chem. Phys.* 6, 1815-1834. doi:10.5194/acp-6-1815-2006
- Kirchstetter, T.W., Novakov, T., Hobbs, P.V., 2004. Evidence that the spectral dependence of light absorption by aerosols is affected by organic carbon. *J. Geophys. Res. Atmos.* 109, n/a-n/a. doi:10.1029/2004jd004999
- Koch, D., Bond, T.C., Streets, D., Unger, N., van der Werf, G.R., 2007. Global impacts of aerosols from particular source regions and sectors. *J. Geophys. Res.* 112. doi:10.1029/2005jd007024
- Koch, D., Del Genio, A.D., 2010. Black carbon semi-direct effects on cloud cover: review and synthesis. *Atmos. Chem. Phys.* 10, 7685-7696. doi:10.5194/acp-10-7685-2010
- Lack, D.A., Cappa, C.D., 2010. Impact of brown and clear carbon on light absorption enhancement, single scatter albedo and absorption wavelength dependence of black carbon. *Atmos. Chem. Phys.* 10, 4207-4220. doi:10.5194/acp-10-4207-2010
- Lack, D.A., Langridge, J.M., 2013. On the attribution of black and brown carbon light absorption using the Ångström exponent. *Atmos. Chem. Phys.* 13, 10535-10543. doi:10.5194/acp-13-10535-2013
- Lack, D.A., Langridge, J.M., Bahreini, R., Cappa, C.D., Middlebrook, A.M., Schwarz, J.P., 2012. Brown carbon and internal mixing in biomass burning particles. *Proc. Natl. Acad. Sci. U. S. A.* 109, 14802-14807. doi:10.1073/pnas.1206575109
- Lack, D.A., Lovejoy, E.R., Baynard, T., Pettersson, A., Ravishankara, A.R., 2006. Aerosol Absorption Measurement using Photoacoustic Spectroscopy: Sensitivity, Calibration, and Uncertainty Developments. *Aerosol Sci. Technol.* 40, 697-708. doi:10.1080/02786820600803917
- Laing, J.R., Jaffe, D.A., Sedlacek, I.I.I.A.J., 2020. Comparison of Filter-based Absorption Measurements of Biomass Burning Aerosol and Background Aerosol at the Mt. Bachelor Observatory. *Aerosol Air Qual. Res.* 20, 663-678. doi:10.4209/aaqr.2019.06.0298
- Lammel, G., Brüggemann, E., Gnauk, T., Müller, K., Neusüss, C., Röhrl, A., 2003. A new method to study aerosol source contributions along the tracks of air parcels and its application to the near-ground level aerosol chemical composition in central Europe. *J. Aerosol Sci* 34, 1-25
- Lau, K.M., Song, Y., 1996. Seasonal Variation, Abrupt Transition, and Intraseasonal Variability Associated with the Asian Summer Monsoon in the GLA GCM. *J. Clim.* 9, 965-985
- Lelieveld, J., Heintzenberg, J., 1992. Sulfate Cooling Effect on Climate Through In-Cloud Oxidation of Anthropogenic SO<sub>2</sub>. *Science* 258, 117-120.

doi:10.1126/science.258.5079.117

- Lesins, G., Chylek, P., Lohmann, U., 2002. A study of internal and external mixing scenarios and its effect on aerosol optical properties and direct radiative forcing. *J. Geophys. Res. Atmos.* 107, AAC 5-1-AAC 5-12. doi:10.1029/2001jd000973
- Levelt, P.F., Oord, G.H.J.v.d., Dobber, M.R., Malkki, A., Huib, V., Johan de, V., Stammes, P., Lundell, J.O.V., Saari, H., 2006. The ozone monitoring instrument. *IEEE Transactions on Geoscience and Remote Sensing* 44, 1093-1101. doi:10.1109/TGRS.2006.872333
- Levin, Z., Cotton, W.R., 2008. *Aerosol pollution impact on precipitation: a scientific review*. Springer Science & Business Media.
- Levy, R., Remer, L., Kleidman, R., Mattoo, S., Ichoku, C., Kahn, R., Eck, T., 2010. Global evaluation of the Collection 5 MODIS dark-target aerosol products over land. *Atmos. Chem. Phys.* 10, 10399-10420
- Levy, R.C., Remer, L.A., Mattoo, S., Vermote, E.F., Kaufman, Y.J., 2007. Second - generation operational algorithm: Retrieval of aerosol properties over land from inversion of Moderate Resolution Imaging Spectroradiometer spectral reflectance. *J. Geophys. Res. Atmos.* 112
- Li, J., Carlson, B.E., Lacis, A.A., 2015a. Using single-scattering albedo spectral curvature to characterize East Asian aerosol mixtures. *J. Geophys. Res. Atmos.* 120, 2037-2052. doi:10.1002/2014jd022433
- Li, K., Li, J., Liggio, J., Wang, W., Ge, M., Liu, Q., Guo, Y., Tong, S., Li, J., Peng, C., Jing, B., Wang, D., Fu, P., 2017. Enhanced Light Scattering of Secondary Organic Aerosols by Multiphase Reactions. *Environ. Sci. Technol.* 51, 1285-1292. doi:10.1021/acs.est.6b03229
- Li, L., Dubovik, O., Derimian, Y., Schuster, G.L., Lapyonok, T., Litvinov, P., Ducos, F., Fuertes, D., Chen, C., Li, Z., Lopatin, A., Torres, B., Che, H., 2019. Retrieval of aerosol components directly from satellite and ground-based measurements. *Atmos. Chem. Phys.* 19, 13409-13443. doi:10.5194/acp-19-13409-2019
- Li, W., Shao, L., Shi, Z., Chen, J., Yang, L., Yuan, Q., Yan, C., Zhang, X., Wang, Y., Sun, J., Zhang, Y., Shen, X., Wang, Z., Wang, W., 2014. Mixing state and hygroscopicity of dust and haze particles before leaving Asian continent. *J. Geophys. Res. Atmos.* 119, 1044-1059. doi:10.1002/2013JD021003
- Li, W.J., Shao, L.Y., Buseck, P.R., 2010. Haze types in Beijing and the influence of agricultural biomass burning. *Atmos. Chem. Phys.* 10, 8119-8130. doi:10.5194/acp-10-8119-2010
- Li, Z., Gu, X., Wang, L., Li, D., Xie, Y., Li, K., Dubovik, O., Schuster, G., Goloub, P., Zhang, Y., Li, L., Ma, Y., Xu, H., 2013. Aerosol physical and chemical properties retrieved from ground-based remote sensing measurements during heavy haze days in Beijing winter. *Atmos. Chem. Phys.* 13, 10171-10183. doi:10.5194/acp-

13-10171-2013

- Li, Z., Guo, J., Ding, A., Liao, H., Liu, J., Sun, Y., Wang, T., Xue, H., Zhang, H., Zhu, B., 2017. Aerosol and boundary-layer interactions and impact on air quality. *Natl. Sci. Rev.* 4, 810-833. doi:10.1093/nsr/nwx117
- Li, Z., Li, L., Zhang, F., Li, D., Xie, Y., Xu, H., 2015b. Comparison of aerosol properties over Beijing and Kanpur: Optical, physical properties and aerosol component composition retrieved from 12 years ground-based Sun-sky radiometer remote sensing data. *J. Geophys. Res. Atmos.* 120, 1520-1535. doi:10.1002/2014jd022593
- Li, Z., Niu, F., Fan, J., Liu, Y., Rosenfeld, D., Ding, Y., 2011. Long-term impacts of aerosols on the vertical development of clouds and precipitation. *Nat. Geosci.* 4, 888-894. doi:10.1038/ngeo1313
- Li, Z., Wei, Y., Zhang, Y., Xie, Y., Li, L., Li, K., Ma, Y., Sun, X., Zhao, W., Gu, X., 2018. Retrieval of Atmospheric Fine Particulate Density Based on Merging Particle Size Distribution Measurements: Multi-instrument Observation and Quality Control at Shouxian. *J. Geophys. Res. Atmos.* 123, 4124-4148. doi:10.1029/2018jd028956
- Liao, T., Wang, S., Ai, J., Gui, K., Duan, B., Zhao, Q., Zhang, X., Jiang, W., Sun, Y., 2017. Heavy pollution episodes, transport pathways and potential sources of PM<sub>2.5</sub> during the winter of 2013 in Chengdu (China). *Sci. Total Environ.* 584-585, 1056-1065. doi:10.1016/j.scitotenv.2017.01.160
- Lim, S., Lee, M., Kim, S.W., Laj, P., 2018. Sulfate alters aerosol absorption properties in East Asian outflow. *Sci. Rep.* 8, 5172. doi:10.1038/s41598-018-23021-1
- Liu, C., Chung, C.E., Yin, Y., Schnaiter, M., 2018. The absorption Ångström exponent of black carbon: from numerical aspects. *Atmos. Chem. Phys.* 18, 6259-6273. doi:10.5194/acp-18-6259-2018
- Liu, D., Whitehead, J., Alfarra, M.R., Reyes-Villegas, E., Spracklen, Dominick V., Reddington, Carly L., Kong, S., Williams, Paul I., Ting, Y.-C., Haslett, S., Taylor, Jonathan W., Flynn, Michael J., Morgan, William T., McFiggans, G., Coe, H., Allan, James D., 2017. Black-carbon absorption enhancement in the atmosphere determined by particle mixing state. *Nat. Geosci.* 10, 184-188. doi:10.1038/ngeo2901
- Liu, J., Bergin, M., Guo, H., King, L., Kotra, N., Edgerton, E., Weber, R.J., 2013a. Size-resolved measurements of brown carbon in water and methanol extracts and estimates of their contribution to ambient fine-particle light absorption. *Atmos. Chem. Phys.* 13, 12389-12404. doi:10.5194/acp-13-12389-2013
- Liu, Q., Liu, Y., Yin, J., Zhang, M., Zhang, T., 2014. Chemical characteristics and source apportionment of PM<sub>10</sub> during Asian dust storm and non-dust storm days in Beijing. *Atmos. Environ.* 91, 85-94. doi:10.1016/j.atmosenv.2014.03.057

- Liu, S., Aiken, A.C., Gorkowski, K., Dubey, M.K., Cappa, C.D., Williams, L.R., Herndon, S.C., Massoli, P., Fortner, E.C., Chhabra, P.S., Brooks, W.A., Onasch, T.B., Jayne, J.T., Worsnop, D.R., China, S., Sharma, N., Mazzoleni, C., Xu, L., Ng, N.L., Liu, D., Allan, J.D., Lee, J.D., Fleming, Z.L., Mohr, C., Zotter, P., Szidat, S., Prevot, A.S.H., 2015a. Enhanced light absorption by mixed source black and brown carbon particles in UK winter. *Nat. Commun.* 6, 8435. doi:10.1038/ncomms9435
- Liu, X., Gu, J., Li, Y., Cheng, Y., Qu, Y., Han, T., Wang, J., Tian, H., Chen, J., Zhang, Y., 2013b. Increase of aerosol scattering by hygroscopic growth: Observation, modeling, and implications on visibility. *Atmos. Res.* 132-133, 91-101. doi:10.1016/j.atmosres.2013.04.007
- Liu, Y., Daum, P.H., 2008. Relationship of refractive index to mass density and self-consistency of mixing rules for multicomponent mixtures like ambient aerosols. *J. Aerosol Sci* 39, 974-986. doi:10.1016/j.jaerosci.2008.06.006
- Liu, Z., Hu, B., Ji, D., Wang, Y., Wang, M., Wang, Y., 2015b. Diurnal and seasonal variation of the PM<sub>2.5</sub> apparent particle density in Beijing, China. *Atmos. Environ.* 120, 328-338. doi:10.1016/j.atmosenv.2015.09.005
- Loeb, N.G., Su, W., 2010. Direct Aerosol Radiative Forcing Uncertainty Based on a Radiative Perturbation Analysis. *J. Clim.* 23, 5288-5293. doi:10.1175/2010jcli3543.1
- Lowenthal, D.H., Kumar, N., 2016. Evaluation of the IMPROVE Equation for estimating aerosol light extinction. *J. Air Waste Manag. Assoc.* 66, 726-737. doi:10.1080/10962247.2016.1178187
- Lowenthal, D.H., Watson, J.G., Saxena, P., 2000. Contributions to light extinction during project MOHAVE. *Atmos. Environ.* 34, 2351-2359. doi:10.1016/S1352-2310(99)00449-5
- Mallet, M., Roger, J.C., Despiiau, S., Dubovik, O., Putaud, J.P., 2003. Microphysical and optical properties of aerosol particles in urban zone during ESCOMPTE. *Atmos. Res.* 69, 73-97. doi:10.1016/j.atmosres.2003.07.001
- Malm, W.C., Schichtel, B.A., Pitchford, M.L., 2011. Uncertainties in PM<sub>2.5</sub> gravimetric and speciation measurements and what we can learn from them. *J. Air Waste Manag. Assoc.* 61, 1131-1149. doi:10.1080/10473289.2011.603998
- Martonchik, J.V., Diner, D.J., 1992. Retrieval of aerosol optical properties from multi-angle satellite imagery. *IEEE Trans. Geosci. Remote Sens.* 30, 223-230. doi:10.1109/36.134073
- Mason, B., Wagner, N.L., Adler, G., Andrews, E., Brock, C.A., Gordon, T.D., Lack, D.A., Perring, A.E., Richardson, M.S., Schwarz, J.P., Shook, M.A., Thornhill, K.L., Ziemba, L.D., Murphy, D.M., 2018. An intercomparison of aerosol absorption measurements conducted during the SEAC4RS campaign. *Aerosol Sci. Technol.*

- 52, 1012-1027. doi:10.1080/02786826.2018.1500012
- Massoli, P., Murphy, D.M., Lack, D.A., Baynard, T., Brock, C.A., Lovejoy, E.R., 2009. Uncertainty in Light Scattering Measurements by TSI Nephelometer: Results from Laboratory Studies and Implications for Ambient Measurements. *Aerosol Sci. Technol.* 43, 1064-1074. doi:10.1080/02786820903156542
- Matsui, H., 2018. Black carbon radiative effects highly sensitive to emitted particle size when resolving mixing-state diversity. doi:10.1038/s41467-018-05635-1
- McComiskey, A., Schwartz, S.E., Schmid, B., Guan, H., Lewis, E.R., Ricchiazzi, P., Ogren, J.A., 2008. Direct aerosol forcing: Calculation from observables and sensitivities to inputs. *J. Geophys. Res.* 113. doi:10.1029/2007jd009170
- McMurry, P.H., 2000. A review of atmospheric aerosol measurements. *Atmos. Environ.* 34, 1959-1999. doi:10.1016/S1352-2310(99)00455-0
- Michel Flores, J., Bar-Or, R.Z., Bluvshstein, N., Abo-Riziq, A., Kostinski, A., Borrmann, S., Koren, I., Koren, I., Rudich, Y., 2012. Absorbing aerosols at high relative humidity: linking hygroscopic growth to optical properties. *Atmos. Chem. Phys.* 12, 5511-5521. doi:10.5194/acp-12-5511-2012
- Minikin, A., Petzold, A., Weinzierl, B., Gayet, J.-F., 2012. In Situ Measurement Methods for Atmospheric Aerosol Particles and Cloud Elements, in: Schumann, U. (Ed.), *Atmospheric Physics: Background – Methods – Trends*. Springer Berlin Heidelberg, Berlin, Heidelberg, pp. 297-315.
- Mishchenko, M.I., Cairns, B., Kopp, G., Schueler, C.F., Fafaul, B.A., Hansen, J.E., Hooker, R.J., Itchkawich, T., Maring, H.B., Travis, L.D., 2007. Accurate monitoring of terrestrial aerosols and total solar irradiance: introducing the Glory Mission. *Bull. Am. Meteorol. Soc.* 88, 677-692
- Mishchenko, M.I., Geogdzhayev, I.V., Cairns, B., Rossow, W.B., Lacis, A.A., 1999. Aerosol retrievals over the ocean by use of channels 1 and 2 AVHRR data: sensitivity analysis and preliminary results. *Appl. Opt.* 38, 7325-7341
- Mishchenko, M.I., Liu, L., Travis, L.D., Lacis, A.A., 2004. Scattering and radiative properties of semi-external versus external mixtures of different aerosol types. *J. Quant. Spectrosc. Radiat. Transfer* 88, 139-147. doi: 10.1016/j.jqsrt.2003.12.032
- Mitchell, J., Johns, T., 1997. On modification of global warming by sulfate aerosols. *J. Clim.* 10, 245-267
- Moosmüller, H., Chakrabarty, R.K., Arnott, W.P., 2009. Aerosol light absorption and its measurement: A review. *J. Quant. Spectrosc. Radiat. Transfer* 110, 844-878. doi:10.1016/j.jqsrt.2009.02.035
- Mori, T., Moteki, N., Ohata, S., Koike, M., Goto-Azuma, K., Miyazaki, Y., Kondo, Y., 2016. Improved technique for measuring the size distribution of black carbon particles in liquid water. *Aerosol Sci. Tech.* 50, 242-254.

- doi:10.1080/02786826.2016.1147644
- Moroni, B., Castellini, S., Crocchianti, S., Piazzalunga, A., Fermo, P., Scardazza, F., Cappelletti, D., 2015. Ground-based measurements of long-range transported aerosol at the rural regional background site of Monte Martano (Central Italy). *Atmos. Res.* 155, 26-36. doi:10.1016/j.atmosres.2014.11.021
- Moteki, N., Kondo, Y., Nakamura, S.-i., 2010. Method to measure refractive indices of small nonspherical particles: Application to black carbon particles. *J. Aerosol Sci.* 41, 513-521. doi:10.1016/j.jaerosci.2010.02.013
- Müller, T., Laborde, M., Kassell, G., Wiedensohler, A., 2011. Design and performance of a three-wavelength LED-based total scatter and backscatter integrating nephelometer. *Atmos. Meas. Tech.* 4, 1291-1303. doi:10.5194/amt-4-1291-2011
- Myhre, G., Samset, B.H., Schulz, M., Balkanski, Y., Bauer, S., Berntsen, T.K., Bian, H., Bellouin, N., Chin, M., Diehl, T., Easter, R.C., Feichter, J., Ghan, S.J., Hauglustaine, D., Iversen, T., Kinne, S., Kirkevåg, A., Lamarque, J.F., Lin, G., Liu, X., Lund, M.T., Luo, G., Ma, X., van Noije, T., Penner, J.E., Rasch, P.J., Ruiz, A., Seland, Ø., Skeie, R.B., Stier, P., Takemura, T., Tsigaridis, K., Wang, P., Wang, Z., Xu, L., Yu, H., Yu, F., Yoon, J.H., Zhang, K., Zhang, H., Zhou, C., 2013. Radiative forcing of the direct aerosol effect from AeroCom Phase II simulations. *Atmos. Chem. Phys.* 13, 1853-1877. doi:10.5194/acp-13-1853-2013
- Myhre, G., Myhre, C., Samset, B., Storelvmo, T., 2013. Aerosols and their relation to global climate and climate sensitivity. *Nature Education Knowledge* 4, 7.
- Nakayama, T., Sato, K., Tsuge, M., Imamura, T., Matsumi, Y., 2015. Complex refractive index of secondary organic aerosol generated from isoprene/NO<sub>x</sub> photooxidation in the presence and absence of SO<sub>2</sub>. *J. Geophys. Res. Atmos.* 120, 7777-7787. doi:10.1002/2015jd023522
- Ng, N.L., Herndon, S.C., Trimborn, A., Canagaratna, M.R., Croteau, P.L., Onasch, T.B., Sueper, D., Worsnop, D.R., Zhang, Q., Sun, Y.L., Jayne, J.T., 2011. An Aerosol Chemical Speciation Monitor (ACSM) for Routine Monitoring of the Composition and Mass Concentrations of Ambient Aerosol. *Aerosol Sci. Technol.* 45, 780-794. doi:10.1080/02786826.2011.560211
- Olson, M.R., Victoria Garcia, M., Robinson, M.A., Van Rooy, P., Dietenberger, M.A., Bergin, M., Schauer, J.J., 2015. Investigation of black and brown carbon multiple-wavelength-dependent light absorption from biomass and fossil fuel combustion source emissions. *J. Geophys. Res. Atmos.* 120, 6682-6697. doi:10.1002/2014jd022970
- Park, S., Son, S.-C., Lee, S., 2018. Characterization, sources, and light absorption of fine organic aerosols during summer and winter at an urban site. *Atmos. Res.* 213, 370-380. doi:10.1016/j.atmosres.2018.06.017
- Park, S., Yu, G.-H., 2018. Absorption properties and size distribution of aerosol

- particles during the fall season at an urban site of Gwangju, Korea. *Environ. Eng. Res.* 24, 159-172. doi:10.4491/eer.2018.166
- Peng, J., Hu, M., Guo, S., Du, Z., Zheng, J., Shang, D., Levy, Z.M., Zeng, L., Shao, M., Wu, Y.S., 2016. Markedly enhanced absorption and direct radiative forcing of black carbon under polluted urban environments. *Proc. Natl. Acad. Sci. U. S. A.* 113, 4266
- Pettersson, A., Lovejoy, E.R., Brock, C.A., Brown, S.S., Ravishankara, A.R., 2004. Measurement of aerosol optical extinction at with pulsed cavity ring down spectroscopy. *J. Aerosol Sci.* 35, 995-1011. doi:10.1016/j.jaerosci.2004.02.008
- Pierce, J.R., Adams, P.J., 2007. Efficiency of cloud condensation nuclei formation from ultrafine particles. *Atmos. Chem. Phys.* 7, 1367-1379. doi:10.5194/acp-7-1367-2007
- Pinero-Garcia, F., Ferro-Garcia, M.A., Chham, E., Cobos-Diaz, M., Gonzalez-Rodelas, P., 2015. A cluster analysis of back trajectories to study the behaviour of radioactive aerosols in the south-east of Spain. *J. Environ. Radioact.* 147, 142-152. doi:10.1016/j.jenvrad.2015.05.029
- Pio, C.A., Cardoso, J.G., Cerqueira, M.A., Calvo, A., Nunes, T.V., Alves, C.A., Custódio, D., Almeida, S.M., Almeida-Silva, M., 2014. Seasonal variability of aerosol concentration and size distribution in Cape Verde using a continuous aerosol optical spectrometer. *Frontiers in Environmental Science* 2. doi:10.3389/fenvs.2014.00015
- Pitz, M., Schmid, O., Heinrich, J., Birmili, W., Maguhn, J., Zimmermann, R., Wichmann, H.E., Peters, A., Cyrys, J., 2008. Seasonal and Diurnal Variation of PM<sub>2.5</sub> Apparent Particle Density in Urban Air in Augsburg, Germany. *Environ. Sci. Technol.* 42, 5087-5093. doi:10.1021/es7028735
- Putaud, J.P., Van Dingenen, R., Mangoni, M., Virkkula, A., Raes, F., Maring, H., Prospero, J.M., Swietlicki, E., Berg, O.H., Hillamo, R., Mäkelä, T., 2000. Chemical mass closure and assessment of the origin of the submicron aerosol in the marine boundary layer and the free troposphere at Tenerife during ACE-2. *Tellus B Chem. Phys. Meteorol.* 52, 141-168. doi:10.3402/tellusb.v52i2.16090
- Qiao, K., Wu, Z., Pei, X., Liu, Q., Shang, D., Zheng, J., Du, Z., Zhu, W., Wu, Y., Lou, S., Guo, S., Chan, C.K., Pathak, R.K., Hallquist, M., Hu, M., 2018. Size-resolved effective density of submicron particles during summertime in the rural atmosphere of Beijing, China. *J. Environ. Sci. (China)* 73, 69-77. doi:10.1016/j.jes.2018.01.012
- Ramana, M.V., Ramanathan, V., Feng, Y., Yoon, S.C., Kim, S.W., Carmichael, G.R., Schauer, J.J., 2010. Warming influenced by the ratio of black carbon to sulphate and the black-carbon source. *Nat. Geosci.* 3, 542-545. doi:10.1038/ngeo918
- Ramanathan, V., Carmichael, G., 2008. Global and regional climate changes due to

- black carbon. *Nat. Geosci.* 1, 221-227. doi:10.1038/ngeo156
- Rastigejev, Y., Brenner, M.P., Jacob, D.J., 2007. Spatial reduction algorithm for atmospheric chemical transport models. *Proceedings of the National Academy of Sciences* 104, 13875-13880. doi:10.1073/pnas.0705649104
- Raut, J.C., Chazette, P., Fortain, A., 2009. Link between aerosol optical, microphysical and chemical measurements in an underground railway station in Paris. *Atmos. Environ.* 43, 860-868. doi:10.1016/j.atmosenv.2008.10.038
- Reddington, C.L., McMeeking, G., Mann, G.W., Coe, H., Frontoso, M.G., Liu, D., Flynn, M., Spracklen, D.V., Carslaw, K.S., 2013. The mass and number size distributions of black carbon aerosol over Europe. *Atmos. Chem. Phys.* 13, 4917-4939. doi:10.5194/acp-13-4917-2013
- Remer, L.A., Kaufman, Y., Tanré, D., Mattoo, S., Chu, D., Martins, J.V., Li, R.-R., Ichoku, C., Levy, R., Kleidman, R., 2005. The MODIS aerosol algorithm, products, and validation. *J. Atmos. Sci.* 62, 947-973
- Riemer, N., West, M., Zaveri, R., Easter, R., 2010. Estimating black carbon aging time-scales with a particle-resolved aerosol model. *J. Aerosol Sci* 41, 143-158. doi:10.1016/j.jaerosci.2009.08.009
- Rim, D., Green, M., Wallace, L., Persily, A., Choi, J.-I., 2012. Evolution of Ultrafine Particle Size Distributions Following Indoor Episodic Releases: Relative Importance of Coagulation, Deposition and Ventilation. *Aerosol Sci. Technol.* 46, 494-503. doi:10.1080/02786826.2011.639317
- Rissler, J., Nordin, E.Z., Eriksson, A.C., Nilsson, P.T., Frosch, M., Sporre, M.K., Wierzbicka, A., Svenningsson, B., Londahl, J., Messing, M.E., Sjogren, S., Hemmingsen, J.G., Loft, S., Pagels, J.H., Swietlicki, E., 2014. Effective density and mixing state of aerosol particles in a near-traffic urban environment. *Environ Sci Technol* 48, 6300-6308. doi:10.1021/es5000353
- Rozwadowska, A., Zielinski, T., Petelski, T., Sobolewski, P., 2010. Cluster analysis of the impact of air back-trajectories on aerosol optical properties at Hornsund, Spitsbergen. *Atmos. Chem. Phys.* 10, 877-893
- Russell, L.M., 2003. Aerosol organic-mass-to-organic-carbon ratio measurements. *Environ. Sci. Technol.* 37, 2982-2987
- Russell, P.B., Bergstrom, R.W., Shinozuka, Y., Clarke, A.D., DeCarlo, P.F., Jimenez, J.L., Livingston, J.M., Redemann, J., Dubovik, O., Strawa, A., 2010. Absorption Angstrom Exponent in AERONET and related data as an indicator of aerosol composition. *Atmos. Chem. Phys.* 10, 1155-1169. doi:10.5194/acp-10-1155-2010
- Sandradewi, J., Prévôt, A.S.H., Szidat, S., Perron, N., Alfarra, M.R., Lanz, V.A., Weingartner, E., Baltensperger, U., 2008. Using Aerosol Light Absorption Measurements for the Quantitative Determination of Wood Burning and Traffic Emission Contributions to Particulate Matter. *Environ. Sci. Technol.* 42, 3316-

3323. doi:10.1021/es702253m
- Schkolnik, G., Chand, D., Hoffer, A., Andreae, M.O., Erlick, C., Swietlicki, E., Rudich, Y., 2007. Constraining the density and complex refractive index of elemental and organic carbon in biomass burning aerosol using optical and chemical measurements. *Atmos. Environ.* 41, 1107-1118. doi:10.1016/j.atmosenv.2006.09.035
- Schmeisser, L., Andrews, E., Ogren, J.A., Sheridan, P., Jefferson, A., Sharma, S., Kim, J.E., Sherman, J.P., Sorribas, M., Kalapov, I., Arsov, T., Angelov, C., Mayol-Bracero, O.L., Labuschagne, C., Kim, S.-W., Hoffer, A., Lin, N.-H., Chia, H.-P., Bergin, M., Sun, J., Liu, P., Wu, H., 2017. Classifying aerosol type using in situ surface spectral aerosol optical properties. *Atmos. Chem. Phys.* 17, 12097-12120. doi:10.5194/acp-17-12097-2017
- Schuster, G., Espinosa, W., Ziemba, L., Beyersdorf, A., Rocha-Lima, A., Anderson, B., Martins, J., Dubovik, O., Ducos, F., Fuertes, D., Lapyonok, T., Shook, M., Derimian, Y., Moore, R., 2019. A Laboratory Experiment for the Statistical Evaluation of Aerosol Retrieval (STEAR) Algorithms. *Remote Sensing* 11, 498. doi:10.3390/rs11050498
- Schuster, G.L., 2005. Inferring black carbon content and specific absorption from Aerosol Robotic Network (AERONET) aerosol retrievals. *J. Geophys. Res.* 110. doi:10.1029/2004jd004548
- Schuster, G.L., Dubovik, O., Arola, A., 2016a. Remote sensing of soot carbon – Part 1: Distinguishing different absorbing aerosol species. *Atmos. Chem. Phys.* 16, 1565-1585. doi:10.5194/acp-16-1565-2016
- Schuster, G.L., Dubovik, O., Arola, A., Eck, T.F., Holben, B.N., 2016b. Remote sensing of soot carbon – Part 2: Understanding the absorption Ångström exponent. *Atmos. Chem. Phys.* 16, 1587-1602. doi:10.5194/acp-16-1587-2016
- Schuster, G.L., Lin, B., Dubovik, O., 2009. Remote sensing of aerosol water uptake. *Geophys. Res. Lett.* 36, n/a-n/a. doi:10.1029/2008gl036576
- Schwarz, J.P., Gao, R.S., Fahey, D.W., Thomson, D.S., Watts, L.A., Wilson, J.C., Reeves, J.M., Darbeheshti, M., Baumgardner, D.G., Kok, G.L., Chung, S.H., Schulz, M., Hendricks, J., Lauer, A., Kärcher, B., Slowik, J.G., Rosenlof, K.H., Thompson, T.L., Langford, A.O., Loewenstein, M., Aikin, K.C., 2006. Single-particle measurements of midlatitude black carbon and light-scattering aerosols from the boundary layer to the lower stratosphere. *J. Geophys. Res.* 111. doi:10.1029/2006jd007076
- Schwarz, J.P., Spackman, J.R., Fahey, D.W., Gao, R.S., Lohmann, U., Stier, P., Watts, L.A., Thomson, D.S., Lack, D.A., Pfister, L., Mahoney, M.J., Baumgardner, D., Wilson, J.C., Reeves, J.M., 2008. Coatings and their enhancement of black carbon light absorption in the tropical atmosphere. *J. Geophys. Res.* 113. doi:10.1029/2007jd009042

- Sciare, J., Oikonomou, K., Cachier, H., Mihalopoulos, N., Andreae, M.O., Maenhaut, W., Sarda-Estève, R., 2005. Aerosol mass closure and reconstruction of the light scattering coefficient over the Eastern Mediterranean Sea during the MINOS campaign. *Atmos. Chem. Phys.* 5, 2253-2265. doi:10.5194/acp-5-2253-2005
- Seigneur, C., 2019. *Air Pollution: Concepts, Theory, and Applications*. Cambridge University Press.
- Shamjad, P.M., Satish, R.V., Thamban, N.M., Rastogi, N., Tripathi, S.N., 2017. Absorbing Refractive Index and Direct Radiative Forcing of Atmospheric Brown Carbon over Gangetic Plain. *ACS Earth and Space Chemistry* 2, 31-37. doi:10.1021/acsearthspacechem.7b00074
- Shamjad, P.M., Tripathi, S.N., Aggarwal, S.G., Mishra, S.K., Joshi, M., Khan, A., Sapra, B.K., Ram, K., 2012. Comparison of experimental and modeled absorption enhancement by black carbon (BC) cored polydisperse aerosols under hygroscopic conditions. *Environ. Sci. Technol.* 46, 8082-8089. doi:10.1021/es300295v
- Shamjad, P.M., Tripathi, S.N., Thamban, N.M., Vreeland, H., 2016. Refractive Index and Absorption Attribution of Highly Absorbing Brown Carbon Aerosols from an Urban Indian City-Kanpur. *Sci Rep* 6, 37735. doi:10.1038/srep37735
- Sharma, S., Leaitch, W.R., Huang, L., Veber, D., Kolonjari, F., Zhang, W., Hanna, S.J., Bertram, A.K., Ogren, J.A., 2017. An evaluation of three methods for measuring black carbon in Alert, Canada. *Atmos. Chem. Phys.* 17, 15225-15243. doi:10.5194/acp-17-15225-2017
- Shen, S., Jaques, P.A., Zhu, Y., Geller, M.D., Sioutas, C., 2002. Evaluation of the SMPS-APS system as a continuous monitor for measuring PM<sub>2.5</sub>, PM<sub>10</sub> and coarse (PM<sub>2.5</sub>-10) concentrations. *Atmos. Environ.* 36, 3939-3950. doi:10.1016/s1352-2310(02)00330-8
- Sinclair, D., La Mer, V.K., 1949. Light Scattering as a Measure of Particle Size in Aerosols. The Production of Monodisperse Aerosols. *Chem. Rev.* 44, 245-267. doi:10.1021/cr60138a001
- Speer, R.E., Edney, E.O., Kleindienst, T.E., 2003. Impact of organic compounds on the concentrations of liquid water in ambient PM<sub>2.5</sub>. *J. Aerosol Sci* 34, 63-77. doi:10.1016/S0021-8502(02)00152-0
- Stocker, T., 2014. *Climate change 2013: the physical science basis: Working Group I contribution to the Fifth assessment report of the Intergovernmental Panel on Climate Change*. Cambridge University Press.
- Stowe, L.L., Ignatov, A.M., Singh, R.R., 1997. Development, validation, and potential enhancements to the second-generation operational aerosol product at the National Environmental Satellite, Data, and Information Service of the National Oceanic and Atmospheric Administration. *J. Geophys. Res. Atmos.* 102, 16923-16934. doi:10.1029/96jd02132

- Subramanian, R., Khlystov, A.Y., Robinson, A.L., 2006. Effect of Peak Inert-Mode Temperature on Elemental Carbon Measured Using Thermal-Optical Analysis. *Aerosol Sci. Technol.* 40, 763-780. doi:10.1080/02786820600714403
- Sun, H., Biedermann, L., Bond, T.C., 2007. Color of brown carbon: A model for ultraviolet and visible light absorption by organic carbon aerosol. *Geophys. Res. Lett.* 34. doi:10.1029/2007gl029797
- Sun, T., Che, H., Qi, B., Wang, Y., Dong, Y., Xia, X., Wang, H., Gui, K., Zheng, Y., Zhao, H., Ma, Q., Du, R., Zhang, X., 2019. Characterization of vertical distribution and radiative forcing of ambient aerosol over the Yangtze River Delta during 2013-2015. *Sci. Total Environ.* 650, 1846-1857. doi:10.1016/j.scitotenv.2018.09.262
- Sun, Y., Du, W., Wang, Q., Zhang, Q., Chen, C., Chen, Y., Chen, Z., Fu, P., Wang, Z., Gao, Z., Worsnop, D.R., 2015a. Real-Time Characterization of Aerosol Particle Composition above the Urban Canopy in Beijing: Insights into the Interactions between the Atmospheric Boundary Layer and Aerosol Chemistry. *Environ. Sci. Technol.* 49, 11340-11347. doi:10.1021/acs.est.5b02373
- Sun, Y., Song, T., Tang, G., Wang, Y., 2013a. The vertical distribution of PM<sub>2.5</sub> and boundary-layer structure during summer haze in Beijing. *Atmos. Environ.* 74, 413-421. doi:10.1016/j.atmosenv.2013.03.011
- Sun, Y., Zhuang, G., Wang, Y., Zhao, X., Li, J., Wang, Z., An, Z., 2005. Chemical composition of dust storms in Beijing and implications for the mixing of mineral aerosol with pollution aerosol on the pathway. *J. Geophys. Res.* 110. doi:10.1029/2005jd006054
- Sun, Y.L., Wang, Z.F., Du, W., Zhang, Q., Wang, Q.Q., Fu, P.Q., Pan, X.L., Li, J., Jayne, J., Worsnop, D.R., 2015b. Long-term real-time measurements of aerosol particle composition in Beijing, China: seasonal variations, meteorological effects, and source analysis. *Atmos. Chem. Phys.* 15, 10149-10165. doi:10.5194/acp-15-10149-2015
- Sun, Y.L., Wang, Z.F., Fu, P.Q., Yang, T., Jiang, Q., Dong, H.B., Li, J., Jia, J.J., 2013b. Aerosol composition, sources and processes during wintertime in Beijing, China. *Atmos. Chem. Phys.* 13, 4577-4592. doi:10.5194/acp-13-4577-2013
- Tang, I.N., 1996. Chemical and size effects of hygroscopic aerosols on light scattering coefficients. *J. Geophys. Res. Atmos.* 101, 19245-19250. doi:10.1029/96jd03003
- Tang, I.N., Munkelwitz, H.R., 2010. Aerosol Phase Transformation and Growth in the Atmosphere. *J. Appl. Meteorol.* 33
- Tao, J., Zhang, L., Cao, J., Zhang, R., 2017. A review of current knowledge concerning PM<sub>2.5</sub>; chemical composition, aerosol optical properties and their relationships across China. *Atmos. Chem. Phys.* 17, 9485-9518. doi:10.5194/acp-17-9485-2017
- Tao, M., Chen, L., Xiong, X., Zhang, M., Ma, P., Tao, J., Wang, Z., 2014. Formation

- process of the widespread extreme haze pollution over northern China in January 2013: Implications for regional air quality and climate. *Atmos. Environ.* 98, 417-425. doi:10.1016/j.atmosenv.2014.09.026
- Taylor, J.W., Allan, J.D., Allen, G., Coe, H., Williams, P.I., Flynn, M.J., Le Breton, M., Muller, J.B.A., Percival, C.J., Oram, D., Forster, G., Lee, J.D., Rickard, A.R., Parrington, M., Palmer, P.I., 2014. Size-dependent wet removal of black carbon in Canadian biomass burning plumes. *Atmos. Chem. Phys.* 14, 13755-13771. doi:10.5194/acp-14-13755-2014
- Tellez-Rojo, M.M., Rothenberg, S.J., Texcalac-Sangrador, J.L., Just, A.C., Kloog, I., Rojas-Saunero, L.P., Gutierrez-Avila, I., Bautista-Arredondo, L.F., Tamayo-Ortiz, M., Romero, M., Hurtado-Diaz, M., Schwartz, J.D., Wright, R., Riojas-Rodriguez, H., 2020. Children's acute respiratory symptoms associated with PM<sub>2.5</sub> estimates in two sequential representative surveys from the Mexico City Metropolitan Area. *Environ. Res.* 180, 108868. doi:10.1016/j.envres.2019.108868
- Textor, C., Schulz, M., Guibert, S., Kinne, S., Balkanski, Y., Bauer, S., Berntsen, T., Berglen, T., Boucher, O., Chin, M., Dentener, F., Diehl, T., Easter, R., Feichter, H., Fillmore, D., Ghan, S., Ginoux, P., Gong, S., Grini, A., Hendricks, J., Horowitz, L., Huang, P., Isaksen, I., Iversen, I., Kloster, S., Koch, D., Kirkevåg, A., Kristjansson, J.E., Krol, M., Lauer, A., Lamarque, J.F., Liu, X., Montanaro, V., Myhre, G., Penner, J., Pitari, G., Reddy, S., Seland, Ø., Stier, P., Takemura, T., Tie, X., 2006. Analysis and quantification of the diversities of aerosol life cycles within AeroCom. *Atmos. Chem. Phys.* 6, 1777-1813. doi:10.5194/acp-6-1777-2006
- Thompson, J.E., Barta, N., Policarpio, D., DuVall, R., 2008. A fixed frequency aerosol albedometer. *Opt. Express* 16, 2191-2205. doi:10.1364/OE.16.002191
- TSI, I., 2004. Model 3321 Aerodynamic Particle Sizer Spectrometer Instruction Manual. TSI, Incorporated Shoreview, Minn.
- Turpin, B.J., Lim, H.-J., 2001. Species Contributions to PM<sub>2.5</sub> Mass Concentrations: Revisiting Common Assumptions for Estimating Organic Mass. *Aerosol Sci. Technol.* 35, 602-610. doi:10.1080/02786820119445
- Valenzuela, A., Olmo, F., Lyamani, H., Antón, M., Quirantes, A., Alados - Arboledas, L., 2012. Classification of aerosol radiative properties during African desert dust intrusions over southeastern Spain by sector origins and cluster analysis. *J. Geophys. Res. Atmos.* 117
- Varma, R., Moosmüller, H., Arnott, W.P., 2003. Toward an ideal integrating nephelometer. *Opt. Lett.* 28, 1007-1009. doi:10.1364/OL.28.001007
- Virkkula, A., Koponen, I.K., Teinilä, K., Hillamo, R., Kerminen, V.M., Kulmala, M., 2006. Effective real refractive index of dry aerosols in the Antarctic boundary layer. *Geophys. Res. Lett.* 33. doi:10.1029/2005gl024602
- Vong, R.J., Vong, I.J., Vickers, D., Covert, D.S., 2010. Size-dependent aerosol

- deposition velocities during BEARPEX'07. *Atmos. Chem. Phys.* 10, 5749-5758. doi:10.5194/acp-10-5749-2010
- Wagner, R., Ajtai, T., Kandler, K., Lieke, K., Linke, C., Müller, T., Schnaiter, M., Vragel, M., 2012. Complex refractive indices of Saharan dust samples at visible and near UV wavelengths: a laboratory study. *Atmos. Chem. Phys.* 12, 2491-2512. doi:10.5194/acp-12-2491-2012
- Wang, J., Nie, W., Cheng, Y., Shen, Y., Chi, X., Wang, J., Huang, X., Xie, Y., Sun, P., Xu, Z., Qi, X., Su, H., Ding, A., 2018. Light absorption of brown carbon in eastern China based on 3-year multi-wavelength aerosol optical property observations and an improved absorption Ångström exponent segregation method. *Atmos. Chem. Phys.* 18, 9061-9074. doi:10.5194/acp-18-9061-2018
- Wang, L., Li, Z., Tian, Q., Ma, Y., Zhang, F., Zhang, Y., Li, D., Li, K., Li, L., 2013. Estimate of aerosol absorbing components of black carbon, brown carbon, and dust from ground-based remote sensing data of sun-sky radiometers. *J. Geophys. Res. Atmos.* 118, 6534-6543. doi:10.1002/jgrd.50356
- Wang, S., Zhao, W., Xu, X., Fang, B., Zhang, Q., Qian, X., Zhang, W., Chen, W., Pu, W., Wang, X., 2017a. Dependence of columnar aerosol size distribution, optical properties, and chemical components on regional transport in Beijing. *Atmos. Environ.* 169, 128-139. doi:10.1016/j.atmosenv.2017.09.016
- Wang, S.C., Flagan, R.C., 1990. Scanning Electrical Mobility Spectrometer. *Aerosol Sci. Technol.* 13, 230-240. doi:10.1080/02786829008959441
- Wang, X., Heald, C.L., Sedlacek, A.J., de Sá, S.S., Martin, S.T., Alexander, M.L., Watson, T.B., Aiken, A.C., Springston, S.R., Artaxo, P., 2016. Deriving brown carbon from multiwavelength absorption measurements: method and application to AERONET and Aethalometer observations. *Atmos. Chem. Phys.* 16, 12733-12752. doi:10.5194/acp-16-12733-2016
- Wang, Y., Zhang, F., Li, Z., Tan, H., Xu, H., Ren, J., Zhao, J., Du, W., Sun, Y., 2017b. Enhanced hydrophobicity and volatility of submicron aerosols under severe emission control conditions in Beijing. *Atmos. Chem. Phys.* 17, 5239-5251. doi:10.5194/acp-17-5239-2017
- Wang, Y.Q., 2004. The transport pathways and sources of PM<sub>10</sub> pollution in Beijing during spring 2001, 2002 and 2003. *Geophys. Res. Lett.* 31. doi:10.1029/2004gl019732
- Wehner, B., Birmili, W., Ditas, F., Wu, Z., Hu, M., Liu, X., Mao, J., Sugimoto, N., Wiedensohler, A., 2008. Relationships between submicrometer particulate air pollution and air mass history in Beijing, China, 2004–2006. *Atmos. Chem. Phys.* 8, 6155-6168
- Welton, E.J., Campbell, J.R., 2002. Micropulse Lidar Signals: Uncertainty Analysis. *Journal of Atmospheric and Oceanic Technology* 19, 2089-2094.

- doi:10.1175/1520-0426(2002)019<2089:MLSUA>2.0.CO;2
- Wexler, A.S., Clegg, S.L., 2002. Atmospheric aerosol models for systems including the ions H<sup>+</sup>, NH<sub>4</sub><sup>+</sup>, Na<sup>+</sup>, SO<sub>4</sub><sup>2-</sup>, NO<sub>3</sub><sup>-</sup>, Cl<sup>-</sup>, Br<sup>-</sup>, and H<sub>2</sub>O. *J. Geophys. Res. Atmos.* 107, ACH 14-11-ACH 14-14. doi:10.1029/2001JD000451
- Wilcox, E.M., Thomas, R.M., Praveen, P.S., Pistone, K., Bender, F.A., Ramanathan, V., 2016. Black carbon solar absorption suppresses turbulence in the atmospheric boundary layer. *Proc. Natl. Acad. Sci. U. S. A.* 113, 11794-11799. doi:10.1073/pnas.1525746113
- Williams, J., de Reus, M., Krejci, R., Fischer, H., Ström, J., 2002. Application of the variability-size relationship to atmospheric aerosol studies: estimating aerosol lifetimes and ages. *Atmos. Chem. Phys.* 2, 133-145. doi: 10.5194/acp-2-133-2002, 2002
- Winker, D.M., Hunt, W.H., McGill, M.J., 2007. Initial performance assessment of CALIOP. *Geophys. Res. Lett.* 34. doi:10.1029/2007gl030135
- Wojtas, J., Mikolajczyk, J., Bielecki, Z., 2013. Aspects of the application of cavity enhanced spectroscopy to nitrogen oxides detection. *Sensors (Basel)*. 13, 7570-7598. doi:10.3390/s130607570
- Wu, C., Wu, D., Yu, J.Z., 2018a. Quantifying black carbon light absorption enhancement with a novel statistical approach. *Atmos. Chem. Phys.* 18, 289-309. doi:10.5194/acp-18-289-2018
- Wu, Y., Cheng, T., Liu, D., Allan, J.D., Zheng, L., Chen, H., 2018b. Light Absorption Enhancement of Black Carbon Aerosol Constrained by Particle Morphology. *Environ. Sci. Technol.* doi:10.1021/acs.est.8b00636
- Wu, Z.J., Cheng, Y.F., Hu, M., Wehner, B., Sugimoto, N., Wiedensohler, A., 2009. Dust events in Beijing, China (2004–2006): comparison of ground-based measurements with columnar integrated observations. *Atmos. Chem. Phys.* 9, 6915-6932. doi:10.5194/acp-9-6915-2009
- Xia, X., Chen, H., Goloub, P., Zong, X., Zhang, W., Wang, P., 2013. Climatological aspects of aerosol optical properties in North China Plain based on ground and satellite remote-sensing data. *J. Quant. Spectrosc. Radiat. Transfer* 127, 12-23. doi:10.1016/j.jqsrt.2013.06.024
- Xia, X., Chen, H., Zhang, W., 2007. Analysis of the dependence of column-integrated aerosol properties on long-range transport of air masses in Beijing. *Atmos. Environ.* 41, 7739-7750. doi:10.1016/j.atmosenv.2007.06.042
- Xie, Y., Li, Z., Li, L., Wang, L., Li, D., Chen, C., Li, K., Xu, H., 2014. Study on influence of different mixing rules on the aerosol components retrieval from ground-based remote sensing measurements. *Atmos. Res.* 145-146, 267-278. doi:10.1016/j.atmosres.2014.04.006

- Xie, Y.S., Li, Z.Q., Zhang, Y.X., Zhang, Y., Li, D.H., Li, K.T., Xu, H., Zhang, Y., Wang, Y.Q., Chen, X.F., Schauer, J.J., Bergin, M., 2017. Estimation of atmospheric aerosol composition from ground-based remote sensing measurements of Sun-sky radiometer. *J. Geophys. Res. Atmos.* 122, 498-518. doi:10.1002/2016jd025839
- Xing, L., Fu, T.M., Cao, J.J., Lee, S.C., Wang, G.H., Ho, K.F., Cheng, M.C., You, C.F., Wang, T.J., 2013. Seasonal and spatial variability of the OM/OC mass ratios and high regional correlation between oxalic acid and zinc in Chinese urban organic aerosols. *Atmos. Chem. Phys.* 13, 4307-4318. doi:10.5194/acp-13-4307-2013
- Xu, W.Y., Zhao, C.S., Ran, L., Deng, Z.Z., Ma, N., Liu, P.F., Lin, W.L., Yan, P., Xu, X.B., 2013a. A new approach to estimate pollutant emissions based on trajectory modeling and its application in the North China Plain. *Atmos. Environ.* 71, 75-83. doi:10.1016/j.atmosenv.2013.01.047
- Xu, X., Zhao, W., Fang, B., Zhou, J., Wang, S., Zhang, W., Venables, D.S., Chen, W., 2018a. Three-wavelength cavity-enhanced albedometer for measuring wavelength-dependent optical properties and single-scattering albedo of aerosols. *Opt. Express* 26, 33484. doi:10.1364/oe.26.033484
- Xu, X., Zhao, W., Qian, X., Wang, S., Fang, B., Zhang, Q., Zhang, W., Venables, D.S., Chen, W., Huang, Y., Deng, X., Wu, B., Lin, X., Zhao, S., Tong, Y., 2018b. The influence of photochemical aging on light absorption of atmospheric black carbon and aerosol single-scattering albedo. *Atmos. Chem. Phys.* 18, 16829-16844. doi:10.5194/acp-18-16829-2018
- Xu, X., Zhao, W., Zhang, Q., Wang, S., Fang, B., Chen, W., Venables, D.S., Wang, X., Pu, W., Wang, X., Gao, X., Zhang, W., 2016. Optical properties of atmospheric fine particles near Beijing during the HOPE-J&lt;sup>3</sup>&lt;/sup>A campaign. *Atmos. Chem. Phys.* 16, 6421-6439. doi:10.5194/acp-16-6421-2016
- Xu, Y., Bahadur, R., Zhao, C., Ruby Leung, L., 2013b. Estimating the radiative forcing of carbonaceous aerosols over California based on satellite and ground observations. *J. Geophys. Res. Atmos.* 118, 11,148-111,160. doi:10.1002/jgrd.50835
- Yang, L.X., Wang, D.C., Cheng, S.H., Wang, Z., Zhou, Y., Zhou, X.H., Wang, W.X., 2007. Influence of meteorological conditions and particulate matter on visual range impairment in Jinan, China. *Sci. Total Environ.* 383, 164-173. doi:10.1016/j.scitotenv.2007.04.042
- Yang, M., Howell, S.G., Zhuang, J., Huebert, B.J., 2009. Attribution of aerosol light absorption to black carbon, brown carbon, and dust in China – interpretations of atmospheric measurements during EAST-AIRE. *Atmos. Chem. Phys.* 9, 2035-2050. doi:10.5194/acp-9-2035-2009
- Yang, Y.R., Liu, X.G., Qu, Y., An, J.L., Jiang, R., Zhang, Y.H., Sun, Y.L., Wu, Z.J., Zhang, F., Xu, W.Q., Ma, Q.X., 2015. Characteristics and formation mechanism of continuous hazes in China: a case study during the autumn of 2014 in the North

- China Plain. *Atmos. Chem. Phys.* 15, 8165-8178. doi:10.5194/acp-15-8165-2015
- Yao, L., Yang, L., Yuan, Q., Yan, C., Dong, C., Meng, C., Sui, X., Yang, F., Lu, Y., Wang, W., 2016. Sources apportionment of PM<sub>2.5</sub> in a background site in the North China Plain. *Sci. Total Environ.* 541, 590-598. doi:10.1016/j.scitotenv.2015.09.123
- Yaws, C.L., 1999. *Chemical properties handbook: physical, thermodynamic, environmental, transport, safety, and health related properties for organic and inorganic chemicals.* McGraw-Hill New York.
- Yu, X., Shi, C., Ma, J., Zhu, B., Li, M., Wang, J., Yang, S., Kang, N., 2013. Aerosol optical properties during firework, biomass burning and dust episodes in Beijing. *Atmos. Environ.* 81, 475-484. doi:10.1016/j.atmosenv.2013.08.067
- Yu, X., Zhu, B., Zhang, M., 2009. Seasonal variability of aerosol optical properties over Beijing. *Atmos. Environ.* 43, 4095-4101. doi:10.1016/j.atmosenv.2009.03.061
- Zanatta, M., Gysel, M., Bukowiecki, N., Müller, T., Weingartner, E., Areskoug, H., Fiebig, M., Yttri, K.E., Mihalopoulos, N., Kouvarakis, G., Beddows, D., Harrison, R.M., Cavalli, F., Putaud, J.P., Spindler, G., Wiedensohler, A., Alastuey, A., Pandolfi, M., Sellegri, K., Swietlicki, E., Jaffrezo, J.L., Baltensperger, U., Laj, P., 2016. A European aerosol phenomenology-5: Climatology of black carbon optical properties at 9 regional background sites across Europe. *Atmos. Environ.* 145, 346-364. doi:10.1016/j.atmosenv.2016.09.035
- Zaveri, R.A., Barnard, J.C., Easter, R.C., Riemer, N., West, M., 2010. Particle-resolved simulation of aerosol size, composition, mixing state, and the associated optical and cloud condensation nuclei activation properties in an evolving urban plume. *J. Geophys. Res.* 115. doi:10.1029/2009jd013616
- Zhai, J., Lu, X., Li, L., Zhang, Q., Zhang, C., Chen, H., Yang, X., Chen, J., 2017. Size-resolved chemical composition, effective density, and optical properties of biomass burning particles. *Atmos. Chem. Phys.* 17, 7481-7493. doi:10.5194/acp-17-7481-2017
- Zhang, G., Peng, L., Lian, X., Lin, Q., Bi, X., Chen, D., Li, M., Li, L., Wang, X., Sheng, G., 2019. An Improved Absorption Ångström Exponent (AAE)-Based Method for Evaluating the Contribution of Light Absorption from Brown Carbon with a High-Time Resolution. *Aerosol Air Qual. Res.* 19, 15-24. doi:10.4209/aaqr.2017.12.0566
- Zhang, H., Lyapustin, A., Wang, Y., Kondragunta, S., Laszlo, I., Ciren, P., Hoff, R.M., 2011. A multi-angle aerosol optical depth retrieval algorithm for geostationary satellite data over the United States. *Atmos. Chem. Phys.* 11, 11977-11991. doi:10.5194/acp-11-11977-2011
- Zhang, J., Chen, J., Xia, X., Che, H., Fan, X., Xie, Y., Han, Z., Chen, H., Lu, D., 2016. Heavy aerosol loading over the Bohai Bay as revealed by ground and satellite

- remote sensing. *Atmos. Environ.* 124, 252-261.  
doi:10.1016/j.atmosenv.2015.03.048
- Zhang, Q., Ma, X., Tie, X., Huang, M., Zhao, C., 2009. Vertical distributions of aerosols under different weather conditions: Analysis of in-situ aircraft measurements in Beijing, China. *Atmos. Environ.* 43, 5526-5535.  
doi:10.1016/j.atmosenv.2009.05.037
- Zhang, R., Li, G., Fan, J., Wu, D.L., Molina, M.J., 2007. Intensification of Pacific storm track linked to Asian pollution. *Proc. Natl. Acad. Sci. U. S. A.* 104, 5295-5299.  
doi:10.1073/pnas.0700618104
- Zhang, T., Claeys, M., Cachier, H., Dong, S., Wang, W., Maenhaut, W., Liu, X., 2008. Identification and estimation of the biomass burning contribution to Beijing aerosol using levoglucosan as a molecular marker. *Atmos. Environ.* 42, 7013-7021.  
doi:10.1016/j.atmosenv.2008.04.050
- Zhang, X., Mao, M., 2015. Brown haze types due to aerosol pollution at Hefei in the summer and fall. *Chemosphere* 119, 1153-1162.  
doi:10.1016/j.chemosphere.2014.08.038
- Zhang, Y., Li, Z., Sun, Y., Lv, Y., Xie, Y., 2018. Estimation of atmospheric columnar organic matter (OM) mass concentration from remote sensing measurements of aerosol spectral refractive indices. *Atmos. Environ.* 179, 107-117.  
doi:10.1016/j.atmosenv.2018.02.010
- Zhao, G., Tan, T., Zhao, W., Guo, S., Tian, P., Zhao, C., 2019. A new parameterization scheme for the real part of the ambient urban aerosol refractive index. *Atmos. Chem. Phys.* 19, 12875-12885. doi:10.5194/acp-19-12875-2019
- Zhao, H., Che, H., Ma, Y., Wang, Y., Yang, H., Liu, Y., Wang, Y., Wang, H., Zhang, X., 2017a. The Relationship of PM Variation with Visibility and Mixing-Layer Height under Hazy/Foggy Conditions in the Multi-Cities of Northeast China. *Int. J. Environ. Res. Public Health.* 14. doi:10.3390/ijerph14050471
- Zhao, T., Yang, L., Yan, W., Zhang, J., Lu, W., Yang, Y., Chen, J., Wang, W., 2017b. Chemical characteristics of PM<sub>1</sub>/PM<sub>2.5</sub> and influence on visual range at the summit of Mount Tai, North China. *Sci. Total Environ.* 575, 458-466.  
doi:10.1016/j.scitotenv.2016.09.173
- Zhao, W., Dong, M., Chen, W., Gu, X., Hu, C., Gao, X., Huang, W., Zhang, W., 2013. Wavelength-resolved optical extinction measurements of aerosols using broadband cavity-enhanced absorption spectroscopy over the spectral range of 445-480 nm. *Anal. Chem.* 85, 2260-2268. doi:10.1021/ac303174n
- Zhao, W., Xu, X., Dong, M., Chen, W., Gu, X., Hu, C., Huang, Y., Gao, X., Huang, W., Zhang, W., 2014. Development of a cavity-enhanced aerosol albedometer. *Atmos. Meas. Tech.* 7, 2551-2566. doi:10.5194/amt-7-2551-2014
- Zhao, W., Xu, X., Fang, B., Zhang, Q., Qian, X., Wang, S., Liu, P., Zhang, W., Wang,

- Z., Liu, D., Huang, Y., Venables, D.S., Chen, W., 2017c. Development of an incoherent broad-band cavity-enhanced aerosol extinction spectrometer and its application to measurement of aerosol optical hygroscopicity. *Appl. Opt.* 56, E16-E22. doi:10.1364/AO.56.000E16
- Zheng, G.J., Duan, F.K., Su, H., Ma, Y.L., Cheng, Y., Zheng, B., Zhang, Q., Huang, T., Kimoto, T., Chang, D., Pöschl, U., Cheng, Y.F., He, K.B., 2015. Exploring the severe winter haze in Beijing: the impact of synoptic weather, regional transport and heterogeneous reactions. *Atmos. Chem. Phys.* 15, 2969-2983. doi:10.5194/acp-15-2969-2015
- Zhou, J., Tung, K.-K., 2013. Deducing Multidecadal Anthropogenic Global Warming Trends Using Multiple Regression Analysis. *J. Atmos. Sci.* 70, 3-8. doi:10.1175/jas-d-12-0208.1
- Zíková, N., Wang, Y., Yang, F., Li, X., Tian, M., Hopke, P.K., 2016. On the source contribution to Beijing PM<sub>2.5</sub> concentrations. *Atmos. Environ.* 134, 84-95. doi:10.1016/j.atmosenv.2016.03.047
- Zuo, M., Zhou, T., Man, W., 2019. Wetter global arid regions driven by volcanic eruptions. *J. Geophys. Res. Atmos.* 124, 13648-13662. doi:10.1029/2019JD031171